OPTICAL AND MINORITY CARRIER CONFINEMENT IN LEAD SELENIDE HOMOJUNCTION LASERS

by

Peter Michael Asbeck

S.B., Massachusetts Institute of Technology
(1969)

S.M., Massachusetts Institute of Technology
(1969)

SUBMITTED IN PARTIAL FULFILLMENT OF THE
REQUIREMENTS FOR THE DEGREE OF
DOCTOR OF PHILOSOPHY

at the

MASSACHUSETTS INSTITUTE OF TECHNOLOGY

February, 1975

Signature of Author..
Department of Electrical Engineering

Certified by.............
Thesis Supervisor

Accepted by.........................
Chairman, Departmental Committee on Graduate Students

ARCHIVES

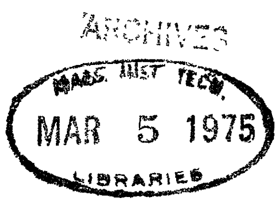

OPTICAL AND MINORITY CARRIER CONFINEMENT IN LEAD SELENIDE HOMOJUNCTION LASERS

by

Peter Michael Asbeck

Submitted to the Department of Electrical Engineering on December 20, 1974, in partial fulfillment of the requirements for the Degree of Doctor of Philosophy

ABSTRACT

An analysis of the spatial distributions of the minority and majority carrier densities and of the lasing radiation mode in the vicinity of the p-n junction of diffused PbSe homojunction lasers is reported. The analysis demonstrates that the width of the distributions depends significantly on the grading of the net donor-acceptor density near the junction. The width of the carrier distributions is affected by junction electric fields which act to retard the diffusion of minority carriers, where the magnitude of the fields is determined by the effective junction grading parameter and the injection level. The width of the lasing radiation mode is controlled by the spatial variation of the real part of the dielectric constant, which reaches a maximum near the junction. The changes of the dielectric constant with position are dominated by the effects, both intraband and interband, of the changing carrier densities with position. Relative confinement effects of the junction grading on the distributions of the carriers and the optical field are found to be greater than in the case of GaAs lasers.

Particular attention is given in this study to lasers fabricated by diffusing excess selenium into substrates that are saturated with lead. It is shown experimentally by a microwave technique that the profile of the net donor-acceptor density resulting from such diffusions is approximately in agreement with the predictions of Walpole, Guldi and Brodersen.

Measurements of far-field patterns obtained at 77°K for a series of PbSe diodes are reported. The mode widths and inferred from the divergence of the laser output beams confirm the analysis presented in this work. The mode widths varied between 6.8 and 14.5 microns for the diodes studied.

The total number of injected minority carriers at threshold in the lasers was inferred from the value of the minority carrier recombination lifetime. Measurements of this lifetime made with a variation of the time-delay technique are reported for the lasers fabricated. Its value was found to be 2 nsec, which indicates a low efficiency of spontaneous radiative recombination below threshold.

An analysis is given for the threshold current density of diffused PbSe lasers which takes into account the confinement of the minority carriers and the optical mode. Improved confinement of either distribution is shown to result in a lower value of threshold current density at high temperatures. Measurements of the temperature variation of the threshold current density are reported for several lasers; the results are consistent with the model presented.

THESIS SUPERVISOR: George W. Pratt, Jr.
TITLE: Professor of Electrical Engineering

ACKNOWLEDGEMENTS

The author is deeply grateful to his thesis advisor, Professor G.W. Pratt, Jr., for continued guidance and support throughout the course of this work. He is also deeply indebted to J.N. Walpole of Lincoln Laboratory for innumerable helpful conversations, suggestions and criticisms, for having made available material prior to publication and for having acted as thesis reader. He would also like to thank Professor D. Adler for having acted as thesis reader and for helpful conversations.

The author thankfully acknowledges the contributions of A.R. Calawa of Lincoln Laboratory, who made available equipment and provided many useful comments; of Professor J.E. Ripper of the Universidade Estadual de Campinas, Campinas, Brasil, who pointed out the possibility and usefulness of the recombination lifetime measurement; of A. Colozzi, who provided much advice and help in the experiments; of P.A. Wolff, who gave advice particularly with regard to Appendix C; and of Professor A. Barrett and J. Barrett of the Research Laboratory of Electronics, who made available the microwave equipment.

Numerous contributions were made by the author's colleagues, especially D. Lee, D. Cammack, J. Lowney, A. Nurmikko, P. McMullin and L. Walker. The author is grateful to all of them.

The author would like to thank his wife, Marcia, for help and support during the writing of the thesis.

Finally, he is very grateful to P. Wallace for excellent work in the typing of the manuscript.

TABLE OF CONTENTS

Page

TITLE PAGE 1

ABSTRACT 2

ACKNOWLEDGEMENTS 4

TABLE OF CONTENTS 5

LIST OF FIGURES 8

LIST OF TABLES 13

CHAPTER I. INTRODUCTION 14

1. Importance of Lead Salt Lasers 14
2. Optical and Carrier Confinement in Junction Lasers 16
3. Scope of this Thesis 18

CHAPTER II. JUNCTION GRADING IN DIFFUSED LASERS 21

1. Introduction 21
2. Junction Preparation Method 22
3. BWG Model of Stoichiometry Profile 23
4. Experimental Characterization of Junction Diffusions 26
   (i) Hall Measurements 26
   (ii) Junction Depth Measurements 27
   (iii) Microwave Reflectivity Measurements 28
   (iv) Junction Capacitance Measurements 32
   (v) Discussion 35

CHAPTER III. MINORITY CARRIER CONFINEMENT IN DIFFUSED LASERS 49

1. Introduction 49
2. Measurements of Minority Carrier Lifetime 50

(i) Experimental Techniques.............. 52
(ii) Results and Discussion................ 52
(iii) Interpretation of Lifetime.............. 53

3. Model for Carrier Distributions under Forward Bias.................................... 57

(i) Model Description...................... 60
(ii) Method of Solution..................... 63
(iii) Model Results.......................... 66
(iv) Validity of Quasineutrality Assumption... 69
(v) Carrier Distributions Above Lasing Threshold............................. 71
(vi) Carrier Distributions for Asymmetric Profiles.............................. 73

CHAPTER IV. OPTICAL MODE CONFINEMENT IN DIFFUSED LASERS.................... 88

1. Introduction................................. 88
2. Sources of Dielectric Constant Variation....... 88

(i) Intraband Contribution................. 89
(ii) Interband Contribution: Extremal Bands. 91
(iii) Far Band Contributions................ 98
(iv) Core and Lattice Contributions......... 100
(v) Stress Effects........................ 102
(vi) Temperature Effects.................. 104

3. Dielectric Profile of PbSe Lasers............ 106
4. Dielectric Waveguide Mode Solutions......... 109

(i) Review of Existing Waveguide Models... 112
(ii) Waveguide Model with Linear Variation of ϵ 115
(iii) Dispersion Relations and Mode Spacings............................. 119
(iv) End Losses and Far-field Patterns...... 122
(v) Distributed Mode Losses................ 126
(vi) Application to PbSe Lasers............. 129

5. Experimental Verifications of Far-field Patterns.................................... 132

(i) Experimental Method.................. 132
(ii) Experimental Results and Analysis...... 134
(iii) Discussion............................ 139

CHAPTER V. EFFECTS OF CARRIER AND OPTICAL CONFINEMENT....................... 171

1. Introduction............................... 171
2. Models for Gain............................ 175
3. Analysis of Threshold Current Density......... 178
4. Measurements of Threshold Current Density... 187

CHAPTER VI. SUMMARY AND CONCLUSIONS......... 205

APPENDICES

A. Laser Fabrication Procedures............... 208
B. Band Model for PbSe....................... 215
C. Many-Body Effects on the Absorption Edge of PbSe.................................. 222
D. Additional Dielectric Waveguide Models...... 247

REFERENCES....................................... 255

BIOGRAPHICAL NOTE............................. 264

LIST OF FIGURES

Page

1 Output Wavelengths of Lead Salt Lasers.......... 19

2 Schematic of Homojunction and Heterojunction Lasers.................................... 20

3 Phase Diagram of PbSe......................... 38

4 Variation of Effective Diffusion Coefficient with Stoichiometry.............................. 39

5 Predicted Stoichiometry Profiles for P into N Diffusions....................................... 40

6 Comparison of Predicted and Measured Variations of Junction Depth with Diffusion Time............ 41

7 Microwave Equipment for Reflectivity Measurements................................ 42

8 Measured Variation of η with Distance from Surface....................................... 43

9 Penetration Depth for PbSe at 74.6 GHz.......... 44

10 Electrical Characteristics of Diodes............. 45

11 Model Profiles for P into N Diffusions........... 46

12 Variation of Total Number of Injected Minority Carriers with Time........................... 77

13 Measured Output Power Versus Pulse Amplitude for Current Pulses of Varying Width............. 78

14 Measured Variation of $\ln(I/(I-I_{th}))$ with Pulse Width.................................. 79

15 Occupation Factor F for Radiative Lifetime Calculation.................................... 80

16 Approximate Band Diagram of Forward-Biased Junction, Showing Definitions of Ψ, ϕ_n and ϕ_p.. 81

17	Variation of Mobility with Temperature in PbSe....................................	81
18	Variation of λ with Temperature in PbSe........	82
19	Variation of the Effective Density of States N_d with Temperature in PbSe........................	82
20	Calculated Variation of Normalized Carrier Densities with Position.........................	83
21	Variation of Normalized Potential and Quasifermi Levels with Position for Various Values of ϑ	84
22	Variation of Normalized Current with ϑ	85
23	Variation with Position of $d^2\Psi/dz^2$ for $\vartheta = 0$, $\lambda = 0$...	86
24	Asymmetric Profile Model for Calculation of Carrier Distributions...........................	87
25	Energy Dependence of m_c^* for PbSe at 77°K........	143
26	Variation of Re ϵ_{fc} and I_m ϵ_{fc} with Carrier Concentration..................................	144
27	Frequency Dependence of Im ϵ_{cv} Near the Bandedge..	145
28	Frequency Dependence of Δ Re ϵ_{cv}............	146
29	Variation of Δ Re ϵ_{cv} with Carrier Concentration..	147
30	Far-Band Resonances of Interest in Calculation of $\Delta\epsilon$	148
31	Results of Model I of Stoichiometry Profile.......	149
32	Results of Model II of Stoichiometry Profile.......	150
33	Results of Model III of Stoichiometry Profile......	151
34	Coordinate System Used for Mode Calculation.....	152
35	Comparison of Model Dielectric Profiles for Mode Calculation...............................	152
36	Comparison of Airy Modes and Hermite-Gaussian Modes of Orders 0 and 4......................	153
37	Variation of Mode Width with Mode Number.......	154

38	Variation of Eigenvalues λ_1 and λ_2, and C_η with Asymmetry Parameter η	155
39	Typical Asymmetrical Airy Mode Shapes	156
40	Variation of Reflection Coefficient with Transverse Wavevector q_x	157
41	Squared Magnitude of the Fourier Transform of the Completely Asymmetric Airy Mode	158
42	Variation with η of Parameter for Calculation of Free Carrier Absorption Losses	155
43	Apparatus for the Measurement of Laser Far-Field Patterns	159
44	Typical Laser Output Spectrum	160
45	Typical Far-Field Pattern in Y-Z Plane	160
46	Typical Far-Field Pattern of Total Laser Output in X-Z Plane	161
47	Effect of Current on Direction of Laser Output	162
48	Typical Irregular Far-Field Pattern Corresponding to a Single Frequency	163
49	Typical Regular Far-Field Patterns Corresponding to Single-Frequencies	164
50	Calculated Relation between $\Delta\theta_{eq}$ and w_o	165
51	Measured Variation of w_o with Junction Depth	166
52	Typical Variation of Local Gain with Injected Carrier Density	190
53	Units of Gain g and Integrated Gain H_m vs. Temperature	190
54	Units of J_A vs. Temperature	191
55	Frequency Dependence of Normalized Gain	192
56	Effect of Broadening on the Frequency Dependence of the Gain	193
57	Effect of Broadening on the Maximum Value of the Gain	194
58	Variation of h_{mo} and g with ϑ	195

59 Plot of h_{mo} vs. ζ Parametrized by ν 196

60 Variation of h_{mo} and ζ with λ 197

61 Plot of h_{mo} vs. ζ Parametrized by λ 197

62 Predicted Variation of Threshold Current Density with Temperature........................ 198

63 Predicted Variation of Threshold Current Density with Junction Grading Parameter.......... 199

64 Variation of h_{ms} with ν 200

65 Predicted Variation of Threshold Current Density with Temperature Including the Effects of Broadening........................... 201

66 Typical Variation of Collected Diode Radiation with Current.......................... 202

67 Measured Variation of Threshold Current Density with Temperature....................... 203

68 Interference Microphotograph of Typical Polished Mirror Facet of a Laser................ 214

69 Calculated Variation of Carrier Concentration with Fermi Energy for PbSe at $77^{o}K$.. 220

70 Spectral Density Functions of Electron States Including the Effects of Coulomb Interaction with Defects......................... 241

71 Calculated Density of States near the Bandedge....................................... 242

72 Variation of Exchange Energy Shift with Carrier Concentration...................... 243

73 Comparison of Frequency Dependence of Homogeneously Broadened Absorption Edge and Urbach's Rule............................. 244

74 Schematic of Different Regimes of Interest in the Calculation of τ 245

75 Dielectric Profile Models A and B................ 251

76 Variation of Eigenvalue λ_m with L_A/x_o and L_B/x_o.................................. 252

77 Typical Mode Shapes for Dielectric Profile Model A.................................. 252

78 Variation of Mode Width w_o with L_A/x_o........... 253

79 Typical Mode Shapes for Dielectric Profile Model B... 254

LIST OF TABLES

Page

I Parameters of BWG Model for Calculation of the Stoichiometry Profile..................... 47

II Results of Hall Measurements.................. 48

III Experimental Values of Characteristic Energy E_s of the Exponential Absorption Edge..167

IV Contributions of Far-Bands to the Variation of ϵ with Carrier Concentration................168

V Dielectric Profile Parameters..................169

VI Experimental Beam Widths and Mode Widths..170

VII Diode Parameters used for the Calculation of J_{th}..204

VIII Parmaeters and Results of k. p Model for PbSe.................................... 221

IX Parameters Used for Estimation of Many-Body Effects in PbSe.......................... 246

CHAPTER I
INTRODUCTION

I.1 Importance of Lead Salt Lasers

Lead salt lasers have been under development since 1964, when stimulated emission was first obtained from a PbTe p-n junction.[1] At present the family of lead salt materials in which laser action has been observed includes a wide range of compounds and pseudobinary alloys, many of which are shown in Fig. 1. Output frequencies of the lasers lie in the infrared region of the spectrum; by adjusting alloy composition, lasers whose output is at any wavelength between 2.5μ and 32μ may be fabricated.[2,3] Individual lasers, in addition, may be tuned over a sizeable frequency range because the value of the energy gap of lead salt semiconductors is highly sensitive to temperature, stress and magnetic field. Commonly lasers are tuned by the convenient method of adjusting the diode current, which affects the temperature of the laser junction.[4]

Measurements have shown that when lead salt lasers are operated continuously, single mode outputs of narrow linewidth (as little as 54 KHz) and high frequency stability may be obtained.[5] The combination of narrow linewidth and tunability has enabled researchers to use lead salt lasers in molecular spectroscopy measurements of unprecedented resolution. Lineshapes narrower than .003 cm^{-1} have been resolved in such measurements,[6] while the best resolution reasonably obtained with a grating monochromator is near .05 cm^{-1}. Among the compounds examined to date are NH_3, CO, NO, SF_6, SO_2 and others.[7-10] Absorption spectra of the compounds have a wealth of structure not resolvable with conventional means due to rotation-vibrational mixing.

The simplicity and high signal to noise ratio of lead salt laser spectroscopy has made such systems attractive for the purpose of detection and concentration monitoring of gaseous contaminants. Atmospheric pollution monitoring via this method has been shown to be possible both in laboratory scale gas cells and over long atmospheric transmission paths.[11]

Other applications of lead salt lasers, demonstrated or proposed, include studies of gain and loss spectra of gas lasers, use as tuned local oscillators in laser communications or radar systems, heterodyne radiometry and remote gas detection using scattered returns.

The widespread use of lead salt lasers has been impeded by the low operating temperature of CW lasers and the low single mode output powers that have generally been available until recently. Much of the laser development effort has been devoted to improvement of these parameters. Recent advances in laser fabrication technology (including the use of stripe-geometry, vapor-grown substrates, polished mirror facets and anti-reflection coatings, and the development of single and double heterostructure lasers) have increased the maximum CW output powers obtainable from about 1 mW (typical of the best lasers in 1970) to more than 300 mW, and the maximum allowable heatsink temperature for CW operation from the vicinity of 20°K to over 80°K.[12-15] It is expected that further increases in these parameters (particularly the achievement of CW operation above 77°K with reasonable yields in a number of alloy systems) will expand the application of lead salt lasers.

I. 2 Optical and Carrier Confinement in Junction Lasers

It is well known that in injection lasers and LED's there are mechanisms which tend to confine the emitted light to the vicinity of the junction.[16,17] The mechanisms serve to establish an effective dielectric waveguide in the junction region, such that the laser radiation is continually refocussed as it propagates within the diode.

The basis of the optical confinement effect is particularly evident in double heterojunction diode lasers.[18,19] As shown schematically in Fig. 2, these lasers consist of (at least) 3 nearly uniform layers, where the epitaxially-grown central layer is a semiconductor of narrower bandgap and higher dielectric constant at the laser frequency than the remaining layers. In this case the dielectric waveguide corresponds to the well-studied dielectric slab model; the focussing effect may be understood as complete internal reflection at the interfaces of plane waves propagating in the central layer.

The nature of optical confinement in homojunction lasers is less understood. Several theories have been advanced to explain the origin of the dielectric constant variation in diffused GaAs lasers;[20-23] it has been attributed to:

(a) the effect of free carriers in the n and p regions;

(b) the change in dielectric constant associated with negative conductivity near the junction; and

(c) the change in ϵ associated with the spatially varying absorption edge.

The amount of dielectric constant change produced near the junction of GaAs lasers is estimated[22] to be $\Delta\epsilon / \epsilon \sim 10^{-3}$.

An additional important effect of heterojunctions on the behavior of DHS lasers is to confine minority carriers injected across

the junction to the central layer.[24] Such confinement results from the presence of discontinuities of the conduction and valence band energies at the interfaces, which in turn are caused by the difference in energy gap of the materials on either side. Provided the size of the energy discontinuities is substantially greater than KT, minority carriers may not flow into the larger bandgap layers.

Corresponding studies of minority carrier confinement in diffused homojunctions have not been made. It has been widely assumed that minority carriers travel a distance of the order of a diffusion length from the junction of homostructure lasers. In this work, however, is presented an analysis of carriers distributions in graded junction diodes where it is demonstrated that an important minority carrier confinement effect is in fact present. In this case electric fields caused by the junction grading retard the flow of minority carriers, thereby confining them to the vicinity of the junction.

The confinement of both the optical field and the minority carrier distribution have important effects on the laser behaviour. In general better confinement of either variable leads to lower threshold current. Successful confinement by use of heterostructures in GaAs lasers led to a dramatic reduction of threshold current density and has allowed CW operation at room temperature.[25] Additionally, the spatial distribution of the radiation within the laser determines the shape and divergence of the output beam; these in some applications limit the fraction of the output power that is useful. The distribution of both carriers and radiation also affects the degree to which output is single-moded, a prime requirement in some applications.

I. 3 Scope of this Thesis

This thesis is an experimental and theoretical study of the confinement of both the lasing radiation and the minority carrier distribution in PbSe homojunction lasers produced by diffusing excess Se into Pb rich substrates. In it, the spatial variation of the optical intensity and the electron and hole distributions in the direction normal to the p-n junction plane are analyzed, and some of the effects of their spatial variation are discussed.

The organization of this report is as follows:

(a) In Chapter II the grading of the net donor density in the vicinity of the junction of PbSe diffused homojunctions is discussed. The grading is later shown to have important influence on the confinement of carriers and radiation.

(b) Minority carrier confinement is analyzed in Chapter III. The analysis consists of theoretical estimates of the behaviour of linearly graded junctions under high forward bias, and measurements of the minority carrier recombination lifetime in PbSe lasers.

(c) In Chapter IV optical mode confinement is analyzed. An estimate is made of the effective dielectric waveguide that is established near the junction of PbSe lasers, and propagating modes of such a waveguide structure are solved for. Experimental far-field observations are then reported for comparison with the theoretical results.

(d) The effects of optical and carrier confinement on the threshold current density of PbSe lasers are discussed in Chapter V. A theoretical model is given for the variation of J_{th} with temperature for lasers with different junction grading, and experimental results are shown for comparison.

(e) Summary and conclusions are contained in Chapter VI.

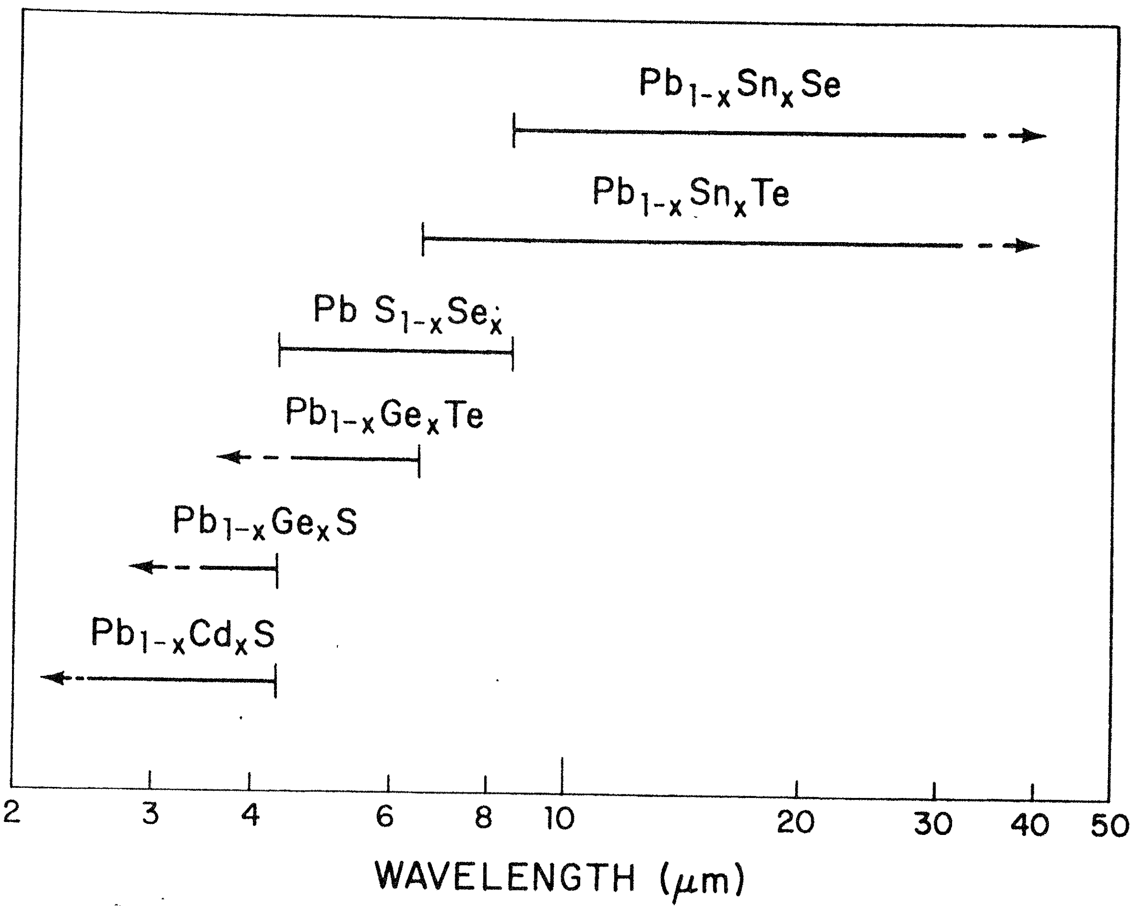

FIGURE 1 : OUTPUT WAVELENGTHS OF LEAD SALT LASERS

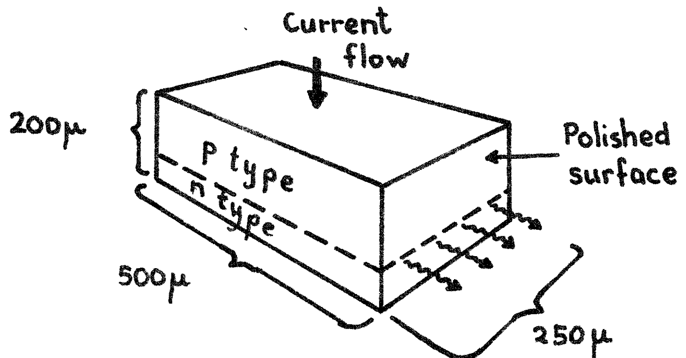

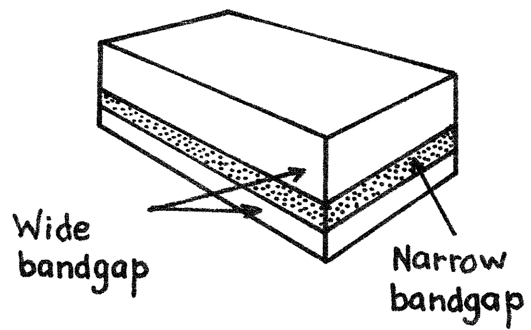

FIGURE 2 : SCHEMATIC OF HOMOJUNCTION AND HETEROJUNCTION LASERS

CHAPTER II
JUNCTION GRADING IN DIFFUSED LASERS

II. 1 Introduction

The optical and carrier confinement in diffused PbSe lasers will be shown to depend significantly on the grading of the net donor-acceptor density near the junction; in this chapter theoretical and experimental results concerning the magnitude of the grading are discussed.

The lasers considered in this study have p-n junctions produced by controlling the stoichiometry of the crystal rather than by diffusion of foreign impurities. This technique, used by Eutler et. al. for the production of the first lead salt laser,[1] remains the most common method of laser preparation.[12, 26]

In what follows, the method of production of p-n junctions by stoichiometry control is first reviewed (Sections 2 and 3). A review of the Brodersen-Walpole-Guldi theory for the resulting profiles of stoichiometry is then given (Section 4). Experimental results related to the profiles obtained in this work, including Hall measurements, junction depth measurements, microwave reflectivity measurements and junction capacitance measurements are given in Section V.

II. 2 Nonstoichiometry in PbSe

The phase diagram of the Pb-Se system, shown in Fig. 3, demonstrates the large excursions from stoichiometric composition obtainable in PbSe.[27, 28] In PbSe the defects responsible for non-stoichiometry are electrically active. In Pb-rich PbSe, vacancies of Se and interstitials of Pb are believed to be the main defects present, and both are believed to act as donors;[29] conversely, in Se rich

material, vacancies of Pb and interstitials of Se, both believed to act as acceptors, are the primary defects.[29] Also present are defect clusters, among which the most numerous are probably electrically inactive Pb vacancy-Se vacancy pairs.[29]

No freeze-out of carrier concentrations derived from deviations from stoichiometry has been observed in the Pb salts. This observation is in accord with the work of Parada and Pratt, whose calculations indicate that no states within the energy gap are formed by the introduction of Te or Pb vacancies in PbTe.[30] The binding energy of a carrier to a localized charge center in PbSe due to Coulomb forces alone is very small, due to the low value of effective mass and high dielectric constant of the material; within the hydrogenic model, a binding energy in PbSe of less than .02 meV is derived at $4.2^{o}K$.

In order to obtain useful carrier densities in the Pb salts, crystals are usually brought into thermal equilibrium with a gaseous ambient of controlled pressure of Pb and Se_2.[31]

II. 3 Junction Preparation Method

The starting material for the preparation of the lasers used in this study was Bridgman-grown PbSe whose carrier density was near 5×10^{18} holes/cm^{-3} (corresponding to composition near that of the maximum melting temperature -- Point A in Fig. 3). To produce the p-n junctions, slices were first uniformly saturated with Pb (during what will be called anneal N, which converted the entire substrates to n type conductivity). Subsequently they were annealed in the presence of excess Se for a controlled, short time (anneal P) in order to form p type surface layers.

Anneals were carried out following techniques developed by Calawa et. al. at Lincoln Laboratory.[28] The sources of Pb and Se

in anneals N and P were mixtures of Pb and PbSe, and Se and PbSe, respectively. These mixtures were prepared so that at the anneal temperature they consisted of both liquid and solid phases; the vapor pressure of constituent species about such 2 phase mixtures is well-known to be uniquely determined at a given temperature. Transport of material between the source and substrate was achieved via the vapor phase in closed quarz ampoules.

Mechanical details of the annealing procedures are described in Appendix A.

Both anneal N and anneal P were carried out at $500^{o}C$. The composition of the substrates after anneal N corresponded to point B of the phase diagram of Fig. 3 ($n = 1.9 \times 10^{18}\ cm^{-3}$); the surface composition achieved after anneal P is indicated by Point C on the phase diagram ($p = 7 \times 10^{18}\ cm^{-3}$).

At the end of anneal P samples were quenched in water in order to freeze in the defect concentration characteristic of the anneal temperature. It is known that if saturated samples are cooled slowly, often microprecipitates of the excess constituent are formed within the crystal due to the fact that the solubility of both Se and Pb in PbSe is retrograde.[32] Microprecipitates of Se were probably present in the original material, formed upon cooling from the crystallization temperature; one of the functions of anneal N, which lasted 90 days, was to allow the Se to redissolve.

Annealing times were calculated on the basis of the data of Calawa et. al.[28]

II. 4 BWG Model of Stoichiometry Profile

The profile of stiochiometry vs. depth that results during

junction diffusions of the type described above in PbSe has been considered theoretically in a series of publications by Walpole, Guldi, Brodersen, Calawa and Rediker.[29,33-35] In their model (hereafter designated BWG model), the simultaneous diffusion of vacancies and interstitials of Se and Pb is taken into account, and large deviations from the complementary error function distribution ordinarily ascribed to impurity diffusions in semiconductors are found to occur. Using the assumption that the concentrations of the defect satisfy mass action laws, with equilibrium values of the Schottky and Frenkel constants, the BWG authors show that the behaviour of the net deviation from stoichiometry may be calculated from a single diffusion equation of the form

$$\frac{\partial \Delta}{\partial t} = \frac{\partial}{\partial x}\left[D_\Delta(\Delta)\frac{\partial \Delta}{\partial x}\right] \tag{II-1}$$

in which an appropriate effective diffusion constant D_Δ is used. D_Δ is strongly dependent on the deviation from stoichiometry Δ, and is given by

$$D_\Delta = \left[D_p f + D_n(1-f)\right]\left[1 + \left(\frac{\Delta^2 + 4k_o}{\Delta^2 + 4n_i}\right)^{1/2}\right], \quad f = \frac{1}{2} - \frac{\Delta}{2(\Delta^2 + 4k_o)^{1/2}} \tag{II-2}$$

where D_p and D_n are effective diffusion coefficients for acceptor-like and donor-like defects, k_o is a reduced Schottky constant and n_i is the intrinsic carrier concentration. All of these parameters depend only on temperature and are given in Reference 29. The behaviour of D_Δ vs. Δ given in (II-2) is shown in Fig. 4. The physical basis of the shape of the curve is the fact that the diffusing species in n and p type materials are different, and the relevant mobilities (and hence diffusion coefficients) are different. One effect

resulting from the behaviour of D_Δ is the fact that the junction motion is more rapid when excess Se is diffused into a Pb rich substrate (p into n case) than when excess Pb is diffused into Se rich material. The diffusions considered in this thesis correspond to the p into n case.

An approximation for D_Δ useful in the prediction of diffusion profiles is the step model described by Brodersen et. al.,[33] in which D_Δ is assumed to be concentration independent in both n and p type material, but different in the two regions. Under such an assumption analytic solutions have been found for the variation of Δ with distance resulting from a junction diffusion. The profile obtained in the diffusions described in this work, evaluated according to the step model using values of the constants shown in Table I, is drawn in Fig. 5.

Numerical solutions of Equation (II-1) using the full dependence of D_Δ on Δ given by (II-2) have been carried out also as part of this work. With the substitutions

$$h_\Delta = \frac{D_\Delta}{D_p} \qquad\qquad z = \frac{x}{\sqrt{D_p t}} \qquad\qquad \text{(II-3)}$$

the equation may be recast into the form

$$\frac{d}{dz}\left(h_\Delta \frac{d\Delta}{dz}\right) + \frac{1}{2} z \frac{d\Delta}{dz} = 0 \qquad\qquad \text{(II-4)}$$

This in turn may be integrated to yield

$$\frac{d\Delta}{dz} = \frac{1}{h_\Delta}\left(h_\Delta \frac{d\Delta}{dz}\right)_{z=0} - \frac{1}{2}\frac{z\Delta}{h_\Delta} + \frac{1}{2h_\Delta}\int_0^z \Delta(z')\,dz' \qquad \text{(II-5)}$$

which is amenable to easy numerical integration. A trial and error method was used to determine one of the boundary conditions at z=0. Solutions of Δ corresponding to diffusion at 500°C and the material parameters of Table I are shown also in Fig. 5.

The BWG model is supported experimentally by the fact that it has enabled a correlation to be made between data from radioactive tracer diffusions under equilibrium conditions and junction depth vs. time measurements in p-n interdiffusions. Excellent agreement was obtained between tracer results and junction depth results for p into n diffusions; discrepancies were found however, between junction depth measurements and predicted values for n into p diffusions. This reflects uncertainty in the most appropriate value of D_n in Table I.

II. 5 Experimental Characterization of Junction Diffusions

In order to experimentally verify the predictions of the BWG model for the junction profiles obtained in the diffusions of this work, several methods of profile characterization were used. These include Hall measurements, junction depth measurements, microwave reflectivity measurements and junction capacitance measurements. The techniques used and results obtained will be presented for each in this section.

(i) Hall Measurements

Measurements of mobility and carrier concentration at room temperature and 77°K were carried out on n type substrates obtained after anneal N and on p type samples obtained by performing an anneal P under conditions analogous to the junction diffusions (except that the anneal was prolonged to the point where the sample became uniformly p type). In the latter case it is expected that the measured quantities correspond to the material at the p surface of the lasers.

The Hall samples were of the standard bar shape and in most cases had the standard 6 lead contacting configuration. Contacts to n samples were made by alloying In balls to the sample and subsequently alloying Au wires to the In. For p samples, contacting was done by welding Pt wires to the sample by the capacitor-discharge method.

Results of the measurements are shown in Table II. Measured values of carrier concentration are in fair agreement with the published data of Calawa et. al.[28] and Harman[29] for the saturation limits of PbSe. The agreement demonstrates that no high impurity concentrations were present in the starting material or in the Pb or Se rich powders used in the anneals. The accuracy of the measurements, limited by geometrical factors in this case, is expected to be no better than 20%.

(ii) Junction Depth Measurements

The p-n junction depth was measured on slabs cut from the same substrates from which the lasers described in Chapter IV were obtained. The measurement of junction depth was done by observing the sign of the thermoelectric voltage when a thermoprobe was used on the surface of angle-lapped samples.

The angle-lapped samples were prepared by the same lapping and polishing procedures used for the lasers (described in Appendix A), except that a polishing block with a surface bevel of 3° was used. Before and after lapping the thickness profile of the samples was measured under a microscope -- thus avoiding errors due to possible nonparellelism of the original samples and possible mismounting of the samples on the beveled block.

The thermoprobe used in the measurements was constructed and is used at Lincoln Laboratory. The author is grateful to

A. R. Calawa for permission to use the system. The system employs a soldering-iron-heated Au wire probe, and all electrical connections in the region where there are substantial thermal gradients are made with Au leads and contacts in order to avoid spurious thermovoltages.

Measurements were performed at room temperature and $77^{\circ}K$. Results of the two sets of measurements were in very good agreement.

Fig. 6 shows the measured values of junction depth for the set of diffusions plotted against the square root of the diffusion time. Also shown are the junction depths predicted from the BWG model. Agreement between the predicted and measured values is good.

Shown also in Fig. 6 are predicted values of junction depth based on a diffusion theory which assumes D_{Δ} independent of stoichiometry. This model displays a slight deviation of depth from the square root of diffusion time law due to the fact that the semiinfinite slab limit is violated for the deepest junctions in the 19 mils thick samples used. Junction depths were computed from the expression[36]

$$\Delta(x,t) = \Delta_s - (\Delta_s - \Delta_o)\frac{4}{\pi}\sum_{k=0}^{\infty}\frac{1}{2k+1}\exp\left[-\frac{(2k+1)^2\pi^2 Dt}{\ell^2}\right]\sin\frac{(2k+1)\pi x}{\ell} \qquad \text{(II-6)}$$

where D was adjusted to give the same depth as the BWG model for shallow junctions. Differences between the predictions of the two models are so slight, however, that the experimental data do not allow a selections between them to be made.

(iii) Microwave Reflectivity Measurements

In order to obtain more directly some measure of the diffusion profile, the reflectivity of a sample at a microwave frequency was measured at various stages of removal of the diffused surface. The reflectivity at this frequency is controlled essentially by the

resistivity of the sample. By assuming the carrier mobility is approximately constant, a comparison can be made between the predictions of the BWG theory for equilibrium carrier concentration profile and the observed reflectivity profile. This method of diffusion profile characterization has comparatively low spatial resolution but does not require preparation of crystal surfaces of high purity and perfection, as do measurements of IR reflectivity,[37] Schottky barrier capacitance[38] and spreading resistance.[39]

The magnitude of the reflection coefficient R of the sample at 74.6 GHz was measured with the microwave circuit shown in Fig. 7. The precision attenuator A1 (FXR Model E164) was adjusted to null the detector outputs D1 and D2 when the waveguide termination T1 was shorted with a gold foil and when the sample was clamped across it. The difference in attenuator readings gave $\eta = -10\log R$. A similar scheme was used by Bichara and Poitevin to measure the resistivity of Si samples.[40] A gasket of indium was used between the waveguide flange and the Pb Se sample in order to minimize the resistance and spatial non-uniformity of the contact.

The sample surface was lapped off in numerous stages, between which measurements of reflectivity were made. Lapping was done with 2 micron alumina powder and was followed by a chemical polish with aqueous solution of CrO_3 (which removed about 5 microns). The surfaces of the sample were maintained parallel during the lapping process to within 0.2 mils over the region where the reflectivity was measured.

The results of η vs. z (distance measured form the original p surface) are shown in Fig. 8. This figure also shows the reflectivity of an identically prepared undiffused n type substrate, which may be compared to the reflectivity of the n region of the diffused

sample. The smooth curves correspond to the reflectivity predicted from the BWG profile according to the analysis below, obtained using values for the carrier mobility of 800 and 1000 cm^2/v sec. In order to fit the measurements a junction depth of 6.25 mils was used (in good agreement with the expected 6.0 mils).

The reflectivity R was calculated from[41]

$$R = \left| \frac{Y_m - Y_g}{Y_m + Y_g} \right|^2 \qquad \text{(II-7)}$$

where Y_m is the ratio of the transverse component of the magnetic field to the electric field amplitude for waves propagating in the semiconductor, and Y_g is the corresponding admittance for the waveguide (RG-99/U, operated in single TE_{10} mode regime). Y_g is given by[41]

$$Y_g = \left[\frac{\epsilon_0}{\mu_0} \left(1 - \frac{\lambda_0^2}{\lambda_c^2} \right) \right]^{1/2} \qquad \text{(II-8)}$$

where λ_c is the free space wavelength at the waveguide cutoff (MKS units are used throughout this discussion). According to the Drude theory,[42] the semiconductor may be characterized by its complex dielectric constant ϵ given by

$$\epsilon = \epsilon_s \left(1 - \frac{ne^2}{m^* \epsilon_s \omega^2} \right) - \frac{ine\mu}{\omega} \qquad \text{(II-9)}$$

where ϵ_s is the static dielectric constant, n the carrier density, μ the carrier mobility and m^* the conductivity effective mass (nearly equal for holes and electrons in PbSe). For a homogeneous slab, the field amplitudes will have z dependence $e^{-\gamma z}$, where

$$\gamma^2 = \frac{4\pi^2}{\lambda_c^2} - \omega^2 \mu_0 \epsilon \qquad \text{(II-10)}$$

Y_m is given by

$$Y_m = \frac{\gamma}{i\omega\mu_0} \qquad \text{(II-11)}$$

In (II-10) it has been assumed that within the semiconductor the transverse variation of the electric field is identical to that in the waveguide.

The penetration depth[41] δ = Re (γ) for homogeneous slabs derived from (II-10) is plotted vs. carrier concentration in Fig. 9, where we have used $\epsilon_s = 206$, $m^* = 0.11m$ and $\mu = 800\ cm^2/v\ sec$. For carrier densities below about $2.5 \times 10^{18}\ cm^{-3}$ it is found that substantial errors might result from regarding the p region as a homogeneous slab in the calculation of reflectivity. For these regions the WKB approximation for the field amplitudes has been used.[43] It was found

$$Y_m = \frac{1}{i\omega\mu_0}\left(\gamma + \frac{1}{2\gamma}\frac{d\gamma}{dz}\right) \qquad \text{(II-12)}$$

Very near the junction this approximate result is invalid, and a more exact analysis has not been carried out.

The good agreement between the predicted and measured results appears to be strong evidence for the validity of the BWG model. These measurements, however, are incapable of resolving the behaviour of the profile within 0.5 mils of the junction. At this depth the surface region is lightly doped and thus quite transparent. Interference

effects must be expected, but the lapping accuracy and simplified analysis given here are inadequate to treat them. It is expected, however, that the profile will scale with distance, and the region of uncertainty will be smaller for diffusions with junction depths smaller than 6 mils.

The discrepancies between theory and experiment may be attributable to contact resistance, which becomes a severe problem for low sample resistivities and particularly for p PbSe.[44] Another possible source of difficulty is variations of mobility, although at room temperature (phonon scattering limited) mobility has been reported to be approximately independent of carrier density in PbSe.

(iv) Junction Capacitance Measurements

Measurements of the capacitance-voltage relation of reverse-biased p-n junctions are particularly suited to the determination of net donor-acceptor densities in the vicinity of the junction. It is well-known that the capacitance per unit area C of abrupt junctions follows the relation[45]

$$\frac{1}{C^2} = \frac{2(N_A + N_D)(V + V_{bi})}{q \epsilon_s N_A N_D} \tag{II-13}$$

while for linearly graded junctions it satisfies[45]

$$\frac{1}{C^3} = \frac{12(V + V_{bi})}{q a \epsilon_s^2} \tag{II-14}$$

Here V_{bi} is the built-in voltage of the junction, V the applied reverse bias, ϵ_s the static dielectric constant of the semiconductor N_D and N_A are the net donor and acceptor densities on the n and p sides of an abrupt junction, respectively, and a indicates the net donor

density grading parameter in the linearly graded case. Values of doping density or grading parameter correspond to those obtained at the edges of the junction depletion region, which for junctions considered here is of the order of 100 to 1000 Å wide. Measurements of the capacitance of p-n junctions fabricated as part of this work were attempted in order to gain additional knowledge of the profile of net donor density near the p-n junction. The measurements proved very difficult to perform due to the large leakage currents in the diodes under reverse bias. The results obtained are in disagreement with the BWG model of stoichiometry distribution in the diodes, and remain unexplained.

Voltage-current curves obtained on the diodes typically had the shape shown in Fig. 10a, where results for a diode of area $6.5 \times 10^{-4} cm^2$ and junction depth 55μ are shown at $300^\circ K$ and $77^\circ K$. While rectification is apparent, the effective reverse leakage resistance for this diode is 24Ω at room temperature and 10Ω at $77^\circ K$. The decrease in leakage resistance as the temperature is lowered is unusual for semiconductor junctions; it has been noted previously in lead salt devices,[46] however, and has been attributed to an increase in reverse tunneling current. This current component is particularly sensitive to the value of the energy gap, and increases as the temperature is decreased since the energy gap also decreases. Generally the presence of tunneling current is indicative of sharply graded junctions, although no numerical model is available to calculate the junction grading from the magnitude of the tunneling current in the lead salts.

Standard methods of junction capacitance determination cannot be used with diodes whose reverse leakage is so large. Approximate capacitance measurements were carried out in this work by noting the phase-shift between junction current and junction voltage when a

1 MHz sinusoidal signal was applied to the junction. The AC junction voltage was maintained at 10 mV while the DC voltage could be altered through bias circuitry. Measurements of the relative phase shift (which was typically .1 to 1°, well below the accuracy of standard vector-voltmeters) were made on the face of a Tectronix 453 oscilloscope, and were corrected numerically for the value of the oscilloscope input capacitance and lead inductance. Typical results of capacitance measurements are illustrated in Fig. 10b where $1/C^3$ is plotted vs. V for a diode of junction depth 178 and area $.94 \times 10^{-3} cm^2$, C was measured at $77^{o}K$. Agreement with the $1/C^3$ law is good, although a similar fit with $1/C^2$ is also possible because of the large amount of scatter of the data. The curve is unusual, however, in that the intercept V_{int} obtained when $1/C^3$ is extrapolated to zero is substantially less than the expected V_{bi} of close to .17 V. The grading of the junction calculated from the measurement of $d(1/C^3)/dV$ and Equation (II-14) yields $a = 1.75 \times 10^{19}\ cm^{-3}/\mu$. This figure is larger by two orders of magnitude than the results expected from the BWG model. Similar results were obtained with other samples, and there was little correlation between calculated values of a and the measured junction depth of the diffusion.

Measurements of capacitance at $300^{o}K$ had less scatter since the leakage resistance was larger. At this temperature, however, the capacitance near zero bias was dominated by diffusion capacitance, while at high reverse bias sufficient junction heating took place to make the measurements unreliable.

The anomalous high values of capacitance of the diodes (and consequently high values of the estimated grading parameter) might be due to the formation of an inversion layer on the surface of either the p or n side of the junction. Such a layer would increase the

effective area of the junction and lead to capacitance estimates that are abnormally high. Impurity effects might also lead to the observed result. In particular, a uniform background of acceptor impurities might cause a shift of the net donor profile from that of Fig. 5 to that shown in Fig. 11a, and thus lead to very high grading values in the immediate vicinity of the junction. Estimates of grading on the n side of the junction according to the BWG model are close to the value of a obtained above. Quantitative arguments however cannot be made since the presence of impurities will very likely induce changes in the value of $D_{\Delta}(\Delta)$ in (II-2), due to vacancy-impurity interactions.

Another mechanism which might lead to the anomalously high capacitance is gross junction non-planarity, such as might be obtained if diffusion is most rapid along dislocations. Then the effective area of the junction is substantially larger than the measured cross-sectional area of the device. A final possibility for the unexplained large capacitance results is, of course, experimental error. In typical measurements the Q $(=\omega C/R)$ of the effective junction capacitor was of the order of 10^{-4} to 10^{-3}, while Qs greater than 1 to 5 are required by standard capacitance testing equipment.

(v) Discussion

The experimental work detailed here is not sufficient to uniquely determine the profile of net donor-acceptor density for the diffusions performed. The microwave reflectivity experiments have indicated that in gross terms the profile predicted by the BWG model is followed, that is, that the acceptor density decreases gradually from its value at the surface to a much lower value near the junction, and that the net donor density on the n side of the junction approaches its bulk value in a distance shorter than would be predicted by a model with diffusion constant independent of carrier density. Uncertainties

remain, however, with regard to the net donor distribution in the immediate vicinity of the junction. Also the particular value of the slope of the donor density on the n side of the junction has not been determined. As noted earlier, some uncertainty surrounds the value of D_n, the effective diffusion constant for donor-like defects; this parameter basically controls the slope of Δ in the n region near the junction. It is possible that diffusion in n type material is strongly affected by substrate dislocation density, and thus proceeds at different rates in samples prepared differently. The plausibility of this effect is enhanced by the fact that observed diffusion rates are very low.

The effect of the p-n junction electric field on the motion of species has not been considered by BWG. At the temperature of diffusion the electric field must be small since there are very large intrinsic carrier densities and V_{bi} for the junction is small. During the quench at the end of the diffusion it is to be expected, however, that the electric field will build up, and may cause species to move over short distances near the junction.

Effects of impurities on the diffusion profiles are unknown at present. It is likely that the effects are complex, however, since many impurities can exist both in substitutional and interstitial form.[47] Thus their solubilities, mobilities and even their donor-acceptor nature will be influenced by the local value of stoichiometry.

As a consequence of the uncertainty of the net donor profile near the junction, several models will be considered in what follows. Model I assumes that the net donor density follows the BWG exact solution for the profile of stoichiometry, obtained using the parameters of Table I. Model II assumes the donor density varies in accordance with Fig. 11a, that is, the transition from high to low

values of D_{Δ} takes place on the p side of the junction, as suggested by the capacitance measurements. Model III assumes that the transition between values of D_{Δ} occurs on the n side of the junction. This might take place if, for example, there were present a uniform concentration of donor impurities in the substrate. The last model leads to a graded junction that effectively has the same grading parameter on both p and n sides over the entire range of interest. Such a junction corresponds to the most natural a priori model for any diffused junction. A number of theoretical studies in the remainder of this thesis depend on the assumption of Model III, since its symmetry can be used to obtain simplified solutions in many cases.

Profiles of the net donor density derived on the basis of the three models are shown in Fig. 11b.

FIGURE 3, PHASE DIAGRAM OF PBSE

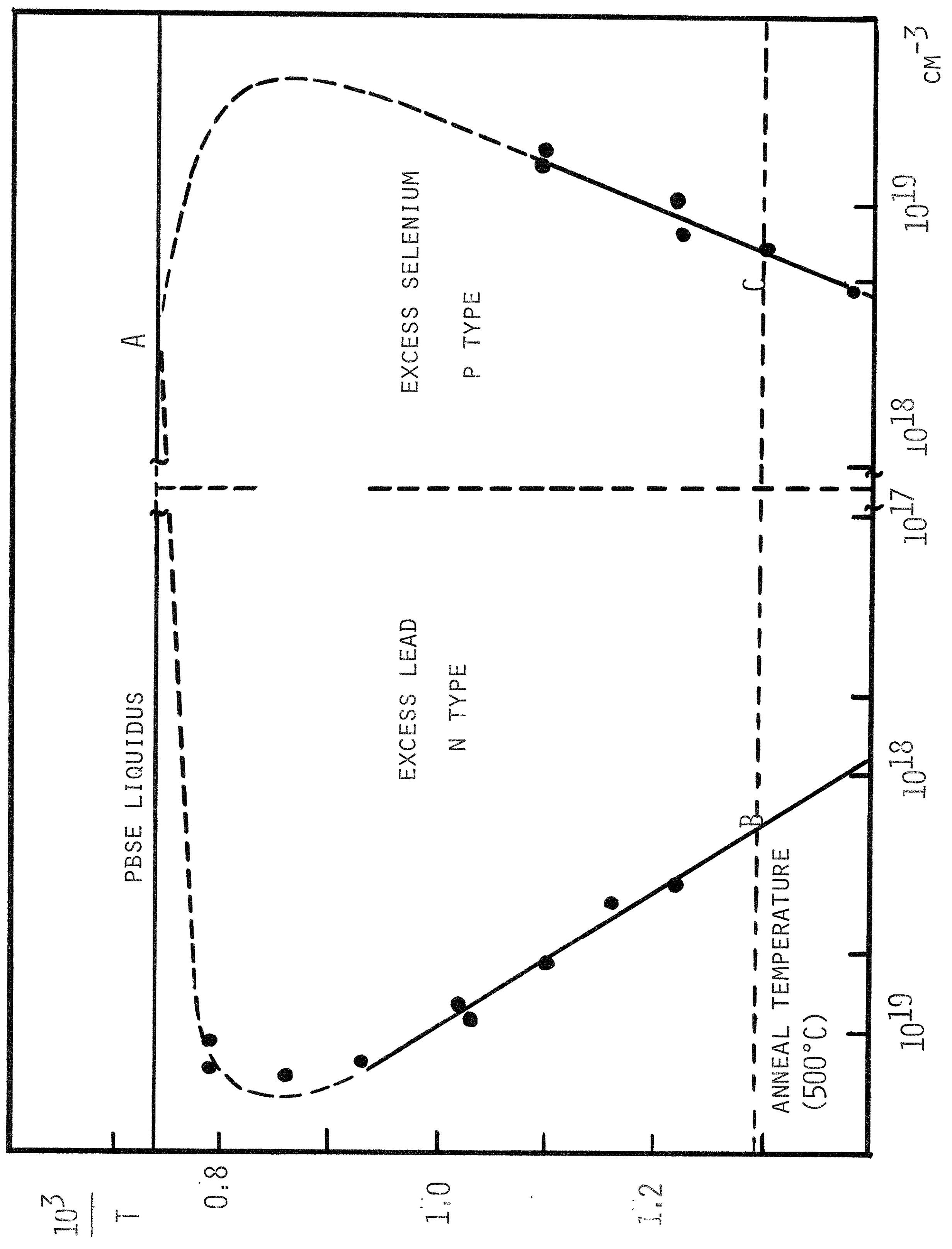

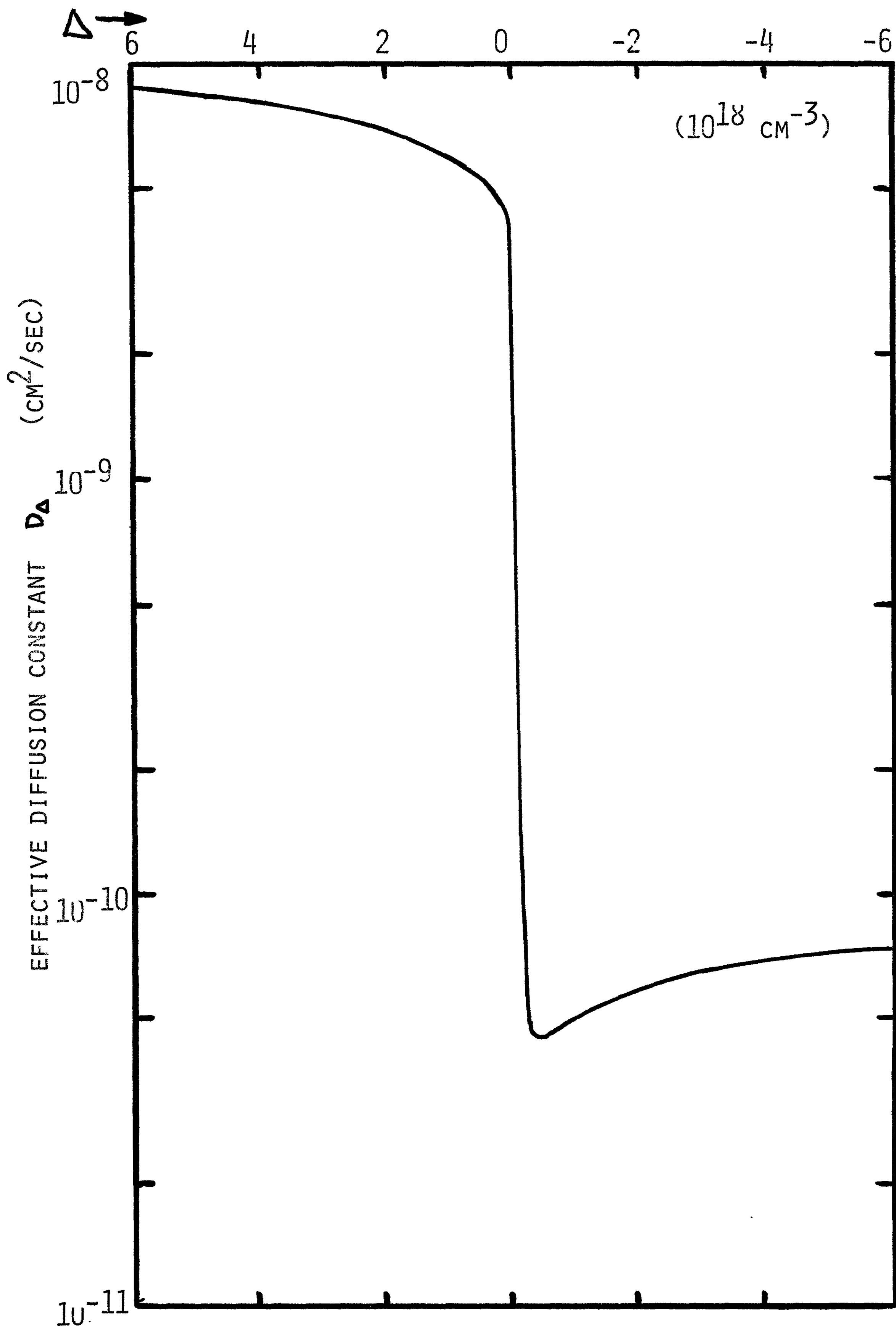

Figure 4: Variation of effective diffusion constant with stoichiometry

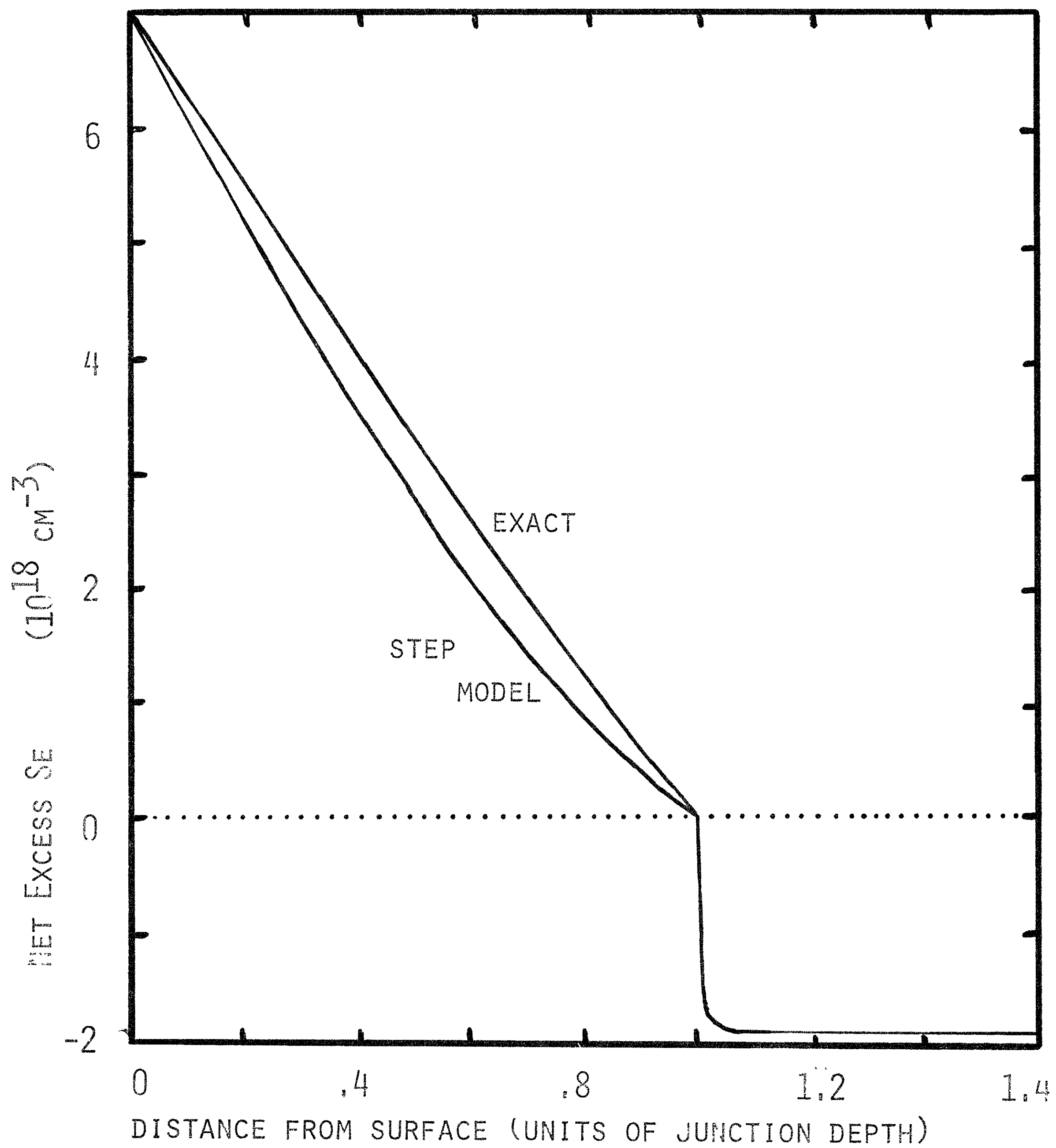

FIGURE 5: PREDICTED STOICHIOMETRY PROFILES FOR P INTO N DIFFUSIONS

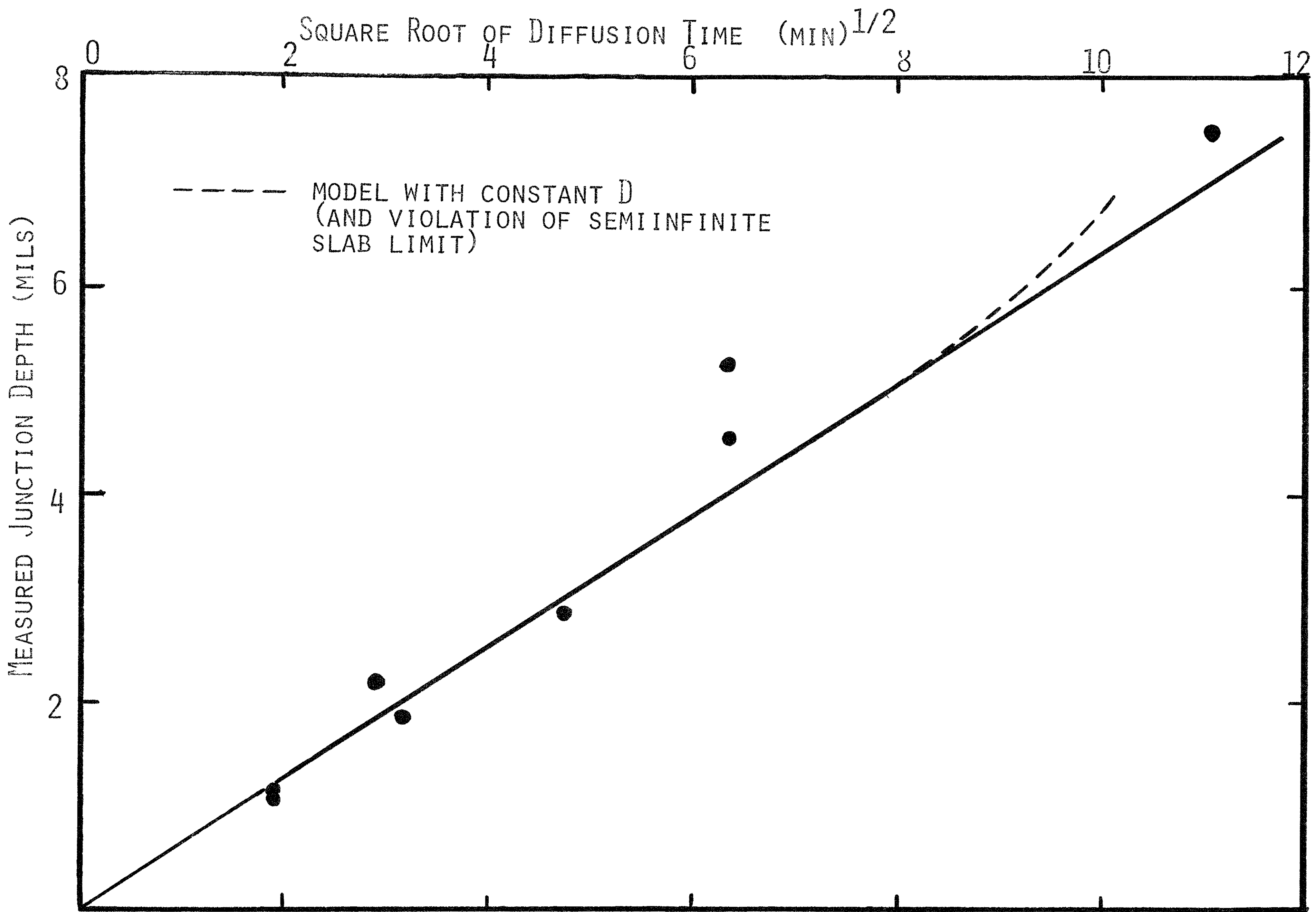

FIGURE 6: COMPARISON OF PREDICTED AND MEASURED VARIATION OF JUNCTION DEPTH WITH DIFFUSION TIME

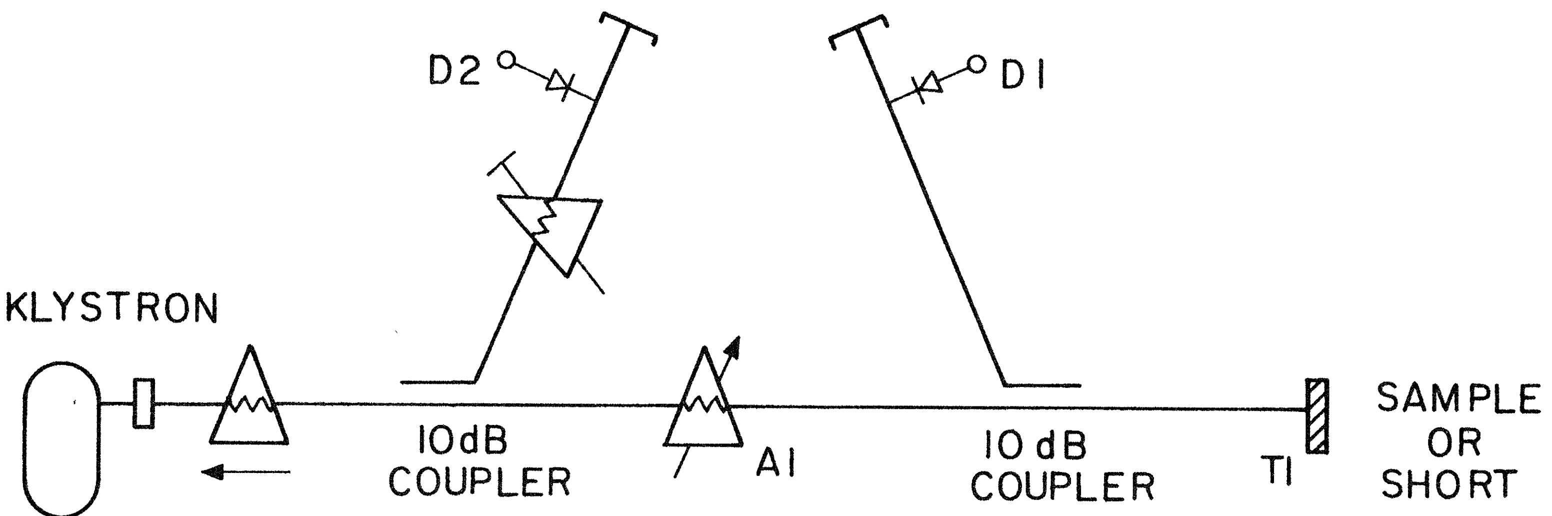

FIGURE 7: MICROWAVE EQUIPMENT FOR REFLECTIVITY MEASUREMENTS

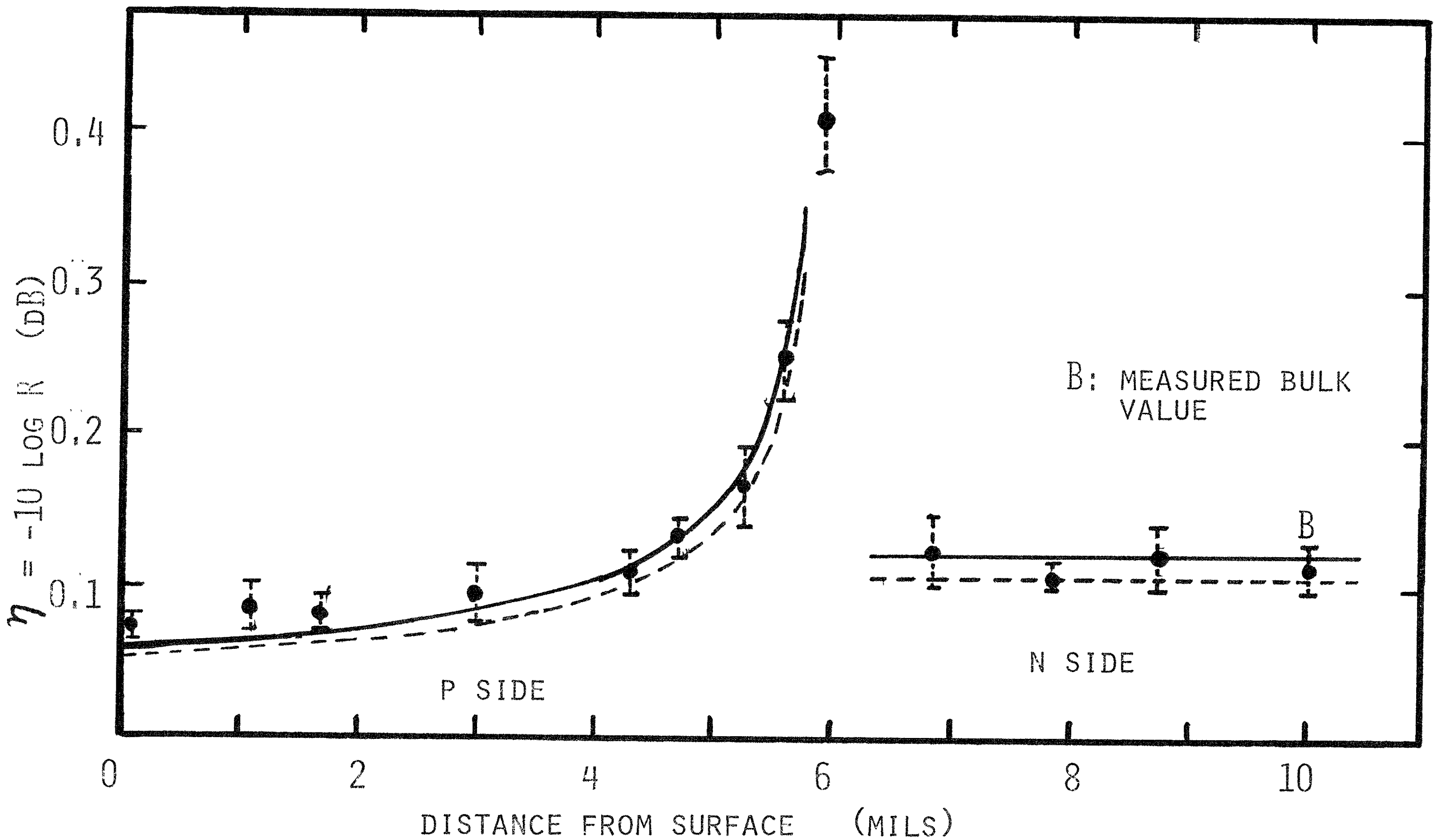

Figure 8: Measured Variation of Reflectivity with Distance from Surface

Figure 9: Penetration Depth of Microwaves at 74.6GHz in PbSe

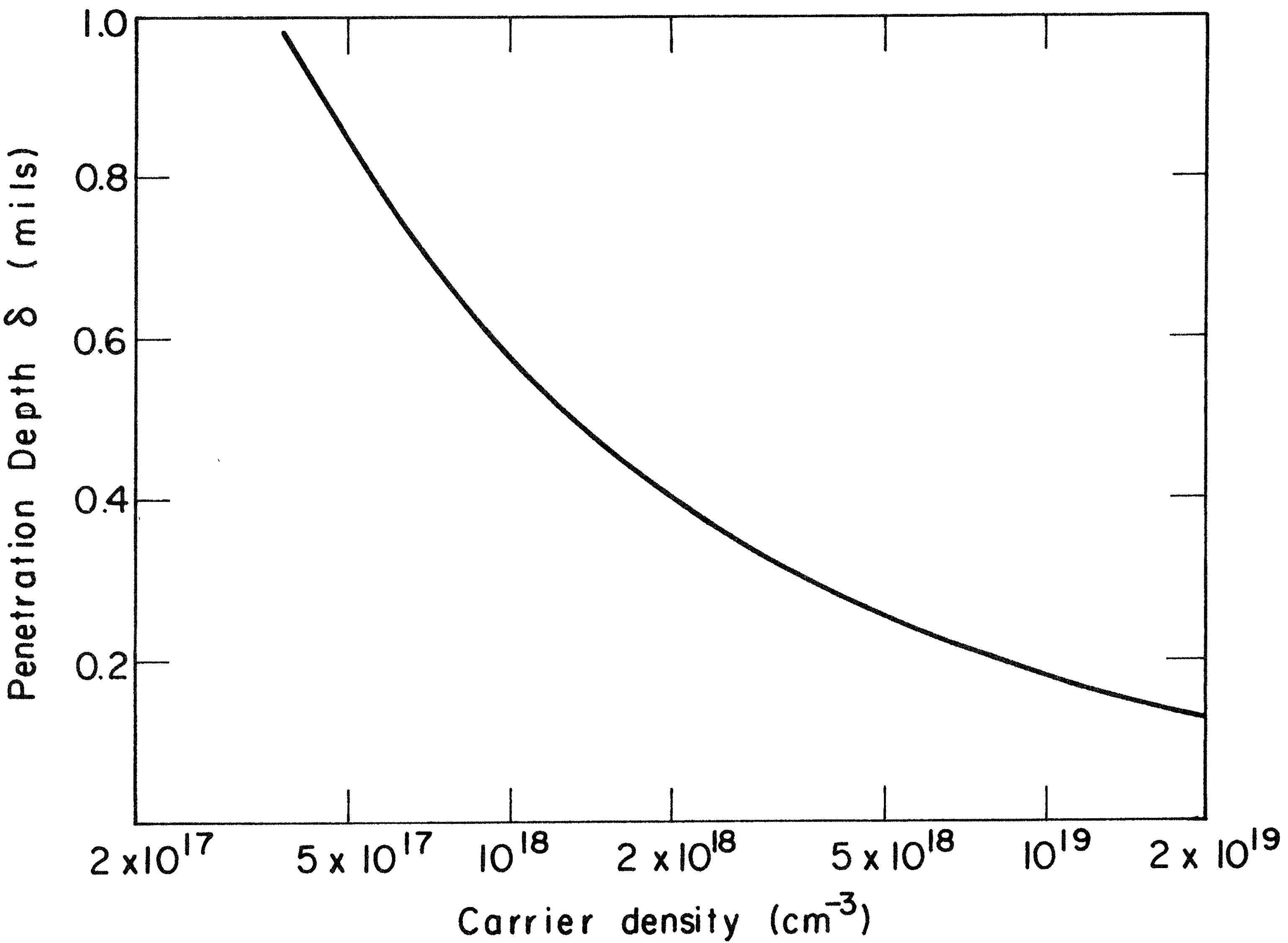

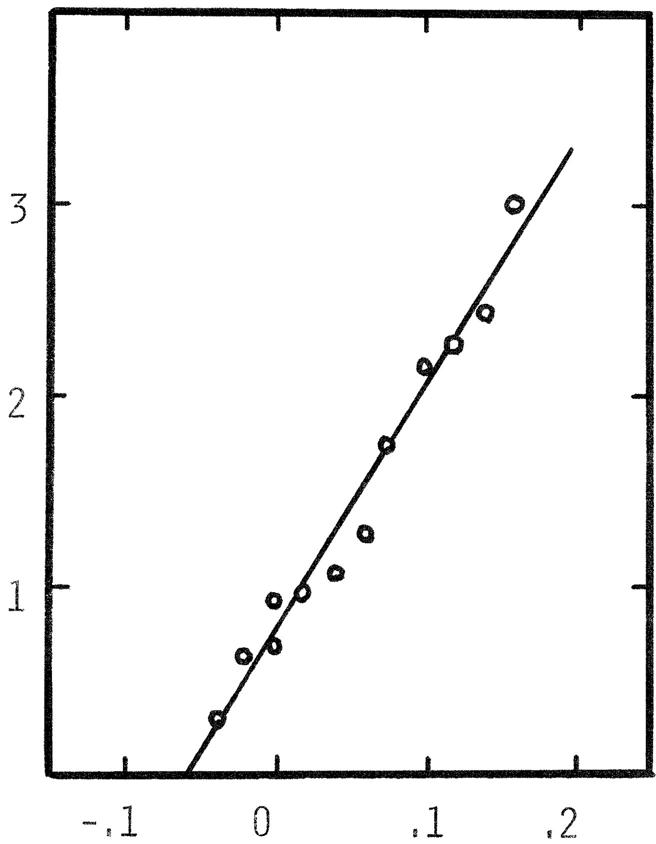

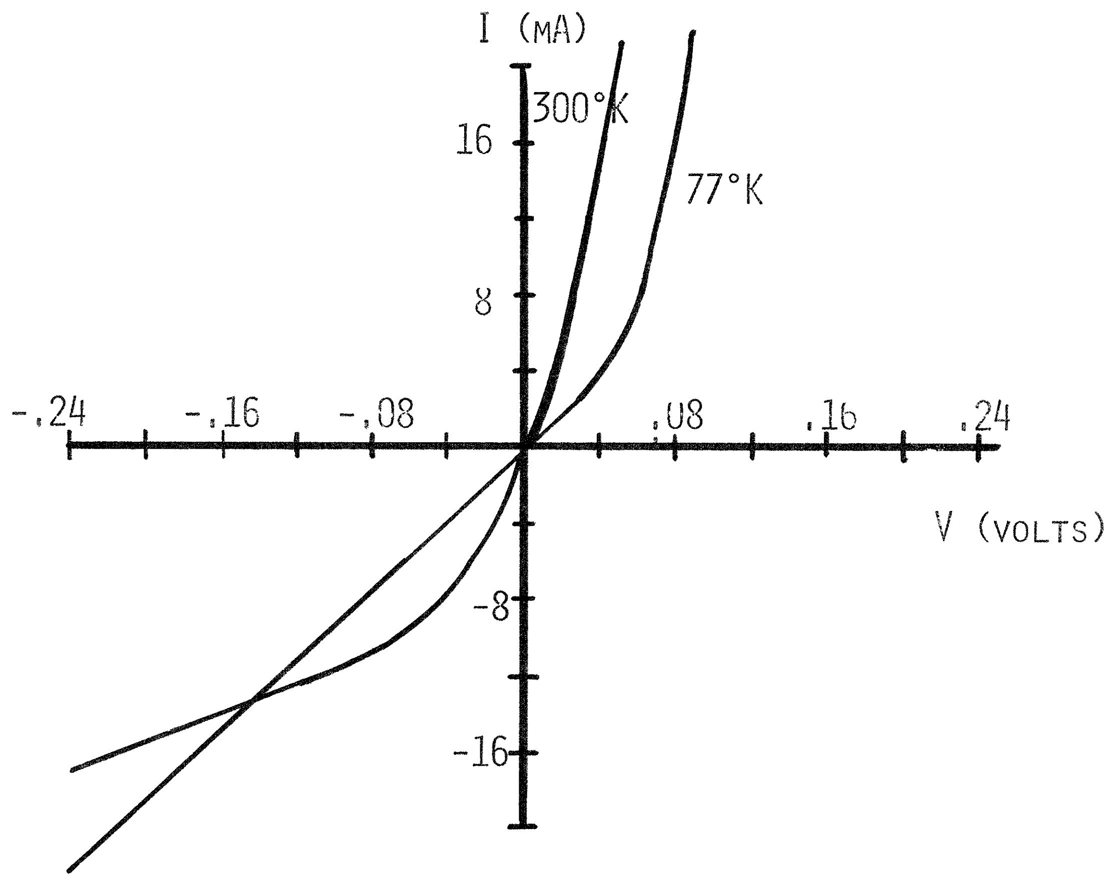

Figure 10: Electrical Characteristics of Diodes

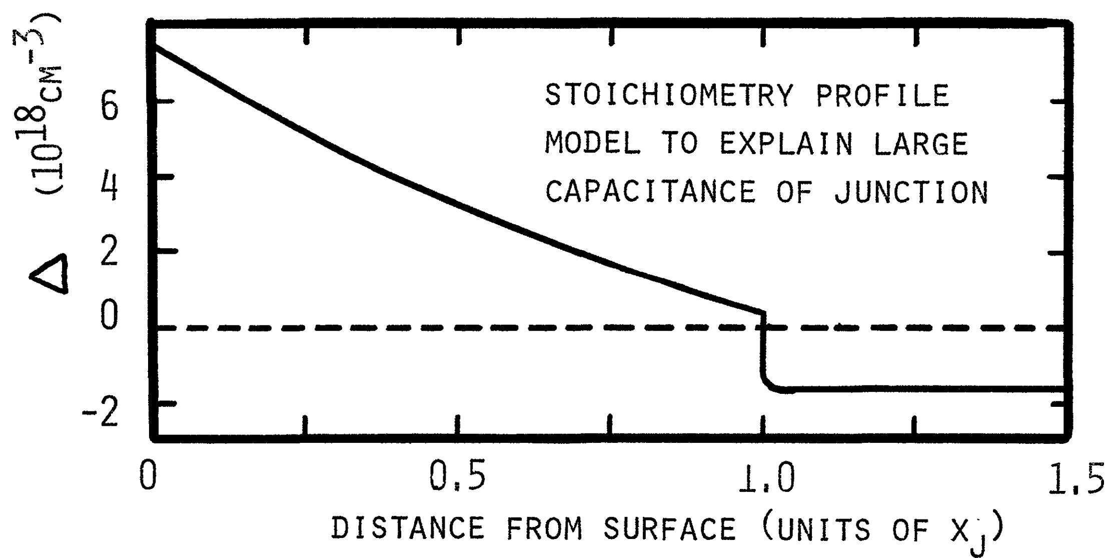

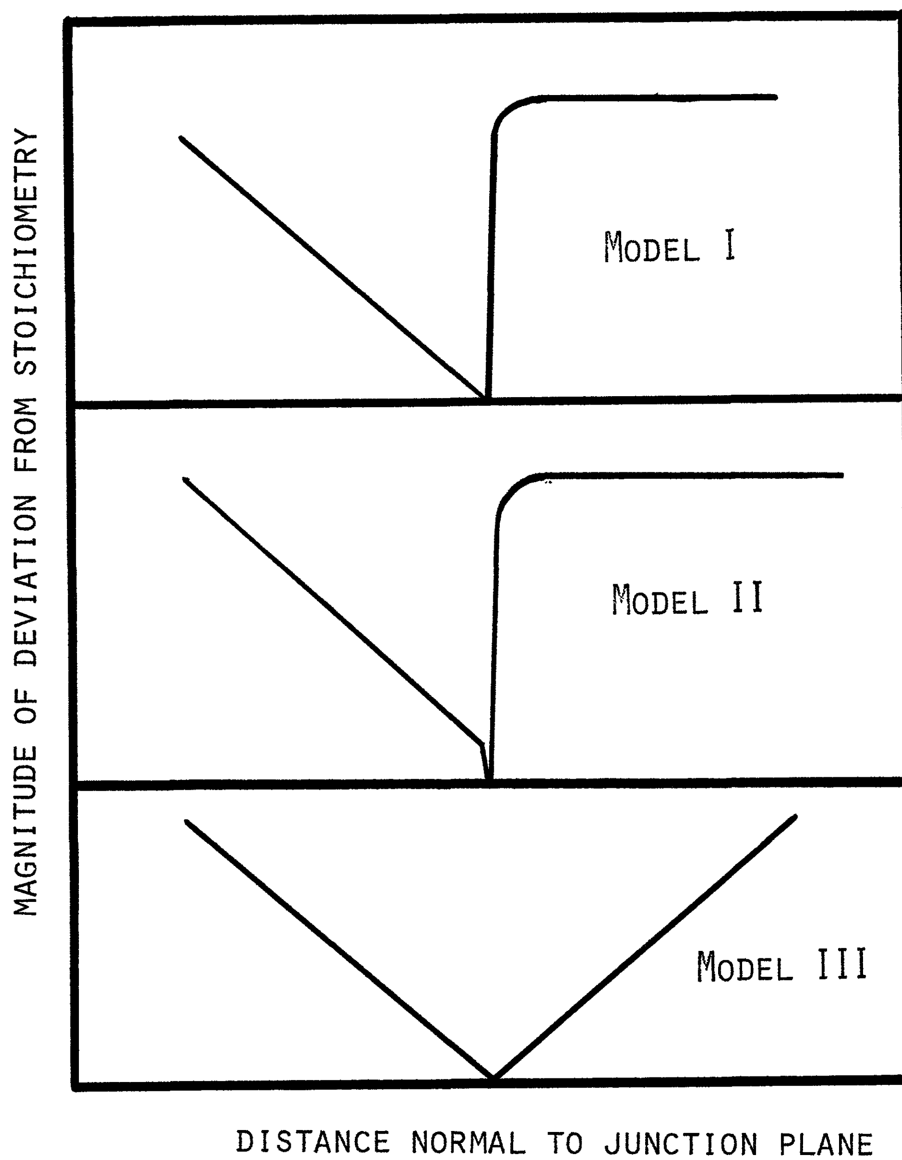

FIGURE 11: MODEL PROFILES FOR P INTO N DIFFUSIONS

TABLE I

PARAMETERS OF BWG MODEL FOR THE CALCULATION OF STOICHIOMETRY PROFILE

PbSe Diffusion Temperature: $500^{o}C$

$\Delta_s = 7.0 \times 10^{18}\ cm^{-3}$

$\Delta_o = -1.9 \times 10^{-18}\ cm^{-3}$

$n_i = 1.83 \times 10^{18}\ cm^{-3}$

$k_o = 2 \times 10^{32}\ cm^{-6}$

$D_p = 4.7 \times 10^{-9}\ cm^2/sec$

$D_n = 4.0 \times 10^{-11} cm^2/sec$

TABLE II

RESULTS OF HALL MEASUREMENTS

Sample	Mobility (cm^2/V sec) 300°K	77°K	Carrier Density (cm^{-3})
N-type substrates			
Sample A	1200	25000	1.9×10^{18}
Sample B	870	19500	1.9×10^{18}
Se-saturated P-type sample	580	8200	1.0×10^{19}

CHAPTER III
MINORITY CARRIER CONFINEMENT

III.1 Introduction

In this chapter is presented an analysis of the spatial distributions of majority and minority carriers in the vicinity of the junction of PbSe diffused lasers when forward biased to levels near, but below, threshold. Semiquantitative considerations are also given which allow extension of the analysis to cover the carrier distributions obtained above threshold.

This aspect of the physics of Pb salt lasers has received little attention in the literature. Harman,[2] Zoutendyck[48] and Sleger et. al.[49] have regarded the "active region" width found from far field pattern measurements to be an experimental measure of the spread of the minority carrier distribution. The measured width was interpreted as the minority carrier diffusion length obtained in homogeneous material. The authors argued that the minority carrier lifetime obtained by using this diffusion length and the (known) majority carrier mobility is in accord with extrapolated values of the lifetime measured in bulk samples. Estimates of the minority carrier penetration depth have ranged from 20μ ($Pb_{.88}Sn_{.12}Te$ at 4.2^{O}K) to 10.5μ (PbSe at 77°K).

Measurements and analysis presented in this work disagree substantially with the above interpretation. In Chapter IV it will be argued that the near field width that may be inferred from far field measurements corresponds to the optical mode width that results from the dielectric constant profile of the junction, and may have little relation to the width of the minority carrier distribution. The minority carrier lifetime has been measured in a laser structure just below

threshold and has been found to be substantially smaller than the value inferred in the above works. Finally, theoretical analysis presented in this chapter indicates that in most diffused Pb salt lasers the junction grading influences strongly the spread of minority carriers due to the establishment of junction electric fields.

In what follows, the minority carrier lifetime measurement is first reported (Section III. 2). After this, is presented a model for the spatial distribution of carriers in diffused junctions which explicitly considers the role of junction grading (Section III. 3).

III. 2 Measurement of Minority Carrier Recombination Lifetime

For GaAs lasers in which traps are absent it has been demonstrated that there is a time delay t_d between the application of a current step $I > I_{th}$ and the appearance of stimulated emission given by[50]

$$t_d = \tau \ln \left(\frac{I}{I - I_{th}} \right) \qquad \text{(III-1)}$$

This relationship may be understood by reference to Fig. 12. The application of a current step results in a build-up of the store of injected minority carriers, measured by

$$N = \int n(x) dx \qquad \text{(III-2)}$$

where n(x) is the local minority carrier density. This build-up, in the simplest model, has exponential behaviour governed by the lifetime τ of the carriers. Lasing occurs when N reaches a critical value necessary to produce optical gain equal to the cavity losses.

For the case that the lifetime varies with the excitation level of the laser, Ripper has shown that the parameter τ in (III-1) corresponds to the average recombination lifetime of minority carriers when the population inversion of the laser is at the threshold level.[51]

Measurements of t_d at various excitation levels has enabled workers to determine τ in numerous GaAs laser systems.[52] In this work related measurements made with PbSe diffused diode lasers at 77°K are reported. Rather than directly measuring the time dependence of the emitted light, however, in this experiment is measured the current level at which emission first appears when short current pulses are applied to a laser. Threshold current for pulse excitation varies with pulse width since stimulated emission will be produced only if the pulse width is greater than the turn-on delay of the laser at a given current level. Application of gives

$$t_p = \tau \ln \left(\frac{I_{th}^p}{I_{th}^p - I_{th}^s} \right) \qquad \text{(III-3)}$$

where I_{th}^p is the amplitude of a current pulse of duration t_p for which stimulated emission first appears, and I_{th}^s is the threshold current for a step excitation. To derive the recombination lifetime τ , the equation (III-3) together with measurements of the dependence of collected light output on pulse amplitude for current pulses of varying width has been used. A similar approach was used by Gorbylev et. al.[53] This method obviates the need for a radiation detector which is both fast and sensitive, as required by direct time-delay measurements. Such detectors are difficult to obtain for the output frequency of Pb Se lasers.

(i) Experimental Techniques

The PbSe laser studied was produced using the techniques described in Appendix A. The depth of its junction was measured to be 2 mils. The completed diode was mounted in a copper heatsink structure whose inductance was measured to be less than 15 nH, and attached to the cold finger of a dewar maintained at 77^oK. The diode area was 1.2×10^{-3} cm^2. Current pulses were generated with an SKL Model 503A pulser and measured with a Tectronix Type 1S1 sampling unit. A resistor of value near 50Ω was placed in series with the diode to eliminate pulse reflections. The risetime of the pulses as measured on the system was 0.9 nsec; values of the pulse-width quoted below correspond to the pulse on-time plus half its risetime. The light output of the laser was collected with an f/1.2 optical system and measured with a Au:Ge photoconductive detector whose response time under operating conditions was 5 μsec. A boxcar integrator was used to enhance the signal-to-noise ratio.

(ii) Results and Discussion

Measurement of the collected light output (in arbitrary units) vs. pulse current are shown in Fig. 13. The sharp rise in collected light with increasing current enables I_{th}^p to be estimated with an uncertainty of less than 0.2 A for the shortest pusle, and much less uncertainty for longer pulses. The results for I_{th}^p are plotted in Fig. 14 vs. t_p in accordance with Equation (III-3), from which the recombination lifetime is found to be 2.1 nsec.

Degradation of the current pulse risetime by circuit inductance could lead to the observed dependence of I_{th}^p on t_p. In the experiment this mechanism was not effective, as seen from the measured value of the sample mount inductance and from observations of the pulse reflected from the sample when its series resistance was changed

from 50 Ω .

Inasmuch as (III-1) is derived under the assumption that current flow in the diode contributes exclusively to the store of minority carriers it might be argued that for p-n junctions in the Pb salts, which have high values of the static dielectric constant,[54] a sizeable correction must be made to account for the majority carriers added to the edges of the depletion region as the diode is forward biased. The majority carrier charge was evaluated from capacitance measurements and found to be near 6×10^{-10} coul, which can be supplied by 5A current pulses in 0.12 nsec. Thus corrections to the functional form of Equation (III-1) are small and have been neglected; a corrected value to the lifetime, as determined from Fig. 14, is 2.0 nsec.

(iii) Interpretation of Lifetime

The contribution to the recombination rate from spontaneous radiative transitions may be obtained from the formula:[55]

$$R_{spon} = \int dE \sum_{u,\ell} \frac{4Ne^2E}{m^2\hbar^2c^3} |M|^2 f_u (1-f_\ell) \qquad \text{(III-4)}$$

which applied to band-to-band transitions in direct bandgap materials. Here R_{spon} is the total number of recombinations per unit time and volume, u and 1 indicate the upper and lower band states respectively, that participate in a transition that generates a photon of energy E, f_u and f_ℓ are their occupation numbers and $|M|^2$ corresponds to the directionally-averaged momentum matrix element between the states; N denotes the index of refraction of the material at energy E.

The application of expression (III-4) to PbSe leads to the relation

$$R_{spon} = \frac{4Ne^2 E_g P_{cv}^2}{m^2 \hbar^2 c^3} \int \rho_{red}(E) f_c(E)[1 - f_v(E)] dE \quad \text{(III-5)}$$

where it has been assumed that the matrix element exists only between conduction and valence band states of the same wavevector k, and the energy of the emitted photons has been approximated by E_g. The averaged momentum matrix element is

$$P_{cv}^2 = \frac{1}{3}(P_\ell^2 + 2P_t^2) \quad \text{(III-6)}$$

as described in Chapter IV-2. The quantity $\rho_{red}(E)$ is the conduction-valence band joint density of states obtained in Appendix B. The dependence on E of the fermi factors is an implied one: within the energy band model of Pb Se used here (described in Appendix B), the conduction and valence bands are symmetric, and the kinetic energy of a carrier contributing to the emission of a photon of energy E is

$$\epsilon = \frac{E - E_g}{2} \quad \text{(III-7)}$$

Since the equilibrium minority carrier density at the temperatures of interest is negligibly small, the minority carrier lifetime is given by the relation

$$R_{spon} = \frac{n}{\tau_{spon}} \quad \text{(III-8)}$$

(p type material assumed) and the lifetime may be written in the form

$$\frac{1}{\tau_{spon}} = W_0 F(\epsilon_{fn}, \epsilon_{fp}) \qquad \text{(III-9)}$$

where

$$W_0 = \frac{4Ne^2 E_g P_{cv}^2}{m^2 \hbar^2 c^3}$$

$$F(\epsilon_{fn}, \epsilon_{fp}) = \frac{\int \rho(E) f_c(E)[1-f_v(E)]\, dE}{\int \rho(E) f_c(E) dE} \qquad \text{(III-10)}$$

and the relation

$$\rho_{red}(E)dE = \rho(\epsilon)d\epsilon \qquad \text{(III-11)}$$

has been used, where $\rho(\epsilon)$ is the density of states in a single band.

The second (dimensionless) factor has been evaluated within a parabolic band model for generality. Within this approximation it is a numerical factor always less than unity that is independent of band parameters and varies solely with the quasifermi levels of electrons and holes. Its values therefore are applicable to all Pb salt semiconductors. For conditions in which the majority carrier population is heavily degenerate (i.e. $f_v(E)=0$ for energies of interest), the second factor is unity, and the lifetime attains its minimum value

$$\tau_{spon\,min} = \frac{m^2 \hbar^2 c^3}{4Ne^2 E_g P_{cv}^2} \qquad \text{(III-12)}$$

In PbSe $\tau_{spon\,min}$, calculated using values of the matrix elements obtained by Bernick[56] as described in Chapter IV.2, is 9.3 nsec at 77°K, and has weak temperature dependence (dominated by the

behaviour of $E_g(T)$). This lifetime is substantially longer than the corresponding number for GaAs (near 1 nsec); the ratio of the two is understandable in terms of the inverse dependence on energy gap, which in turn stems from the energy dependence of the number of photon modes per unit energy.

The occupation factor $F(\epsilon_{fn}, \epsilon_{fp})$ has been evaluated numerically and is displayed in Fig. 15 as a function of the dimensionless variables $\frac{\epsilon_{fn}}{KT}$, $\frac{\epsilon_{fp}}{KT}$. Values of $\frac{\epsilon_{fn}}{KT}$ and $\frac{\epsilon_{fp}}{KT}$ appropriate to the junction region near threshold at 77°K in diffused PbSe lasers are near 0.1 to 0.5, as discussed in Section V-3 (although both quantities very spatially). The occupation factor is thus expected to be of the order of 0.2 to 0.4. The overall lifetime due to spontaneous recombination is therefore found theoretically to be near 20 to 40 nsec. Since the measured lifetime is 2 nsec, it is clear that other recombination processes must be important.

An interesting feature of the results of Fig. 15 is that the lifetime is relatively independent of minority carrier density, particularly at low carrier degeneracies. This allows the occupation factor to be conveniently approximated by its value in the limit $\epsilon_{f\,min} \rightarrow -\infty$:

$$F(\epsilon_{fn}, \epsilon_{fp}) = \frac{2}{\sqrt{\pi}} \int_0^\infty \frac{\sqrt{x}\, e^{-x}\, dx}{1 + e^{x - \epsilon_{fp}/KT}} \qquad \text{(III-13)}$$

The above integral may in turn be approximated by

$$F(\epsilon_{fn}, \epsilon_{fp}) = \frac{1}{1 + \sqrt{8}\, e^{-\epsilon_{fp}/KT}} \qquad \text{(III-14)}$$

whose values are shown in Fig. 15.

Corrections may be necessary to the above calculation of the radiative lifetime due to several sources. To obtain the net recombination rate one should take into account the generation of minority carriers due to reabsorption of spontaneously emitted photons. This generation rate depends strongly on geometrical factors of the laser, and has been omitted in this work. Similarly, the possibility exists that spontaneously emitted photons in low Q (non-lasing) modes may cause additional recombinations by stimulated emission. In lasers with lossy cavities the density of photons in non-lasing modes may build up appreciably before the onset of lasing. Preliminary calculations indicate, however, that this effect causes only negligible changes in the net recombination rate.

Among the non-radiative recombination mechanisms that may be present in the PbSe diffused lasers are Auger recombination, Auger recombination assisted by defects or phonons,[57] recombination at isolated centers with electronic levels lying within the energy gap, and recombination at extended defects such as dislocations or microprecipitates. A review of available data on recombination in bulk samples of PbSnTe (expected to have behaviour similar to PbSe) is given by Cammack.[58] Present data do not allow identification of the dominant recombination mechanism. Since it is likely that the recombination rate observed in present lasers is higher than the theoretical minimum value (given by radiative and Auger processes), it is possible that further studies of minority carrier lifetime in laser structures will contribute to lowering the value of threshold current density in lasers.

III. 3 Model for Carrier Distributions under Forward Bias

In this section a formalism is presented which allows approximate calculation of the variation of carrier densities, quasifermi

levels and electrostatic potential near the junction of graded p-n diodes at high forward bias and low temperature. The model assumes that the net donor density in the vicinity of the junction is a linear function of distance normal to the junction, with the same grading parameter on either side of the junction. This assumption, made for simplicity, restricts the applicability of the results to Model III of the profile of net donor density of PbSe diffused diodes, as discussed in Section II. 4 (v). Considerations are presented at the end of this chapter which allow the results to be approximately extended to asymmetric donor profiles.

A sufficient set of equations to calculate the current distribution of arbitrary one-dimensional junctions at arbitrary bias levels in the steady state is given by[45]

$$\frac{d^2\psi}{dx^2} = -\frac{q^2}{\epsilon}\left[N_D(x) - N_A(x) + p - n\right] \tag{III-15.1}$$

$$n = \mathcal{N}_{dc}\,\mathcal{F}_{1/2}\left(\frac{\psi + \phi_n - \frac{1}{2}E_g}{kT}\right) \tag{III-15.2}$$

$$p = \mathcal{N}_{dv}\,\mathcal{F}_{1/2}\left(\frac{\psi - \phi_p - \frac{1}{2}E_g}{kT}\right) \tag{III-15.3}$$

$$\frac{d}{dx}\left(n\mu_n\frac{d\phi_n}{dx}\right) = q\,U(n,p,x) \tag{III-15.4}$$

$$\frac{d}{dx}\left(p\mu_p\frac{d\phi_p}{dx}\right) = -q\,U(n,p,x) \tag{III-15.5}$$

Here ψ is the electrostatic potential, ϕ_n and ϕ_p are quasifermi levels for electrons and holes, respectively, μ_n and μ_p are their respective mibilities, U(n, p, x) is the number of electron-hole recombinations per unit volume and time, $\mathcal{N}_{dc}$ and $\mathcal{N}_{dv}$ are effective densities of states for conduction and valence band and $\mathcal{F}_{1/2}$ is the fermi integral. For convenience, a list of symbol definitions is presented at the end of this section. The sign and reference level used in the definition of the quasifermi levels may be seen in Fig. 16: ϕ_n and ϕ_p are measured from the conduction and valence band edges and are positive for degenerate electron and hole densities, respectively.

While some approximations are inherent in the set (III-15), notably quasithermal equilibrium, generally solutions of the equations are regarded as an "exact" solution of the set (restricted to classical statistics) have been presented, including those of Gummel,[59] DeMari,[60] Choo[61] and Hachtel.[62] However, the methods are expensive in computer time and their convergence is not assured under conditions of very high forward bias. Numerous approximate solutions have also been developed for the case of linearly graded junctions. Sah and others[63, 64] have considered approximate carrier distributions and current flow in the case of low injection and nondegenerate statistics. Morgan and Smits[65] have calculated exactly the variation of the electrostatic potential under the assumptions of constant hole and electron quasifermi levels and classical statistics. However, no consideration is given in the literature to the solution of linearly graded junctions under high forward bias and under conditions where carrier concentrations may be degenerate.

(i) Model Description

In order to obtain a solution to the set (III-15) according to the present model, the approximation is made that the system is everywhere quasineutral. It is thus assumed that the space-charge region dissappears under high forward bias, and only negligible amounts of unneutralized space-charge exist to establish the required electric fields near the junction. A similar result has been postulated by Moll[66] and demonstrated by Morgan and Smits[65] for graded junctions in the classical statistics regime. The validity of the quasi-neutrality approximation restricts the model applicability to the condition of high forward bias. It may be noted, however, that to obtain optical gain the forward bias voltage of the junction must exceed the bandgap of the semiconductor; the required high injection is certainly obtained in the vicinity of laser threshold.

With the use of the quasineutrality approximation, Equation (III-15.1) becomes

$$\frac{d^2\psi}{dx^2} = -\frac{q^2}{\epsilon}\left[N_D(x) - N_A(x) + p - n\right] = 0 \qquad \text{(III-16.1)}$$

or

$$n - p = N_D(x) - N_A(x) = ax \qquad \text{(III-16.2)}$$

where linear grading of the net donor density has been assumed. Thus Equations (III-16.2), (III-15.2) and (IV-15.3) form a set which may be solved algebraically at any point to obtain ψ in terms of

ϕ_n and ϕ_p. The resultant variation with distance of the electrostatic potential Ψ is found to be slightly nonlinear, indicating that some spacecharge is necessary to satisfy Poisson''s equation; however, the space charge is negligible with respect to the concentrations of electrons and holes present at every point.

The form of the recombination rate U(n, p, x) to be used must be selected in accordance with the model of the dominant recombination process. For example, under lasing conditions it is reasonable to assume that the recombination rate is determined primarily by the (spatially varying) stimulated recombination rate. In the present chapter consideration is limited to forward bias below threshold. In the absence of a detailed model of the dominant recombination processes in the Pb salts, and for simplicity, the function U(n, p, x) is taken to be of the form

$$U(n,p,x) = \frac{n_{min}}{\tau} \qquad \text{(III-17)}$$

where n_{min} is the minority carrier density. This choice allows comparison to be made with other theories, in many of which a constant minority carrier lifetime is also assumed.

It is convenient to cast the set of equations into a dimensionless form. With the definitions:

$$\rho = \frac{p}{\mathcal{N}_d} \qquad \theta_p = \frac{\phi_p}{kT} \qquad \Psi = \frac{\psi}{kT}$$

$$\eta = \frac{n}{\mathcal{N}_d} \qquad \theta_n = \frac{\phi_n}{kT} \qquad z = \frac{ax}{\mathcal{N}_d} \qquad \text{(III-18)}$$

$$\lambda^2 = \frac{\mathcal{N}_d^2 e}{a^2 \mu kT\tau}$$

the set of equations to be solved becomes

$$\eta - \rho = z \tag{III-19.1}$$

$$\eta = \mathcal{F}_{1/2}(\theta_n + \Psi) \tag{III-19.2}$$

$$\rho = \mathcal{F}_{1/2}(\theta_p - \Psi) \tag{III-19.3}$$

$$\frac{d\theta_n}{dz} = \frac{\lambda^2}{\eta} \int_{-\infty}^{z} \rho(z')\,dz' \tag{III-19.4}$$

$$\frac{d\theta_p}{dz} = -\frac{\lambda^2}{\rho} \int_{z}^{\infty} \rho(z')\,dz' \tag{III-19.5}$$

The Equations (III-19.4) and (III-19.5) are first integrals of the corresponding equations in the original set, obtained by noting that $d\theta_p/dz$ correspondingly vanishes on the p side.

A sufficient set of boundary conditions is given by

$$\theta_n = \theta_p = \tfrac{1}{2} \mathcal{V} \qquad \text{at } z = 0$$

$$\lim_{z \to \infty} \eta(z) = z \tag{III-20}$$

Here $\mathcal{V}$, defined by

$$\mathcal{V} = \theta_n + \theta_p \quad \text{at} \quad z = 0 \qquad \text{(III-21)}$$

may be regarded as an input parameter, which corresponds in the limit of small λ to the applied voltage minus the energy gap, normalized by KT.

The system considered allows solution of junction characteristics at arbitrary temperature for arbitrary grading value, provided the quasineutrality assumption is applicable. Results are obtained in terms of the 2 parameters: $\mathcal{V}$ (reduced applied voltage) and λ^{-1} (normalized diffusion length). The range of $\mathcal{V}$ of interest is $0 < \mathcal{V} < \mathcal{V}_{lasing}$, corresponding to high forward bias below threshold. For simplicity, a unique value of λ is used to characterize the junction in this model, which corresponds to the assumption of equal hole and electron mobilities and lifetimes, and the neglect of variations of mobility with defect and carrier density often observed in bulk samples. Using values of μ depicted by the dotted line of Fig. 17 and minority carrier lifetime of 2 nsec at all temperatures, values of the parameter λ appropriate to PbSe may be calculated and are shown in Fig. 18 vs. T for a = 10^{17} cm^{-3}/μ . The effective density of states $\mathcal{N}_d$ has been calculated using a parabolic band model (which should be appropriate for conditions where electron and hole densities are less than 10^{18} cm^{-3}) and is displayed in Fig. 19.

(ii) Method of Solution

The set of Equations (III-19) is nearly in a form appropriate for numerical solution by Euler's forward-integration method

(direct integration). A difficulty exists, however, due to the fact that part of the set of necessary boundary conditions are specifications as $z \to \infty$ and the boundary conditions known at z=0 are insufficient to determine an allowable solution. The difficulty is evident when Equations (III-19.4) and (III-19.5) are written in the form

$$\frac{d\theta_n}{dz} = \frac{\lambda^2}{\eta}\left[\mathcal{J}_0 + \int_0^z \rho(z')dz'\right] \qquad \text{(III-22.1)}$$

$$\frac{d\theta_p}{dz} = -\frac{\lambda^2}{p}\left[\mathcal{J}_0 - \int_0^z \rho(z')dz'\right] \qquad \text{(III-22.2)}$$

where

$$\mathcal{J}_0 = \int_0^\infty \rho(z')dz' \quad \text{with} \quad J = \frac{2q\mathcal{N}_d^2}{\mathcal{T}a}\mathcal{J}_0 \qquad \text{(III-22.3)}$$

Evaluation of the derivatives in (III-22) requires knowledge of $\mathcal{J}_0$, a quantity which in this scheme is not obtained till the solution has been carried out. In this work a trial and error method has been used to obtain solutions. After solving the set with a trial value of $\mathcal{J}_0$, the integral of $\rho(z)$ is compared with $\mathcal{J}_0$ and a new trial value of $\mathcal{J}_0$ is determined. This sequence is repeated until self-consistency is obtained.

It may be noted that when $\lambda = 0$ the set (III-19) reduces to a set of non-linear algebraic equations, and may be solved without recourse to boundary conditions. This limit is reached for the case of infinite recombination lifetime or infinitely large carrier

mobility; the solution for $\lambda = 0$ has the feature that the quasifermi levels are constant. Values of ϑ_o for $\lambda = 0$ have been found to be very good initial trial values for solutions with low values of λ. In this work values of ϑ_o for finite, small λ were then used as the starting point for solutions with successively larger values of λ.

The errors that occur when an incorrect trial value of ϑ_o is used are magnified in Equation (III-22.2) for large values of z. The quantity ρ in the denominator (normalized minority carrier density) becomes small for large z. In a proper solution, the numerator also vanishes, by the definition of ϑ_o. If the trial ϑ_o and the integral of ρ disagree, however, major errors may result. The difficulty is overcome in this work by using a modified expression for $\frac{d\theta_p}{dz}$ in this regime. For large values of z the minority carrier density is non-degenerate; if it is further assumed that it decays exponentially in z and the local electric field is approximately constant than it may be shown that

$$\theta_p' = \frac{1}{2}\left(\Psi' - \sqrt{\Psi'^2 + 4\lambda^2}\right) \qquad \text{(III-24)}$$

This expression is analogous to the well known expression for the effective carrier diffusion length in a constant electric field E:[45]

$$\frac{1}{L_{diff}} = \frac{1}{2}\left(\frac{q\mathcal{E}}{kT} + \sqrt{\left(\frac{q\mathcal{E}}{kT}\right)^2 + \frac{4}{D\tau}}\right) \qquad \text{(III-25)}$$

For typical values of λ considered in this work, self consistency of ϑ_o (to the level of 5%) was achieved with one to four iterations. The total calculation employs only pennies of CPU time

on the IBM 370/65 of the M.I.T. Information Processing Center.

To numerically evaluate the fermi integral $\mathfrak{F}_{1/2}(u)$ the well known approximations[67]

$$\mathfrak{F}_{1/2}(u) = \frac{e^u}{1+0.27e^u} \quad , \; u < 1.0$$

$$\mathfrak{F}_{1/2}(u) = \frac{4}{3\sqrt{\pi}}\left(u^2+1.7\right)^{3/4} , \; u > 1.0 \qquad \text{(III-26)}$$

were used. These have been shown to be valid within 3% over their range of application.

(iii) Results of the Model

The calculated variation of carrier density near the junction for several values of the parameters ϑ and λ is shown in Fig. 20. Variation of the net donor density is shown by the dotted line. On the figure also is indicated the slope of ρ or η that would be obtained on the basis of classical diffusion in a homogeneous semiconductor (i. e., if abrupt junctions and nondegeneracy were assumed). It may be noted that values of ϑ that correspond to laser thresholds are in the vicinity of 0.1-0.5 at 77°K, as will be shown in Chapter V; it was shown in Part (ii) above that values of λ near 0.1 to 0.3 are most appropriate to diffused PbSe lasers. The curves for these parameter values indicate dramatically that the minority carrier distribution is much more confined to the junction region than would be found by the classical diffusion model.

An interesting feature of the results of Fig. 20 is the apparent

insensitivity of the carrier distributions to the parameter λ. This results from the choice of initial conditions used in the solutions. A choice of the parameter υ (which is directly related to the applied voltage for $\lambda = 0$, but for the other values may be different) effectively specifies the minority carrier concentration at $z = 0$. Furthermore, by the symmetry of electrons and holes it may be readily derived that under all conditions

$$\frac{d\eta}{dz} = -\frac{d\rho}{dz} = \frac{1}{2} \quad \text{at } z = 0 \tag{III-27}$$

in this model. In effect, then, the shape of $\eta(z)$ and $\rho(z)$ near $z = 0$ is completely specified by υ alone, and subsequent variation caused by different values of λ must be slight.

The variation of the electrostatic potential Ψ and the quasi-fermi level for one species is shown in Fig. 21 for $\lambda = 0.32$ and a variety of bias levels. We recall that for $\lambda = 0$ the quasifermi levels remain constant in space. For small υ approximately the same result holds if $\lambda = 0.32$. The variation of Ψ indicates that there is a sizeable electric field present which tends to oppose the flow of carriers. For $\upsilon = 0$, and representative values of $T = 77^{\circ}K$, and $a = 10^{17}$ cm$^{-3}/\mu$, the electric field at the junction is of the order of 25 v/cm. In regions of small minority carrier density, the potential variation may be directly related to the variation of chemical potential ($\theta_n + \Psi$) of the majority carriers. For example, for $\lambda = 0$ (constant quasifermi level) and low temperature it is clear that Ψ must change so that the distance between the majority carrier fermi level and the band edge increases as needed to accomodate more carriers in the band. The electric field decreases far from the junction because the variation of carrier density with chemical potential is sublinear.

For increasing values of $\mathcal{V}$ and λ, the junction electric field decreases and finally changes sign. In this regime where very sizeable currents are flowing the finite sample resistance strongly influences the behaviour of Ψ and Θ n. The reduction of the electric field is largest at the junction, where the net carrier density is the smallest and the resistance is largest. Ultimately the current flow is too large to be supplied by diffusion alone even under flat band condition and the electric fields aid the flow of both minority and majority carriers. Under such conditions, the minority carriers are substantially less confined that would be predicted by the classical diffusion model. As will be shown in Section V, lasing occurs long before this regime is reached in standard structures.

The regime of $\mathcal{V}$ and λ for which the junction electric field changes sign (which we will call the resistive regime) may be readily determined after noting that the normalized electric field $d\Psi/dz$ at the origin is given by

$$\frac{d\Psi}{dz} = \frac{1}{2\left(\frac{d\mathcal{F}_{1/2}(u)}{du}\right)_{u=\frac{\mathcal{V}}{2}}} - \frac{\lambda^2 \mathcal{J}_o(\mathcal{V},\lambda)}{\mathcal{F}_{1/2}\left(\frac{\mathcal{V}}{2}\right)} \quad \text{at } z=0 \tag{III-28}$$

Using the result that the value of $\mathcal{J}_o$ is approximately independent of λ, it is possible to calculate from (III-28) a limiting value $\mathcal{V}_{lim}$ of $\mathcal{V}$ for each λ so that for $\mathcal{V} > \mathcal{V}_{lim}$ the electric field is negative (which corresponds to the resistive regime). Values of $\mathcal{V}_{lim}$ vs. λ are shown in Fig. 23b.

The normalized current density flowing through the junction for various values of $\mathcal{V}$ and λ is shown in Fig. 22. For $T = 77^oK$, $a = 10^{17}\ cm^{-3}/\mu$ and $\tau = 2$ nsec, units of $\mathcal{J}_o$ are 3600 A/cm^2. Thus,

for these values the flat band condition is not reached till the current density becomes greater than 35000 A/cm^2.

Calculations of the J - V relation for junctions should be possible on the basis of this model. For $\lambda \neq 0$, however, there is difficulty in separating the voltage drops across the junction and resistive drops across the bulk regions. The structure considered in this model extends to infinity in the positive and negative z directions; it is not obvious whether θ_n and Ψ reach finite limits for increasing z. Some artifice (such as the inclusion of contacts or the definition of a region where the donor profile ceases to be linearly graded) must be employed to define with precision what is meant by the junction region. No such extension was carried out in this work, however.

(iv) Validity of Quasineutrality Assumption

The argument in support of local charge neutrality parallels the standard discussion based on the concept of Debye length,[68] which will be reviewed here briefly. The function $_o(x)$ is defined as the potential variation obtained under the assumption of strict quasineutrality (III-16). If the actual potential (x) is near $_o(x)$ then Poissons equation may be written

$$\frac{d^2\Psi}{dx^2} = -\frac{q}{\epsilon'}\left[p(\Psi) - p(\Psi_o) - n(\Psi) + n(\Psi_o)\right] \approx \frac{1}{L_{db}^2}(\Psi - \Psi_o) \qquad \text{(III-29)}$$

where

$$\frac{1}{L_{db}^2} = \frac{q^2 N_d}{\epsilon KT}\left[\left(\frac{dF_{1/2}(u)}{du}\right)_{n_o} + \left(\frac{dF_{1/2}(u)}{du}\right)_{p_o}\right]$$

(III-30)

The solution to (III-29) is given by

$$\Psi - \Psi_o = C_1 e^{-x/L_{db}} + C_2 e^{x/L_{db}} \tag{III-31}$$

The deviation of the potential from Ψ_o will be reduced by e^{-1} over a distance L_{db}. If only small variations in N_D-N_A take place over a region of this size, then the semiconductor will be substantially neutral. Typical values of L_{db} for PbSe structures for $\mathcal{V} > 0$ are in the range of 200 to 500 Å, which is very small with respect to the scale of variation of N_D-N_A.

A somewhat more quantitative argument may be made by re-casting Equation (III-15.1) into dimensionless units:

$$\eta(\Psi) = z + \rho(\Psi) + \sigma \frac{d^2\Psi}{dz^2} \tag{III-32}$$

where

$$\sigma = \frac{\epsilon k T a^2}{q^2 \mathcal{K}_d^3}$$

In the model solutions for Ψ the last term of the r.h.s. has been neglected with respect to the other terms. At z = 0, the last term is identically zero by symmetry, yet $\rho(\Psi)$ is appreciable. For large z, the derivative term is again unimportant. It may be further shown for solutions Ψ^* obtained by assuming quasineutrality that self consistently at every point $\sigma\, d^2\Psi^*/dz^2$ is negligible. For example, for $\mathcal{V} = 0$, $\lambda = 0$, values of $d^2\Psi/dz^2$ are plotted vs. z in Fig. 23. The value of σ for 77°K and $a = 10^{17}$ cm$^{-3}/\mu$

is 2.5×10^{-4}. Thus the neglected term is at every point less than 6.5×10^{-5}.

To complete the argument, it may be noted that uniqueness of solutions to (III-15) is intuitive (it may be easily proven for $\lambda = 0$). Thus the selfconsistent solutions Ψ^* must be the correct solutions.

(v) Carrier Distributions Above Lasing Threshold

As noted earlier, above the threshold for laser action the model of Section III. 3 (i) must be modified to take into account the stimulated emission recombination rate. From Reference 55, the rate of recombination per unit volume due to stimulated emission of photons of energy E into one cavity mode is given by

$$W_{stim}(E) = \frac{4 N e^2 \hbar |M|^2 \rho_{red}(E)[f_c(E) - f_v(E)]}{\pi^2 m^2 E} \qquad \text{(III-33)}$$

where N is the local density of photons in the mode and the remaining symbols have the same meaning as in (III-5). The rate varies spatially because N is proportional to $|\psi_m(x)|^2$ (where $\psi_m(x)$ is the electric field amplitude of the lasing mode) and because of the dependence of (III-33) on quasifermi levels of both electrons and holes.

The total number of injected carriers per unit area $N_{min} = \int n_{min}(x)dx$ may be readily estimated under lasing conditions. $N_{min}(J)$ is known to be approximately independent of current density above threshold, since the gain coefficient for any laser cavity mode may not increase above the value set by the loss coefficient for that mode. Thus

$$N_{min}(J) = N_{min}(J_{th}) \quad \text{for} \quad J \geq J_{th} \tag{III-34}$$

$N_{min}(J_{th})$ may in turn be obtained by the relation

$$J_{th} = \frac{q\, N_{min}(J_{th})}{\tau_{rec}(J_{th})} \tag{III-35}$$

where $\tau_{rec}(J_{th})$ is the average minority carrier recombination lifetime when carrier densities are at the threshold level. (III-35) corresponds to the fact that there is one net electron-hole recombination for each carrier that crosses the junction of the device.

Under restricted conditions approximate carrier distributions may be calculated without recourse to (III-33). If the width of the lasing radiation mode is substantially greater than the region where the minority carrier density is appreciable, then N may be effectively regarded as independent of position. Also, if the majority carrier density is sufficiently degenerate, then $W_{stim}(E)$ is approximately proportional to the minority carrier density. Under such conditions, the total recombination rate may again be represented by

$$U(n,p,x) = \frac{n_{min}}{\tau(J)} \tag{III-36}$$

where $\tau(J)$ is independent of position, but dependent on the power output of the laser and hence on the value of current density flowing through the junction. The value of may be obtained with the expression

$$J = \frac{q N_{min}(J)}{\tau(J)} \tag{III-37}$$

which together with (III-32) and (III-33) yields

$$\tau(J) = \tau_{rec}(J_{th}) \cdot \frac{J_{th}}{J} \tag{III-38}$$

The solutions presented earlier then give carrier distributions under lasing conditions, provided the proper value of $\lambda(J)$ is used. In view of the relative insensitivity of the distributions to the value of λ, it is expected that for lasers operated near threshold carrier distributions are approximately the same as at threshold.

(vi) Carrier Distributions for Asymmetric Profiles

Discussion in earlier sections of this chapter has been limited to p-n junctions that are symmetrically graded, that is, junctions for which the grading constant is identical in both the n and p regions. The symmetry was used explicitly to obtain simplified boundary conditions at $x = 0$; furthermore, the quasineutrality approximation is valid only if the net donor density profile has continuous first derivatives. In this section, semiquantitative arguments are presented that extend the analysis to junctions with asymmetry. In particular the carrier distributions under forward bias will be considered for the donor profile model shown in Fig. 24a. This profile approximately corresponds to the variation of net donor density of Model I of Section II. 4(v). It is idealized, however, to the extent that it is assumed here that the net donor density on the n side varies discontinuously at $x = 0$ between zero and its bulk value (which is of

the order of 2×10^{18} cm^{-3} for the lasers considered in this work).

For this profile the assumption that quasineutrality applies everywhere is unjustified, since the donor density varies appreciably in a distance shorter than the Debye length. Standard discussions of one-sided abrupt pn^+ junctions[69] demonstrate that for profiles of this type under forward bias a space-charge layer is formed near the junction, where the largest contribution to charge on the n side is provided by unneutralized donors, and on the p side it is given by excess injected electrons (see Fig. 24b).

If the potential drop across the SCL is $\Delta\psi$, then the concentrations of carriers on either side of the SCL are related by

$$\frac{n_{no}}{n_{po}} = \frac{\mathcal{F}_{1/2}\left(\frac{\Delta\psi + \phi_n}{KT}\right)}{\mathcal{F}_{1/2}\left(\frac{\phi_n}{KT}\right)}$$

$$\frac{p_{po}}{p_{no}} = \frac{\mathcal{F}_{1/2}\left(\frac{\phi_p}{KT}\right)}{\mathcal{F}_{1/2}\left(\frac{\phi_p - \Delta\psi}{KT}\right)} \qquad \text{(III-39)}$$

Here the zero reference of ψ has been assigned to its value on the p side edge of the SCL. Using typical values of $n_{no} = 2 \times 10^{18}$ cm^{-3}, $n_{po} = 2 \times 10^{17}$, $p_{po} = 2 \times 10^{17}$ cm^{-3} for PbSe at 77°K, p_{no} is found to be near 3×10^{15} cm^{-3}. Thus the injection of holes into the n region is negligible, and junction current flows solely by injection of electrons into the p side.

Quasineutrality is expected to apply within the p region beyond the SCL edge (that is, for $x < -W_p$ as defined in Fig. 24b). At $x = -W_p$ the density of electrons must thus equal the density of holes (apart from a negligible contribution of the net donor density at that

point), and

$$\phi_n(-W_p) = \phi_p(-W_p) \qquad \text{(III-40)}$$

The current due to recombination in the very narrow space charge region is negligible and thus

$$\left.\begin{aligned} \frac{d\phi_p}{dx} &= 0 \\ \frac{d\phi_n}{dx} &= \frac{J}{n_{po}e\mu} \end{aligned}\right\} \text{ at } x = -W_p \qquad \text{(III-41)}$$

In the p region of the junction for $x < -W_p$ the equations governing the distribution of carriers are the same as the set considered previously for the symmetric junction. The boundary conditions at $x=-W_p$, given by (III-41) are somewhat different from those used earlier, but in the limit $\lambda = 0$ (that is, very large μ or τ) they become identical. Since it has been observed that for moderately graded junctions at moderate bias levels the value of λ has little influence on the carrier distribution, it is expected that solutions obtained for the symmetric junction are approximately valid for the present case also. The earlier solutions must be interpreted, however, in the following way:

(a) Appreciable numbers of minority carriers are present only on the p side of the junction; the solutions are one-sided.

(b) The point $z = 0$ corresponds to $x=-W_p$ in the present model. Values of current density must be large enough that the concentration $N_D(-W_p)$ is negligible with respect to carrier densities of interest.

(c) The parameter $\mathcal{V} = \theta_n + \theta_p$ at z = 0 no longer has the meaning of normalized applied voltage, since there is an additional potential drop $\Delta\psi$.

(d) The units used to obtain J from the dimensionless parameter γ_o are smaller by 50% for the asymmetric case than the corresponding units in (III-23), since carrier distributions on only one side of the junction are considered.

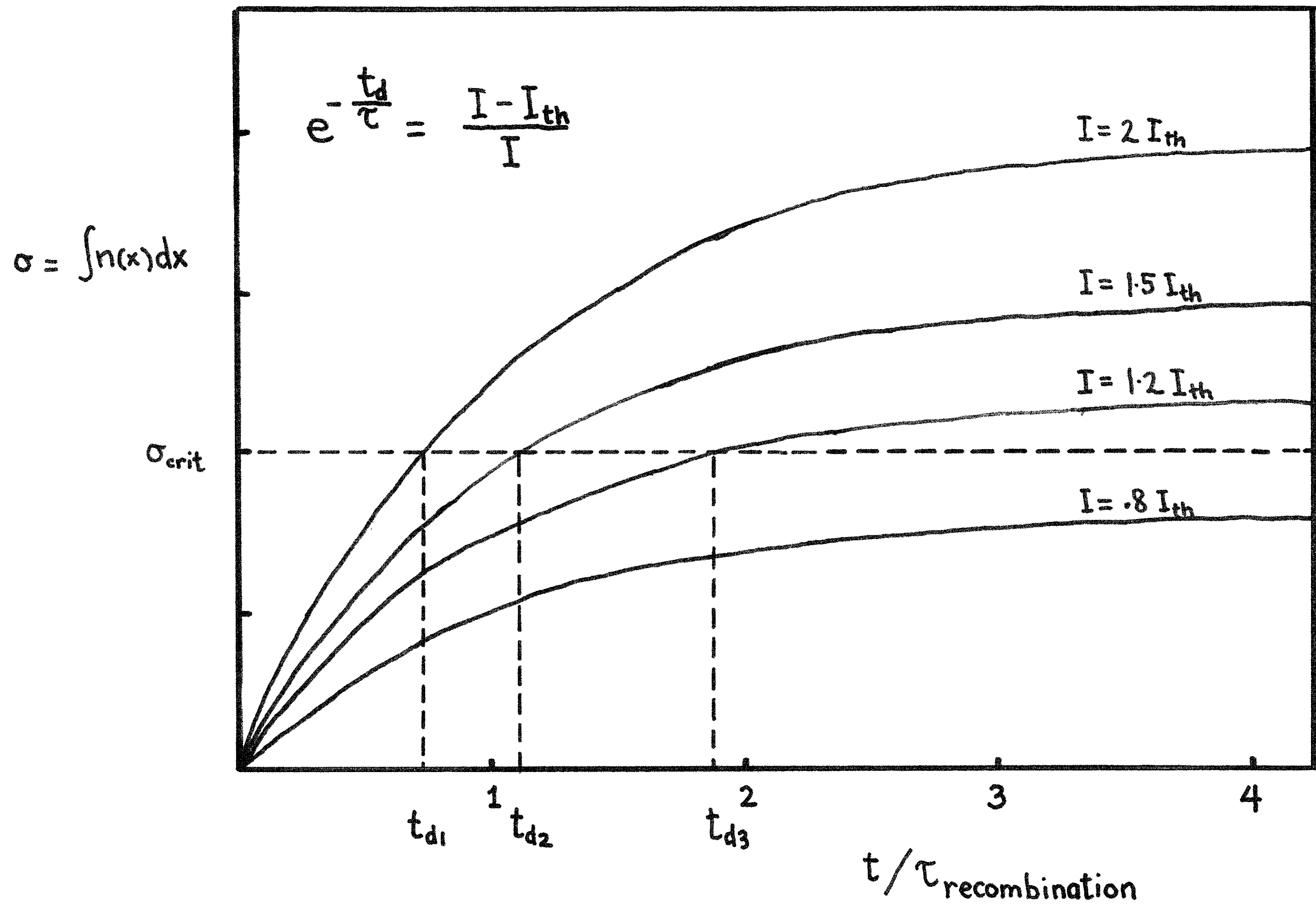

FIGURE 12: VARIATION OF TOTAL NUMBER OF INJECTED MINORITY CARRIERS WITH TIME AFTER APPLICATION OF CURRENT PULSE

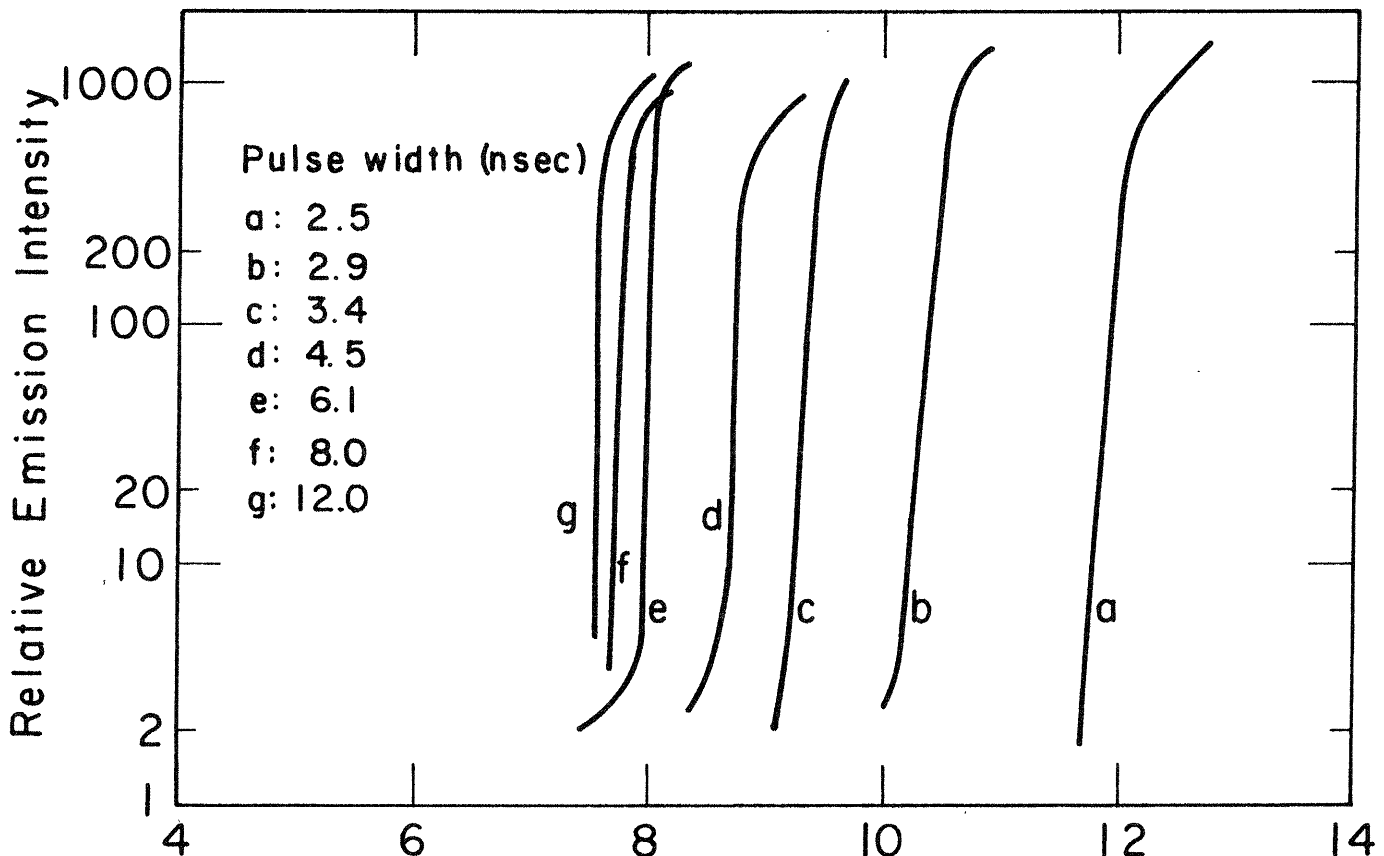

FIGURE 13: MEASURED OUTPUT POWER VERSUS PULSE AMPLITUDE FOR CURRENT PULSES OF VARYING WIDTH

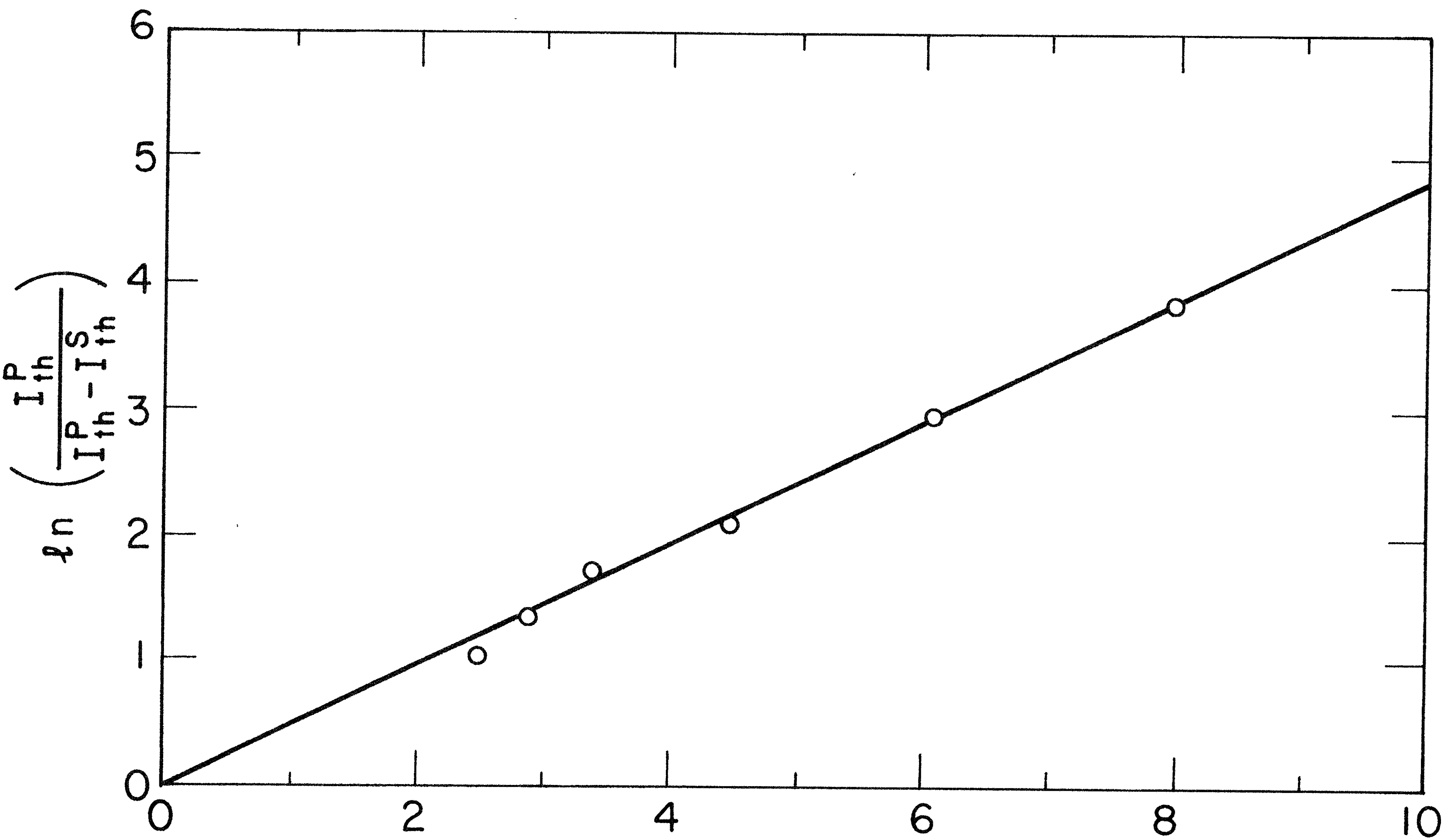

FIGURE 14: COMPARISON OF THEORETICAL AND EXPERIMENTAL DEPENDENCE OF THRESHOLD CURRENT ON PULSE WIDTH

Figure 15: Occupation Factor F for Radiative Lifetime Calculation

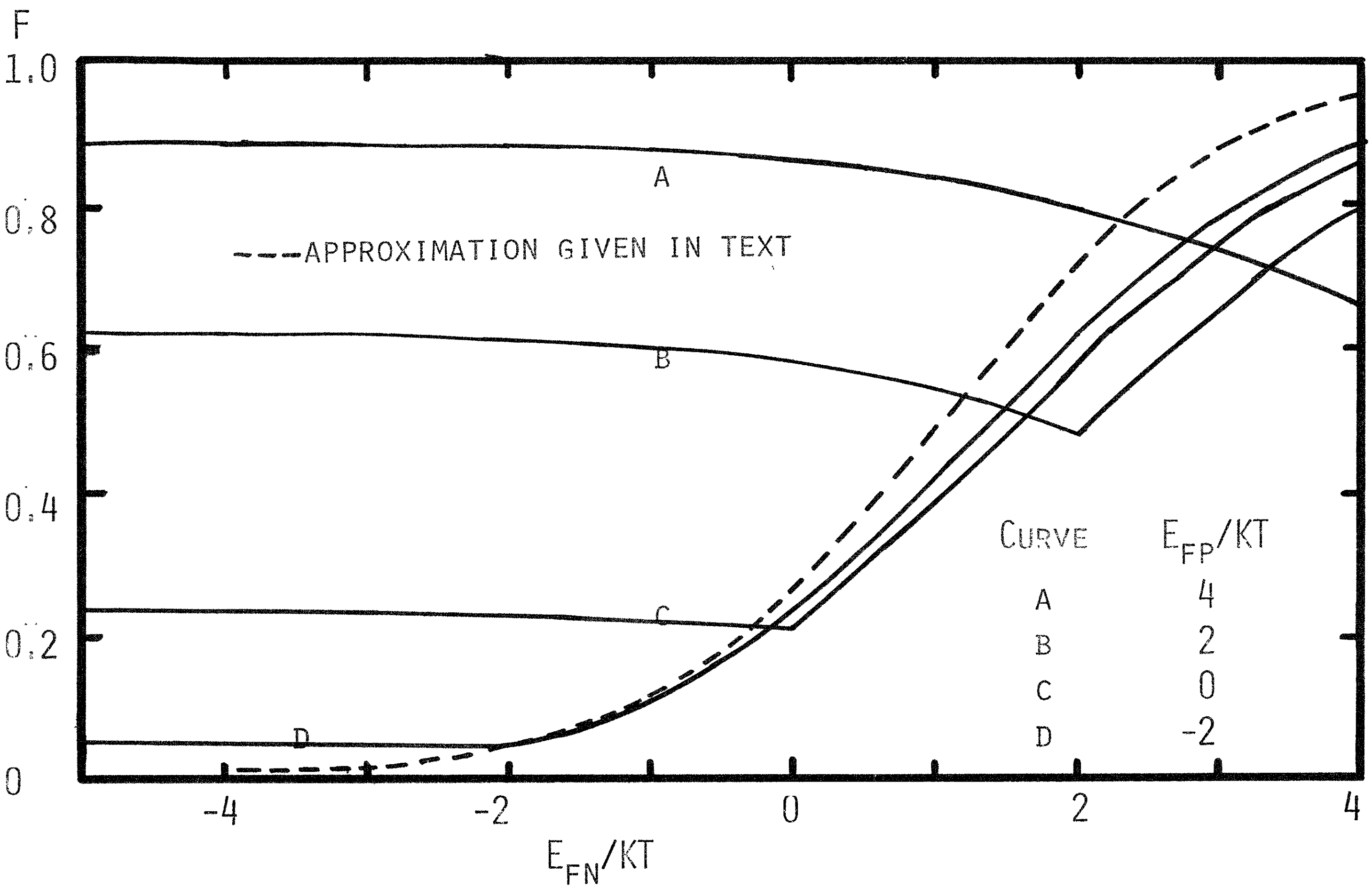

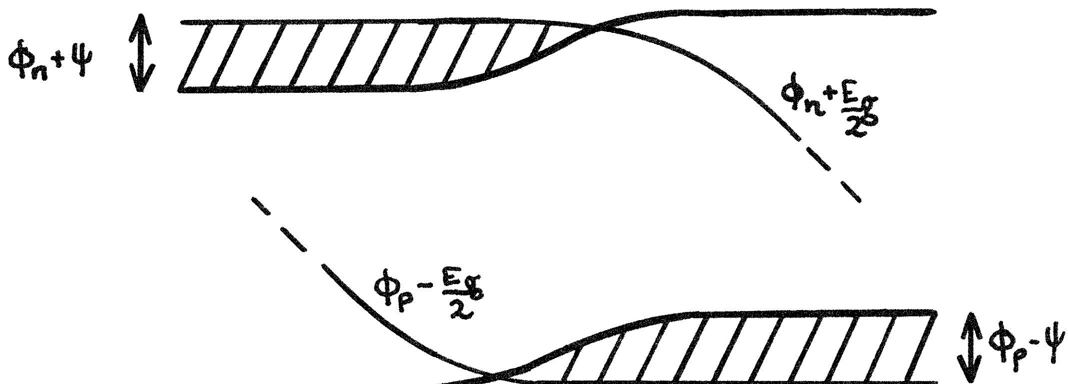

FIGURE 16: APPROXIMATE BAND DIAGRAM FOR FORWARD-BIASED DIODE JUNCTION

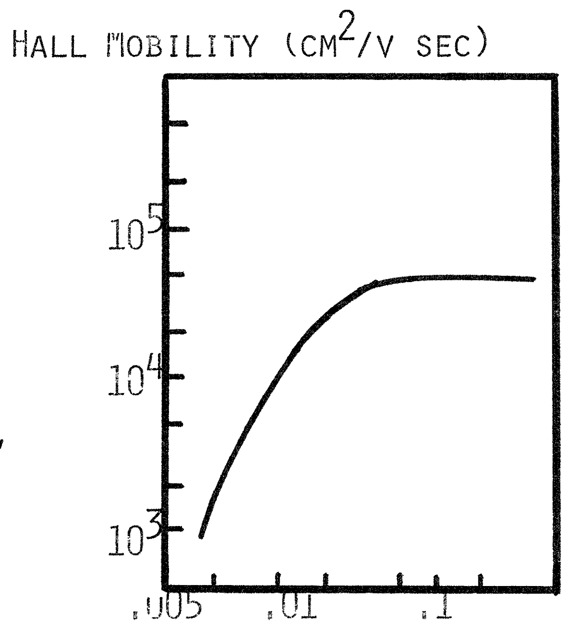

FIGURE 17: VARIATION OF CARRIER MOBILITY WITH TEMPERATURE IN PBSE

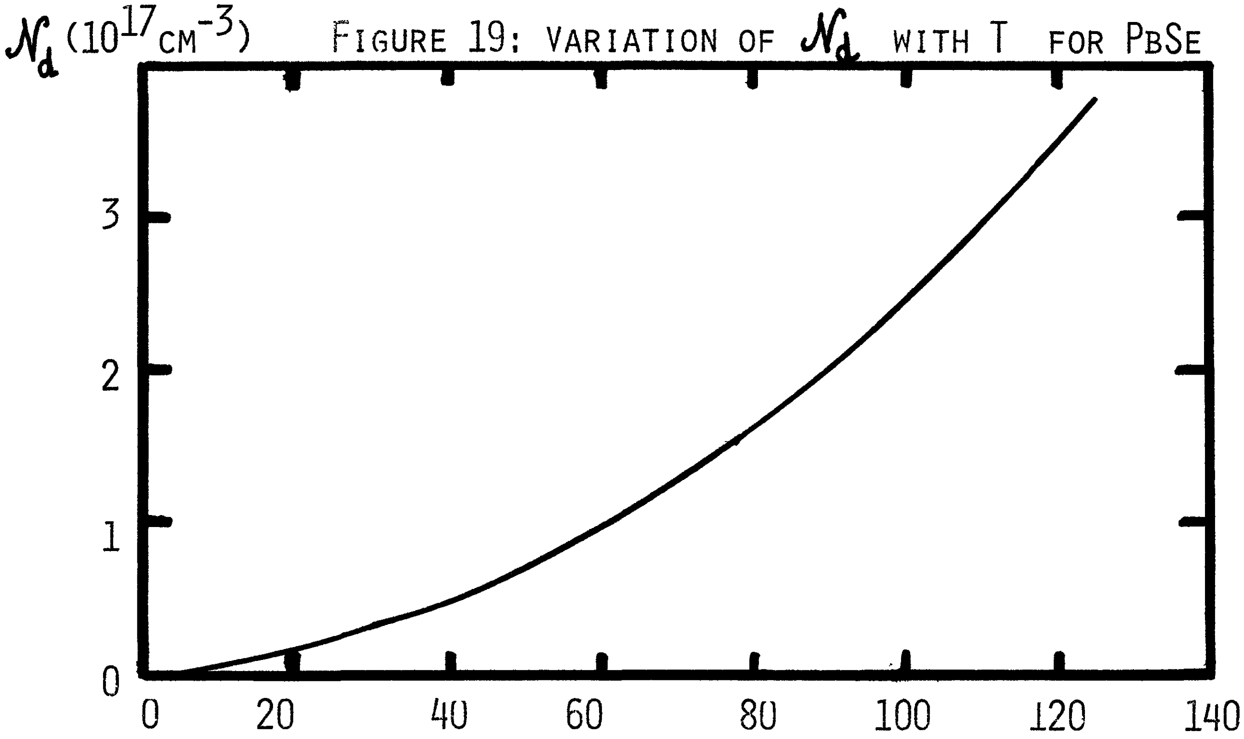

Figure 19: Variation of $\mathcal{N}_d$ with T for PbSe

Temperature (°K)

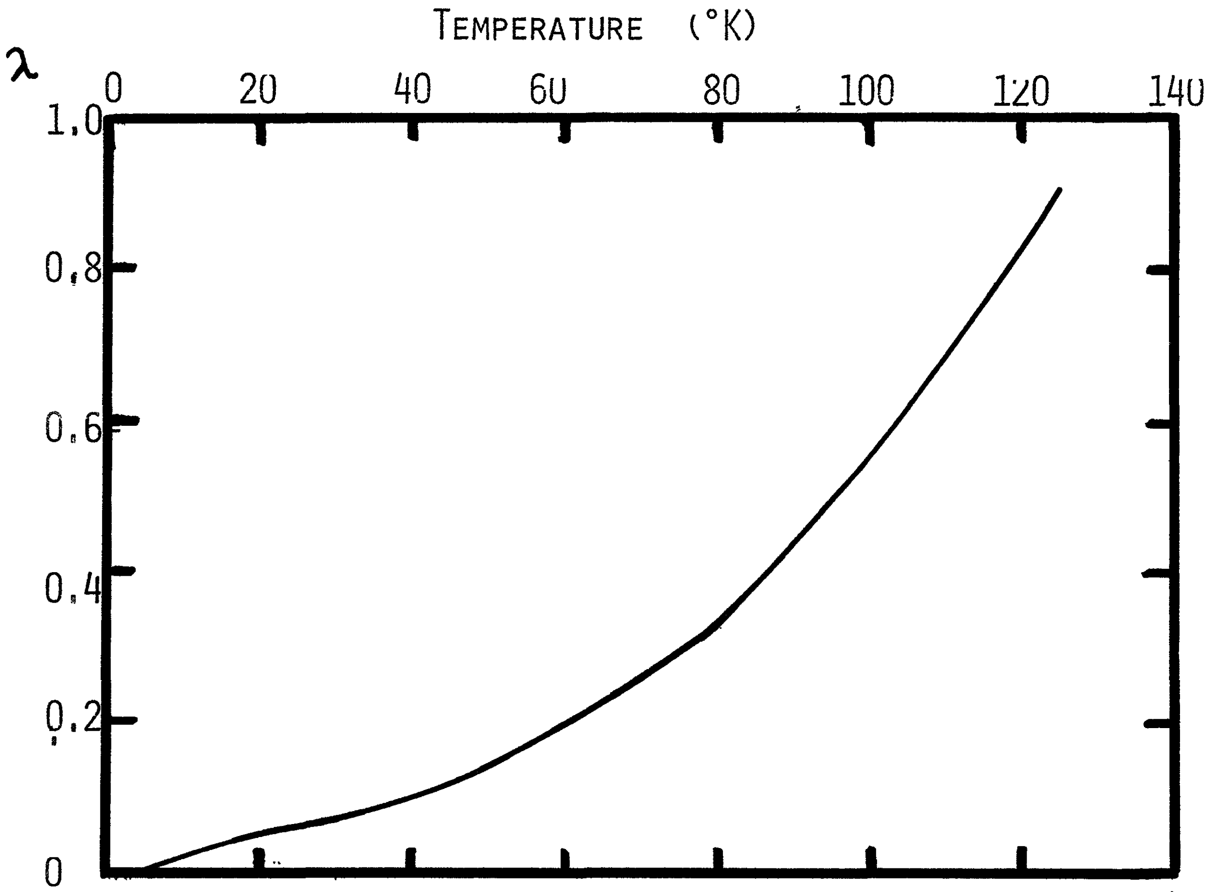

Figure 18: Variation of Parameter λ with Temperature in PbSe

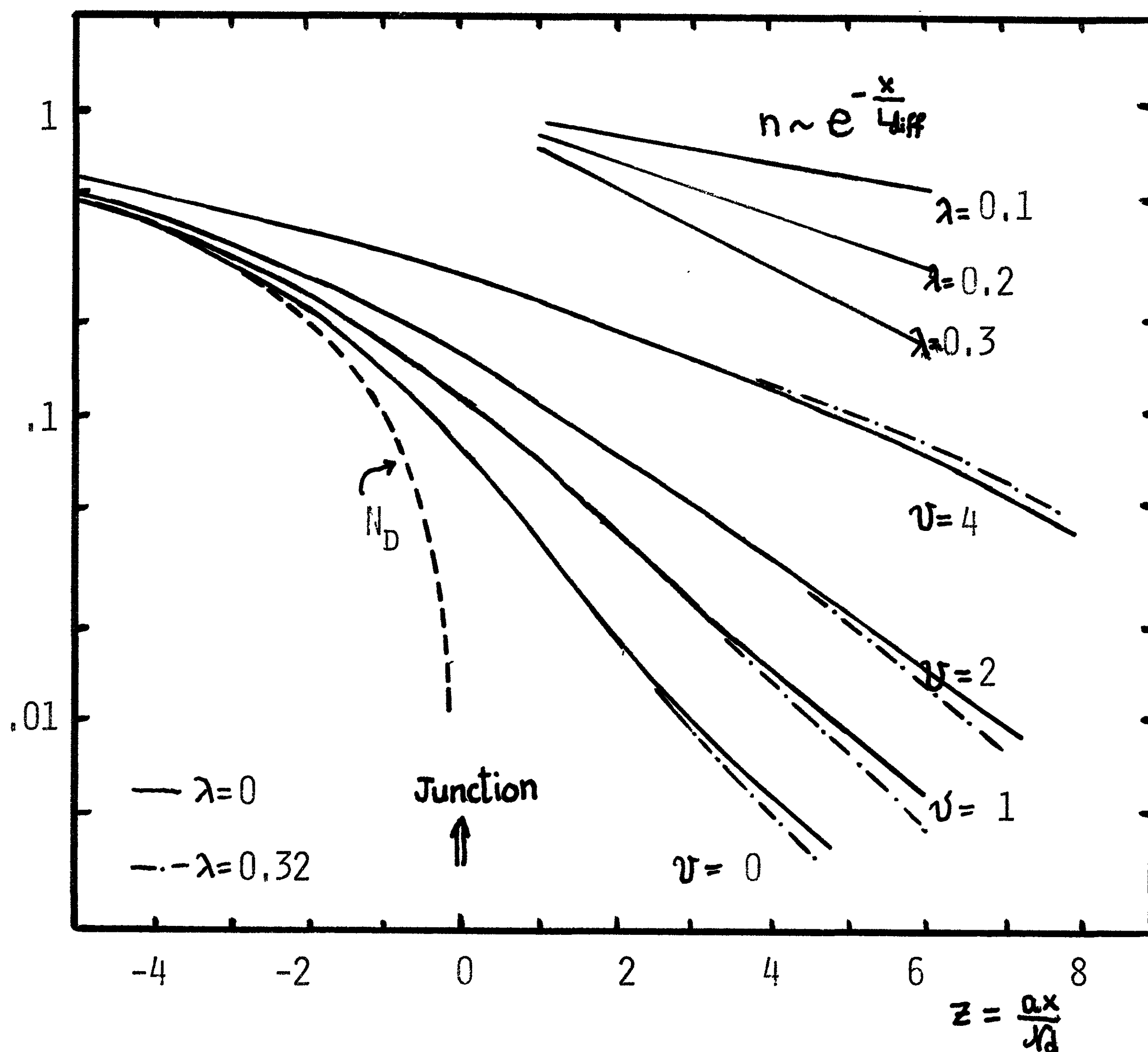

FIGURE 20: CALCULATED VARIATION OF NORMALIZED CARRIER DENSITY WITH POSITION

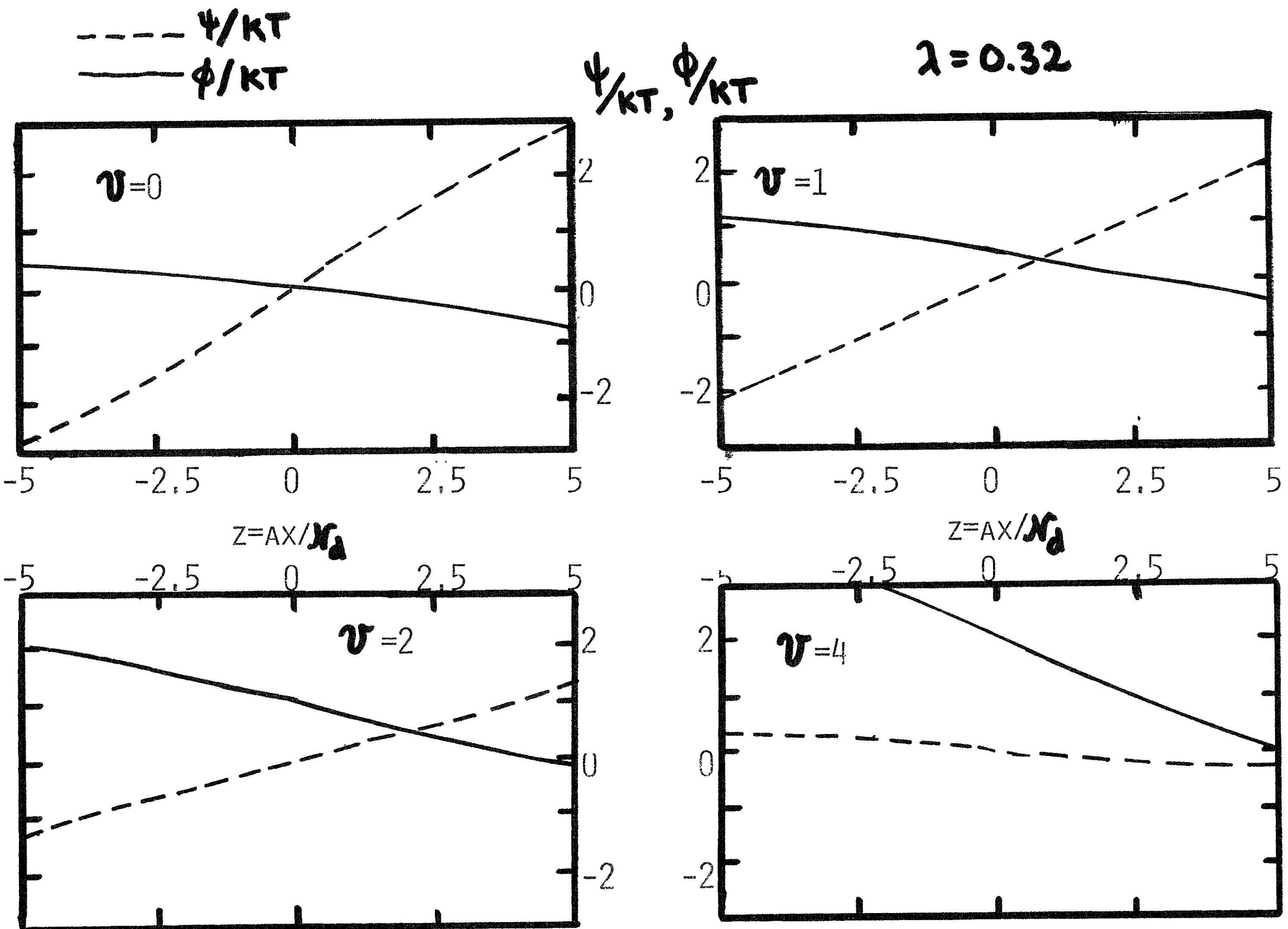

FIGURE 21: VARIATION OF POTENTIAL AND QUASIFERMI LEVELS WITH POSITION (NORMALIZED UNITS)

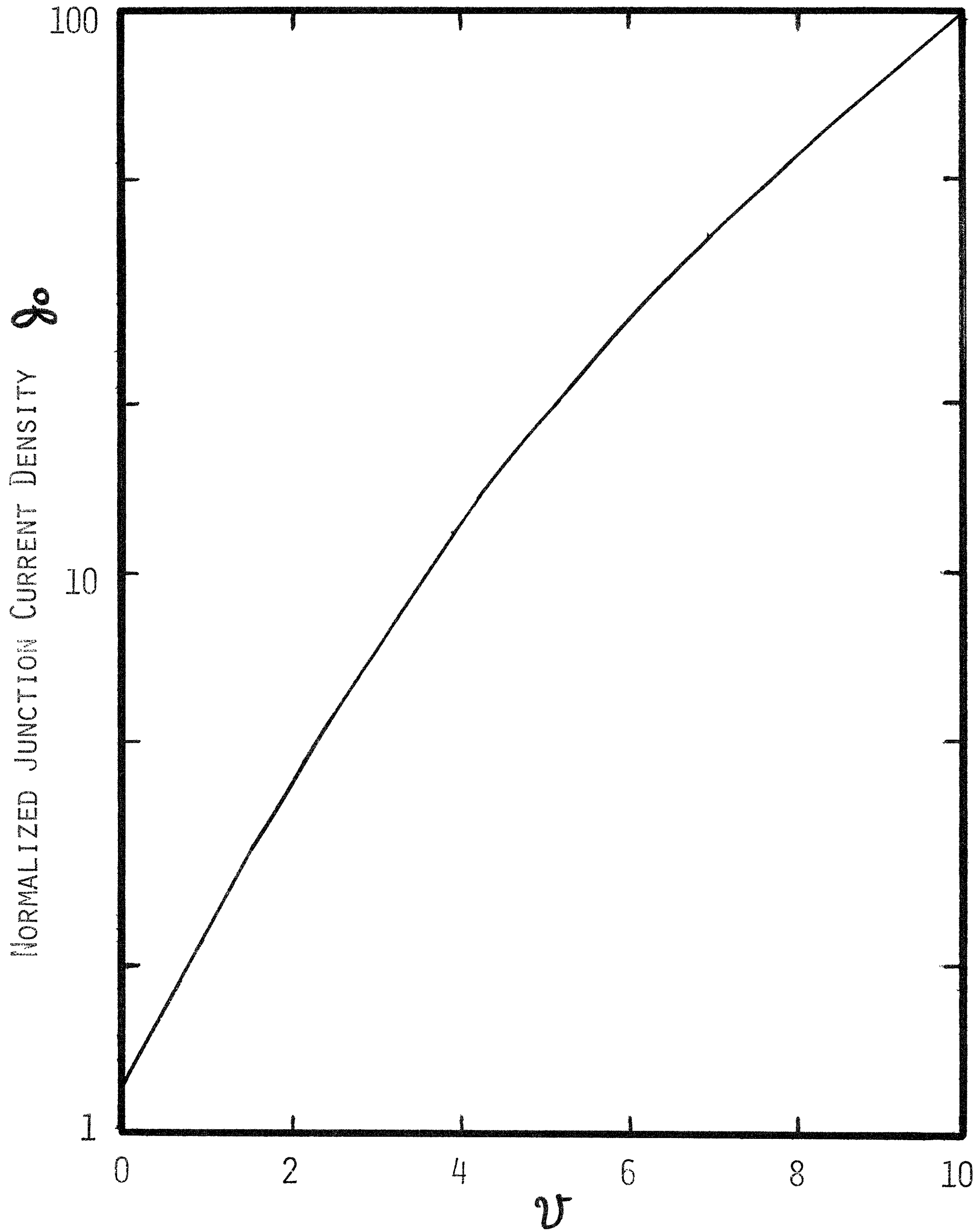

Figure 22: Variation of Normalized Current j_o with v (case $\lambda = 0$)

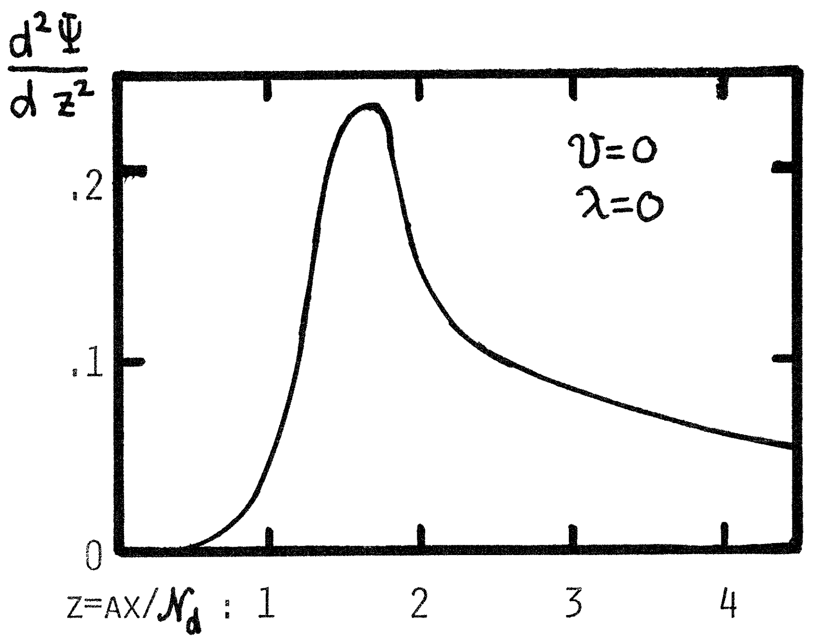

Figure 23: A. Variation with position of $d^2\Psi/dz^2$ and of Ψ

B. Variation of υ_{LIM} with λ

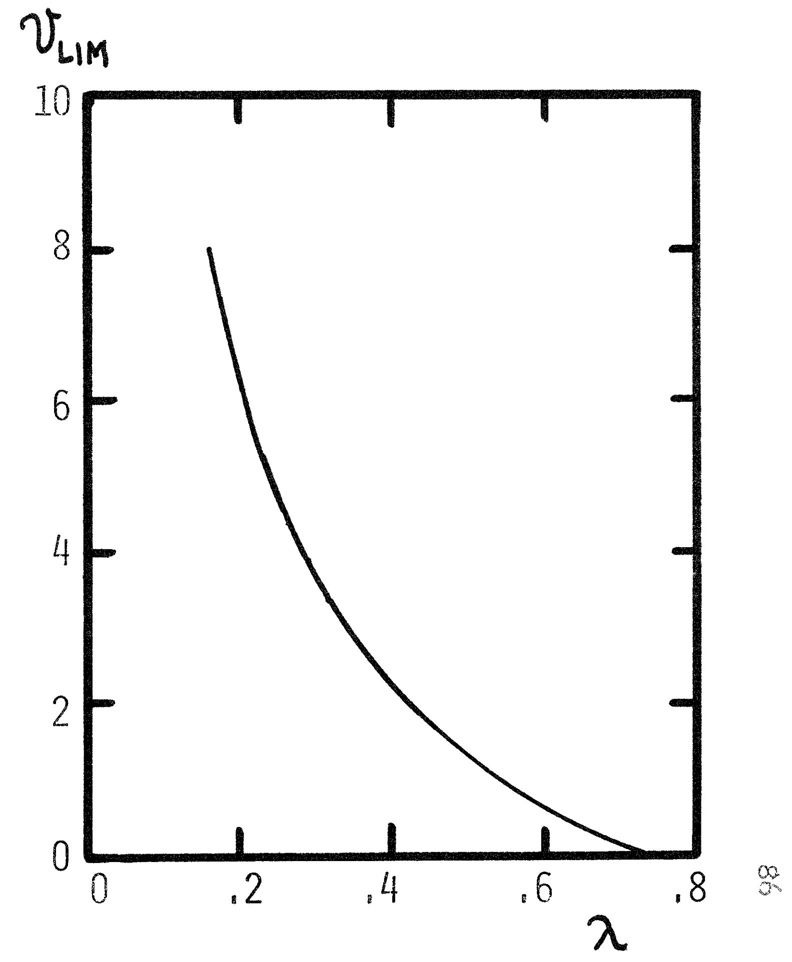

Figure 24: Asymmetric Profile Model for Calculation of Carrier Distributions

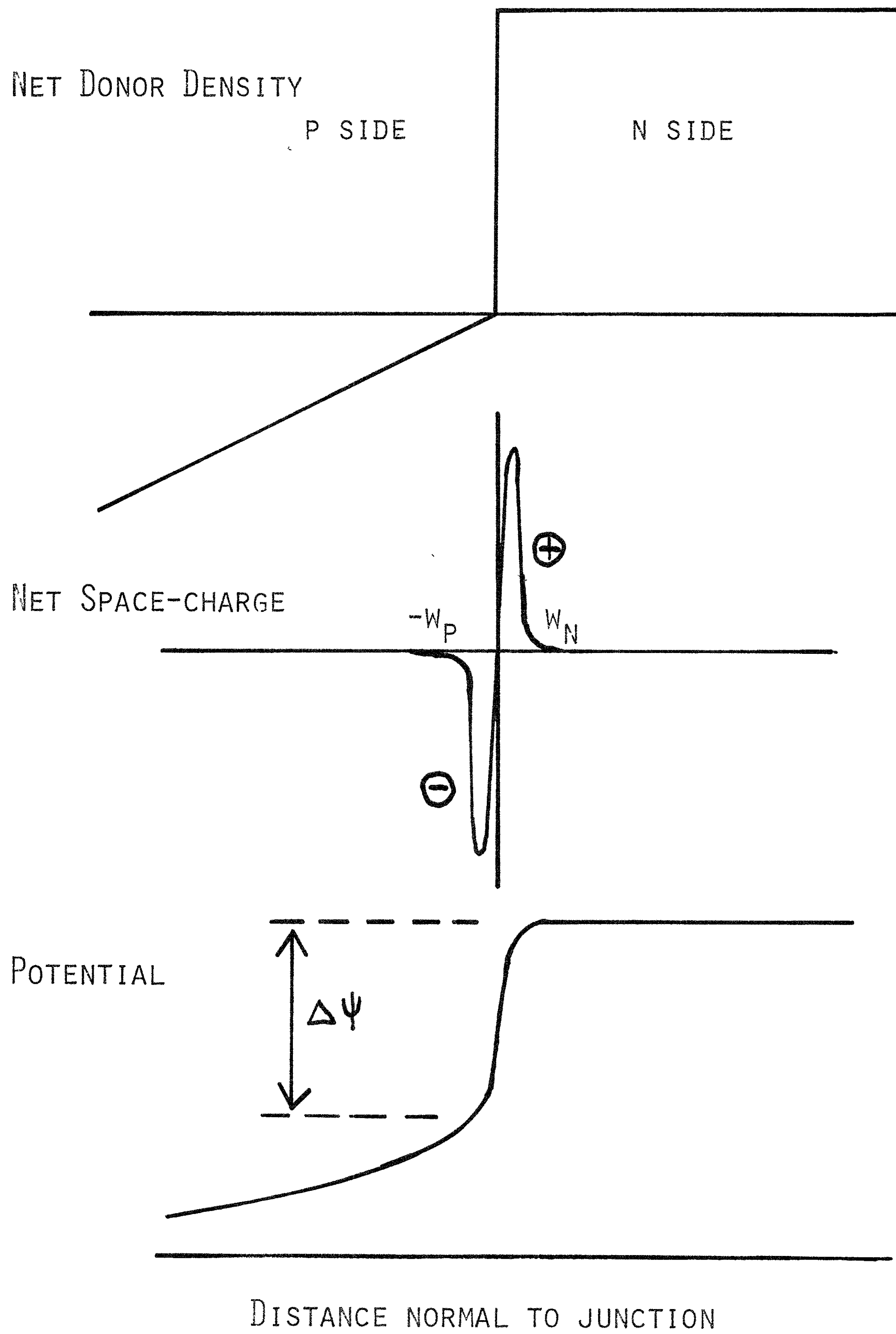

CHAPTER IV
OPTICAL MODE CONFINEMENT

IV. 1 Introduction

In this chapter is presented an analysis of the spatial distribution of the optical field within PbSe diffused homojunction lasers in the direction normal to the junction. The analysis is predicated on the fact that the optical field at a given laser output frequency has the distribution corresponding to a high Q mode of the effective laser cavity. The high Q cavity modes may be evaluated by considering the confined, travelling-wave modes of an effective optical waveguide obtained in the vicinity of the junction. The overall laser cavity is given by taking into account terminations of the optical waveguide corresponding to the mirror facets.

Sections 2 and 3 of this chapter discuss theoretically the effective optical waveguide obtained in diffused Pb Se lasers. It is shown that the dielectric constant of the material reaches a maximum near the metallurgical junction, primarily in response to the low carrier densities present there. The propagating modes of the waveguide are then solved for in Section 4, and some of their properties are discussed. In Section 5 measurements of laser far-field patterns are reported in order to provide experimental support for the earlier theoretical results.

IV. 2 Sources of Dielectric Constant Variation

The dielectric constant of PbSe at 77°K at the lasing frequency is in the vicinity of 28.[70] Its value varies with distance normal to the junction plane, however, in response to the spatially varying electron and hole densities, vacancy concentrations, temperature, stress,

static electric field and optical field intensity. The dependence of ϵ on most of these parameters is examined in what follows. The effects of the static and optical electric fields are omitted, however; while potentially important for GaAs lasers, they must be small in PbSe since the lowest order electrooptic tensor and nonlinear susceptibility tensor vanish for this structure. The intraband and interband effects of the carriers will be considered separately.

(i) Intraband Contribution

The net contribution to the transverse dielectric constant at frequency ω from carriers within a band due to real or virtual transitions within the same band is given by[71]

$$\Delta\epsilon_{fc}^{\alpha\beta} = -\sum_{\substack{\text{occupied}\\ \text{states}\\ j}} \frac{\partial f}{\partial \epsilon} \frac{4\pi e^2 \langle j|v_\alpha|j\rangle\langle j|v_\beta|j\rangle}{\omega\left(\omega + \frac{i}{\tau_j}\right)} \tag{IV-1}$$

where f is the Fermi function and $v_{\alpha,\beta}$ is the component of the velocity operator in the α,β direction. (IV-1) is a generalization of the more standard Drude expression which allows the nonparabolicity of PbSe to be taken into account. If constant carrier lifetime is assumed, the equation may be rewritten as

$$\Delta\epsilon_{fc} = -\frac{4\pi n e^2}{\omega\left(\omega + \frac{i}{\tau}\right)} \left\langle \frac{1}{m_c^*} \right\rangle \tag{IV-2}$$

where n is the carrier density and $\langle 1/m_c^* \rangle$ corresponds to the value of conductivity effective mass averaged over energy and direction. It is given by

$$\left\langle \frac{1}{m_c^*} \right\rangle = \int_0^\infty \frac{\partial f}{\partial \epsilon} \cdot \frac{1}{3} \left(\frac{2}{m_{tc}^*} + \frac{1}{m_{lc}^*} \right) d\epsilon \qquad \text{(IV-3)}$$

where

$$\frac{1}{m_{tc}^*} = \frac{1}{\hbar^2 k_t} \frac{\partial \epsilon}{\partial k_t} \qquad \frac{1}{m_{lc}^*} = \frac{1}{\hbar^2 k_l} \frac{\partial \epsilon}{\partial k_l} \qquad \text{(IV-4)}$$

For simplicity, averaging over an energy interval several KT wide as indicated in (IV-3) has been omitted, and to evaluate $\Delta\epsilon_{fc}$ values of $\langle 1/m_c^* \rangle$ have been taken to be

$$\left\langle \frac{1}{m_c^*} \right\rangle = \frac{1}{m_c^*} \quad \text{at fermi level for } \epsilon_f > 0 \qquad \text{(IV-5)}$$

$$\left\langle \frac{1}{m_c^*} \right\rangle = \frac{1}{m_c^*} \quad \text{at band edge for } \epsilon_f < 0$$

The conductivity masses at the required energies were obtained from the approximate PbSe band model described in Appendix B (quasi-2 band model). Resulting values of $m_c(\epsilon)$ at 77°K are shown in Fig. 25. Within the approximate model, the conduction and valence bands are symmetric so that these values are applicable to both electrons and holes.

The scattering lifetime appropriate for (IV-2) has been studied in PbSe by Mycielski et. al.[72] by fitting measured lineshapes in magnetoplasma reflectivity measurements. The value of obtained at 30°K was approximately independent of carrier concentration in their samples and given by 1.5×10^{-13} sec. It should be noted that this value is more than an order of magnitude shorter than the lifetime derived from dc mobility measurements on their samples.

An explanation of the discrepancy has been offered by Balkanski et. al.,[73] who argue that scattering events with the emission of optical phonons is permitted if the frequency of the exciting electric field exceeds ω_{lo}. The lasing frequency is sufficiently high, in any case, that any uncertainty in τ will cause negligible error in the real part of $\Delta\epsilon_{fc}$.

Real and imaginary parts of ϵ obtained from (IV-2) for PbSe at 77°K are shown vs. carrier concentration in Fig. 26. Corresponding values for GaAs lasers are very substantially smaller, due to the ω^{-2} dependence of (IV-2). Since the carrier density attains its smallest value in the vicinity of the junction, the sign of $\Delta\epsilon_{fc}$ is favorable to mode confinement.

(ii) Interband Contribution: Extremal Bands

The presence of a degenerate carrier density in low effective mass semiconductors is known to shift the absorption edge towards energies higher than the edge of intrinsic material.[74] The corresponding alteration of the real part of the dielectric constant in the vicinity of the band edge is calculated in this section. The analysis is based on a model which assumes k conservation in the valence-conduction band transitions and allows for homogeneous broadening; the calculation includes the following steps:

(a) Derivation of the imaginary part of the dielectric constant due to the valence-conduction transitions without including broadening ($\mathrm{Im}\ \epsilon^{o}_{cv}$).

(b) Identification of that portion of $\mathrm{Im}\ \epsilon^{o}_{cv}$ that is eliminated when a degenerate carrier population is taken into account ($\Delta\ \mathrm{Im}\ \epsilon^{o}_{cv}$).

(c) Calculation of the corresponding change in the real part of the dielectric constant ($\Delta\ \mathrm{Re}\ \epsilon_{cv}$) by use of a modified

Kramers-Kronig relation that includes the effect of homogeneous broadening.

Following Reference 75, Im $\epsilon_{cv}^{o(\alpha\beta)}$ is given by ($\omega > 0$ portion only):

$$\mathrm{Im}\ \epsilon_{cv}^{o(\alpha\beta)} = \frac{4\pi^2 e^2}{\omega^2 m^2} \sum_{(v,k)} \sum_{(c,k')} \langle v,k|p^\alpha|c,k'\rangle\langle c,k'|p^\beta|v,k\rangle \delta(\hbar\omega - E_{ck'} + E_{vk})(f_{vk} - f_{ck'}) \tag{IV-6}$$

Here α , β denote coordinate directions, (v, k) and c, k') denote a complete set of valence and conduction band quantum numbers and $f_{v,k}$ and $f_{c,k'}$ are thermal occupation numbers for the respective states. The superscript ^{o} indicates that broadening has not been considered. With the assumption of k conservation and constancy of the matrix elements over the energy range of interest (see Appendix B) we obtain

$$\mathrm{Im}\ \epsilon_{cv}^{o(\alpha\beta)} = \frac{4\pi^2 e^2}{\omega^2 m^2} \sum_{v} \sum_{c} \langle v|p^\alpha|c\rangle\langle c|p^\beta|v\rangle \cdot \frac{1}{8\pi^3} \int d^3k\ \delta(\hbar\omega - E_{ck} + E_{vk})(f_{vk} - f_{ck}) \tag{IV-7}$$

The abbreviated quantum numbers v and c contain valley index and spin-subband index. The sum over matrix elements may be simplified by noting that for this cubic material, ϵ_{cv} is diagonal and $\epsilon_{cv}^{xx} = \epsilon_{cv}^{yy} = \epsilon_{cv}^{zz}$. Similarly, the net contributions from the spin-up and spin-down valence subbands are equal. It is found

$$\begin{aligned} \sum_{v} \sum_{c} \langle v|p^\alpha|c\rangle\langle c|p^\beta|v\rangle &= \frac{8}{3} \sum_{\uparrow,\downarrow} |\langle\uparrow|p^\ell|j\rangle|^2 + 2\,|\langle\uparrow|p^t|j\rangle|^2 \\ &= 8\, P_{cv}^2 \end{aligned} \tag{IV-8}$$

where p^l and p^t are momentum operators in the longitudinal and transverse directions of a given valley. The spin-up valence band (chosen arbitrarily as the initial state) couples to the spin-up conduction band via p^l and with the spin-down valence band via p^t (this occurs because each subband results from the admixture of both pure spin-up and spin-down wavefunctions). Evaluation of the matrix elements using the formalism of Mitchell and Wallis[76] gives

$$P_{cv}^2 = \frac{1}{3}\left(P_{\parallel}^2 + 2P_{\perp}^2\right) \tag{IV-9}$$

where $P_{\parallel}^2$ and $P_{\perp}^2$ are given in Appendix B.

The resulting expression for $\mathrm{Im}\,\epsilon_{cv}^{o}$ is

$$\mathrm{Im}\,\epsilon_{cv}^{o} = \frac{4e^2 P_{cv}^2}{\pi m^2 \omega^2} \int_{E_g}^{\infty} d\xi \left[f_v(\xi) - f_c(\xi)\right] \delta(\hbar\omega - \xi) \int_{S_\xi} \frac{dS}{|\nabla_k \xi|} \tag{IV-10}$$

where $\xi = E_{ck} - E_{vk}$ and the surface integral is evaluated over a surface S_ξ of constant ξ. The quasi-2-band model used in this work for the energy bands of PbSe near the L point is described in Appendix B; there it is shown that the reduced density of states per unit energy and volume for a single spin and valley has the form

$$\frac{1}{8\pi^3} \int_{S_\xi} \frac{dS}{|\nabla_k \xi|} = \frac{\sqrt{2}\, m_{to}\, m_{lo}^{1/2}}{4\pi^2 \hbar^3} \cdot \frac{\xi}{E_g} \cdot \left(\frac{\xi^2}{E_g} - E_g\right)^{1/2} \tag{IV-11}$$

The final result for Im ϵ^{o}_{cv} is then given by

$$\mathrm{Im}\,\epsilon^{o}_{cv} = \frac{4\sqrt{2}\,e^2 P_{cv}^2 m_{to} m_{lo}^{1/2}}{m^2 \omega^2 \hbar^3} \cdot \frac{\hbar\omega}{E_g} \cdot \left[\frac{(\hbar\omega)^2}{E_g} - E_g\right]^{1/2} \left[f_v(\hbar\omega) - f_c(\hbar\omega)\right] \qquad \text{(IV-12)}$$

The fermi functions are to be evaluated at the conduction and valence band energies corresponding to the states that participate in the transition at ω , that is,

$$E = \frac{\hbar\omega - E_g}{2}$$

where E is the energy of the state measured with respect to the band edge. Values of Im ϵ^{o}_{cv} obtained from (IV-12) for PbSe at 77°K using the band parameters of Appendix B are shown in Fig. 27. For comparison are shown values of Im ϵ_{cv} calculated from a model which neglects the nonparabolicity of PbSe and assumes the effective mass is given by its band edge value.

For material with no carriers present, $f_v = 1$ and $f_c = 0$ for all ω . In unpumped n type material, f_c will increase for suitable values of ω , and the change in Im ϵ^{o}_{cv} incurred by the presence of carriers is

$$\Delta \mathrm{Im}\,\epsilon^{o}_{cv} = \frac{4\sqrt{2}\,e^2 P_{cv}^2 m_{to} m_{lo}^{1/2}}{m^2 \omega^2 \hbar^3} \cdot \frac{\hbar\omega}{E_g} \cdot \left[\frac{(\hbar\omega)^2}{E_g} - E_g\right]^{1/2} f_c(\hbar\omega) \qquad \text{(IV-13)}$$

The sizeable change that can result may be appreciated in Fig. 27 where Im ϵ^{o}_{cv} at 77°K with 5×10^{17} cm^{-3} electrons present is plotted. The corresponding change in the real part of the dielectric

constant may be calculated by using the Kramers-Kronig relation[77]

$$\Delta \mathrm{Re}\ \epsilon(\omega) = \frac{1}{\pi} P\int_{-\infty}^{\infty} \frac{\Delta \mathrm{Im}\ \epsilon(\omega')\, d\omega'}{\omega - \omega'} = \frac{2}{\pi} P\int_{0}^{\infty} \frac{\omega' \Delta \mathrm{Im}\ \epsilon(\omega')\, d\omega'}{\omega'^2 - \omega^2} \qquad \text{(IV-14)}$$

As a computational aid, however, and to improve the approximation to reality, the effects of lifetime broadening on Im ϵ_{cv} and Re ϵ_{cv} are taken into account. With homogeneous broadening, Im ϵ_{cv} is given by[77]

$$\Delta \mathrm{Im}\ \epsilon_{cv}(\omega) = \int_{-\infty}^{\infty} \Delta \mathrm{Im}\ \epsilon^{\circ}_{cv}(u) \cdot \frac{\Delta\omega}{\pi} \cdot \frac{du}{(\omega - u)^2 + \Delta\omega^2} \qquad \text{(IV-15)}$$

where $2\ \Delta\omega = 2\ \hbar/\tau$ is the full width at half magnitude of the line and τ is the phase-destroying collision lifetime. In (IV-15) the values of Δ Im ϵ_{cv} for both positive and negative frequencies are required; the negative frequency portion may be found from

$$\mathrm{Im}\ \epsilon_{cv}(-\omega) = -\mathrm{Im}\ \epsilon_{cv}(\omega) \qquad \text{(IV-16)}$$

From (IV-14) - (IV-16) we obtain

$$\Delta \mathrm{Re}\ \epsilon_{cv}(\omega) = \frac{2}{\pi} \int_{0}^{\infty} \Delta \mathrm{Im}\ \epsilon^{\circ}_{cv}(u)\ \frac{u(\omega^2 - u^2 - \Delta\omega^2)\, du}{(\omega^2 - u^2)^2 + 2(\omega^2 + u^2)\Delta\omega^2 + \Delta\omega^4} \qquad \text{(IV-17)}$$

This modified Kramers-Kronig relation is considerably more suited to machine computation than (IV-14), since there is no singularity in its kernel.

Results for Δ Re ϵ_{cv} for PbSe at 77°K obtained by numerical

integration of (IV-17) are plotted in Fig. 28, with carrier concentration as a parameter. In Fig. 29 the values of Δ Re ϵ_{cv} at the energy gap are plotted vs. carrier concentration for several τ ; since the frequency dependence of these values is slight, it is assumed that they apply also at the lasing frequency.

The values obtained for Δ Re ϵ_{cv} are expected to be considerably more accurate than values for Re ϵ_{cv} obtained by Kramers-Kronig analysis, since Δ Im ϵ_{cv} is non-zero only in a small frequency range near the absorption edge. A proper estimate of Re ϵ_{cv}, however, requires knowledge of the bahaviour of Im ϵ_{cv} for all frequencies, and far from the absorption edge the band model used here is obviously inaccurate.

The inclusion of homogeneous broadening takes into account in an ad hoc fashion numerous effects outside of the simple one-electron picture that is the basis for (IV-6), including electron-phonon, electron-local defect and electron-electron interactions. It is conventional in treatments of the GaAs laser to include these effects by relaxation of k conservation and by invoking band-tailing.[55] In Appendix C is presented a discussion of the interactions listed above for PbSe. It is concluded there that the amount of band-tailing expected from Coulomb interaction with defects is extremely small and that an assumption of non-k conservation is completely unjustified over the energy range of interest in (IV-13) (which extends over tens of milivolts). The exchange energy shifts of the bandgap computed in Appendix C are small for the range of carrier density of interest also and have been omitted from the calculation of Δ Re ϵ_{cv}. The value of τ to be used in (IV-17) is considered also in the Appendix, where it is concluded that a reasonable value is $\tau = 1.65 \times 10^{-13}$, which yields $\Delta\omega = 4$ meV. In view of the uncertainties of this calculation, τ must be regarded to a considerable extent as a variable parameter

of theory, however. For temperatures greater than $50^{\circ}K$ the uncertainty in τ is substantially relieved by the large thermal broadening already considered in (IV-17). However, the exact value of τ strongly affects the values predicted for $\Delta \text{Re}\, \epsilon_{cv}$ at $4.2^{\circ}K$.

In PbSe pumped by injection across a p-n junction, the minority carrier density may be appreciable. If pumped n type material is considered as an example, then f_c is greater than 0 as before and f_v is less than one due to the presence of the minority carriers. It is evident from (IV-12) that the minority carriers induce also a change $\Delta \text{Im}\, \epsilon^{o}_{cv}$ in the interband contribution to ϵ. Since (IV-12) is linear in f_c and f_v, $\Delta \text{Re}\, \epsilon_{cv}$ for the minority carriers may be calculated independently from the estimation of majority carrier effects. The derivation of $\Delta \text{Re}\, \epsilon_{cv}$ for the minority carriers is identical to that given above for the majority carriers, and the results of Fig. 29 apply. In both cases the presence of carriers causes a decrease in the dielectric constant of the material at the lasing frequency.

It might be argued that in the calculation of the minority carrier contribution the most appropriate value of the broadening parameter τ is different from the best fit value for the majority carriers, since scattering is less rapid for carriers that occupy states near the band edge. No correction, however, was made in this work to take into account the energy dependence of τ.

There are very few experimental results concerning the absorption edge of PbSe available for verification of the theory of this section. Scanlon has measured the absorption coefficient of PbSe as well as of PbS and PbTe at $296^{\circ}K$ up to absorption levels of the order of $10^{5}\ cm^{-1}$ on thin polished samples.[78] However, Schoolar and Dixon later found discrepancies between their data[79] (which was self-consistent with index of refraction measurements) and Scanlon's data for PbS, so that

a detailed fit with Scanlon's PbSe results would not be meaningful. Prakash has observed an exponential absorption edge[80] (following Urbach's rule: $\alpha = \alpha_o \exp((\hbar\omega - E_o)/E_g)$ for low absorption coefficients ($< 2 \times 10^3$ cm $^{-1}$) in PbSe at room temperature. A similar result has been found for PbS and PbTe,[80,81] and for those materials, studies have been extended to lower temperatures. In Table III are listed reported values of the characteristic energy E_s of the absorption edge in PbSe, PbTe and PbS. From the results in the other Pb salts it may be inferred that E_S for PbSe is of the order of 3 mev at 77°K, although its dependence on carrier concentration, if any, is not apparent. Corrections to the data of Table III to account for effects of the fermi function were not made. Experimental measurements of the edge are notoriously difficult since surface preparation, stress and temperature gradients in the thin samples that are necessary may strongly affect the results. It is believed that there is no basis to date for a more adequate treatment of the absorption edge than the theory of this section.

Measurements by Piccioli et. al. on polycrystalline PbTe films have shown experimentally the sizeable Burstein shifts obtainable in the Pb salts.[82] Their data, however, is not susceptible to accurate fitting because of uncertainty in the value of the bandgap.

(iii) Far-Band Contributions

In addition to the elimination of oscillator strength from the $L_6^- - L_6^+$ extremal band resonsnace discussed above, the presence of carriers modifies the oscillator strengths of transitions between these bands and bands lying further away from the fermi level. For example, if electrons are added to the bottom of the conduction band, oscillator strength is eliminated from the $L_6^+(L_3^+)$-L_6^- and L_4^+, L_5^+-L_6^- resonances, as shown in Fig. 30. The change in dielectric constant

at the laser frequency may be found from an expression analogous to (IV-6):

$$\epsilon(\omega) = -\frac{4\pi^2 e^2}{m^2} \sum_{ij} \frac{(f_i - f_j)\,|P_{ij}|^2}{\hbar\,\omega_{ij}^2} \left[\frac{1}{\pi} \frac{1}{\omega_{ij} - \omega} + i\,\delta(\omega - \omega_{ij}) \right] \qquad \text{(IV-18)}$$

where i, j indicate quantum numbers for initial and final states of the transition. Since $\hbar/\tau$ and the spread of energies of the conduction band states are small with respect to energies of interest, τ has been omitted and (IV-18) may be written

$$\Delta\epsilon(\omega) = -\sum_{\substack{\text{far}\\ \text{bands}}} \frac{4\pi e^2 |P_{ij}|^2 \Delta n}{m^2 \hbar\, \omega_{ij}^2} \left[\frac{1}{\pi} \frac{1}{\omega_{ij} - \omega} + i\delta(\omega - \omega_{ij}) \right] \qquad \text{(IV-19)}$$

An identical expression applies to the case of holes added to the valence band. Using matrix elements and energy separations obtained from Bernick,[56] values of $\Delta\epsilon$ at the lasing frequency incurred by adding 10^{18} cm^{-3} electrons (or holes) for some transitions are shown in Table IV. The values obtained are smaller than the uncertainty in the evaluation of $\Delta\epsilon_{cv}$, and thus may be neglected.

It is clear that there are no further contributions to the total change in dielectric constant due to the addition of carriers that we have omitted from consideration. A well-known sum rule establishes that the net change in oscillator strengths of all transitions is given by[83]

$$\int_0^\infty \omega\, \Delta \mathrm{Im}\, \epsilon(\omega)\, d\omega = \frac{2\pi^2 e^2 \Delta n}{m} \qquad \text{(IV-20)}$$

The free carrier contribution accounts for

$$\int_0^\infty \omega \, \Delta \mathrm{Im}\, \epsilon_{fc}(\omega) d\omega = \frac{2\pi^2 e^2 \Delta n}{m^*} \qquad \text{(IV-21)}$$

while the interband contributions give approximately

$$\int_0^\infty \omega \, \Delta \mathrm{Im}\, \epsilon_{interband}(\omega) d\omega = - \sum \frac{4\pi^2 e^2 |P_{ij}|^2 \Delta n}{m^2 \hbar \omega_{ij}} \qquad \text{(IV-22)}$$

The fact that (IV-20) is satisfied may then be established by the result

$$\frac{m}{m^*} = 1 + \sum_{ij} \frac{2|P_{ij}|^2}{\hbar \omega_{ij} m} \qquad \text{(IV-23)}$$

derived from k. p theory.[83]

(iv) Core and Lattice Contributions

When a vacancy is generated in a PbSe crystal, valence and core electrons as well as a positive nucleus are removed. If electrons and nuclei on neighboring sites were completely non-interacting, one electron state from each band (both below and above the fermi level) and one mode of each phonon branch would be removed as well. No new resonances would be created, and the dielectric constant would change in proportion to the ratio of vacancies to lattice sites. In PbSe the concentration of lattice sites is 1.7×10^{22} cm^{-3}, while vacancy concentrations of interest are of the order of 10^{17} -10^{18} cm^{-3}. This analysis is expected to apply to a good approximation to resonances involving core levels of Pb and Te, whose contribution to is thus found to be negligible.

The non-localized character of excitations must be taken into account in consideration of the lattice contributions and (upper) valence band contributions. Within the band picture, no states are removed from the Brillouin zone by the introduction of a vacancy, since the state-counting is based on volume (or phase space) considerations. The vacancy potential perturbs the states within the zone, however, with the creation of local modes or states. Pratt and Parada[30] have given a detailed account of the energies of the localized valence-electron states in PbTe and shown how a sufficient number of them are moved across the fermi level to account for the addition of two holes per Pb vacancy and two electrons per Te vacancy; the electrons and holes then move to the extremal L_6^+ and L_6^- states. The intraband and interband contributions calculated above account for the effects of these electrons and holes on the dielectric constant. It is apparent that an additional contribution must be considered, that of transitions involving the localized states. The results for PbTe indicate that these states occur far from the fermi level, so that their influence on ϵ at the lasing frequency is slight.

Local phonon modes have not been studied in PbSe, although they are known in other semiconductors.[84] It is not expected, however, that any resonance near the frequency of lasing will be created. Their effect on ϵ is thus neglected.

The lattice modes, in particular the L0 phonon mode near the Γ point, will be affected by the presence of free carriers by screening effects and by acoustic and optical deformation potential interactions. The screening effect does not cause a change of the dielectric constant contribution of the lattice, as shown by Varga.[85] The effect of the latter interactions is expected to be slight, since the overall contribution of the (perfect) lattice is small. The di-

electric constant contribution of the lattice polarizability is given by[86]

$$\Delta\epsilon_{lattice} = (\epsilon_0 - \epsilon_\infty) \frac{\omega_{TO}^2}{\omega_{TO}^2 - \omega^2} \qquad \text{(IV-24)}$$

which evaluated at the lasing frequency at 77^oK gives
$\Delta\epsilon_{\text{lattice}} = -0.21$.

(v) Stress Effects

A number of theoretical and experimental studies have demonstrated the strong variation of the index of refraction and energy gaps of PbSe with stress.[87-90] In the Pb salts the variation is among the largest of all semiconductors studied. The results of Reference 89 obtained with laser diodes at 77^oK indicate that $dE_g/dP=-9x10^6$ ev/bar and $(1/n)(dn/dP)=1.3x10^{-3}$ bar^{-1}. If uniaxial stress is applied in a general direction, there is the further effect of splitting of the L point valley degeneracy.[91]

If the material in the vicinity of the junction of a PbSe laser is uniformly stressed, there will be a negligible effect on optical mode confinement, however. This stems from the fact, shown in Section IV.3, that the properties of the effective junction waveguide are nearly independent of the absolute magnitude of the dielectric constant, and are dominated by the gradients of ϵ . Several mechanisms are considered here which are capable of producing a spatially varying stress (or strain) in the vicinity of the junction.

(a) The total density of cacancies in the lattice reaches a minimum at the p-n junction according to the BWG model, where it is given by

$$[V_{Pb}] + [V_{Se}] = 2\left[K_S(T_{diff})\right]^{1/2} \qquad \text{(IV-25)}$$

Here K_s is the Schottky constant for PbSe at the temperature of diffusion. Using the data of Ohashi and Igaki,[92] the vacancy density is found to be 2.8 x 10^{16} cm^{-3}. On either side of the junction the vacancy concentration increases to values comparable to the net carrier density. This spatially-varying vacancy density must produce varying amounts of strain in the lattice. Accurate data is not available for PbSe to estimate the magnitude of this effect. However, the dependence of lattice constant on carrier concentration in SnTe at room temperature has been studied by Bis and Dixon using x-ray techniques[93] and the results may apply approximately to PbSe. It was found for p-type SnTe that the lattice constant change was given by

$$\frac{\Delta a_o}{a_o} = -0.127\, f \qquad \text{(IV-26)}$$

where f is the fraction of lattice sites occupied by Sn vacancies. On the basis of this, the strain ϵ expected in PbSe for material of carrier concentration p is

$$\epsilon = \frac{p}{1.35 \times 10^{23}\, cm^{-3}} \qquad \text{(IV-27)}$$

It is thus found that the effect on the dielectric constant is negligible since for 10^{18} cm^{-3} material

$$\Delta\epsilon = 2n \frac{dn}{dP} \epsilon (c_{11} + 2c_{12}) = 7.5 \times 10^{-3} \qquad \text{(IV-28)}$$

using elastic stiffness coefficients found by Ilisavskii.[94]

(b) Stress may be introduced by differential contraction of the laser diode and laser mount during cooling to the laser operating temperature. Since the stress is relaxed over a finite distance, this may lead to stress gradients at the junction. If the strain engendered by the mismatched thermal contraction is not absorbed at all in the Cu mount then the strain $\underline{\epsilon}$ at the PbSe diode surface[90] at 77°K may reach $\underline{\epsilon} = 1.05 \times 10^{-3}$; the corresponding change of the dielectric constant from its value in an unstrained crystal may be near unity. The diodes used in this work were mounted with an intervening layer of In, however, which is expected to relax the stresses developed. Hence only a small change in ϵ is expected over the width of the optical mode.

(vi) Temperature effects:

Measurements of the absorption edge behaviour as well as of the temperature-tuning of laser output modes of PbSe at 77°K have yielded the values[80, 95, 96] $(1/n)(dn/dT) = 3 \times 10^{-4}\ {}^{o}K^{-1}$ and $dE_g/dT = 5 \times 10^{-4}$ eV ${}^{o}K^{-1}$. As in the case of stress, only temperature gradients may affect the dielectric waveguide behaviour.

Lasers were excited on a pulse basis only in the experiments included in this work. During these pulses, which were commonly of the order of 100 nsec in length, the temperature distribution of the laser did not reach steady state. Using heat capacity C_v of 1.0 j/cm^3 ^{o}K, and thermal conductivity K of .08 w/cm^{o}K for PbSe at 77°K,[96] it is found that thermal diffusion during a 100 nsec period may typically take place over a distance

$$l_d = \sqrt{\frac{\kappa \Delta t}{C_v}} = 1\mu \qquad \text{(IV-29)}$$

Thus during a current pulse the thermal energy generated serves mainly to increase the local temperature in the region where it is generated. The net energy per unit area dissipated at the junction for $J = 10^4$ A/cm^2 is $E_{th} = V_j \cdot J \cdot \Delta t = 1.7 \times 10^{-4}$ j/cm^2(since the resistance of the diode itself is negligible).

If it is assumed that the entire energy serves to increase the local temperature ($\eta_{int} = 0$) , and that it is dissipated over a region 4μ wide then over this region the temperature rise ΔT_j obtained at the end of a pulse would be 0.43°K. The maximum value of the dielectric constant change produced by this mechanism is therefore judged to be negligible.

The time averaged power dissipated in the lasers studied in this work is strongly affected by the resistance of the contacts to the PbSe p and n regions, which in some cases was as large as $0.5\,\Omega$ for a 10^{-3} cm^2 diode area. The duty cycle r was of the order of 2×10^{-5}, however, such that the total average power per unit area p found to be

$$p = (J V_j + J^2 R_c A) r = 1.04 \text{ W cm}^{-2} \qquad \text{(IV-30)}$$

Using the value of thermal conductivity for PbSe given above, and diode dimensions of $500\mu \times 200\mu \times 200\mu$, it is calculated that the net temperature rise of the junction in the steady state is less than .03°K.

IV. 3 Dielectric Constant Profile of PbSe Lasers

In this section estimates are given for the spatial variation of the dielectric constant of diffused PbSe lasers at $77^{o}K$, evaluated at the lasing frequency. The most important contributions to changes in ϵ were shown in the last section to be due to the intraband and interband effects, which in turn depend on the carrier distributions. Thus attention is first given to the distribution of the carriers near the junction.

As indicated in Chapter II, the profile of the net donor-acceptor density near the junction is not known exactly. Several models for the profile were presented in Section II. 4(v); each will be considered here. The donor density profiles are shown in Figs. 31a, 32a and 33a, for Models I, II and III, respectively. The profiles were determined using values of surface and bulk carrier concentration corresponding to the lasers fabricated in this work, and the junction depth for each was taken, as an example, to be 50 μ . The most appropriate value of the hole concentration bordering the junction in Model II is not known; a value of 3×10^{17} cm^{-3}, which is consistent with capacitance measurements, was assumed.

Since intrinsic carrier densities are negligible in PbSe at $77^{o}K$ the net donor-acceptor profiles correspond to the distribution of carriers in the devices when there is no applied bias (apart from small space-charge regions). Under lasing conditions there are in addition sizeable numbers of injected minority carriers near the junction; the density of majority carriers also increases in order to maintain quasineutrality. As described in Section III. 3(v) the total number of injected minority carriers per unit area N_{min} above threshold may be readily calculated (independently of profile model) by the relation

$$J_{th} = \frac{q N_{min}}{\tau_{rec}} \qquad \text{(IV-31)}$$

The measurements detailed in Section III. 2 have demonstrated that the value of τ_{rec} appropriate for the lasers of this study is 2 nsec at 77°K. In the numerical examples of this section, the value of J_{th} was assumed to be 5000 A/cm^2. This value is representative of typical experimental results for the lasers fabricated. It is then calculated that $N_{min} = 6.25 \times 10^{17}$ cm^{-3} μ.

The distribution of minority carriers has been discussed in Section III. 3. For Model III (symmetric junction case) the calculated results of that section apply directly, while for Model I the approximate results of Section III. 3(vi) may be used. To obtain the parameter ϑ necessary to describe the distributions, the value of J_{th} together with the curves of $\mathcal{J}_o$ vs ϑ of Fig. 22 have been used. The grading parameter a for these junctions was evaluated from Figs. 31, 32 and 33 to be 1.25 cm$^{-3}/\mu$. Values of $\mathcal{J}$ and ϑ were found to be 3.47 and 1.7, and 1.74 and 0.6 for Models I and III, respectively. Solutions for the minority carrier distribution in the case of Model II have not been obtained, and it was assumed here that the distrubution is identical to that of Model I. This is reasonable since if the donor density grading at the junction proper is sufficiently rapid, then the number of carriers needed to "fill the notch" near the junction will be small, and will not affect the distribution of carriers elsewhere. The minority carrier distributions for Models I, II and III are shown in Figs. 31b, 32b and 33b, respectively.

To obtain the dielectric constant variation near the junction, the values of $\Delta\epsilon_{fc}$ and $\Delta\epsilon_{cv}$ of Figs. 26 and 29 have been used. Contributions from majority and minority carriers were evaluated

separately; in this manner the nonlinear character of $\Delta\epsilon$ vs. carrier density is properly taken into account. For each profile, the local values of majority carrier density have been evaluated by summing the net donor-acceptor density and minority carrier density.

Resulting profiles for Δ Re ϵ vs. position for the 3 models are shown in Figs. 31c, 32c and 33c. The zero reference level of $\Delta\epsilon$ in these graphs corresponds to the dielectric constant at the bandgap frequency of PbSe with no free carriers; this value is not accurately known, but is estimated to be between 28 and 30.[70]

The dielectric profiles for all 3 models show pronounced peaks near the metallurgical junction. The increase of ϵ in the central region meets the requirements for optical waveguiding; light propagates more slowly in the central region than in the fringes, so that a unit length of material acts as a convergent lens.

Values of $\Delta\epsilon$ calculated here are very substantially higher than those known to occur in other semiconductor laser systems. For example, in GaAs diffused lasers it is estimated that the total change in ϵ between its value at the center of the effective junction waveguide and its value in the bulk semiconductor is of the order of .015.[23]

For lasers with junction depths other than the value 50μ chosen as an example here, the profile of ϵ may be calculated to a close approximation by simply scaling the units of distance by the factor $x_j/50\mu$, where x_j is the junction depth of the laser. This is valid because of the following:

(a) The donor-acceptor density profile scales with junction depth, as shown in Section II. 3.

(b) The shape of the minority carrier distribution scales with the grading parameter of the junction, which in turn depends linearly

on x_j. This result, shown in Section III. 3, follows because the junction electric fields basically determine the minority carrier distribution. It is not valid in the limit of very shallow diffusions, however, since these cannot be regarded as linearly graded over the entire range of interest.

(c) The magnitude of the minority carrier density at the junction is not strongly dependent on the junction depth. This occurs because J_{th} at 77°K must vary with junction depth, as shown in Section V. 3. For the scaling law proposed here to be strictly valid, an inverse relation between J_{th} and x_j must hold; although this is not strictly true, it is expected that only small errors in the profile will be made if it is assumed. For very shallow junctions the assumption is no longer valid, however.

IV. 4 Dielectric Waveguide Mode Solutions

In this section the propagation of electromagnetic waves at the lasing frequency in the dielectric waveguide formed near the junction of diode lasers is considered. Results are presented concerning the shape and size of low-order propagating waveguide modes as well as their losses, dispersion relations, and far field patterns. General theoretical results will be presented in the early sections of this chapter, where particular attention is given to the linear variation of ϵ model. Later the results are applied to the specific case of PbSe lasers.

The waveguide modes are obtained by solving the wave equation which is given by the equivalent forms[41]

$$\nabla^2 \bar{E} + \omega^2 \mu_0 \epsilon \bar{E} = -\nabla \left(\bar{E} \cdot \frac{\nabla \epsilon}{\epsilon} \right) \qquad \text{(IV. 32a)}$$

$$\nabla^2 \bar{H} + \omega^2 \mu_o \epsilon \bar{H} = -\frac{\nabla \epsilon}{\epsilon} \times \nabla \times \bar{H} \qquad \text{(IV-32b)}$$

MKS units and the assumption of exp ($i\omega t$) time dependence are used throughout the discussion. A coordinate system is adopted whereby the x direction is normal to the laser junction and propagation occurs in the z direction (see Fig. 34). The dielectric constant is in general complex, and varies spatially in the x (and possibly y) direction.

A well-known approximation used for waveguide modes that are loosely confined is the assumption that both E and H are approximately normal to the direction of propagation (quasi-TEM approximation).[97, 98] Furthermore the terms on the right hand side of (IV-32) are neglected. The resulting equation has the form of the scalar wave equation:

$$\nabla^2 \psi + \omega^2 \mu_o \epsilon(x,y) \psi = 0 \qquad \text{(IV-33)}$$

where ψ may represent E_x, E_y, H_x or H_y. This equation is equivalent to the time-independent Schrödingers equation for a particle in a 2 dimensional well. This approximation will be used throughout the discussion.

The calculations given in the earlier chapters of this section have dealt with the variation of ϵ in the x direction. For the broad contact lasers measured in this work an appropriate model including y direction variation is

$$\epsilon(x,y) = \epsilon(x) \quad \text{for } -\tfrac{1}{2}W < y < \tfrac{1}{2}W$$
$$\epsilon(x,y) = 1 \quad \text{for } |y| > \tfrac{1}{2}W \qquad \text{(IV-34)}$$

For lasers displaying filamentary behavior and for stripe-geometry lasers, an appropriate model is

$$\epsilon(x,y) = \epsilon(x) - \frac{y^2}{y_0^2} \qquad \text{(IV-35)}$$

(Experimental evidence concerning the possible formation of filaments in the lasers measured in this work is given in Chapter IV. 5). The form (IV-35) when used in (IV-33) yields a separable wave equation, in which x and y dependence of ψ may be solved for separately. The form (IV-34) may be rendered (nearly) separable also if the approximation

$$\epsilon(x,y) = \epsilon(x) + (1 - \langle\epsilon\rangle)\left[\theta(y - \tfrac{1}{2}W) + \theta(y + \tfrac{1}{2}W)\right] \qquad \text{(IV-36)}$$

is used. The technique of separation of variables will be followed in the discussion of the Zachos and Ripper model below, but for other models it will be only assumed possible, and the solutions will be limited to the one dimensional wave equation involving only variation.

If the one-dimensional variation of ϵ is strictly valid (that is, if the structure is assumed to be homogeneous and infinite in the y direction), then solutions of the full wave equation may be rigorously separated into 2 classes:[99] TE and TM modes. Mode shapes, losses

and dispersion relations for the 2 cases are found to be slightly different because of the (small) terms involving $\nabla\epsilon$ in (IV-32). In this work the difference in properties of TE and TM modes (and hence the polarization characteristics of the laser output) will be ignored.

An (exact) numerical mode solution for the particular dielectric waveguide obtained inPbSe lasers will not be given in this work. Rather, several models of the dielectric constant variation will be considered and solved. While less exact, the solutions obtained with this approach have a wider range of applicability. Previously published dielectric constant models are first reviewed. A profile model with linear fall-off of E is then discussed. Several additional more complex models are considered in Appendix D.

(i) Review of Existing Waveguide Models

Early treatments of mode confinement in GaAs lasers were developed in terms of the slab model.[23,100] The dielectric waveguide was assumed to consist of a series of layers, each with homogeneous properties (see Fig. 35a). Solutions to Maxwell's equations are derived simply by matching boundary conditions at the interfaces with plane-wave-like solutions within each of the layers. The width and dielectric constant of each slab could be varied to achieve best fit to a given dielectric waveguide. Effects of both real and imaginary parts of ϵ are readily included. Solutions have cosine-like variation within the central layer(s) and exponential decay (in the x direction) in the outermost layers. This model is not very appropriate to diffused structures since ϵ varies continuously in them. However, it has gained renewed attention since it is a very good description of the waveguide of heterostructure lasers.

The model of Zachos and Ripper,[98] developed for stripe geometry lasers but extendable to other structures, assumes quadratic fall-off

of the dielectric constant (which is assumed real), as shown in Fig. 35b. This quadratic variation is justifiable since it results from the lowest order Taylor expansion of any dielectric profile displaying a maximum. If the structure furthermore has mirror symmetry then the correction terms involving odd powers of x vanish. The approximation is the same as the one whereby most often all oscillators are regarded as harmonic oscillators in classical or quantum mechanics. According to this model, the wave equation may be written

$$\nabla^2 \psi + \omega^2 \mu_0 \bar{n}^2 \left(1 - \frac{x^2}{x_0^2} - \frac{y^2}{y_0^2}\right) \psi = 0 \qquad \text{(IV-37)}$$

With z dependence of the form exp $(-i\gamma z)$ assumed, mode solutions are found to be

$$\psi_{mp}(x,y,z) = A_{mp} X(x) Y(y) e^{-i\gamma_{mp} z} \qquad \text{(IV-38)}$$

where

$$X_m(x) = H_m\left(\sqrt{\frac{2\pi\bar{n}}{\lambda x_0}}\, x\right) \exp\left(-\frac{\pi \bar{n} x^2}{\lambda x_0}\right)$$

$$Y_p(y) = H_p\left(\sqrt{\frac{2\pi\bar{n}}{\lambda y_0}}\, y\right) \exp\left(-\frac{\pi \bar{n} y^2}{\lambda y_0}\right) \qquad \text{(IV-39)}$$

$$\gamma_{mp} = \bar{n}\left(1 - \frac{2m+1}{\bar{n} x_0 k} - \frac{2p+1}{\bar{n} y_0 k}\right)$$

H_m and H_p denote m- and p-th order Hermite polynominals, respectively; m and p are the mode indices and A_{mp} is a normalization constant. The lowest order mode has strictly Gaussian dependence in both x and y directions.

The model of Zachos and Ripper has attained widespread use for the interpretation of diode laser modes. Support for the model is based on numerous facts including:

(a) Gaussian or Hermite Gaussian variation of near and far-fields of laser output has often been observed.

(b) The model has given quantitative c orrelation between mode frequency spacings and far-field patterns of different modes.

(c) The gaussian and Hermite Gaussian mode patterns are mathematically tractable.

Dielectric waveguide models more complex than the Zachos-Ripper model are developed in this work because it is not evident a priori how good the parabolic approximation is when applied to the dielectric profile estimated above for PbSe lasers. The spirit of Zachos-Ripper model applications to date has been to parametrize the dielectric profile by observations of laser output. Considered here are models which fit better the first principles calculation of the profile given in this work; some of the predictions of these models are found to agree well with the Zachos-Ripper model for a properly chosen x_o.

Other model dielectric waveguides considered in the literature include ones with dielectric constant variation[101, 102]

$$\epsilon(x) = \epsilon_a + \epsilon_b \cosh^2\mu \left[\tanh\left(\frac{x}{W} - \mu\right) + \tanh\mu\right]^2 \qquad \text{(IV-40)}$$

and

$$\epsilon(x) = \epsilon_a + \epsilon_b(2e^{-\beta x} - e^{-2\beta x}) + i\epsilon_c(e^{-2\beta x} - 2e^{-\beta x})$$

Solutions for the optical field in both cases are given in terms of hyper-geometric functions.

(ii) Waveguide Model with Linear Variation of ϵ

In this section propagating modes are considered in a dielectric waveguide characterized by the dielectric constant profile (see Fig. 35c)

$$\begin{aligned} \epsilon(x) &= \epsilon_p + \epsilon_0\beta_1 x \quad \text{for } x<0 \\ \epsilon(x) &= \epsilon_p - \epsilon_0\beta_2 x \quad \text{for } x>0 \end{aligned} \qquad \text{(IV-41)}$$

The dielectric constant is assumed purely real. With this profile the wave equation in the quasi-TEM approximation for positive or negative x takes the form

$$\frac{d^2\psi}{dx^2} + (\omega^2\mu_0\epsilon_p - \gamma^2)\psi - \omega^2\mu_0\epsilon_0\beta x\,\psi = 0 \qquad \text{(IV-42)}$$

where $\exp(i\gamma z)$ z dependence is assumed, and the parameter β may be positive or negative. With the substitutions

$$\zeta = (\omega^2\mu_0\epsilon_0\beta)^{1/3}x \quad , \quad \lambda = \frac{\omega^2\mu_0\epsilon_p - \gamma^2}{(\omega^2\mu_0\epsilon_0\beta)^{2/3}} \qquad \text{(IV-43)}$$

Equation (IV-42 becomes

$$\frac{d^2\psi}{d\xi^2} + (\lambda - \xi)\psi = 0 \qquad \text{(IV-44)}$$

The solutions are given by

$$\psi(\xi) = C_1 Ai(-\lambda + \xi) + C_2 Bi(-\lambda + \xi) \qquad \text{(IV-45)}$$

Here Ai(z) and Bi(z) denote Airy functions of the 1st and 2nd kind.[103] An appropriate set of boundary conditions is given by

$$\lim_{x \to \pm\infty} \psi = 0$$

$$\psi, \frac{d\psi}{dx} \text{ continuous at } x = 0 \qquad \text{(IV-46)}$$

For the case $\beta_1 = \beta_2$ the waveguide displays mirror symmetry about the x = 0 plane, and modes have a definite parity. Even modes are given by

$$\psi_m(x) = C\, Ai\left(-\lambda_m + \frac{x}{x_0}\right) \qquad \text{(IV-47)}$$

where λ_m is the argument z_m of the mth zero of dAi(-z)/dz. Odd modes correspond to

$$\psi_n(x) = C\, Ai\left(-\lambda_n + \frac{x}{x_0}\right) \quad \text{for } x > 0 \qquad \text{(IV-48)}$$

where λ_n is the argument of the nth zero of Ai(z). Here x_o, the natural unit of width of the modes, is given by

$$x_o = (\omega^2 \mu_o \epsilon_o \beta)^{-1/3} = \left(\frac{\lambda^2}{4\pi^2\beta}\right)^{1/3} \tag{IV-49}$$

The shape of the calculated modes of order 0 and 4 are plotted in Fig. 36. Also shown in the graphs are Hermite-Gaussian modes of the same order. The very close agreement of mode shapes predicted by the parabolic model of ϵ and the model with linear fall-off can be readily seen.

For the purpose of optical mode confinement calculations, the most important result of the model is the effective width of the optical mode. For the fundamental Airy mode in the symmetric profile, the eigenvalue λ_o has the value 1.02, and w_o, the full width between e^{-1} amplitude points of the mode, is given by

$$w_o = 3.36\, x_o \tag{IV-50}$$

For higher order modes, mode width may be defined as the full width between outermost points where the mode amplitude falls to e^{-1} of its maximum value. It is interesting to note that differences exist between the present model and the parabolic model with regard to the way the widths of higher order modes vary with mode order. The ratio of the width of modes of order m to the width of the fundamental mode is shown in Fig. 37 for the two waveguide models. This result implies that observations of laser output mode widths including a sufficient number of modes might allow a choice between the models to be made. No such experiment was included in this work, however, since for the lasers used only the lowest order mode was recognizable

in the output.

If the dielectric constant profile is asymmetric, then $\beta_1 \neq \beta_2$. The solutions to (IV-44) are then given by

$$\psi(x) = C_1 \, Ai\left(-\lambda_1 - \frac{x}{x_1}\right)$$

$$\psi(x) = C_2 \, Ai\left(-\lambda_2 + \frac{x}{x_2}\right) \qquad \text{(IV-51)}$$

where

$$\lambda_2 = \lambda_1 \cdot \frac{1}{\eta^2} \qquad\qquad x_2 = \frac{x_1}{\eta} = \frac{1}{\eta}\left(\frac{\lambda^2}{4\pi^2\beta_1}\right)^{1/3} \qquad \text{(IV-52)}$$

and η is an asymmetry parameter defined by

$$\eta = \left(\frac{\beta_2}{\beta_1}\right)^{1/3} \qquad \text{(IV-53)}$$

The boundary conditions require that the eigenvalue λ_1 satisfy

$$\frac{1}{Ai(-\lambda_1)} \frac{dAi(z)}{dz}\bigg|_{z=-\lambda_1} = -\frac{\eta}{Ai\left(-\frac{\lambda_1}{\eta^2}\right)} \frac{dAi(z)}{dz}\bigg|_{z=-\frac{\lambda_1}{\eta^2}} \qquad \text{(IV-54)}$$

This equation has been solved numerically to yield the values of λ_1 and λ_2 for profiles of a given asymmetry. Curves of λ_1 and λ_2 vs. η are shown in Fig. 38. Some typical mode shapes for the fundamental mode are shown in Fig. 39. The width w_o of the asymmetric modes is given by the expression

$$w_o = C_\eta x_1 \qquad \text{(IV-55)}$$

Here C_η is a parameter that has been obtained numerically, and is shown vs. η in Fig. 38.

The solutions given above describe the behaviour of the optical amplitude in the dielectric waveguide. In the sections that follow some properties of interest will be calculated from those solutions, including laser output mode frequency spacings, mode losses and laser far-field patterns. Application to the particular case of PbSe lasers will be made after the discussion.

(iii) Dispersion Relations and Mode Spacings

The travelling-wave modes calculated above propagate according to $\exp(-i\gamma z)$. According to (IV-43), the propagation constant γ_m of mode m satisfies

$$\gamma_m^2 = \bar{n}^2 k_o - \frac{\lambda_m}{x_o^2} \qquad \text{(IV-56)}$$

where $\bar{n}^2 = \epsilon_p$, $k_o = 2\pi/\lambda_o$, λ_o is the free space wavelength of the optical field and x_o has been defined above. Consideration is limited here to the symmetric waveguide profile; results for the asymmetric case are similar.

From (IV-56) it may readily be seen that the waveguide is cut off when

$$x_o \leq 1.01 \frac{\lambda_o}{2\pi\bar{n}} \qquad \text{(IV-57)}$$

and it is single-moded when

$$1.01 \frac{\lambda_o}{2\pi\bar{n}} < x_o < 1.53 \frac{\lambda_o}{2\pi\bar{n}} \qquad \text{(IV-58)}$$

This condition requires values of x_o much smaller than those achieved in practices.

If stripe geometry lasers are considered or if a filament is present, then (IV-56) must be corrected to account for the variation of the mode in the y direction. Following Zachos and Ripper, this is readily done by including a new term to obtain

$$\gamma_{mp}^2 = \bar{n}^2 k_o^2 - \frac{\lambda_m}{x_o^2} - \frac{(2p+1)\, n k_o}{y_o} \qquad \text{(IV-59)}$$

where p is the transverse (y direction) mode order and y_o is the dielectric constant parameter of the ZR model.

High Q cavity modes result when the length of the waveguide is an integer number of half-wavelengths of the propagating field, or

$$\gamma_{mpq} = \frac{\pi q}{L} \qquad \text{(IV-60)}$$

where q is an integer (axial mode number) and L is the laser length. From (IV-59) and (IV-60) the dispersion relation of the cavity may be obtained

$$\bar{n}^2 \nu_{mpq}^2 = \frac{c^2 q^2}{4L^2} + \frac{\lambda_m c^2}{4\pi^2 x_o^2} + \frac{(2p+1)\, \bar{n}\, \nu_{mpq}\, c}{2\pi y_o} \qquad \text{(IV-61)}$$

where ν_{mpq} is the frequency of the mode of order m, p and q.

The frequency separation of cavity modes differing by one unit in mode order in any direction may be readily derived from this equation. Taking into account the fact that the index of refraction is frequency dependent the following is obtained by differentiation and

the neglect of small terms:

$$\Delta\nu = \frac{c}{2L\bar{n}} \cdot \frac{1}{1 + \frac{\nu}{n}\frac{dn}{d\nu}} \cdot \Delta q \qquad \text{(IV-62)}$$

for the longitudinal mode separation;

$$\Delta\nu = \frac{\nu}{8\pi^2 \bar{n}^2} \cdot \frac{\lambda_o^2}{x_o^2} \cdot \frac{1}{1 + \frac{\nu}{n}\frac{dn}{d\nu}} \cdot \Delta\lambda_m \qquad \text{(IV-63)}$$

for the transverse mode separation (x direction); and

$$\Delta\nu = \frac{c}{2\pi \bar{n} y_o} \cdot \frac{1}{1 + \frac{\nu}{n}\frac{dn}{d\nu}} \cdot \Delta p \qquad \text{(IV-64)}$$

for the transverse mode separation (y direction).

In (IV-63) it must be recalled that λ_m is the mode eigenvalue found in Equation (IV-47). Since for Δ m=1 slightly different values of $\Delta\lambda_m$ are found, it is thus predicted that the modes with equal p and q but different m are not evenly spaced in frequency.

The last two expressions may be conveniently reformulated by eliminating x_o and y_o (which are not observables) and including the observable quantities w_{ox} and w_{oy} (the full widths of the fundamental mode in the x and y directions). This yields

$$\Delta\nu = 0.143 \frac{\lambda_o^2}{\bar{n}^2 w_{ox}^2} \cdot \frac{\nu}{1 + \frac{\nu}{n}\frac{dn}{d\nu}} \cdot \Delta\lambda_m \quad \text{(x direction)} \qquad \text{(IV-65)}$$

$$\Delta\nu = 0.203 \frac{\lambda_o^2}{\bar{n}^2 w_{oy}^2} \cdot \frac{\nu}{1 + \frac{\nu}{n}\frac{dn}{d\nu}} \cdot \Delta p \quad \text{(y direction)}$$

Keeping in mind that $\Delta\lambda_m$ is slightly larger than unity for low order modes, it may be seen from the similarity of these expressions that there is close agreement between predictions of the ZR model and the present model for mode spacings.

(iv) End Losses and Far-field Patterns

The optical field incident upon the end mirror-facet of the laser will be partially transmitted into free space and partially reflected back into the effective junction waveguide, where its energy may be redistributed among many waveguide modes. A complete solution to the boundary problem involves matching tangential E and H fields among the incident field, reflected discrete and continuum waveguide modes and transmitted propagating and evanescent plane waves.[104] This approach has been followed in approximate numerical solutions for DH GaAs waveguides by Ikegami.[105] An alternate, approximate method of solution is to Fourier analyze the incident electric field and compute the transmission and reflection coefficients of each Fourier component on the basis of Fresnel theory for the boundary of a homogeneous dielectric slab.[106-108] The latter approach will be followed here.

The incident optical field, assumed to correspond to a pure waveguide mode according to the solutions obtained above, may be represented by

$$\Psi_m(x,z) = \psi_m(x) e^{-i\gamma z} = \int_{-\infty}^{\infty} \hat{\psi}_m(q_x) e^{iq_x x - i\gamma z} dq_x \qquad \text{(IV-66)}$$

Here $\hat{\psi}_m(q_x)$ is the Fourier transform of $\psi_m(x)$. It is convenient to assume that the dielectric constant within the semiconductor is

constant and has the value $\epsilon_p = n^2$, and to ignore the (small) difference between the propagation constant γ and nk_o, which would apply to a uniform plane wave of the same frequency travelling in the homogeneous semiconductor. The reflection and transmission coefficients of each Fourier component are then given by

$$r_{TM} = t_{TM} - 1 = \frac{n^2(k_o^2 - q_x^2)^{1/2} - (n^2k_o^2 - q_x^2)^{1/2}}{n^2(k_o^2 - q_x^2)^{1/2} + (n^2k_o^2 - q_x^2)^{1/2}}$$

$$r_{TE} = t_{TE} - 1 = \frac{(k_o^2 - q_x^2)^{1/2} - (n^2k_o^2 - q_x^2)^{1/2}}{(k_o^2 - q_x^2)^{1/2} + (n^2k_o^2 - q_x^2)^{1/2}} \qquad \text{(IV-67)}$$

The reflectivity is plotted as a function of q_x in Fig. 40 for $\epsilon_p = 28$, which corresponds to PbSe at 77^oK. Shown also are the equivalent angles of incidence and transmission for plane waves at the frequency of lasing that correspond to each q_x. Within this approximation, the transmitted electric field at z=0+ is given by its Fourier transform $\hat{\psi}_t(q_x)$ where

$$\hat{\psi}_t(q_x) = [1 + r(q_x)]\,\hat{\psi}_m(q_x) \qquad \text{(IV-69)}$$

If the incident waveguide mode has only a slow spatial variation, then its Fourier transform will be appreciable only at small q_x, and the reflectivity for all its components will approximate ly constant. This limit was obtained for nearly all the lasers examined in this work.

The optical field in the Fraunhofer far-field region may be found by considering the free-space propagation of the transmitted field $\Psi_t(x)$, given at $z=0^+$ by

$$\Psi_t(x,0) = \int_{-\infty}^{\infty} \hat{\psi}_t(q_x)\, e^{iq_x x}\, dq_x \tag{IV-70}$$

By the linearity of Maxwell's equations, at a distance r from the mirror along a direction making angle θ with the mirror normal in the x-z plane, the field will be given by[109]

$$\Psi_t(r,\theta) = \int_{-\infty}^{\infty} \hat{\psi}_t(q_x)\, e^{ir\left(\sqrt{k_o^2 - q_x^2}\cos\theta + q_x \sin\theta\right)} dq_x \tag{IV-71}$$

This integral may be evaluated approximately by the method of stationary phase,[110] valid for $k_o r \gg 1$, and is found to yield

$$\Psi_t(r,\theta) = i\sqrt{\frac{2k_o}{r}}\cos\theta\ \hat{\psi}_t(q_x = k_o \sin\theta) \tag{IV-72}$$

Radial decay of the electric field according to $r^{-1/2}$ is found in this expression because of the assumed two-dimensional form of the problem. An equivalent solution is found in the three-dimensional case (with the proper r^{-1} dependence) provided the far-field is observed at small angles to the mirror normal in the y-z plane (orthogonal to direction of interest). This approximation was valid for the far-field pattern studies reported in this work.

Measured far-field patterns correspond to the distribution of optical intensity, proportional to $|\Psi(r,\theta)|^2$. Thus far-field patterns are given by

$$P(\theta) = C\cos^2\theta\, |\hat{\psi}_t(q_x = k_o \sin\theta)|^2 \tag{IV-73}$$

where C is an arbitrary constant.

In order to determine the far-field patterns corresponding to the optical modes obtained with the linear fall-off dielectric profile model, Fourier transforms of the mode amplitude distributions were computed numerically. It was found that the resulting curves were very closely Gaussian in shape. This was true even for amplitude distributions that were relatively unlike Gaussians (e.g. those corresponding to the asymmetric profiles). For example, in Fig. 41 is shown the magnitude squared of the Fourier transform of the mode distribution of the completely asymmetric profile ($\eta = \infty$), and for comparison a Gaussian curve. The two functions agree everywhere but in the tail region.

For Gaussian modes there is a simple relation between the width of the amplitude distribution (or near field pattern) and the width of the magnitude squared of its Fourier transform (or far field pattern) given by

$$w_o \cdot q_o = 8 \qquad \text{(IV-74)}$$

Here w_o is the full width between e^{-1} amplitude points and q_o is the full width between e^{-2} points of the corresponding magnitude squared of the transform. For the amplitude distributions computed above it was found that this relationship is also valid to a very close approximation. For example, for the fully asymmetric mode ($\eta = \infty$) the error incurred by the use of (IV-74) is less than .5%, provided q_o is measured on the most closely matched Gaussian.

(v) Distributed Mode Losses

Free carrier absorption represents an unavoidable power loss mechanism to waves propagating in the effective junction waveguide. Additional loss mechanisms may be present, such as scattering or absorption from defects such as microprecipitates or inclusions, and scattering due to junction nonplanarity. Only the free carrier component will be considered here.

The mode distributed loss coefficient A_m is defined by the relation

$$I_m = I_{mo} e^{-A_m z} \qquad \text{(IV-75)}$$

where I_m is the optical field intensity of mode m propagating in the z direction if there is no interband gain or loss. A_m may be obtained approximately by the relation

$$A_m = \frac{\int_{-\infty}^{\infty} \alpha(x) \, |\psi_m(x)|^2 dx}{\int_{-\infty}^{\infty} |\psi_m(x)|^2 dx} \qquad \text{(IV-76)}$$

where $\alpha(x)$ is the (spatially varying) local value of the free carrier absorption coefficient. Using (IV-2) it is found that α is given by

$$\alpha = \frac{4\pi e^2 n}{N c \tau_{sc} \left(\omega^2 + \frac{1}{\tau_{sc}^2}\right)} \cdot \left\langle \frac{1}{m_c^*} \right\rangle \qquad \text{(IV-77)}$$

Here n denotes the local net carrier concentration, N is the index of refraction and τ_{sc} is the phase-destroying collision lifetime of the carriers. As noted in Section IV. 2(i), an appropriate value of is near 1.5×10^{-13} sec in PbSe, although some uncertainty surrounds its value. No data is presently available indicating the variation of

τ_{sc} with temperature.

Neglecting for simplicity the variation of m_c^* with carrier density, α may be written

$$\alpha(x) = F_\alpha \, n(x) \tag{IV-78}$$

where F_α , evaluated at the lasing frequency for PbSe at 77°K, is 3.69×10^{-17} cm ^{2}.

To evaluate the integral defined in (IV-76) it is convenient to consider separately the absorption due to the carrier density present with no applied bias and that due to injected carriers. The net donor density may be assumed to vary linearly with distance in the vicinity of the junction. For the symmetric dielectric waveguide the equilibrium carrier density then follows

$$n(x) = F_x |x| \tag{IV-79}$$

The mode loss coefficient due to these carriers A_m^{eq} is then

$$A_m^{eq} = F_\alpha F_x \frac{\int |x| \, \psi_m^2(x) dx}{\int \psi_m^2(x) \, dx} = 0.67 \, F_\alpha F_x x_o \tag{IV-80}$$

which has been obtained by numerical integration for the fundamental mode. The parameter x_o is the unit of mode width defined in (IV-49).

For the asymmetric waveguide characterized by the symmetry factor η it is assumed that the equilibrium carrier density varies near the junction according to

$$n(x) = F_{x1}|x| \quad \text{for } x<0$$
$$n(x) = F_{x2}|x| \quad \text{for } x>0 \qquad \text{(IV-81)}$$

where

$$F_{x1} = \eta^3 F_{x2} \qquad \text{(IV-82)}$$

(This is reasonable since the dielectric constant gradient must be nearly proportional to the equilibrium carrier density gradient.) Then the mode loss coefficient A_m^{eq} is

$$A_m^{eq} = F_\alpha F_{x1} \frac{\int_{-\infty}^{0}|x|\,\psi_m^2(x)dx + \eta^3\int_0^\infty |x|\,\psi_m^2(x)dx}{\int_{\infty}^{\infty}\psi_m^2(x)dx} = F_\eta F_\alpha F_{x1} x_1 \qquad \text{(IV-83)}$$

where F_η is a numerical coefficient which varies with η as shown in Fig. 42.

To evaluate the mode losses due to absorption by the injected carriers it is assumed that the width of the optical mode is much greater than the width of the region where the injected carrier density is appreciable. This assumption is valid for the mode widths obtained experimentally in this work. Then the integral of (IV-76) may be simplified to

$$A_m = \frac{\psi_m^2(0)\int\alpha(x)dx}{\int\psi_m^2(x)dx} = \frac{F_\alpha}{w_\ell}\int n(x)dx \qquad \text{(IV-84)}$$
$$= \frac{2F_\alpha \tau_{rec} J_{th}}{w_\ell q}$$

where w_l is an effective width of the lasing mode given by

$$w_l = \frac{\int \psi_m^2(x)dx}{\psi_m^2(0)} \qquad \text{(IV-85)}$$

and the total number of injected carriers has been taken to be

$$\int n(x)dx \approx \frac{2 J_{th} \tau_{rec}}{q} \qquad \text{(IV-86)}$$

as described in Section III. 3. A factor of two accounts for the increase in majority carrier density necessary to maintain quasi-neutrality near the junction. The effective width of the mode w_l may be readily related to the mode width w_o between e^{-1} amplitude points by

$$w_l = 0.6267\ w_o \qquad \text{(IV-87)}$$

which applies to the symmetric modes, and to a close approximation to the asymmetric modes as well.

(vi) Application to PbSe Lasers:

On the basis of the dielectric constant profiles displayed in Chapter IV-3 for diffused PbSe lasers, it is expected that the dielectric profile model with linear variation of ϵ should provide a good description of these devices. In this section the formalism of the preeeding sections is used to calculate parameters of interest for PbSe lasers. All three profile models described in Chapter IV-3 are considered.

For Models I and II of the dielectric constant profile (shown in Figures 31c and 32c) the completely asymmetric model ($\eta = \infty$) is an adequate approximation, while for Model III the symme tric

model may be used. The parameter β (which describes d ϵ /dx) for each is shown in Table V, where values are given for the example of a 50μ deep junction. Following the discussion of Chapter IV-3, we note that β varies inversely with junction depth. Values of x_o (natural unit of width for the modes) and w_o (full width between amplitude points of the mode) corresponding to the 50μ junctions are shown in Table V. These values were obtained by application of (IV-49) and (IV-50). Both x_o and w_o vary with junction depth according to $x_j^{1/3}$.

It was found that differences between the dielectric profiles of Chapter IV.3 and the model with linear variation of ϵ were capable of broadening the modes. In Appendix D are considered several waveguide models that approximate Models II and III more closely than the linear model. The results of Part A of that appendix may be applied to the profile Model III, using a value of L_A/x_o of 0.814 to account for the curvature of ϵ near x=0. The corrected mode width found from the Appendix is larger by 15% than the former estimate, as indicated in Table V. A corrected mode shape is shown in Fig. 77 . Similarly, Part B of the appendix may be used to determine the extent to which the mode penetrates the homogeneous bulk n type region. The parameter L_B/x_o for Model II was evaluated from Fig. 32c to be 5.826. From the corrected mode shape shown in Fig. 79 it is found that the mode spreads appreciably into the bulk n region; however, as shown also in Table V, the corresponding correction to the mode width is slight.

The small values of w_o predicted above constitute the central result of this chapter. The substantial mode confinement stems from the very large changes in ϵ caused by the spatial variation of carrier density, as described earlier.

Frequency spacings of the modes, as well as end losses and free carrier absorption losses are expected to be similar for all the model profiles. In this section only the results for the symmetric junction will be evaluated.

Using an estimated value of the index of refraction of 5.3 for PbSe at 77°K, the value of $1 + \frac{\nu}{n} \frac{dn}{d\nu}$ may be determined from the measured frequency separation of adjacent longitudinal modes of the laser; its value is found to be near 1.2. Then, according to (IV-63), the frequency separation of adjacent (x direction) transverse modes is calculated to be 270 Gc. As mentioned earlier, if the mode width of a given laser has been measured, for example by observation of its far-field pattern, then a more accurate determination of the mode frequency spacing may be obtained from (IV-65).

As discussed in Section (iv), the mirror-facet reflectivity for the modes calculated here (fairly deep junction case) is effectively identical to the results obtained for plane waves with normal incidence, given by $r = 0.68$ and $R = r^2 = 0.466$. End losses for the laser are given by

$$A^{end} = \frac{1}{L} \ln \frac{1}{R} \qquad \text{(IV-88)}$$

wher A^{end} is the customarily defined distributed loss equivalent to the transmission loss. For a 500μ long laser, (IV-88) yields $A^{end} = 15.26 \text{ cm}^{-1}$.

Following (IV-80) and (IV-84), the distributed mode loss due to free carrier absorption is given by

$$A_m = 0.67 F_\alpha F_x x_o + 0.92 \frac{F_\alpha \tau_{rec} J_{th}}{x_o q} \qquad \text{(IV-89)}$$

for symmetric modes. Using parameters corresponding to Model III with $x_j = 50\mu$ and $J_{th} = 5000$ A/cm^2, (IV-89) yields

$$A_m = 5.7\ cm^{-1} + 11.5\ cm^{-1} = 17.2\ cm^{-1} \qquad \text{(IV-90)}$$

A sizeable portion of the loss is thus expected to be caused by the minority carriers.

IV. 5 Experimental Verification of Far-field Patterns

This section reports measurements of far-field patterns of PbSe diode lasers which provide an experimental test of the optical confinement theory detailed in earlier sections of this chapter. According to (IV-73), the angular width of far-field patterns allows estimation of the width of the corresponding near-field pattern, which is given by the width of the propagating optical modes of the dielectric waveguide. Far-field patterns were obtained at 77°K for a series of lasers which were diffused at the same temperature (500°C) and had identical surface and bulk carrier concentrations. The diodes differed, however, in junction depth x_j and consequently in stoichiometry grading. According to Chapter IV. 3, the profile of ϵ in the junction region of the lasers scales with x_j. As will be shown, the mode widths of the lasers inferred from the measurements reported here vary according to $x_j^{1/3}$ as predicted by Section IV. 4. Also the mode width for a given x_j is in rough agreement with the theoretical predictions.

(i) Experimental Method

Laser diodes, whose fabrication is described in Appendix A, were mounted on the copper cold-finger of a Janis dewar equipped with BaF_2 windows. They were operated with pulses of current of

duration less than 200 nsec and duty cycle less than 5×10^{-3}. The current pulses were supplied by a laboratory-built capacitor discharge pulser in which switching action was obtained with a high-speed SCR, or by an SKL Model 503A vibrating reed transmission-line pulser (for which case a series resistor near 50Ω was placed near the diode to maintain pulse shapes). Radiation was detected with a Ge:Au detector cooled to 77°K; its output into a 1 MegΩ load resistor was amplified and served as input to a boxcar integrator, which enhanced the S/N ratio. The boxcar output was displayed on a chart recorder. Linearity of the detection system for the power levels attained was confirmed by observation of the changes in response when neutral density filters (wire meshes) were placed in front of the detector.

The angular distribution of the output could be measured by the system depicted in Fig. 43a or with the system of Fig. 43b. With the latter scheme the far-field pattern corresponding to a single laser frequency could be measured; this was found to be necessary because of the generally multimode nature of the laser output, together with the fact that far-field patterns differed for different modes. A Spex Model 1400-II double grating monochromator with 8.0μ blazed gratings was used to obtain output spectra and select individual modes for study. Radiation from the diode was focussed by a toroidal mirror onto the spectrometer slit, after traversing a slit of width approximately 0.4 cm. This external slit limited the acceptance angle of the system to approximately 1.2° in the horizontal plane (corresponding to the x-z plane of the laser coordinate system), while in the vertical plane the acceptance angle was approximately 15°, limited by the spectrometer. The sample dewar was mounted on a rotating table that could be positioned manually to allow radiation emerging from the diode at different angles to enter the spectrometer system. After each change in the diode's angle, the diode was repositioned at the focus of the

mirror by using light from a He-Ne laser, run through the spectrometer, to determine the focal spot. By monitoring the reflection of the He-Ne beam from the front diode mirror facet very accurate reproducibility of measurements of laser line intensities between successive repositionings could be achieved.

Often the diode output spectra were found to change slowly in time, probably due to thermal drift of the dewar cold-finger. For such cases, frequency-resolved far-field patterns were obtained by checking repeatedly the output spectrum at a reference position and then correcting by renormalization of the spectrum for the small (less than 5%) drifts that occured in the intervening time.

(ii) Experimental Results and Analysis

A typical output spectrum of a diode laser when operated pulsed at 77°K at a current of $1.48 I_{th}$ is shown in Fig. 44. The basic periodicity of output mode frequencies is 42.8Gc, which corresponds closely to what is expected for adjacent longitudinal cavity modes (if the average value of the index of refraction is assumed to be 5.3 for this 535μ long diode, then $(\nu/n)(dn/d\nu)$ is calculated to be .235). Several strong modes are slightly shifted (by up to 2.2 Gc) from their position expected on the basis of the mode periodicity. In addition, barely resolved low intensity "satellite" peaks accompany the high intensity modes, at a spacing of the order of 4 to 8 Gc. These modes were later found to have the same far-field pattern in the x-z plane as the more prominent modes. It is possible that they correspond to imperfections of the effective dielectric waveguide or mirror facets of the laser, or to modes with different optical field distributions in the y-z plane. If a frequency spacing of 6 Gc is interpreted as the separation between (y direction) transverse modes for a single lasing filament, then the filament width obtained on the basis of (IV-65) is near

50 μ . In several lasers the satellite peaks were not present, or not resolvable.

The output spectrum at higher pulse currents in general displays many more modes. As current pulse amplitude is raised the output power in each mode increases (although not linearly with $I-I_{th}$), the width of the overall envelope of the emission increases and more satellite modes appear. For current pulses in the vicinity of threshold the number of output modes was found to decrease, but in general 2 to 5 modes were still present in the spectrum at the limit of detectability of the output spectrum.

In an effort to determine if heating during the pulse was responsible for the observation of broad emission, lasers were excited successively with current pulses of equal peak amplitude but different duration. No change was found in the output spectrum nor in behaviour of x-z plane far-field patterns when the pulses were in the range 10 to 500 nsec (although for longer pulses the spectrum broadened towards higher energies). This negative result is consistent with the small temperature rise (less than 1° K) expected to occur near the junction for short pulses of less than 10A, as discussed in Section IV. 2.

The far-field pattern in the plane of the junction was measured for a small number of lasers. Typical results are shown in Fig. 45 where the angular dependence of the total intensity is displayed. The narrow angular width of the pattern is consistent with uniform emission over the entire width of the junction (205 μ in this case), although the mode shape is not the theoretical one. This data supports the contention that filaments were normally absent in the diodes. In one case, however, a diode was measured to have a value of I_{th} lower by a factor of 6 than the normal results. It is likely that this occurred because of the formation of a filament, in which the threshold current density had a more normal value.

The far-field pattern in the x-z plane of the total emission of a typical diode is shown in Fig. 46. Subsequent study showed that the far-field patterns of individual output modes were slightly different, as shown also in Fig. 46. It was in general observed that different modes had patterns of the same shape, but the direction of the center of the pattern was slightly different, such that the overall intensity pattern of a sum of modes was broader than the pattern of each mode.

The direction of the center of a single-lobed far-field pattern did not in general coincide with the normal to the diode output mirror, and misalignment angles of up to 15° were measured. Most of this difference is expected to have resulted from misalignment between the mirror normals and the plane of the junction caused during the laser mirror polishing (as described in Appendix A). It is known that for small misalignment angles θ_{mis} the far-field pattern is not materially changed, but the direction of the center of the pattern is offset by an angle $n\,\theta_{mis}$, where n is an average of the index of refraction of the semiconductor.

Additional misdirection of far-field patterns was found to result from other sources. When current pulses of high amplitude were applied, in general the far-field pattern shifted in direction in the x-z plane, without appreciable change in shape. Fig. 47 shows total emission far-field patterns observed for several current values for the same diode. Similar shifts were observed for individual mode far-field patterns. The direction in which the shift occurred was for some diodes towards the n side of the junction, while towards the p side for others. Similarly, in some cases it was in the direction of the heatsink, while in some cases it was away from it. The cause of this directional effect is not understood; it may stem from the influence of the imaginary part of ϵ on the propagation of the modes within the waveguide. The distribution of Im ϵ is known to affect the shape of constant phase

surfaces of the modes; it is expected also that the distribution of Im is affected by the level of excitation in asymmetric junctions.

For a number of diodes, x-z plane mode far-field patterns of very irregular shape were found; a typical irregular pattern is shown in Fig. 48. For diodes that displayed this characteristic, as well as for diodes with single-lobed patterns, reproducibility of the far-field patterns was very good. The same results were obtained for neighboring longitudinal modes (apart from directional effects), and were obtained also if a diode was warmed to room temperature, remounted in the dewar and tested again. The cause of these irregular patterns was not determined. It is likely, however, that they result from geometrical imperfections of the cavity, such as flaws in the mirror facets or sidewalls, or large scattering centers (inclusions or stressed regions) present in the interior of the diode. No further data was taken with diodes displaying the irregular patterns.

Over 50% of the diodes studied displayed regular far-field patterns, that is, patterns that were single-lobed, approximately symmetric, and directed from the laser at an angle not greater than 15° from the mirror normal. Several typical far-field patterns are shown in Fig. 49, and for comparison closely matched Gaussian curves. For the case of diode A1 the fit with the mathematical curve is very good for the two different modes shown. Deviations from Gaussian behaviour occur for the remaining laser mode patterns. In many cases these deviations were shown to be reproducible by repeated measurements. These output patterns and the ones discussed below were measured for diode currents in the range 1.2 and 1.8 I_{th}. The far-field pattern shapes and widths were shown to be independent of current over this range. No regular, symmetric patterns that might be interpreted as higher order mode patterns were observed.

To determine the mode width corresponding to the observed far-field patterns, an equivalent angular width $\Delta\theta_{eq}$ was first found for each pattern according to the relation

$$\Delta\theta_{eq} = \frac{\int_{\theta_{.3}^{-}}^{\theta_{.3}^{+}} P(\theta)\,d\theta}{P(\theta_{max})} \qquad \text{(IV-91)}$$

where $P(\theta)$ is the relative power observed at angle θ from the diode normal in the x-z plane. Numerical integration following the trapezoidal rule was used with the measured data points to compute the numerator of (IV-91), while visual estimation was used to determine $P(\theta_{max})$. This somewhat arbitrary definition of the equivalent width of the pattern was found to be a convenient method of eliminating subjective considerations from the process of data fitting. The angular integral was carried out between the angles $\theta_{.3}^{-}$ and $\theta_{.3}^{+}$ where the relative power reached .3 times its maximum value $P(\theta_{max})$; the value .3 was selected because the S/N ratio of the measurements deteriorated for lower detected powers. Values of $\Delta\theta_{eq}$ for the set of lasers studied are shown in Table VI, together with values of their junction depth (measured by a thermoelectric probe on remaining sections of the substrates the lasers originated from).

From values of $\Delta\theta_{eq}$ the mode widths w_o (full width between e^{-1} amplitude points) were found for the lasers using the theoretical curve of Fig. 50. This graph was obtained by calculating far-field patterns corresponding to a series of Gaussian modes of different width w_o, and then numerically obtaining values of $\Delta\theta_{eq}$ for each far-field pattern. The graph also applies to the modeshapes predicted in Chapter IV.4 because, as shown in Section IV.4(iv) the far-field patterns of the modes of width w_o of the linear model agree with the far-field patterns of Gaussians of the same width w_o everywhere but in the tail region

to better than 1%. Using (IV-73) the far-field pattern corresponding to the Gaussian near-field amplitude was found to be

$$P(\theta) = C \cos^2\theta \exp\left(-\frac{\pi^2 w_o^2 \sin^2\theta}{2\lambda_o^2}\right) \qquad \text{(IV-92)}$$

where λ_o is the free-space wavelength of the laser output.

The complexity of this analysis was motivated by the need to properly take into account the $\cos^2\theta$ factor in (IV-92). The slight deviation from linearity of the curve of Fig. 50 is a consequence of this factor.

The mode width w_o inferred from the measurements is shown in Table VI for the lasers studied. A graph of w_o vs. the laser junction depth x_j is shown in Fig. 51. Despite scatter, the measured points agree well with the $x_j^{1/3}$ dependence predicted in Section IV.4(vi). Also shown in Fig. 51 are values of mode width w_o calculated in Section IV.4(vi) on the basis of the three models of the donor-acceptor density profile near the junction discussed earlier. The predictions made with the profile models are smaller than the observed best-fit $x_j^{1/3}$ law by 42%, 35% and 24% for Models I, II and III, respectively.

(iii) Discussion

The observed variation of mode width with junction depth for the set of lasers is direct evidence that the grading of the junction affects the degree of optical confinement in the lasers. Agreement with the predicted $x_j^{1/3}$ dependence furthermore tends to support the validity of the mode confinement calculations of Section IV.4.

The discrepancies between the observed widths and the predictions obtained earlier are bigger than might be expected solely on the

basis of uncertainties in the values of fundamental parameters of PbSe used in the calculations (including m* (ϵ) and P_{cv}^2). A possible source of the discrepancy, as well as of some of the scatter of the data might be incorrect evaluation of the number of injected minority carriers. This could arise because of uncertainty in the value of either J_{th} or τ_{rec} to be used in (IV-31). The real values of J_{th} could be considerably higher than the values used in the model if filaments with large current concentration formed at the junction of the lasers. This unlikely, however, in view of the reasonable accord between the calculated and measured values of J_{th} to be shown in Chapter V. The possibility remains that the value of τ_{rec} varied widely among the different lasers.

The sensitivity of the estimated mode width to the value of the injected minority carrier density may be evaluated by using the results of Appendix D for the case of the symmetrically graded junction model (Model III). If it is assumed that in addition to the total number of minority carriers per unit junction area N_{min} determined in Chapter IV.3, there is a present an amount ΔN_{min} then the dielectric constant shown in Fig. 33c will be lower near x=0. The necessary correction to the dielectric profile when integrated over the junction must yield approximately

$$\Delta \int \epsilon(x)dx = 2\Delta N_{min} \langle \frac{d\epsilon}{dn} \rangle \qquad \text{(IV-93)}$$

where $\langle d\epsilon/dn \rangle$ is an average of $d\epsilon/dn$ over the junction, and a factor of 2 has been included to account for the increase in majority carrier density. In terms of the model of Part A of Appendix D the change in the profile may be conveniently approximated by a change in the parameter L_A. The change ΔL_A necessary to account for a

given $\Delta \int \epsilon(x)dx$ is given by

$$\Delta L_A = -\frac{1}{2\epsilon_0 \beta L_A} \Delta \int \epsilon(x)dx \qquad \text{(IV-94)}$$

The results of Fig. **78** indicate that the calculated mode width changes with the value of L_A in a nonlinear fashion. If the change ΔL_A in (IV-94) is small, however, then we may use

$$\Delta w_0 = \frac{dw_0}{dL_A} \Delta L_A \qquad \text{(IV-95)}$$

and thus

$$\Delta w_0 = -\frac{1}{\epsilon_0 \beta L_A} \cdot \frac{dw_0}{dL_A} \cdot \left\langle \frac{d\epsilon}{dn} \right\rangle \Delta N_{min} \qquad \text{(IV-96)}$$

As an example of the application of (IV-96), if ΔN_{min} is assumed to originate from a change in J_{th} from its estimated value, then for Model III with the parameters of Section IV. 4(vi) (50 μ deep junction) we find

$$\Delta w_0 = 1.6 \times 10^{-3} \mu / \text{Acm}^{-2} \cdot \Delta J_{th} \qquad \text{(IV-97)}$$

There was some correlation between scatter of the data and scatter in values of threshold current density found for the individual lasers. No calculations have been carrier out, however, to obtain better fits to individual devices.

The effects of junction nonplanarity on the propagation of the lasing modes is now known. It is possible, if the junction waveguides

of the lasers were sufficiently irregular, that considerable mixing of the eigenmodes of the perfect guides took place. The resultant waves might have regular shapes and larger widths than the fundamental modes of the unperturbed waveguides.

Finally, as noted in Chapter II, there is considerable uncertainty surrounding the grading of the donor-acceptor profile near the junction. The calculated results indicate that loss of mode confinement results if the high vacancy gradient region of the BWG profile occurs on either the p or n side of the junction. Changes in the assumed profiles by the effect of impurities or junction electric fields may have a further broadening effect on the waveguide modes.

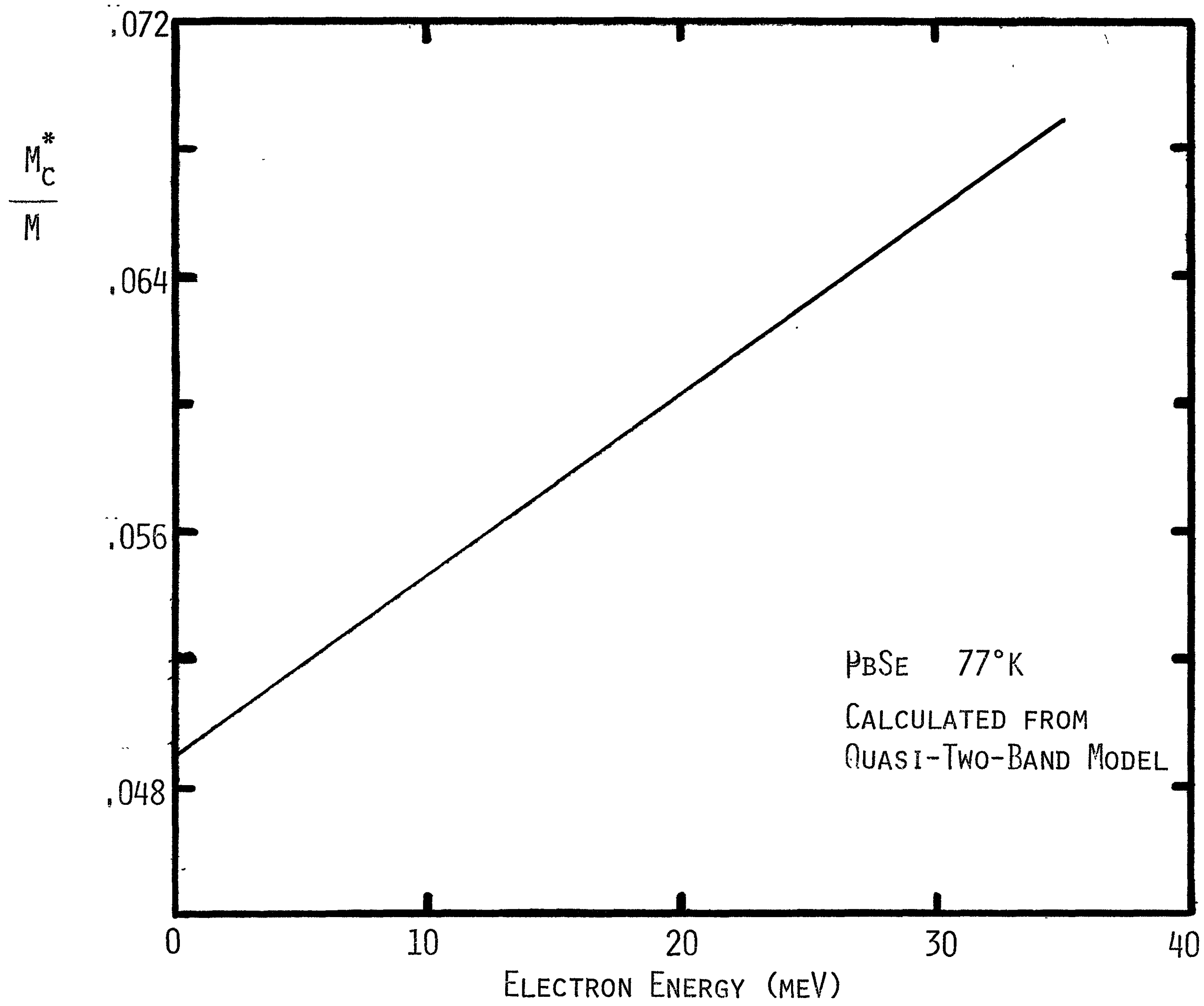

FIGURE 25: CALCULATED ENERGY DEPENDENCE OF CONDUCTIVITY EFFECTIVE MASS IN PBSE

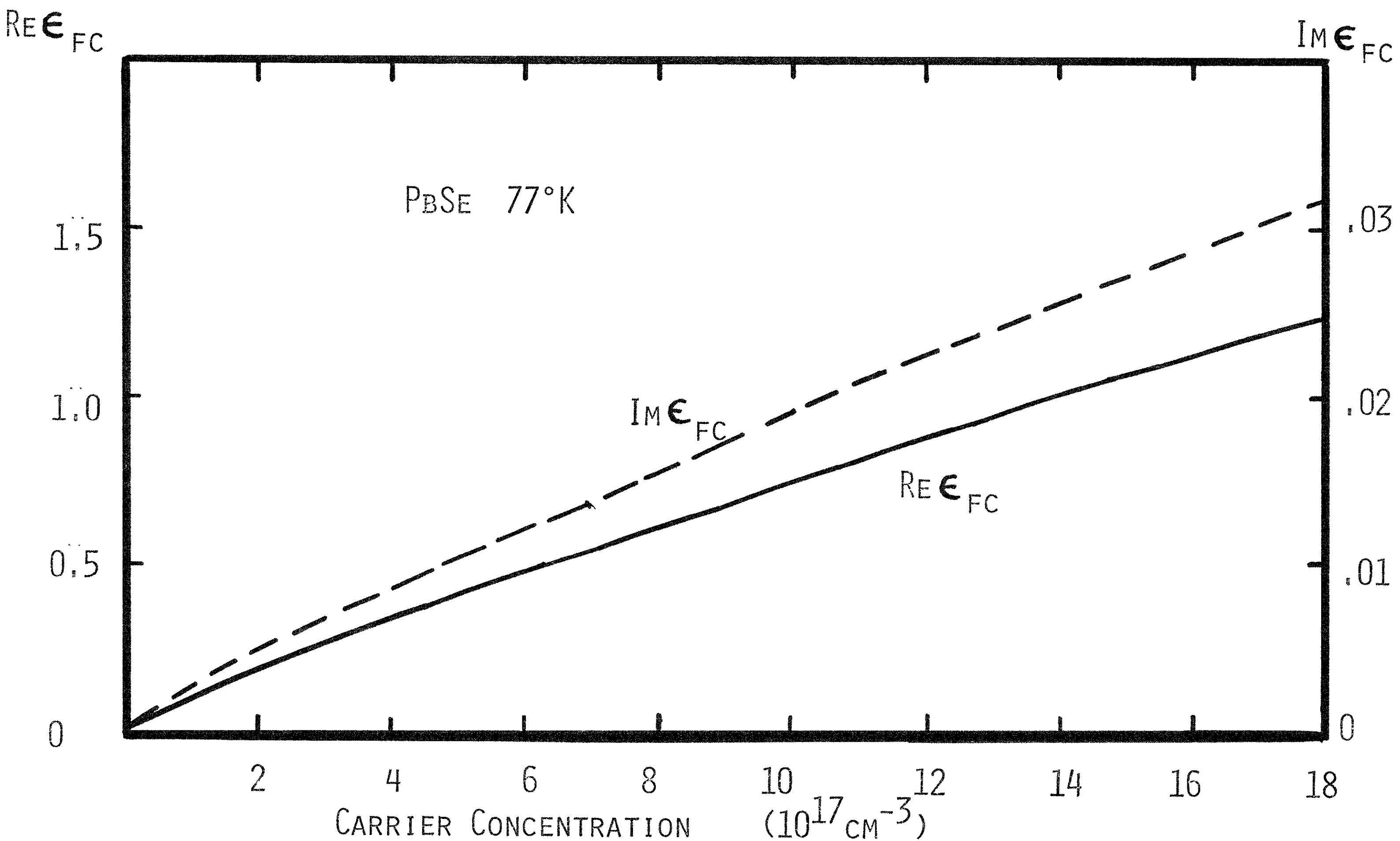

Figure 26: Variation with Carrier Concentration of Free-Carrier Contribution to the Dielectric Constant

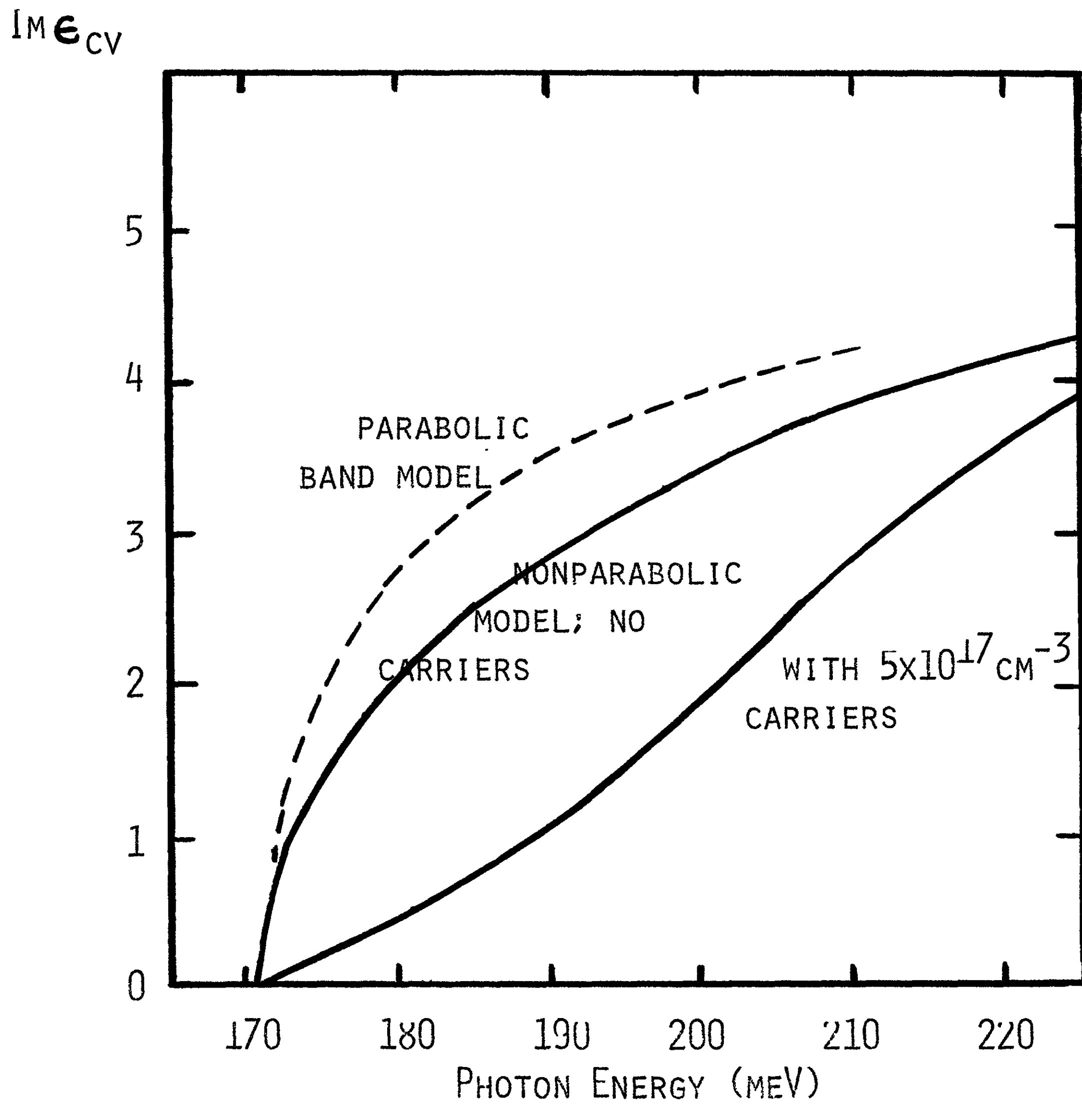

Figure 27: Frequency Dependence of Im ϵ_{cv} near the Absorption Edge

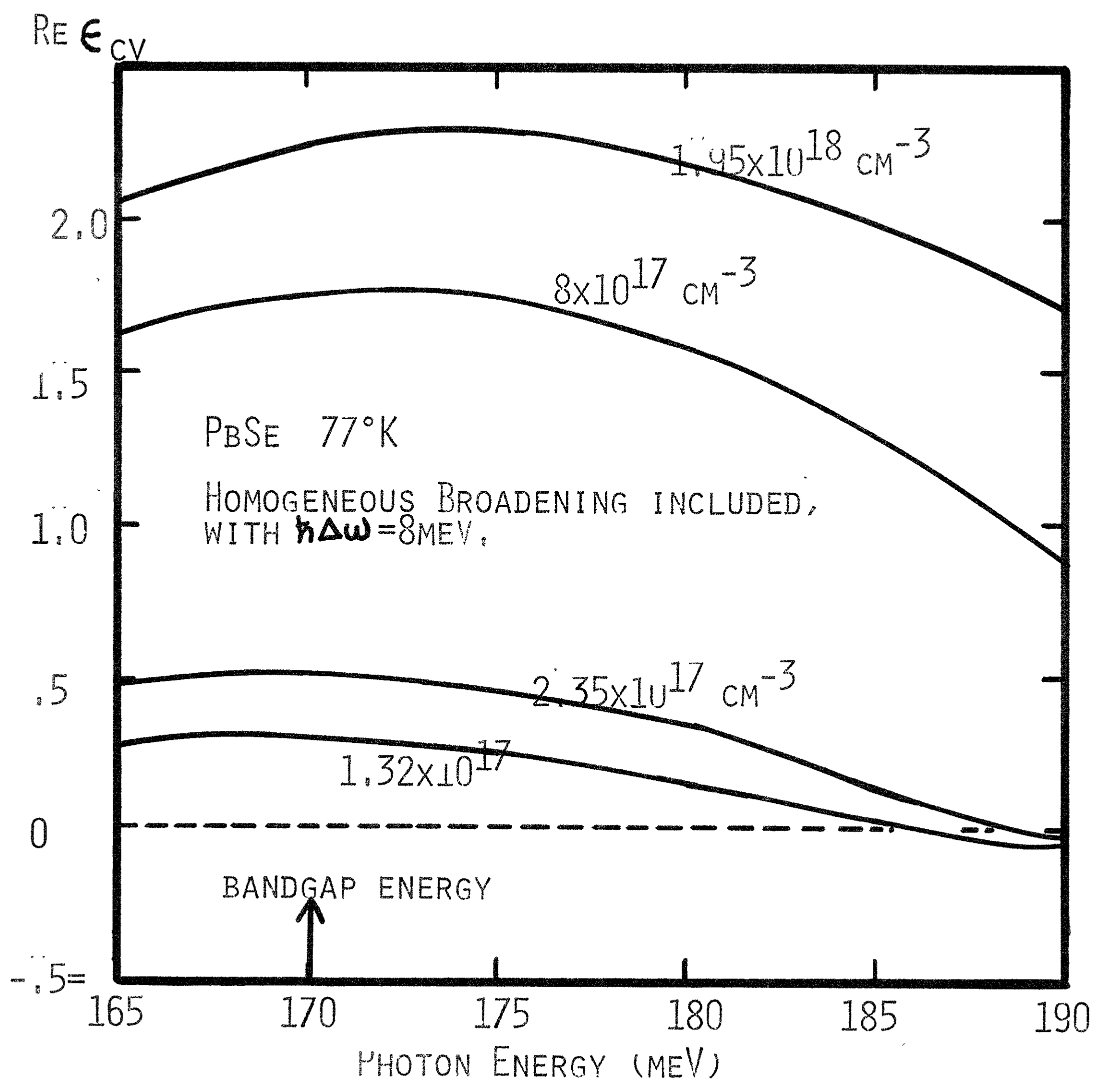

Figure 28: Frequency Dependence of Re $_{cv}$ near the Absorption Edge for various values of Carrier Concentration

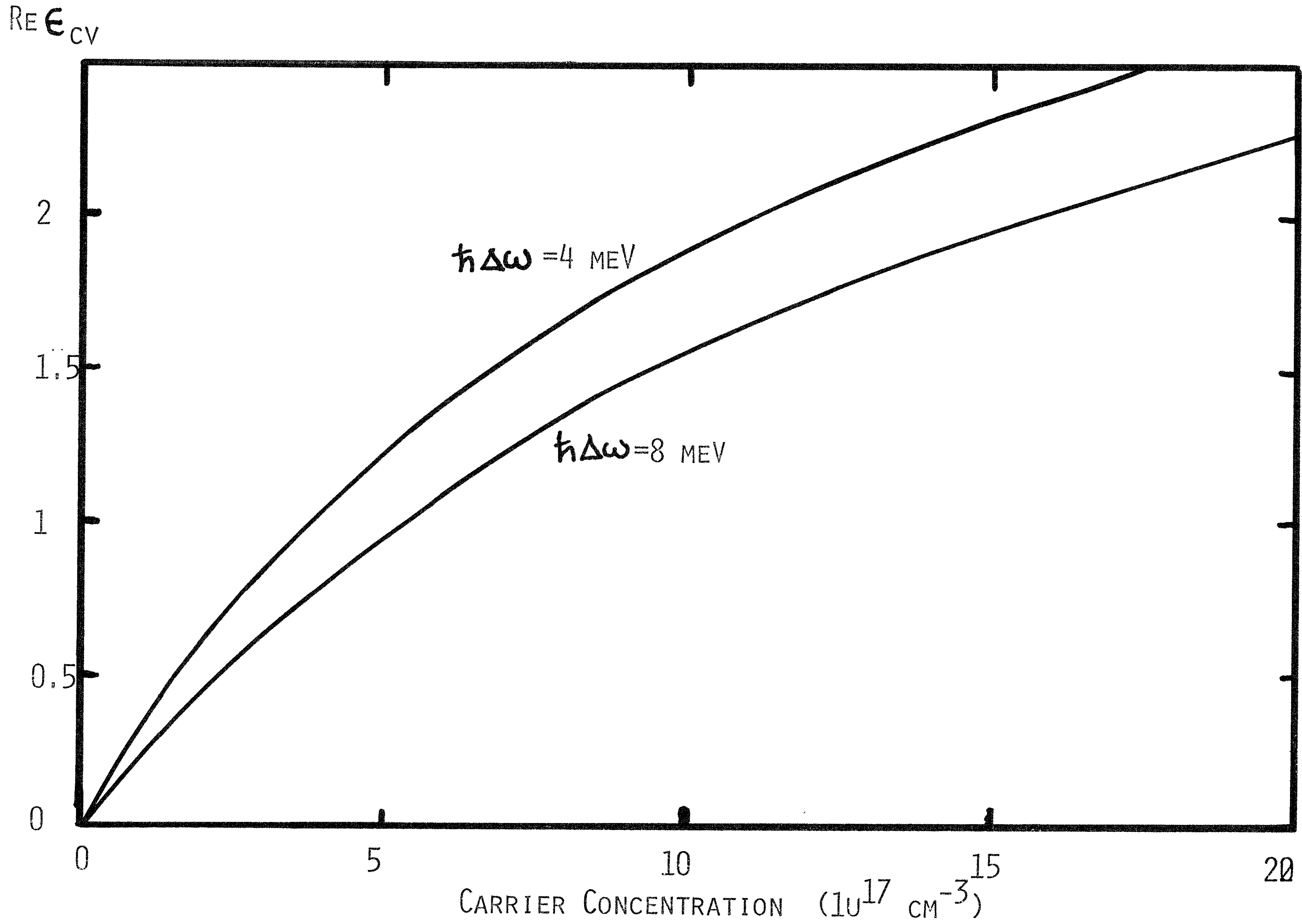

Figure 29: Variation of Re ϵ_{cv} at the Lasing Frequency with Carrier Density

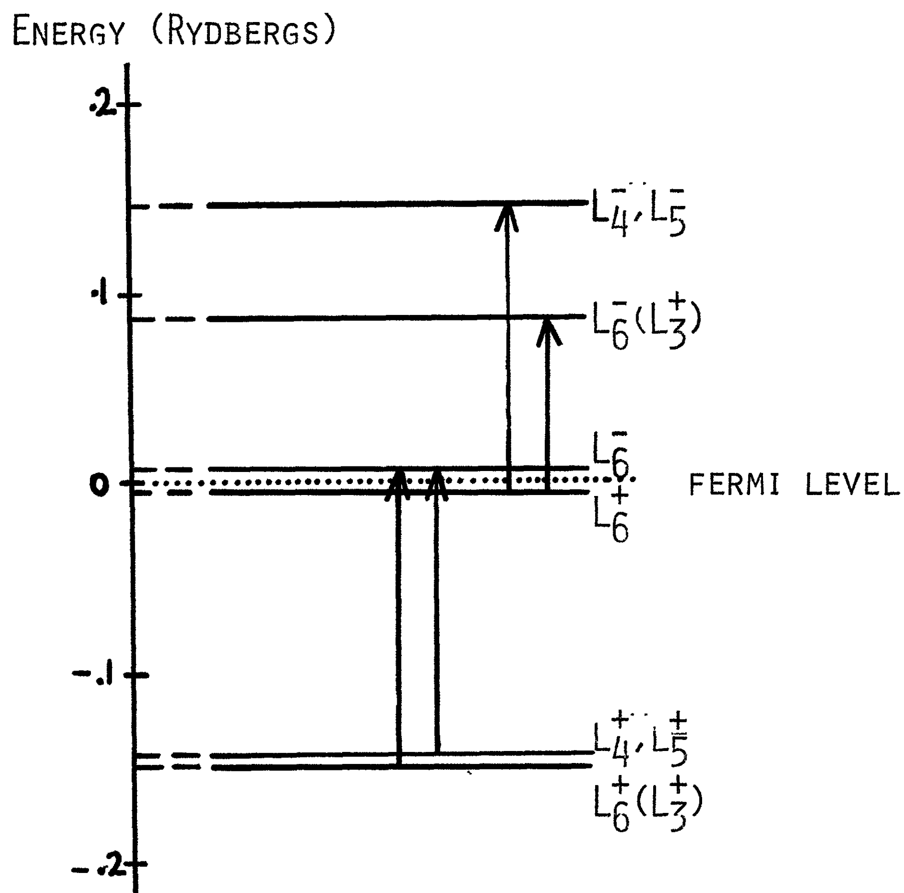

FIGURE 30: FAR-BAND RESONANCES OF INTEREST IN THE CALCULATION OF THE DIELECTRIC CONSTANT CHANGE

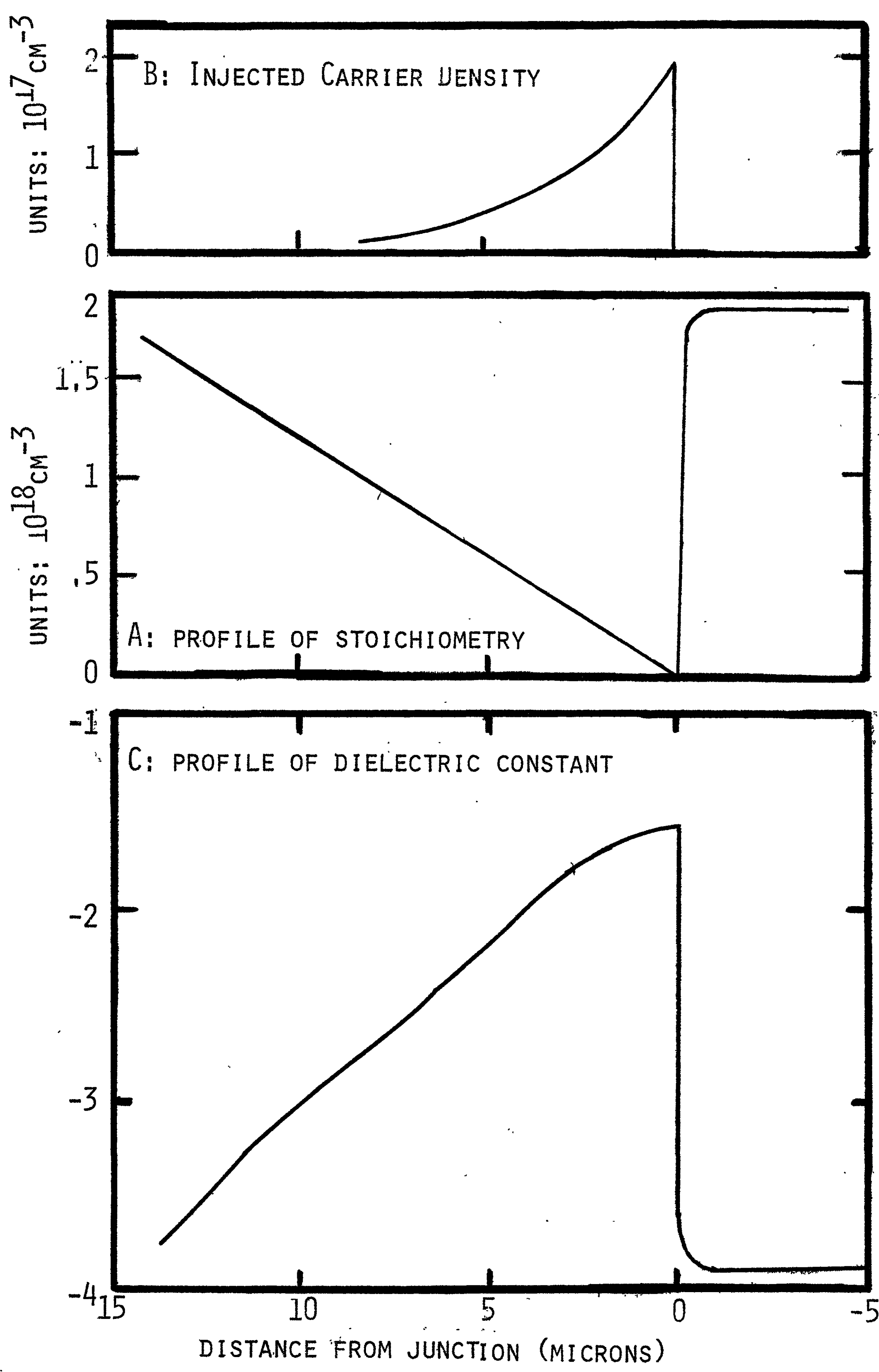

FIGURE 31: RESULTS OF MODEL I OF STOICHIOMETRY PROFILE

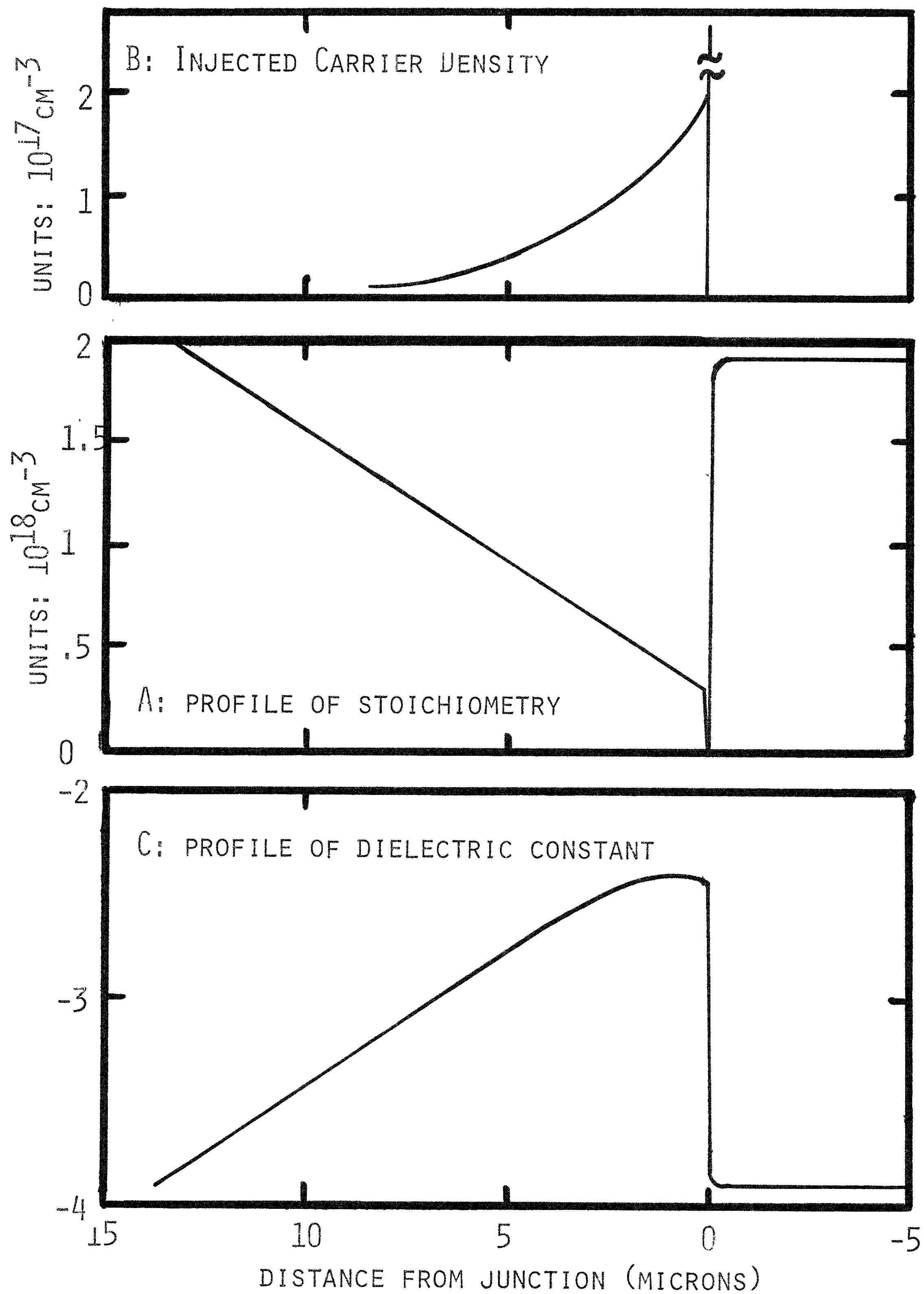

FIGURE 32: RESULTS OF MODEL II OF STOICHIOMETRY PROFILE

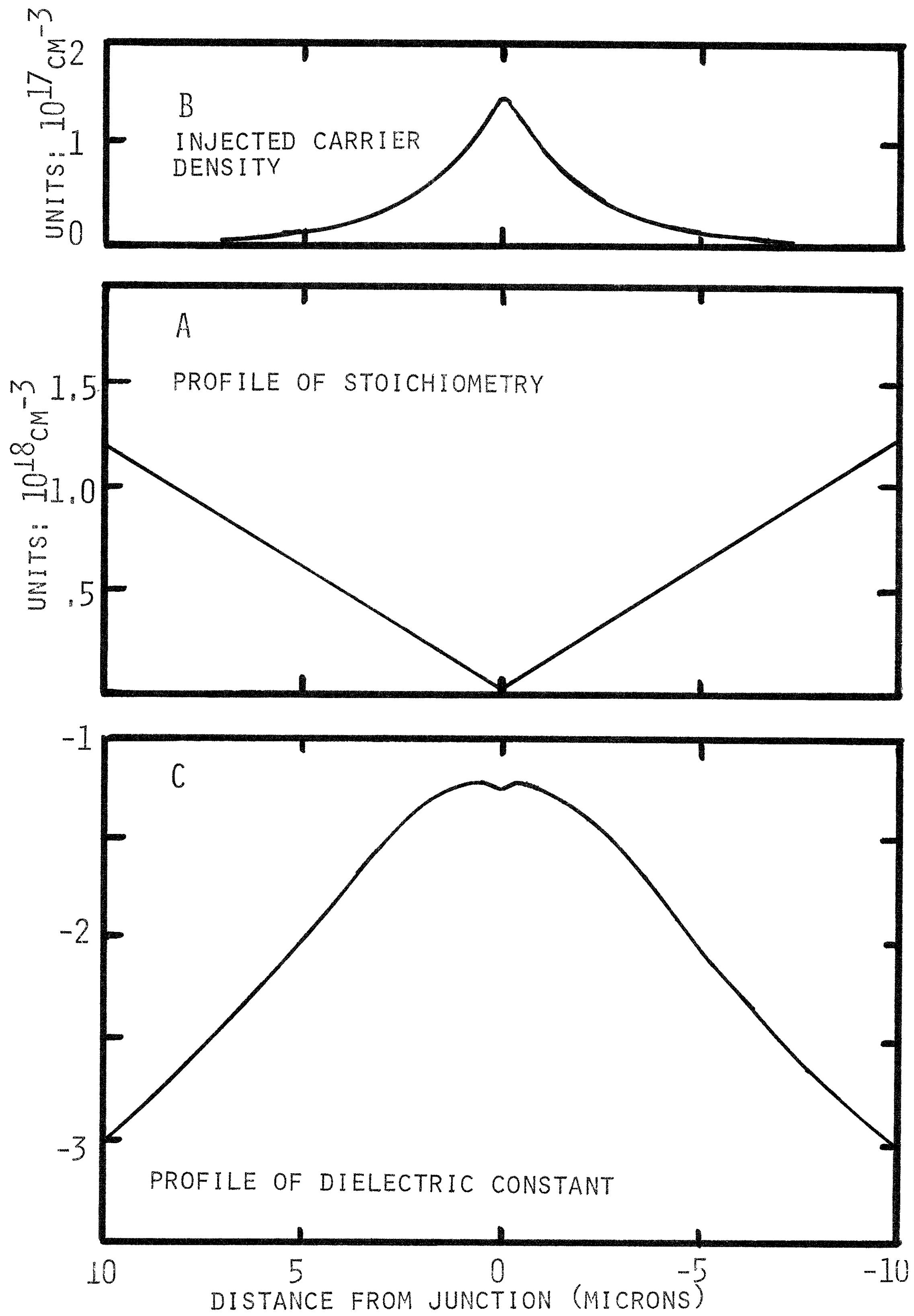

FIGURE 33: RESULTS OF MODEL III OF STOICHIOMETRY PROFILE

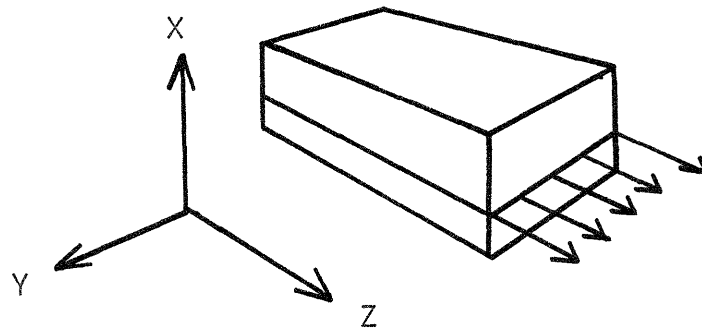

Figure 34: Coordinate System Used for Mode Calculations

Dielectric Slab Model

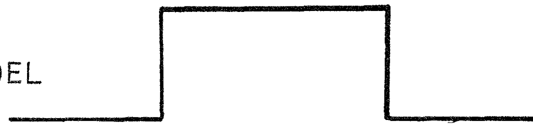

Model of Zachos and Ripper

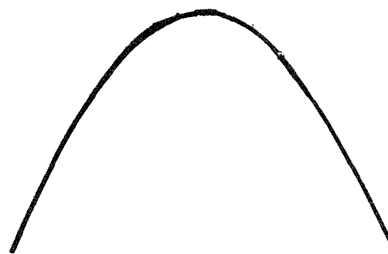

Model of This Work

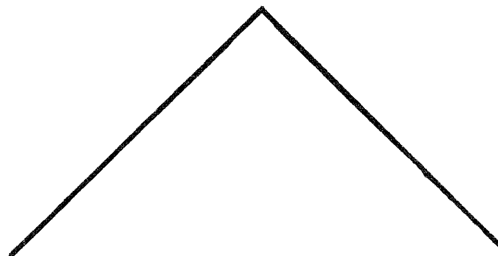

Figure 35: Comparison of Model Dielectric Profiles for Mode Calculations

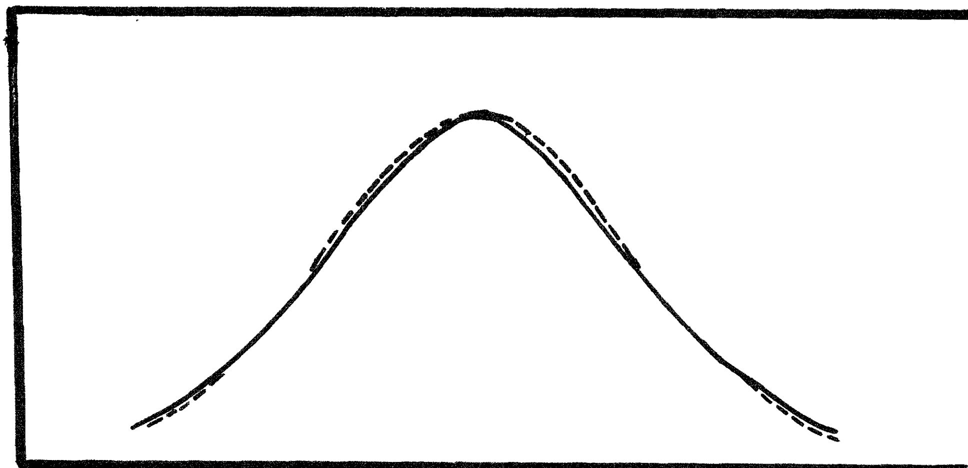

Comparison of Lowest Order Airy Mode (dark line) and Gaussian Curve (dashed line)

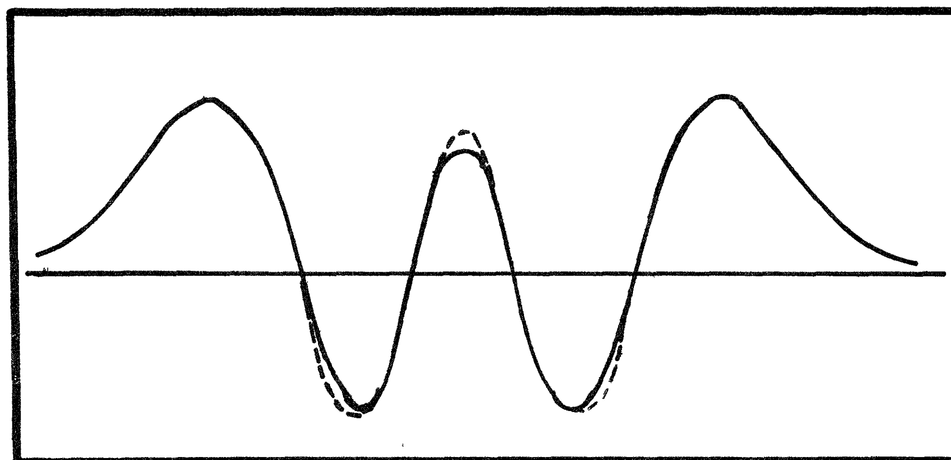

Comparison of Airy Mode and closely matched Hermite-Gaussian Mode of Order 4 (Airy Mode is Solid Line)

Figure 36: Comparison of Shapes of Airy and Hermite-Gaussian Modes

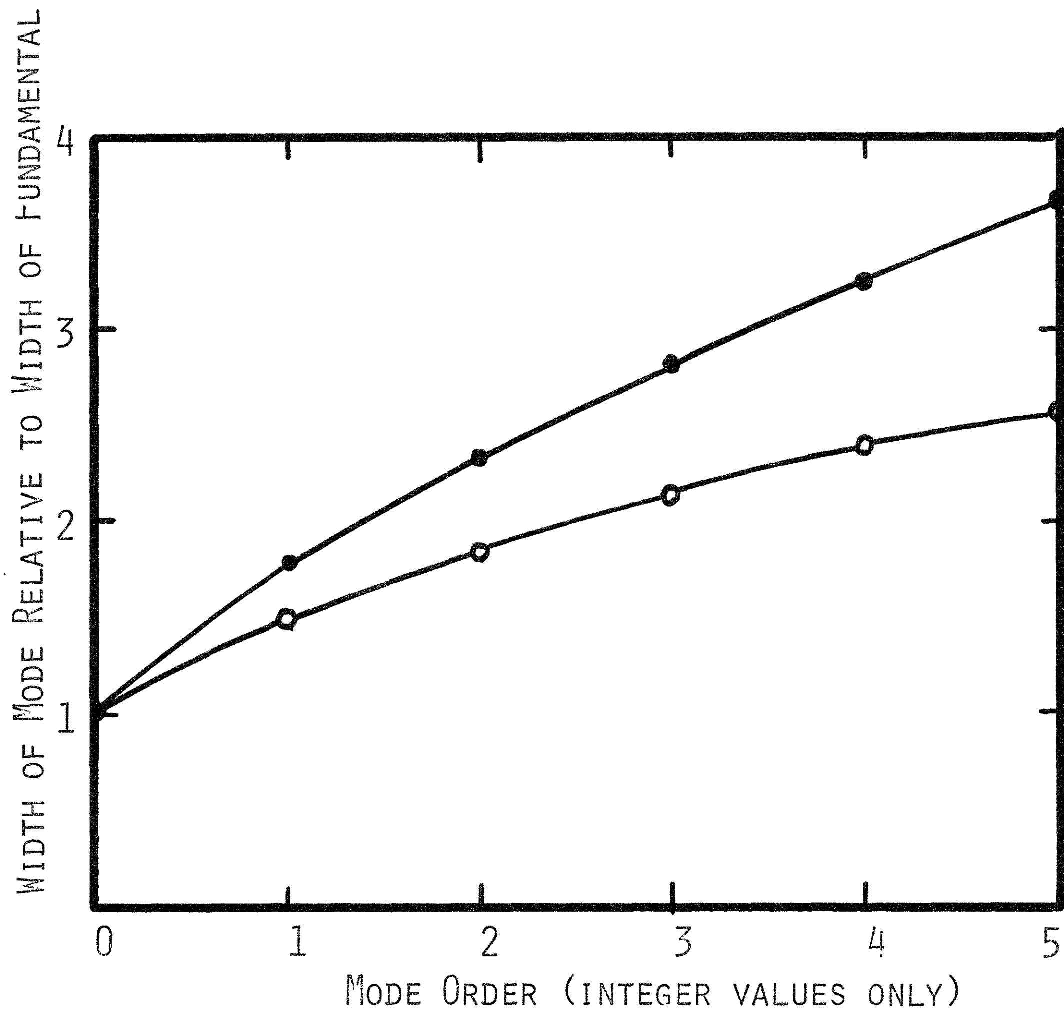

Figure 37: Variation of Mode Width with Mode Order for Airy and Hermite-Gaussian Modes

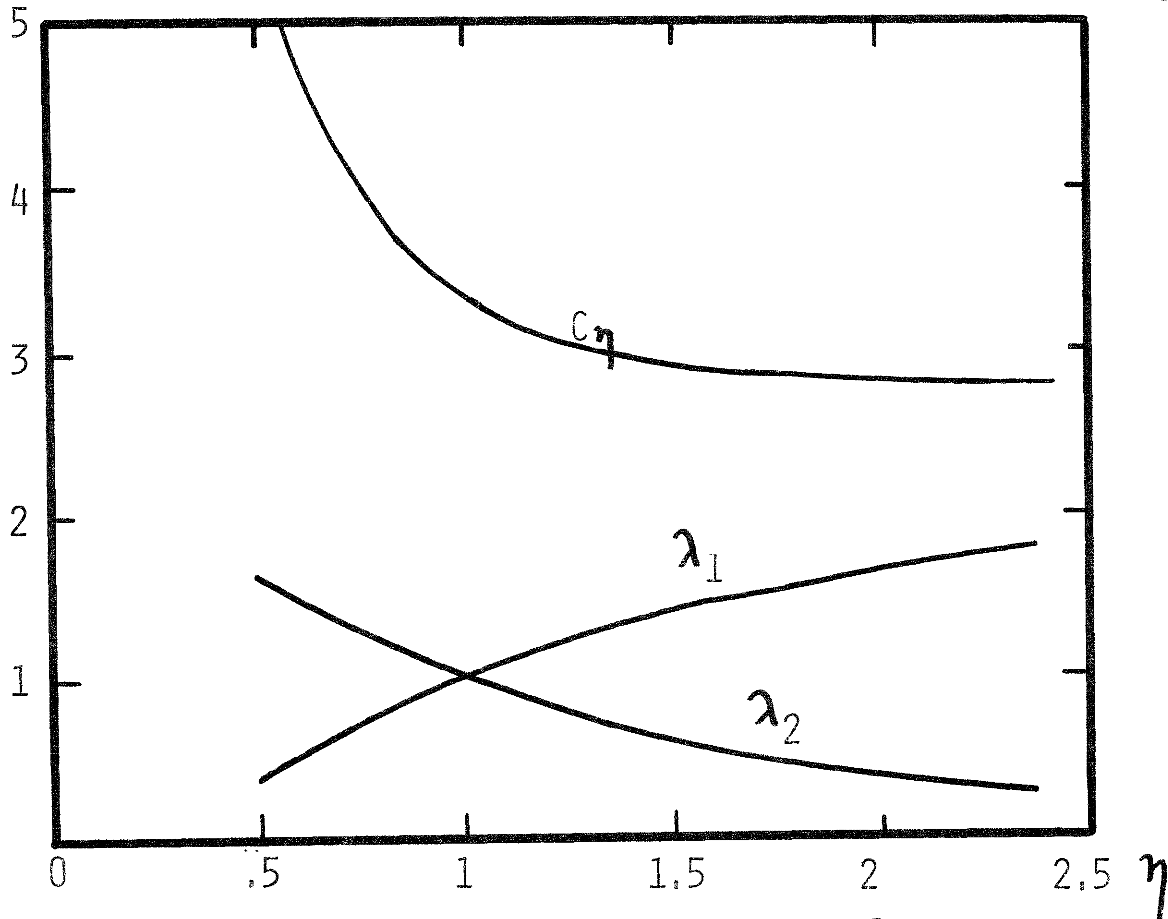

FIGURE 38: VARIATION OF EIGENVALUES λ_1 AND λ_2, AND MODE WIDTH PARAMETER C_η WITH ASYMMETRY PARAMETER η FOR ASYMMETRIC AIRY MODES

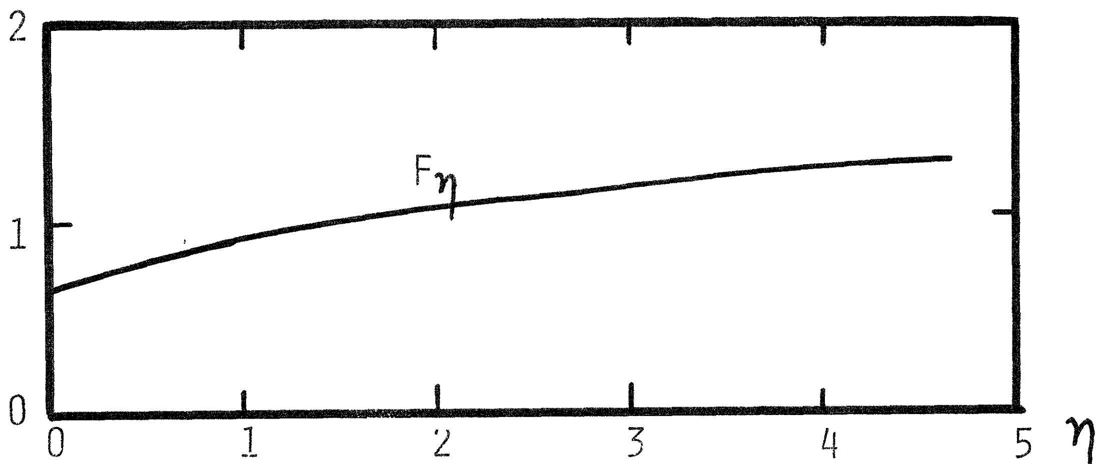

FIGURE 42: VARIATION WITH η OF PARAMETER F_η FOR CALCULATION OF FREE CARRIER ABSORPTION LOSSES

FIGURE 39: TYPICAL ASYMMETRICAL AIRY MODE SHAPES

THE DASHED LINE INDICATES THE SHAPE OF THE DIELECTRIC CONSTANT PROFILE CORRESPONDING TO EACH VALUE OF η

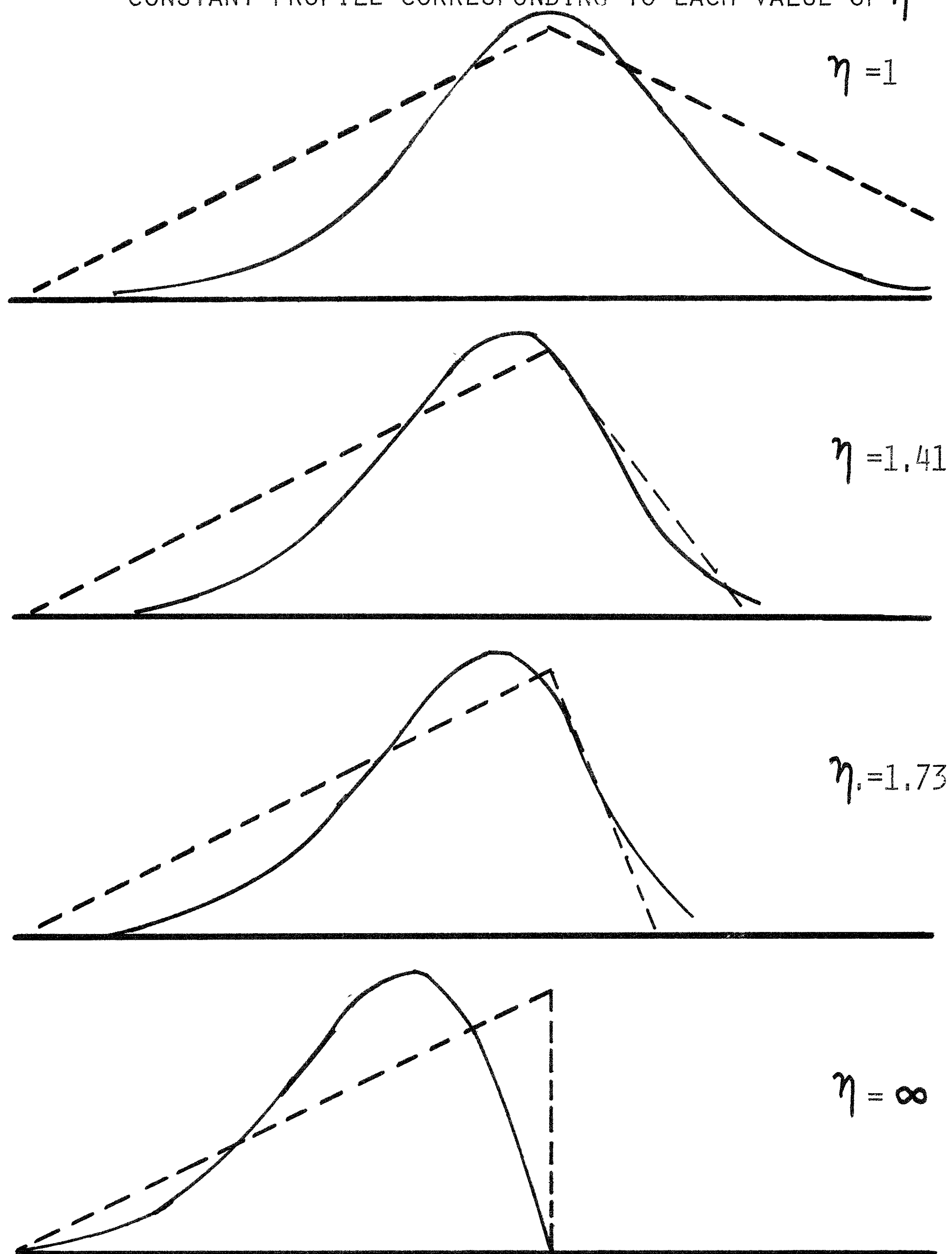

FIGURE 40: VARIATION OF FIELD AMPLITUDE REFLECTION COEFFICIENT WITH TRANSVERSE WAVEVECTOR Q_X FOR PLANE WAVES AT A PBSE-AIR INTERFACE

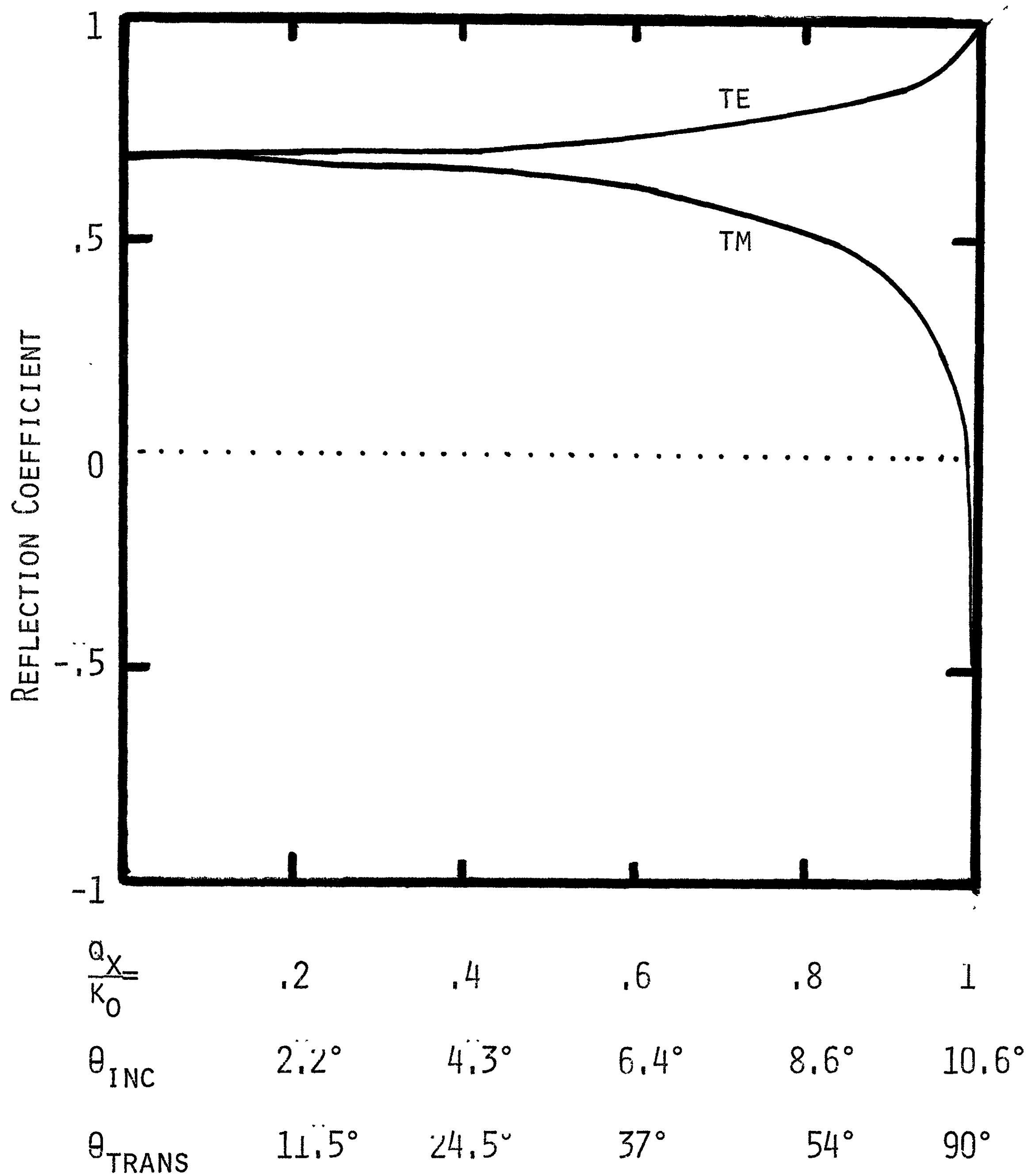

$\frac{Q_X}{K_0}=$	.2	.4	.6	.8	1
θ_{INC}	2.2°	4.3°	6.4°	8.6°	10.6°
θ_{TRANS}	11.5°	24.5°	37°	54°	90°

Figure 41: Squared Magnitude of the Fourier Transform of the Completely Asymmetric Airy Mode ($\eta = \infty$)

For comparison is shown a Gaussian curve (dotted line)

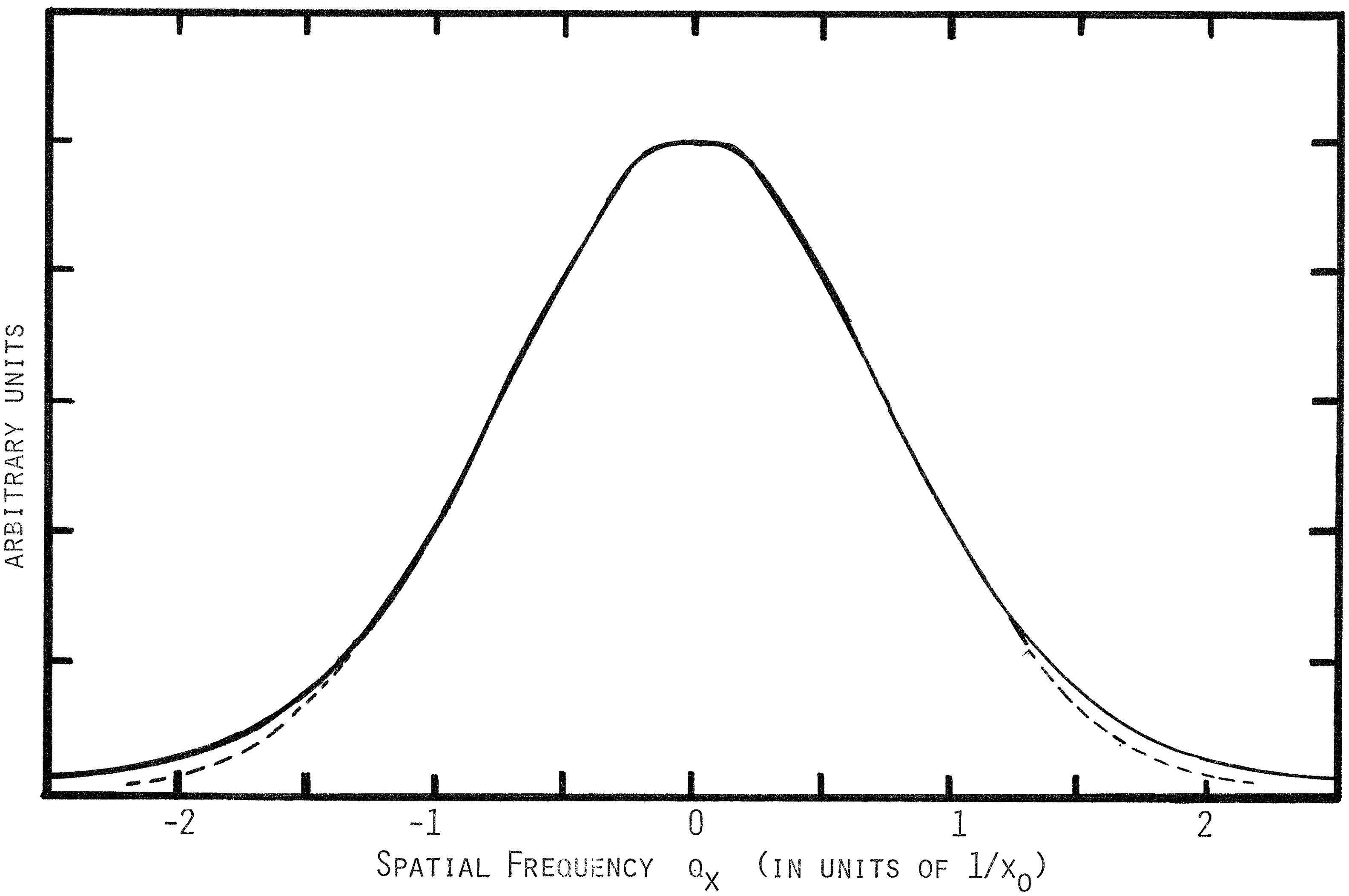

FIGURE 43: APPARATUS FOR THE MEASUREMENT OF LASER FAR-FIELD PATTERNS

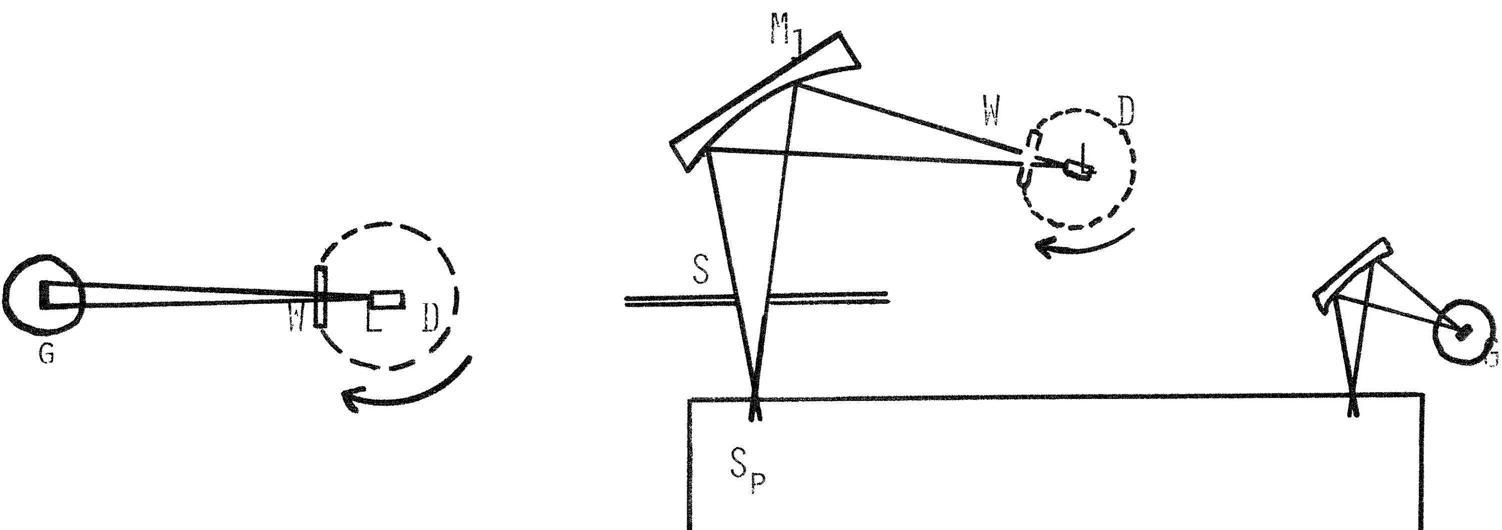

A. FOR MEASUREMENT OF TOTAL DIODE OUTPUT

B. FOR MEASUREMENT OF FAR-FIELD PATTERNS OF INDIVIDUAL MODES

D: ROTATABLE DEWAR G: GE:AU DETECTOR L: LASER M_1: TOROIDAL MIRROR
S: SLIT TO DEFINE SMALL SOLID ANGLE FOR MEASUREMENT S_p: SPECTROMETER
W: BaF_2 WINDOW

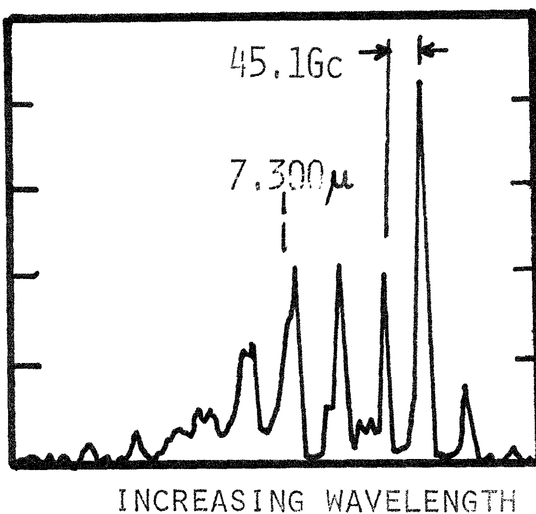

Figure 44: Typical Laser Output Spectrum. Diode was operated pulsed at 77°K.

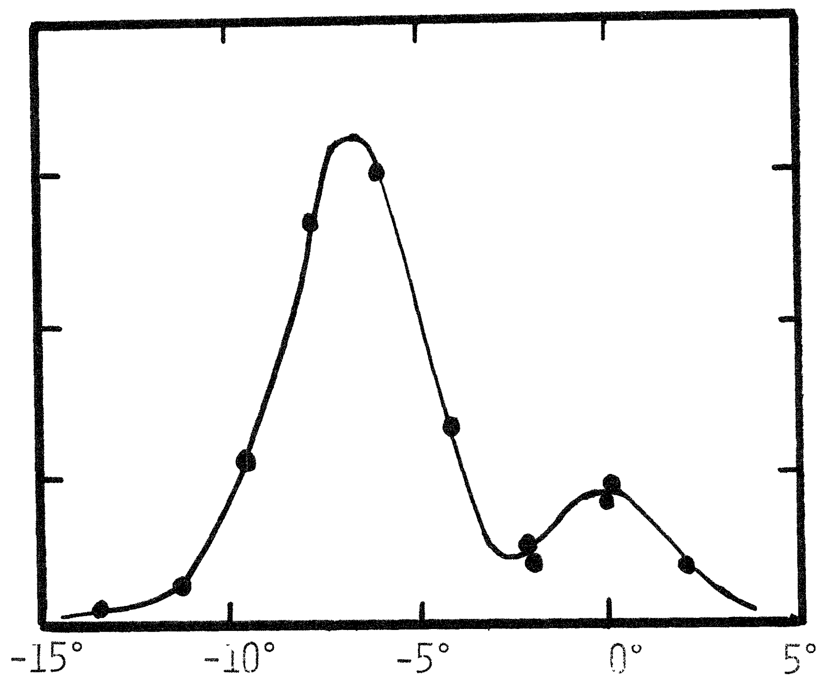

Figure 45: Typical Far-Field Pattern in Y-Z plane of Total Laser Output

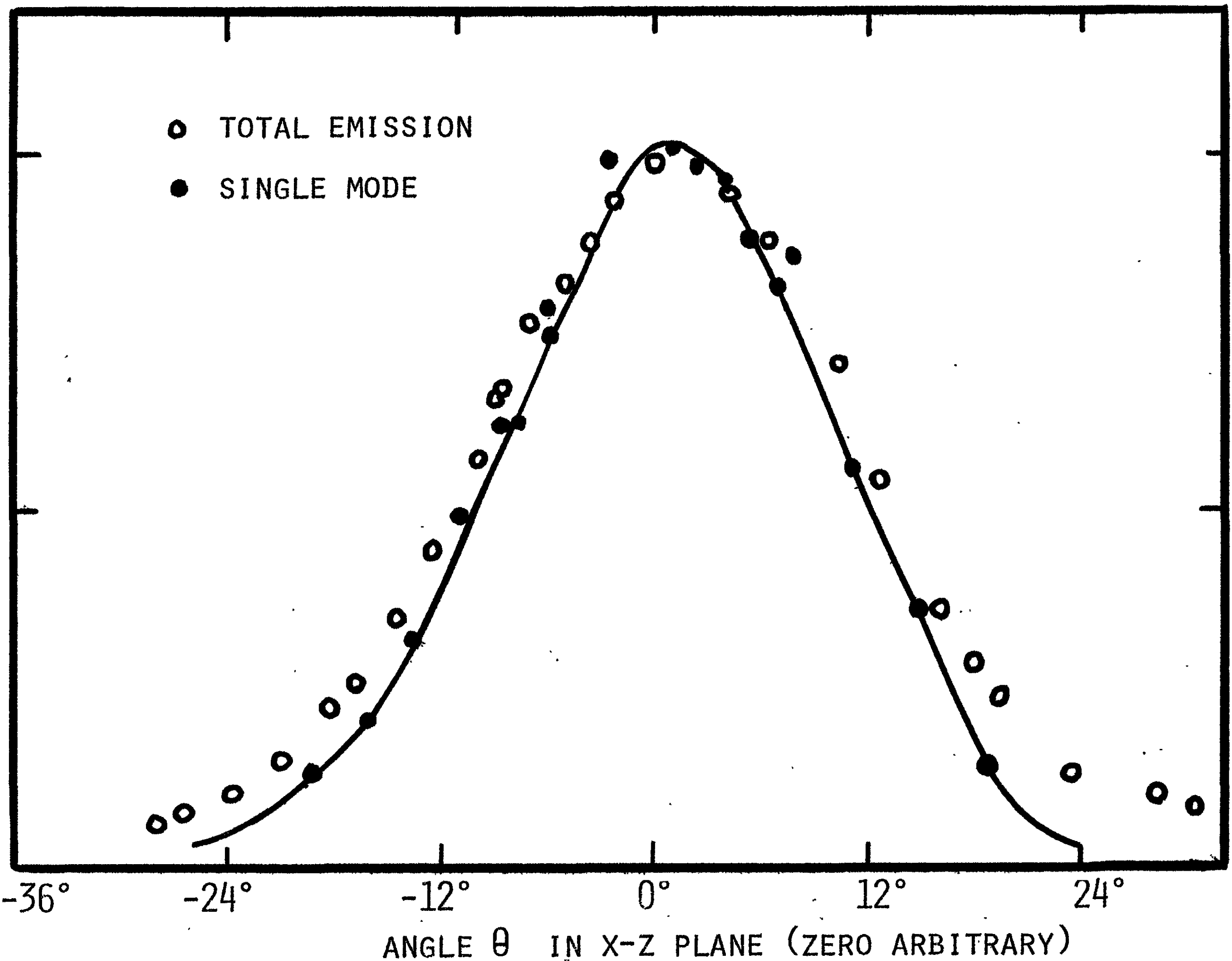

FIGURE 46: TYPICAL FAR-FIELD PATTERN OF TOTAL LASER OUTPUT IN X-Z PLANE (OPEN CIRCLES). FOR COMPARISON IS SHOWN A FAR-FIELD PATTERN MEASURED AT A SINGLE FREQUENCY SEQUENTIALLY ON THE SAME DIODE (DARK CIRCLES)

Figure 47: Total Emission x-z Plane Far-Field Patterns Taken at Different Current Levels. The tendency of the current to steer the beam is apparent.

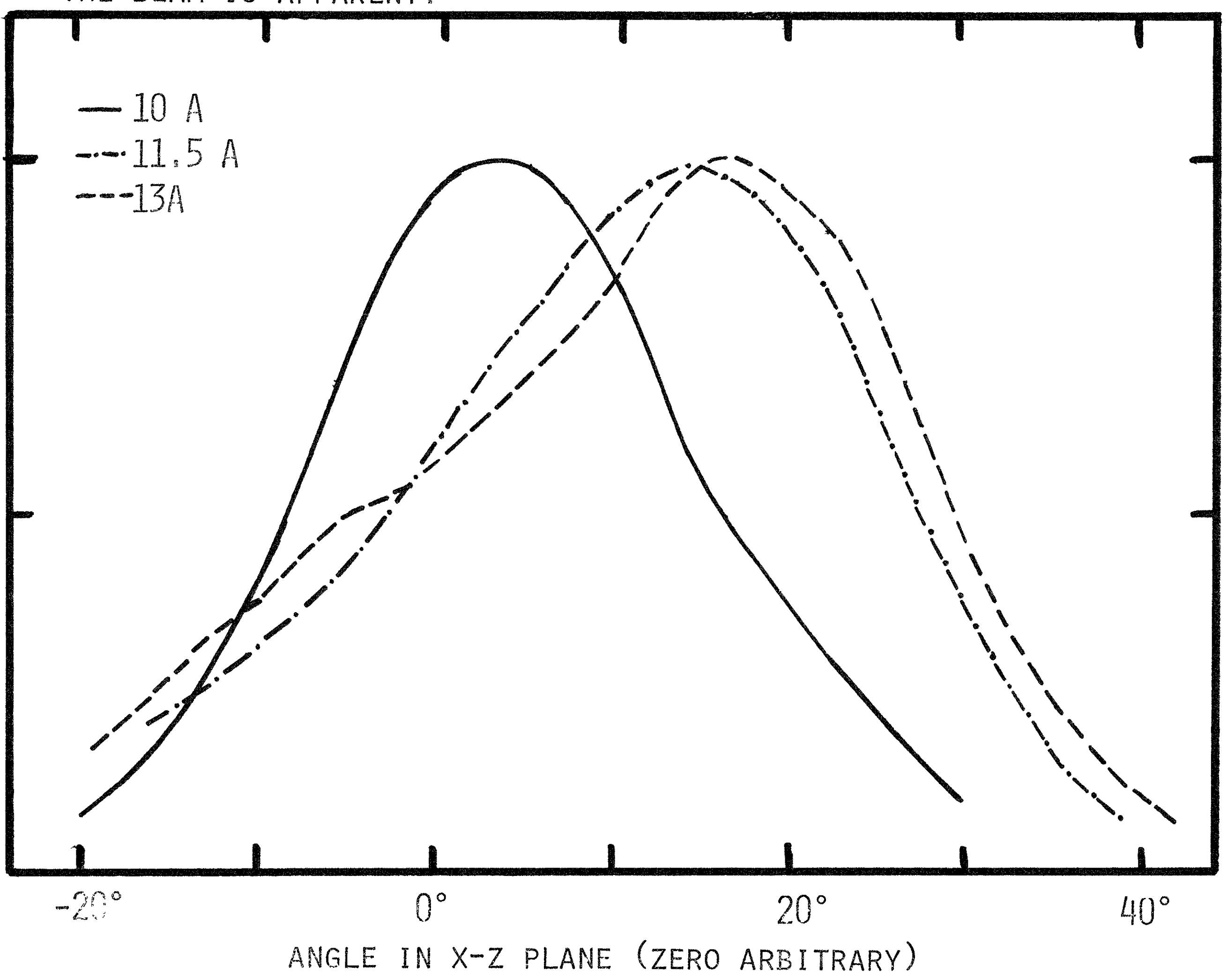

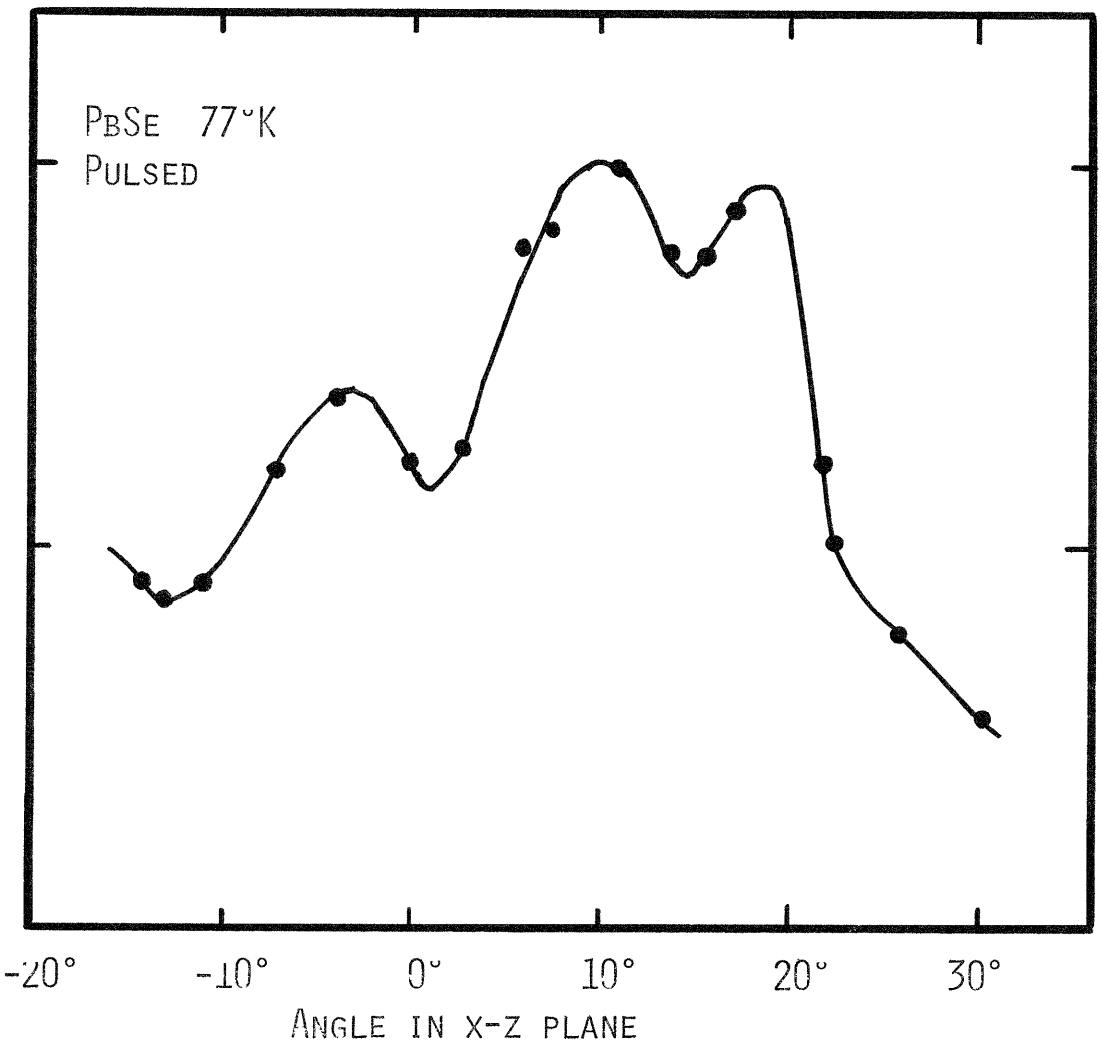

Figure 48: Typical Irregular Far-Field Pattern Corresponding to a Single Frequency.

FIGURE 49: TYPICAL REGULAR FAR-FIELD PATTERNS CORRESPONDING TO SINGLE FREQUENCIES. FOR COMPARISON ARE SHOWN GAUSSIAN CURVES.

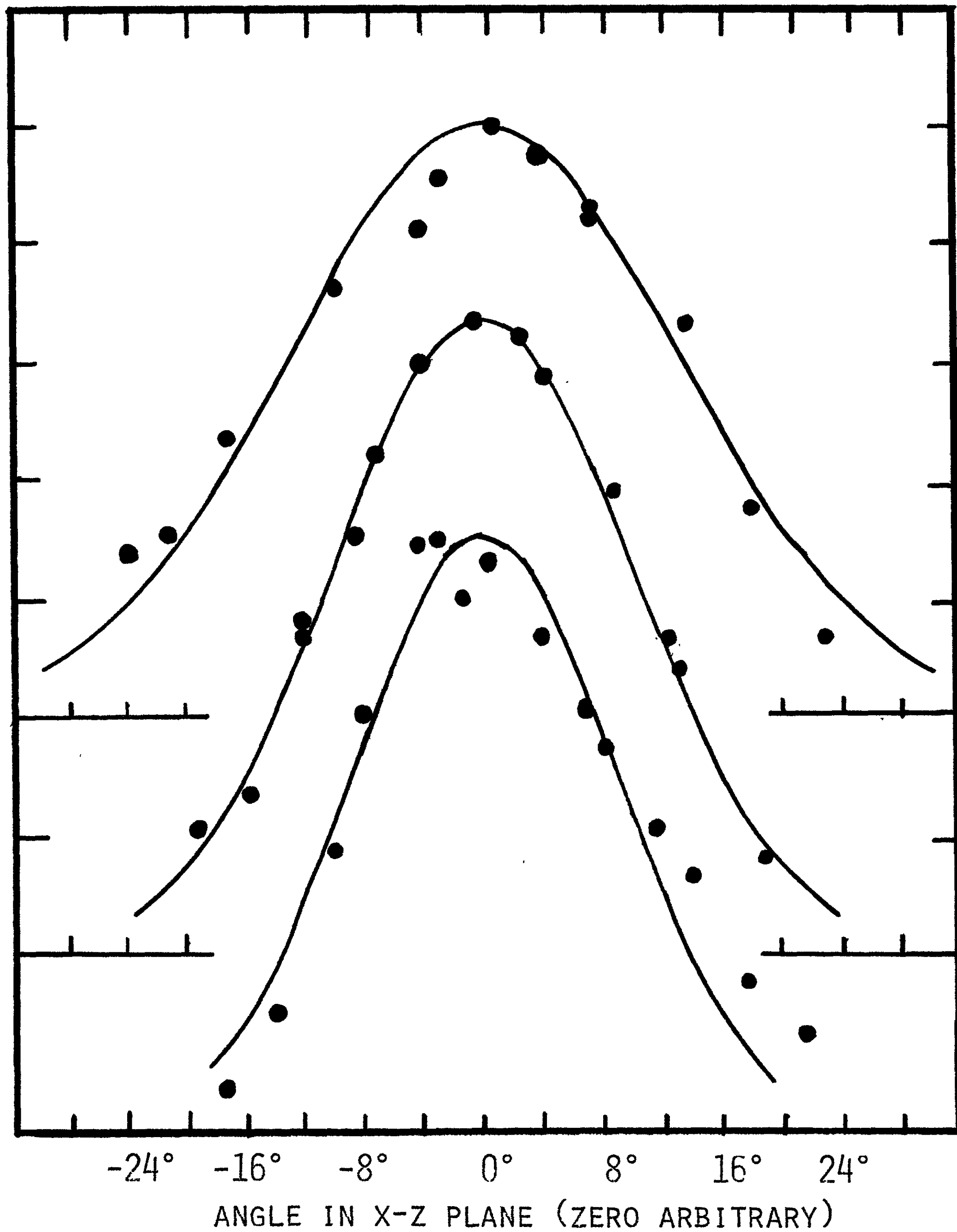

FIGURE 50: CALCULATED RELATION BETWEEN $\Delta\theta_{EQ}$ AND MODE WIDTH w_0. RELATION IS VALID FOR RADIATION OF WAVELENGTH 7.3 MICRONS.

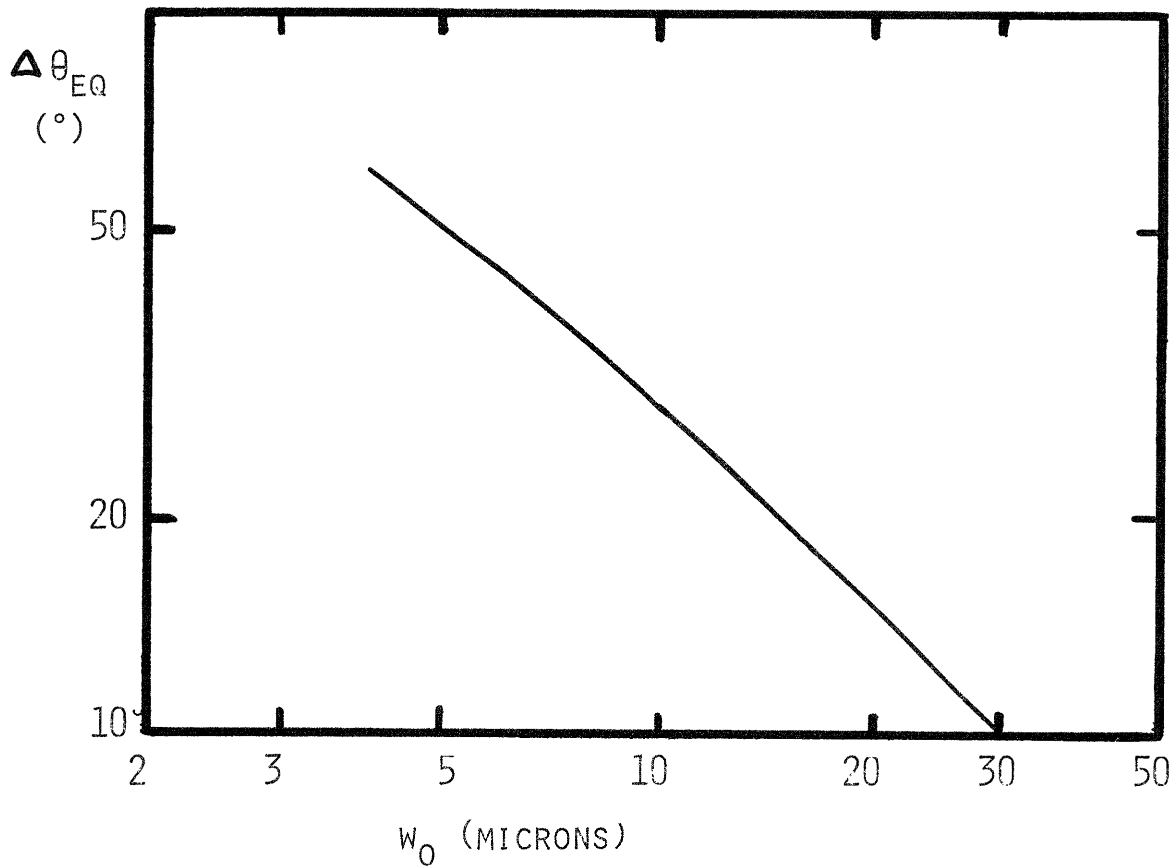

Figure 51: Measured Variation of Mode Width w_0 with Junction Depth x_J. For comparison are indicated the predicted curves based on models I, II and III.

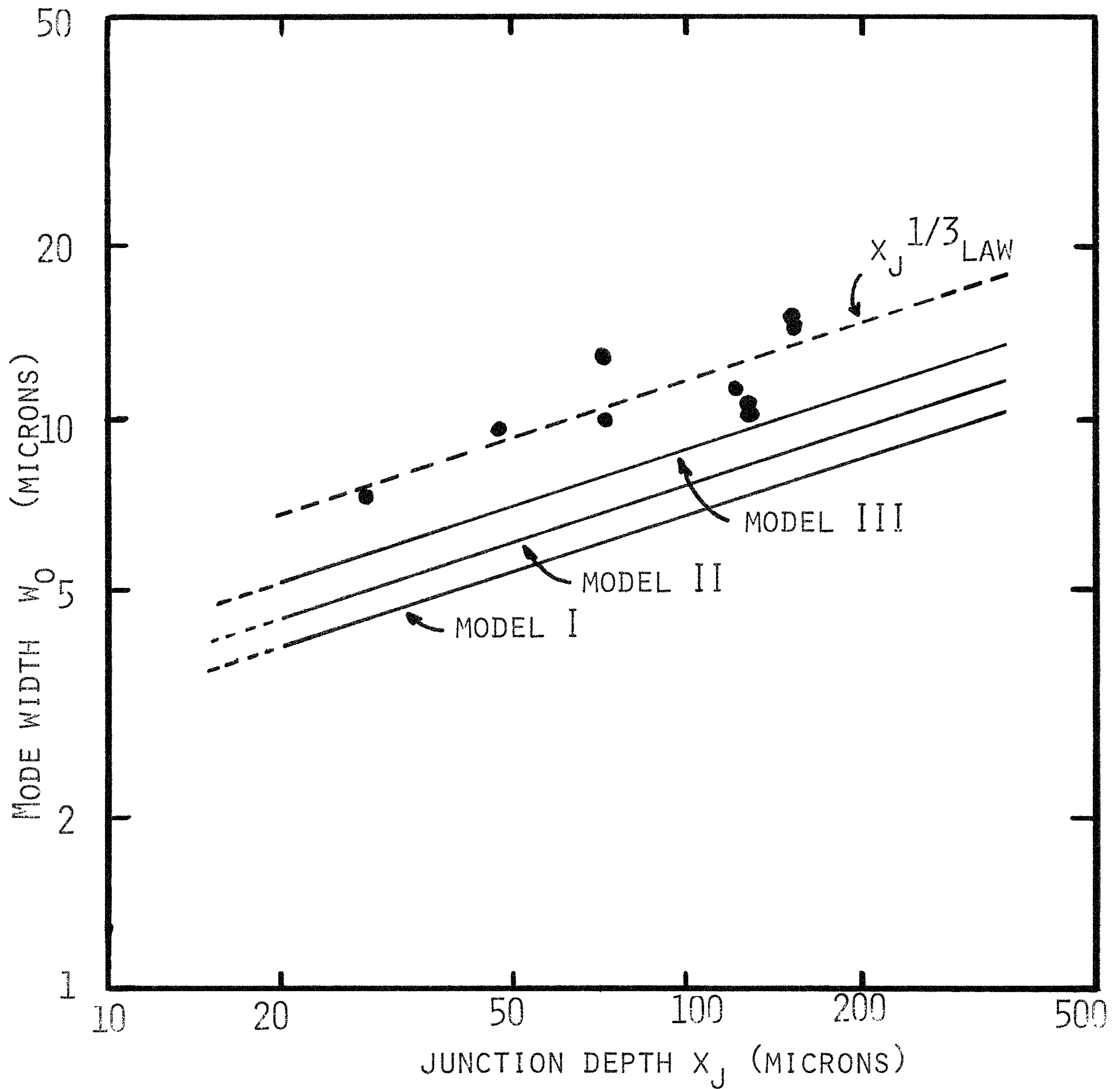

TABLE III

EXPERIMENTAL VALUES OF CHARACTERISTIC ENERGY E_s OF EXPONENTIAL ABSORPTION EDGE OF LEAD SALT SEMICONDUCTORS

Material	Carrier Concentration (cm^{-3})	Temperature (^oK)	Characteristic Energy E_s (meV)
PbS	$1.7x10^{17}$	296	8.9[a]
	$1.7x10^{17}$	220	7.1[a]
	$1.7x10^{17}$	153	6.1, 4.8[a]
	$1.7x10^{17}$	90	3.63[a]
PbTe	$2x10^{18}$	296	6.2[a]
	$3x10^{17}$	300	6.35[a]
	$3x10^{17}$	210	5.4[b]
	$3x10^{17}$	160	4.2[b]
	$3x10^{17}$	90	3.4[b]
	n.a.	296	6.0[c]
PbSe	10^{17}	296	6.2[a]

Source: a -- Prakash (Ref. 80)
b -- Kurik (Ref. 81)
c -- Scanlon (Ref. 78)

TABLE IV

CONTRIBUTIONS OF FAR-BANDS TO THE VARIATION OF WITH CARRIER CONCENTRATION

Transition	Energy[a,b]	Matrix Element[a,b,d]	$\Delta\epsilon$ [c]
$L_6^+ - L_6^- (L_3^-)$	.089	.109	4.14×10^{-3}
$L_6^- - L_4^-, L_5^-(L_3^-)$	.131	.249	2.83×10^{-3}
$L_6^- - L_4^+, L_5^+(L_3^+)$	.151	.215	1.57×10^{-3}
$L_6^- - L_6^+ (L_3^+)$	.156	.093	6.1×10^{-4}

[a] Atomic units

[b] Source: Reference 56

[c] Calculated change in when 10^{18} cm^{-3} carriers are added

[d] Matrix element is $P_{eq}^2 = 1/3(P_z^2 + 2 P_t^2)$ evaluated between states at the band extrema

TABLE V

DIELECTRIC PROFILE PARAMETERS

PbSe 77°K

	Model I	Model II	Model III
x_j	50 μ	50 μ	50 μ
β	0.171 μ^{-1}	0.130 μ^{-1}	0.2166 μ^{-1}
w_o	5.40 μ	5.91 μ	6.19 μ
w_{ocorr}	---	6.02 μ	7.04 μ
x_o	1.992 μ	2.18 μ	1.842 μ

TABLE VI

EXPERIMENTAL BEAM WIDTHS AND MODE WIDTHS

Laser	$\Delta\theta_{eq}$ (°)	w_o (μ)	x_j (μ)
A1	22.52	12.7	72.4
A2	28.42	10	72.4
B1	19.37	15.2	152.4
B2	20.15	14.4	152.4
C1	29.22	9.6	47.8
D1	27.54	10.2	127
D2	26.84	10.6	127
E4	36.9	7.35	27.94
G3	24.98	11.35	124.5

CHAPTER V
EFFECTS OF MINORITY CARRIER AND OPTICAL CONFINEMENT

V.1 Introduction

In this chapter is given an analysis of the temperature dependent laser threshold current density of diffused lasers in which minority carrier and optical confinement effects are taken into account. Experimentally measured values of threshold current density on a number of PbSe lasers are also reported for comparison with the theoretical results.

Previous analyses of diffused Pb salt laser threshold current density have been carrier out on the basis of the equation[2]

$$J_{th} = \frac{8\pi e N^2 E_g^2 d \Delta\nu \left(\alpha_T + \frac{1}{L}\ln\frac{1}{R}\right)}{c^2 h^2 \eta_{int}} \qquad \text{(V-1)}$$

where d is the "active region" width within a slab approximation, $\Delta\nu$ is the spontaneous emission linewidth, η_{int} is the internal quantum efficiency of spontaneous emission, α_T is the distributed waveguide loss (due to free carrier absorption and scattering) and the remaining symbols have standard meaning. This expression assumes a linear relationship between gain and current density, which is known to be inadequate at other than low temperatures.[55] In addition the effect of carrier confinement is not properly included, since within the slab model carrier distributions and gain are assumed homogeneous over a finite width (d), and optical mode confinement effects are not taken explicitly into account.

Effects of optical and carrier confinement on laser threshold current density may be qualitatively understood on the basis of the

following considerations:

(i) It may be readily shown that the mode gain coefficient G_m is given approximately by

$$G_m = \frac{\int g(x) |\psi_m(x)|^2 dx}{\int |\psi_m(x)|^2 dx} \tag{V-2}$$

(This expression is identical to (IV-76), used to describe the mode losses). Here G_m is defined such that the integrated time-averaged power I_m of the waveguide mode m propagates according to

$$I_m(z) = I_m(0)\, e^{G_m z} \tag{V-3}$$

in an infinite waveguide; g(x) is the local gain coefficient or negative absorption coefficient of the material, which varies spatially in diffused lasers in response to the spatially varying injection level near the junction. Below threshold, the local gain distribution g(x) is uniquely determined for a given structure by the current density J flowing through the junction. On the basis of (V-2) it may be seen that the mode gain G_m obtainable for a given current density J will increase if the normalized optical mode intensity is increased in the region where g(x) is largest. This will occur if the mode is better confined to the vicinity of the junctions.

(ii) The relationship between the local gain and the (local) minority carrier density is known to be a nonlinear one in semiconductor lasers.[111] At high temperatures a typical gain-minority carrier concentration curve (for fixed majority carrier concentration) is superlinear as shown in Fig. 52 (where the maximum value of the frequency-dependent gain is plotted). The shape of the curve may be understood by reference to the well-known fact that the gain is identically zero

until the separation of majority and minority carrier fermi levels reaches the lasing frequency. Because of this a threshold minority carrier density n_o exists, below which positive gain cannot be obtained. The superlinearity of the relationship has the effect that improved confinement of minority carriers leads to greater values of the mode gain G_m for a fixed number of injected carriers, as may be understood from the following example. Within the slab model, the total number of minority carriers injected may be represented by $N \sim nd$, where d is the active region thickness; similarly, the mode gain is given by $G_m \sim gd$ where g is the local gain (assuming that the optical mode width is independent of d, for simplicity). If then the relationship $g \sim n^b$ holds, it is found $G_m \sim n^b d \sim N^b d^{1-b}$. Thus if b is greater than 1 (superlinear relation) it follows that G_m increases as d decreases and N is maintained constant.

It may be remarked that at very low temperatures the relationship of g and n may be sublinear. This corresponds to the fact that upon increasing the injection level band-filling occurs and the width of the gain lineshape grows larger. Under such circumstances improvements in carrier confinement have a slight adverse effect on the threshold current density.

In this chapter, the threshold current density of diffused PbSe lasers is calculated taking into account quantitatively the above effects. The calculation is restricted to the model of symmetrically graded junctions (Model III discussed earlier) and is carried out according to the following plan:

(a) Electron and hole distributions n(x) and p(x) in the forward biased, linearly-graded PbSe p-n junctions are computed following the formalism of Chapter III. 3.

(b) The current density flowing through the junction is computed

by integrating over space the number of recombinations that occur at every point. Two models for the recombination rate will be considered in this chapter: a model with minority carrier lifetime τ independent of carrier concentration (Model A), and a model where the recombination rate is determined exclusively by radiative recombination (Model B). The latter is expected to yield a theoretical lower limit to threshold current densities obtainable (although perhaps a weak one).

(c) The local gain g(x) is computed from the calculated carrier densities at every point, following formalisms to be presented below.

(d) The mode gain G_m is computed from g(x) with the use of an approximate form of (V-2). Since it has been verified experimentally that the width of the propagating radiation mode is much larger than the width of the region where gain is appreciable, the optical intensity is approximately constant over the gain region and

$$G_m = \frac{|\psi_m(0)|^2 \int g(x)\,dx}{\int |\psi_m(x)|^2 dx} \qquad \text{(V-4)}$$

It is convenient to consider the integrated gain H_m where

$$H_m = \int g(x)\,dx \qquad \text{(V-5)}$$

which is independent of mode confinement properties of the junction in this approximation. The mode gain G_m is then given by

$$G_m = \frac{H_m}{w_\ell} \qquad \text{(V-6)}$$

where w_ℓ is the equivalent width of the lasing mode defined by

$$w_\ell = \frac{\int |\psi_m(x)|^2 dx}{|\psi_m(0)|^2} \qquad \text{(V-7)}$$

(e) The threshold value of current density is taken to be that value which corresponds to mode gain G_m equal to the mode losses for the laser, whose calculation is described in Chapter IV. 4.

In what follows, the model used to calculate the local gain is first described (Section 2), after which theoretical results for G_m vs. current density and threshold current density vs. temperature are presented (Section 3). Finally, the dependence of threshold current density measured experimentally on several diodes is presented for comparison with the theory.

V. 2 Models for Gain Calculation

The local gain $g(\omega, x)$ is defined to be the negative of the local value of the (power) absorption coefficient of the material, a quantity that is less than zero at energies near the band edge in semiconductors with population inversion.

The calculation of the gain may be readily carried out if it is assumed that the band structure corresponds to that of defect free, intrinsic material at T=0 and that k conservation holds in radiative transitions. Under such circumstances its magnitude is given by the

well-known formula for the absorption coefficient in direct bandgap semiconductors,[112] which when applied to PbSe yields the expression:

$$\alpha = \frac{2 M_v e^2 P_{cv}^2 m_d^{3/2} (\hbar\omega - E_g)^{1/2}}{N c m^2 \omega \hbar^3} \qquad \text{(V-8)}$$

Equivalently, the absorption coefficient may be obtained from Equation (IV-12) of Chapter IV-3 after noting

$$\alpha = \frac{2\pi \, \mathrm{Im}\,\epsilon}{N\lambda} \qquad \text{(V-9)}$$

Effects of band nonparabolicity on the frequency dependence of the gain may be safely neglected, since the energy range of interest is very near the band edge.

It is known, however, thet perturbations to the perfect crystal potential that exist in real materials affect strongly the energies of the slow-moving electrons close to the band-edge, and cause modifications to the band-edge density of states and the k conservation requirement.[55] The gain magnitude and lineshape, particularly at low temperatures, is very sensitive to these perturbations, much more so, for example, than the dielectric constant dispersion considered in Chapter IV. 3, since the gain is governed primarily by those states lying very near the band-edge. In p type or compensated GaAs, numerous studies have indicated that realistic computations of the gain at a given injection level must take into account the formation of bandtails and the relations of k conservation.[55,113] Appendix C contains a discussion of some of the effects of the perturbations in the case of PbSe. It is shown that even for high defect densities the extent of bandtailing is slight, and in any case the method of p-n junction preparation for the lasers used in this study probably leads to low defect densities in the vicinity of

the p-n junction, since the acceptor-like defects introduced annihilate the donor-like defects of the substrate rather than merely compensating them. Consequently it will be assumed for the gain calculation that the states involved in the transitions are nonlocalized and bandlike, and that k conservation holds.

It may be remarked that while the assumed absence of bandtails in PbSe makes the gain calculation very much easier, it may be detrimental to the high temperature performance of the lasers. It has been argued that for GaAs laser the formation of bandtails with comparatively low densities of states greatly facilitates the achievement of population inversion.[114]

Effects of the perturbing potentials established by defects, phonons and electron-electron interactions may be included in the present model by allowing homogeneous broadening of the gain lineshape with a constant lifetime for all states. A similar ad hoc inclusion of the perturbation effects was used in the dielectric constant calculation in Chapter IV. In that case, however, it was most important to allow for the finite lifetime of states very far from the bandedge in comparatively heavily doped material, so that the best-fit lifetime figure in that calculation may be expected to be different from the one to be used for gain. In particular, scattering events with the emission of optical phonons are not allowed at low temperature for carriers near the bandedge in lightly doped materials. Some theoretical values for lifetime of electron states in PbSe are given in Appendix C. However, due to the numerous uncertainties of the calculation, the magnitude of the broadening to be included will be regarded here as a variable parameter.

Although the Lorentzian lineshape appropriate to homogeneous broadening is used here, it is expected that this formalism also may take into account inhomogeneous broadening present in the lasers.

Such broadening may be caused by spatially varying stresses impurity content or temperature, or nonplanarity of the junction.

With the inclusion of the broadening, the gain is given by

$$g(\omega, x) = \frac{\Delta\omega}{\pi} \int \frac{g_0(u, x)\, du}{(\omega - u)^2 + \Delta\omega^2} \qquad \text{(V-10)}$$

V. 3 Analysis of Threshold Current Density

It is convenient to use dimensionless variables in the calculation of the integrated gain H_m. With the use of these quantities, relationships may be obtained that are applicable to all lead salt lasers, and for all temperatures and values of the junction grading parameter a. As noted earlier however, the analysis is restricted to junctions that are symmetrically graded (which corresponds to Model III of the PbSe profile as discussed in Section II. 4(v)).

The dimensionless junction variables introduced in Section III. 3 will be used here; in addition the following quantities are defined:

$$u = \frac{\hbar\omega - E_g}{2KT} \qquad s = \frac{\hbar\Delta\omega}{2KT} \qquad \text{(V-11.1)}$$

$$y_c = \frac{\epsilon_{fn}}{KT} = \theta_n + \Psi \qquad y_v = \frac{\epsilon_{fp}}{KT} = \theta_p - \Psi \qquad \text{(V-11.2)}$$

$$\gamma_0(u) = \sqrt{u}\left(\frac{1}{1 + \exp(u - y_c)} + \frac{1}{1 + \exp(u - y_v)} - 1\right) \qquad \text{(V-11.3)}$$

$$\gamma_s(u) = \frac{s}{\pi} \int \frac{du_o \, \gamma_o(u_o)}{(u-u_o)^2 + s^2} \tag{V-11.4}$$

$$h_{mo} = \int_0^\infty \gamma_o \, dz \qquad h_{ms} = \int_0^\infty \gamma_s \, dz \tag{V-11.5}$$

$$\mathcal{J}_A = \int_0^\infty \rho(z) dz \qquad \mathcal{J}_B = \int_0^\infty \frac{\rho(z) dz}{1 + \sqrt{8} \exp(-y_n)} \tag{V-11.6}$$

Here u is the reduced photon energy, s the reduced broadening parameter and γ and h are reduced local gain and integrated gain, respectively. The subscripts $_s$ and $_o$ denote variables that do or do not take into account the homogeneous broadening. Corresponding dimensioned variables are given by:

$$g_{o,s} = \frac{8\sqrt{2}\, e^2 P_{cv}^2 m^{*3/2} \sqrt{kT}}{m^2 \hbar^2 c N E_g} \gamma_{o,s} \tag{V-12.1}$$

$$H_{mo,s} = \frac{16\sqrt{2}\, e^2 P_{cv}^2 m^{*3/2} \sqrt{kT}\, \mathcal{N}_d}{m^2 \hbar^2 c N E_g a} h_{mo,s} \tag{V-12.2}$$

$$J_A = \frac{2q \mathcal{N}_d^2}{\tau a} \mathcal{J}_A \qquad J_B = \frac{2q \mathcal{N}_d^2}{a \tau_{spon\ min}} \mathcal{J}_B \tag{V-12.3}$$

The current densities J_A and J_B are calculated according to different recombination models as described earlier. In Model A the lifetime of minority carriers is assumed to be constant, while in Model B only spontaneous radiative recombination is considered, and the re-

combination lifetime varies with the injection level. The approximation for τ_{spont} outlined in Section III. 2(iii) (which may be in error by 20% in some regions) is used in connection with Model B.

The units of g, H_m and J in terms of γ, h_m and $\mathcal{J}$ given in (V-12) depend on temperature, and in the case of H_m and J, on the grading parameter of the junction. The temperature dependence of the units is both explicit and implicit, through the variation of $\mathcal{N}_d$, Eg, N and m* with temperature. Units of g, H_m and J_A are shown vs. temperature in Figs. 53 and 54 for PbSe lasers, for the example of $a = 10^{17}$ cm^{-3}/μ and τ = 2 nsec.

To obtain the variation of h_m with $\mathcal{J}$, the method described in Section III. 3(ii) was used to calculate the variation of carrier densities and quasi-fermi levels near the junction for different values of $\mathcal{V}$ (reduced junction voltage) and λ^{-1} (normalized diffusion length). For each $\mathcal{V}$ and λ the appropriate integrals of (V-11. 5) and (V-11. 6) were carried out to obtain h_m and $\mathcal{J}$.

The calculation of h_m is complicated by the fact that the gain $\gamma_o(u)$ is a frequency-dependent quantity. For the purpose of this analysis it is desired to evaluate h_m at the frequency u_{max} for which h_m is maximum; u_{max} was taken to be that frequency for which the local gain $\gamma_o(u)$ was maximum at z = 0. This approximation may be justified on the basis of the following:

(a) The frequency dependence of the gain $\gamma_o(u)$ is largely independent of the quantity $D = 1/2\,(y_c - y_v)$, although it depends sensitively on $Y = 1/2(y_c+y_v)$. This may be appreciated in Figs. 55a and b, where $\gamma_o(u)$ is plotted vs. u for several values of D and constant Y. In the case of Fig. 55a (Y= .1) the gain lineshape is seen to be remarkably constant when D is varied; in Fig. 55b (Y = 5) some deviation from the rule is noticeable, although primarily for large values of D,

whose contribution to the integral of (V-11.5) is not substantial.

(b) For the case $\lambda = 0$ (limit of large μ or τ) the quantity $Y = 1/2(y_c+y_v)$ does not vary with position near the junction, since $d\theta_n/dz = d\theta_p/dz = 0$. This fact, together with (a) implies that the gain lineshape is approximately constant everywhere, and the integrated gain $h_m(u)$ has the same frequency dependence as $\gamma_o(u)$. For positive λ this argument is not strictly valid, since Y varies spatially. However, the largest contributions to the integral of (V-11.5) come from the vicinity of $z = 0$, where the gain is largest, and at this point it may be readily shown that $dY/dz = 0$.

The use of the approximation for u_{max} outlined above has the effect of slightly underestimating the value of h_{mo}, since it is evaluated here at a frequency other than the frequency of its maximum value. The error incurred increases with increasing ν and λ .

In order to evaluate the gain h_{ms} in the presence of Lorentzian broadening use was also made of the fact that the frequency dependence of γ_o is approximately independent of position over the region important in the calculation of h_m. The broadened lineshape computed from $\gamma_o(u, z = 0)$ with the use of (V-4) thus applies approximately throughout the junction region, and is the same lineshape as that of the integrated gain $h_{ms}(u)$. The effect of broadening on the lineshape of γ (or h_m) may be appreciated in Fig. 56, where $\gamma_s(u)$ is plotted for various values of s, using $y_c = y_v = 5$. As the broadening parameter s is increased, the maximum value of γ_s decreases and shifts to lower frequencies; for sufficiently large s, γ_s becomes negative everywhere. The maximum value of γ_s (and thus h_{ms}) was obtained numerically for a series of values of s and $Y = 1/2\ (y_c + y_c)$. The results are plotted in Fig. 57, where $\gamma_{s\,max}/\gamma_{omax}$ is shown vs. S/Y; γ_{smax} is the maximum value attained by $\gamma_s(u)$ -- even though

the frequency of the maximum may differ from the frequency of the maximum of $\gamma_o(u)$. The results of Fig. 57 may be used to obtain plots of h_{ms} vs. ϑ for any value of the broadening parameter s, since the graph provides the factor by which $h_{ms}(\vartheta)$ is reduced from h_{mo} (ϑ) for a given s and Y = $1/2\,\vartheta$.

The results of the numerical integrations for h_{mo} vs. ϑ and $\mathcal{J}_A$ and $\mathcal{J}_B$ vs. ϑ are given in Figs. 58a and b, for the case λ =0. The results may be combined to form a plot of h_{mc} vs. $\mathcal{J}_A$, $\mathcal{J}_B$ which is indicated in Figs. 59a and b. The log-log scale of Fig. 59a demonstrates clearly regions of sublinear and superlinear behaviour of h_{mo} vs. $\mathcal{J}$. Since the units of both h_m and $\mathcal{J}$ are rapidly increasing functions of T, it may be noted that at high temperatures, values of h_m and $\mathcal{J}$ are small at threshold and thus lie in the region where h_m varies superlinearly with $\mathcal{J}$; the converse holds at low temperatures. The linear scale of Fig. 59b shows that the behaviour of h_m vs. $\mathcal{J}$ may be characterized as having an offset current below which positive gain is unattainable.

Similar calculations of h_{mo} (ϑ) and $\mathcal{J}_A(\vartheta)$ were carried out for positive values of λ . Typical results for the variation of h_m and $\mathcal{J}_A$ with λ for constant ϑ are shown in Fig. 60. Except in the resistive regime of junction behaviour (see Section III. 3(iii)) the results indicate that lower gain as well as lower current is obtained for a constant ϑ as λ is increased. Examinations of the spatial dependence of γ_o indicated that in many cases far from the junction the gain γ_o was negative (which corresponds to the fact that the separation between quasifermi levels had dropped below the lasing photon energy).

Plots of $h_m(\vartheta)$ vs. $\mathcal{J}_A(\vartheta)$ for positive λ have the interesting feature that they very closely match the corresponding plot for λ =0. In effect, the numerical results indicate

$$\left(\frac{\partial h_m}{\partial g_A}\right)_{\upsilon} = \left(\frac{\partial h_m}{\partial g_A}\right)_{\lambda} \tag{V-13}$$

This behaviours is shown graphically in Fig. 61, where dark lines indicate the variation of h_m with g_A while υ is kept constant and λ varied; the dotted line was obtained by keeping λ constant (at zero) and varying υ . The result (V-13) has the important simplifying effect that the curve of h_{mo} vs. g_A of Fig. 59 may be interpreted as a universal curve, applicable to all values of λ . To obtain the threshold current density in the absence of broadening, the results of Fig. 59 may be used together with the equation

$$H_m(J_{th}) = w_\ell G_m(J_{th}) = w_\ell (A_m + A^{end}) \tag{V-14}$$

which restates the fact that the mode gain must equal the mode losses at threshold. Here w_ℓ is the equivalent width of the lasing mode, given by $w_\ell = 0.6267\ w_o$, and A_m and A^{end} are the distributed mode loss and equivalent end-loss coefficients for the mode of highest Q.

In this chapter the variation of threshold current density is calculated for PbSe lasers using as typical examples of the junction grading parameter the values $a = 10^{17} cm^{-3}/\mu$ and $a = 5 \times 10^{17} cm^{-3}/\mu$. The width w_o of the lasing modes at 77^oK may be obtained for such lasers by reference to the experimentally measured curve of mode width vs. x_j; the appropriate estimates are shown in Table VII. It is assumed in this work that the mode width is independent of temperature; this is reasonable since the variation of w_o with output wavelength due to the change of Eg with temperature is exactly cancelled by the λ^2 dependence of the dielectric constant change for a given number of carriers.

It neglects, however, the broadening of w_o that is expected due to the increased number of injected carriers as the threshold increases. This last effect may be taken into account over a narrow range of ΔJ_{th} with the use of the analysis of Section IV. 5(iii), at a cost of considerable difficulty in the graphical solution.

Following Section IV. 4 the mode loss coefficients have the form

$$A_m = \alpha + \beta J_{th} \qquad A^{end} = \delta \tag{V-15}$$

Values of α, β and δ for the lasers considered as examples are shown in Table VII, where a laser length of 500μ has been assumed. From (V-14)the threshold condition may be expressed as

$$h_m(\mathcal{J}_{th}) = \frac{0.6267\, w_o}{c_h(T,a)} \left[\alpha + \beta c_{\mathcal{J}}(T,a)\mathcal{J}_{th} + \delta\right] \tag{V-16}$$

where c_h and $c_{\mathcal{J}}$ are the units of H_m and J in terms of h_m and $\mathcal{J}$, respectively. In order to obtain the threshold current at a given temperature, Equation (V-16) and the relation of h_{mo} vs. $\mathcal{J}_{th}$ of Fig. 59 were simultaneously solved by graphical methods. It was found, however, that proper inclusion of the loss term proportional to $\mathcal{J}_{th}$ had a negligible effect on the outcome, so that with little error the value of $\mathcal{J}_{th}$ may be directly read from Fig. 59.

Results for the two lasers considered as examples are shown in Fig. 62a where the results obtained with Model A of the recombination rate are plotted. Model A assumes that the lifetime of carriers is independent of injection level. In the application of the model it was further assumed that the value of τ is independent of temperature, and given by 2 nsec. Over much of the temperature range examined, the

variation of J_{th} is close to a T^3 law, in accord with the result of a similar, more approximate analysis by Pikus,[115] and also with experimental observations for a number of laser systems.[12, 24] It may be shown that a T^3 dependence is the high temperature limit of the present theory if the variation of m*, Eg and N with temperature is ignored. If minority carriers were confined to a region whose thickness were temperature-independent, then it could be shown that the high temperature limit of the variation of J_{th} would follow a $T^3/2$ law, Thus, qualitatively, a factor of $T^3/2$ is introduced into the $J_{th}(T)$ relation on account of the progressive loss of minority carrier confinements as T is increased.

The behaviour of J_{th} with junction grading parameter a may be qualitatively determined from Fig. 62a. At high temperatures J_{th} is considerably lower for the laser with the higher value of a; in this regime minority carriers confinement is very effective in lowering the threshold current due to the superlinearity of h_m vs. J. At low temperatures, however, the values of J_{th} are comparable for the lasers; the analysis in fact, predicts a slightly lower J_{th} for the slowly graded laser, on account of the sublinearity of h_m vs. J in this regime.

A more precise determination of the variation of J_{th} with grading parameter a may be readily carried out with the present analysis. Curves of J_{th} vs. a at 77°K and at 10°K are shown in Fig. 63. The results reinforce the conclusion that for high temperature operation minority carrier confinement effects are of great importance, although they are not at low temperatures.

The behaviour of J_{th} vs. T for the case where the recombination rate is evaluated according to Model B(spontaneous radiative transitions only) is shown in Fig. 62b. The qualitative behaviour of the curves is the same as for the previous case; however, the calculated values of J_{th} are lower due to the assumed higher radiative efficiency. Threshold

currents increase slightly less rapidly with temperature, due to the fact that at high temperatures the radiative lifetime is somewhat larger.

A major discrepancy between the calculated curves of Figs. 62a and b, and experimental results commonly observed is the very substantial reduction of the predicted J_{th} as temperature is lowered below $20^{\circ}K$; frequently the experimental value of J_{th} is found to be nearly temperature independent below 10 to $20^{\circ}K$. It was pointed out by J.N. Walpole that a possible source of the discrepancy is the neglect of broadening in the curve of h_{mo} vs. $\mathcal{J}_{th}$.[116] Corresponding curves of J_{th} vs. T have been obtained in this work that confirm this hypothesis.

To ob tain the value of J_{th} in the presence of broadening a method similar to the graphical solution outlined above was followed, using calculated curves of h_{ms} vs. $\mathcal{V}$ shown in Fig. 64. These curves were obtained from the $h_{mo}(\mathcal{V})$ relation found earlier, together with the curves of Fig. 56 that indicate the effects of broadening for a given value of S . In connection with the use of Fig. 64 it should be noted that for a constant value of the broadening linewidth $\Delta\omega$ the value of $s = \frac{1}{2}\hbar\Delta\omega/KT$ changes with temperature. Graphical interpolation was used to find the value of $\mathcal{V}$ necessary to attain a given gain h_{ms} for a given s; the estimated accuracy of the results for J_{th} is 10%.

Results of J_{th} vs. T for a PbSe laser with $a = 5 \times 10^{17} cm^{-3}/\mu$ and the parameters listed in Table VII are shown in Fig. 65a for values of the Lorentzian linewidth $\Delta\omega$ corresponding to 2, 4, and 8 meV. Broadening of the gain shape is found to have the expected effect of altering the value of J_{th} substantially more at low temperature than at high temperature.

A similar effect is produced by increasing the value of the losses A^{m} and A^{end} used in the model. In Fig. 65b the J_{th} -T curve is shown for a laser with grading parameter a = $5 \times 10^{17} cm^{-3}/\mu$ obtained by neglecting broadening of the gain but assuming temperature independent mode loss coefficients of 100 cm^{-1} and 150 cm^{-1}.

V. 4 Measurements of Threshold Current Density

In order to test the conclusions of the preceding sections, the behaviour of J_{th} vs. temperature was measured for several diodes prepared identically except for their junction depth x_j. As detailed earlier, it is expected that the effective grading parameter a varies inversely with junction depth for these diodes.

The preparation and contacting of the diodes is described in Appendix A. In order to measure their threshold current density, the diodes were mounted on the cold finger of a Janis variable temperature dewar equipped with a BaF_2 window. Control of the diode temperature was achieved with a Cryogenics Research Model TC-103 Temperature Controller . Accurate measurement of the temperature was made with a copper-constantan thermocouple whose reference junction was immersed in liquid nitrogen. The diodes were excited by pulses of current of duration 100 nsec generated with an SKL Model 503A transmission line pulser. Their output was collected over an F/1.2 solid angle with a toroidal first-surface mirror and sensed with a Au doped Ge phtoconductive detector. The value of threshold current for a diode was obtained at a given temperature by observing the behaviour of its collected light output vs. the amplitude of the exciting current pulses. The typical shape of the observed curves of light output vs. I is shown in Fig. 66. The position of the break in the curves when plotted in log-log scales was interpreted as the value of

threshold current. To obtain the threshold current density it was assumed that current flowed uniformly over the cross-section of the device, and no filamentary behaviour occurred.

The measured values of J_{th} vs. T for diodes B_1 and C_1 are shown in Fig. 67a. The corresponding junction depths for the diodes are 48μ and 152μ, respectively; if the profile of net donor density of Model III is assumed, then their effective grading parameters are $0.41 x 10^{17} cm^{-3}/\mu$ for diode B1 and a = $1.30 x 10^{17} cm^{-3}/\mu$ for diode C1. The length of the diodes was 560μ within 5% for both devices.

The results show qualitatively many of the features described earlier; at low temperature the behaviour of the diodes is nearly equivalent, while at high temperature the most sharply graded diode has the lowest threshold current density. Above $60^{o}K$, the two curves are nearly parallel on the log-log scale, indicating an approximately constant factor of improvement of about 1.8 for the diode with the shallower diffusion.

Quantitative comparison of the relative improvement predicted by theory and achieved experimentally for diodes Bl and C1 is probably unjustified, since the threshold current density is sensitive to many parameters that may differ between the two diodes. Although they were fabricated from the same slice of starting material, it is possible that the effective minority carrier recombination lifetime was different for the two devices. The role of minority carrier confinement effects is evident, however, from the different temperature dependences of J_{th} for the diodes.

Both diodes display the feature that J_{th} is relatively independent of temperature below $15^{o}K$, and thus disagree with the theoretical loss values. In Fig. 67b the predicted curves which take broadening into account are shown for comparison with the experimental curves. The

theoretical curve based on $\hbar\Delta\omega = 8$ meV is in remarkably close coincidence with the experimental variation of diode B1. This agreement is probably fortuitous, since the grading parameter a used to obtain the curves has the value 5×10^{17} cm^{-3}/μ , while on the basis of Model III the value of a for diode B1 was 0.41×10^{17} cm^{-3}/μ. The analysis of threshold current density based on donor profile Models I and II has not been carried out; it is possible that similar J_{th}-T curves would result, except that the effective grading parameters a should be calculated differently than required by the assumption of Model III. In any case, the agreement suggests the fact that for these diodes a broadening mechanism is effective which is characterized by a linewidth of 4 to 8 meV. This linewidth is in agreement with the number used earlier to compute the broadening of the absorption edge; however, it is somewhat larger than values estimated on the basis of the lifetime of states lying very near the bandedge. The detailed course of the broadening is thus unknown. It is possible that good fits to the experimental J_{th}-T curves may be obtained by considering somewhat smaller linewidths, but substantially larger mode loss coefficients as described earlier. Such detailed fits were not carried out in this work.

The very reasonable agreement between theoretical values of J_{th} and the observed results supports the fact that the analysis of Section V. 3 contains most elements necessary for the consideration of the diodes fabricated in this study. It further indicates that if filaments formed in the junction region their size was of the order of magnitude of the laser width (which was near 200μ for lasers B1 and C1).

Figure 52: Typical Variation of Local Gain with Injected Carrier Density

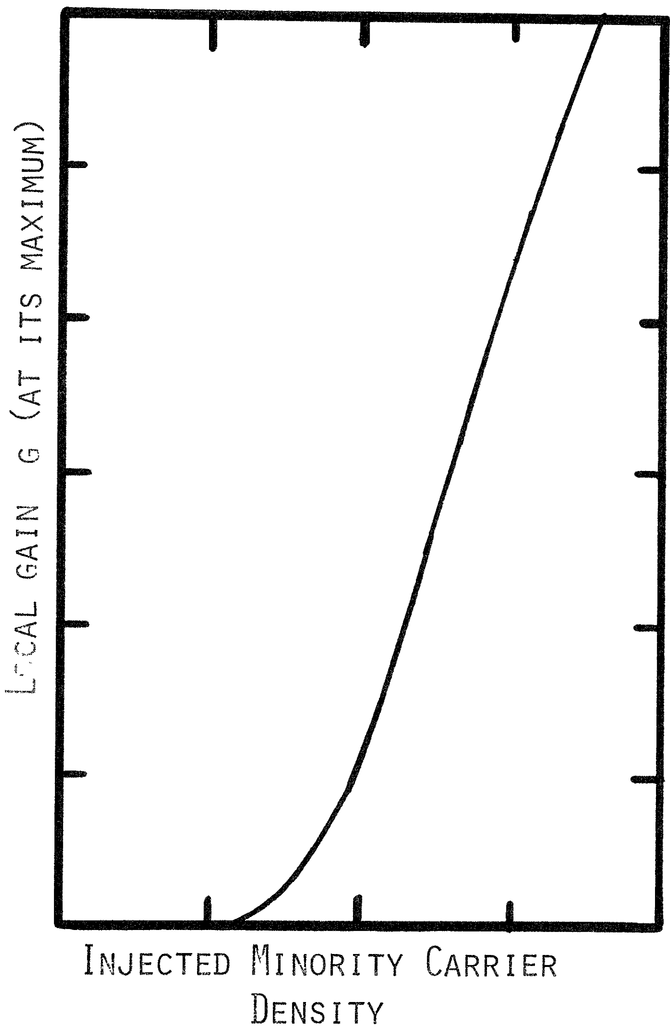

(assuming fixed number of majority carriers)

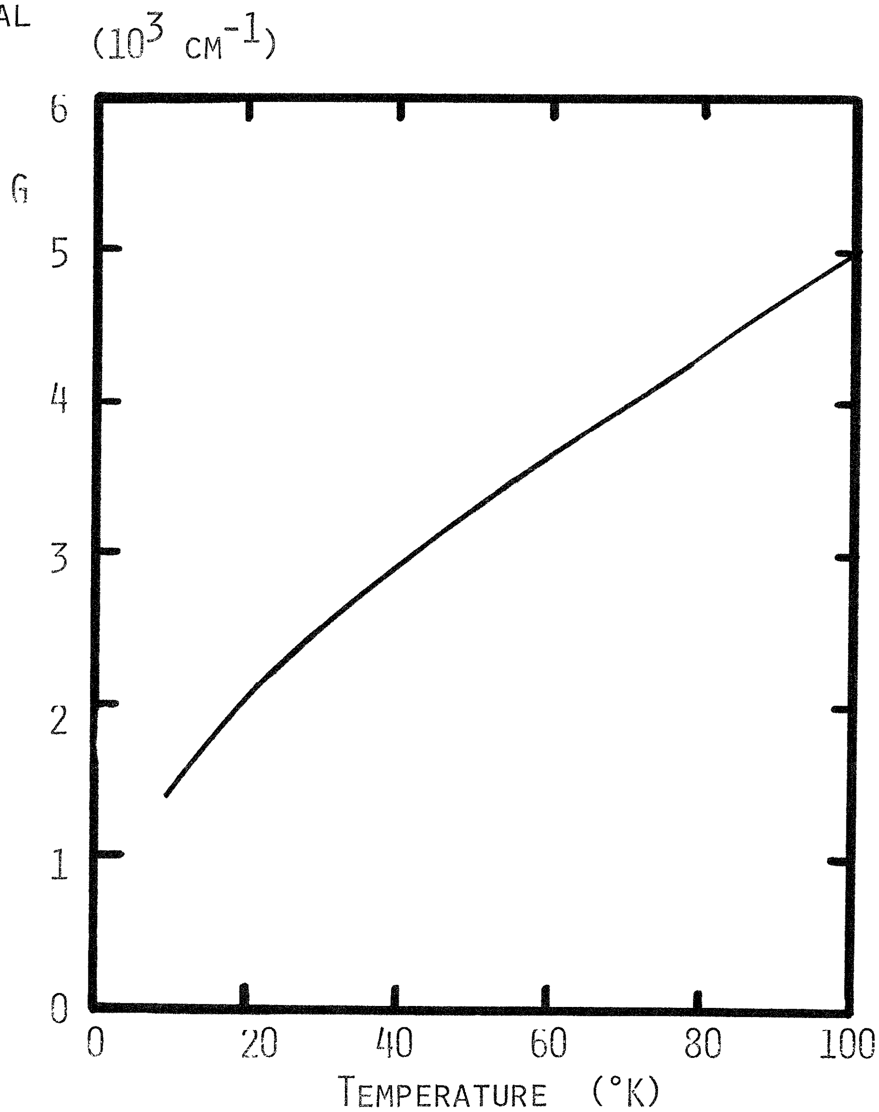

Figure 53: Units of Gain G in terms of γ as a Function of Temperature for PbSe

Figure 54: Variation with Temperature of C_J (the constant of proportionality between $\mathcal{J}_A$ and J_A) and C_H (the constant of proportionality between $\mathcal{H}_M$ and h_M) for PbSe

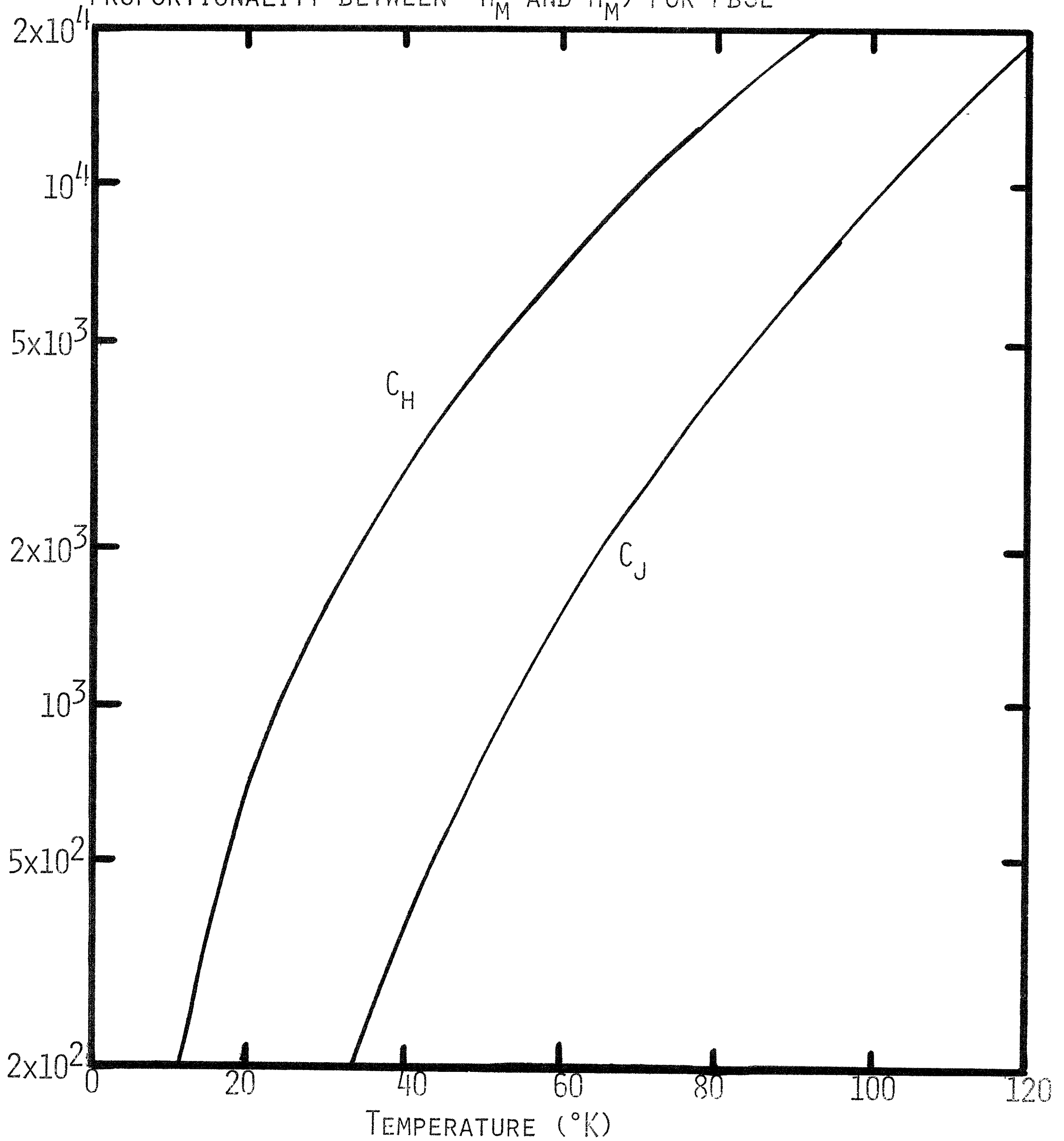

The units of C_J are Acm^{-2}; the units of C_H are $cm^{-1} \cdot \mu$

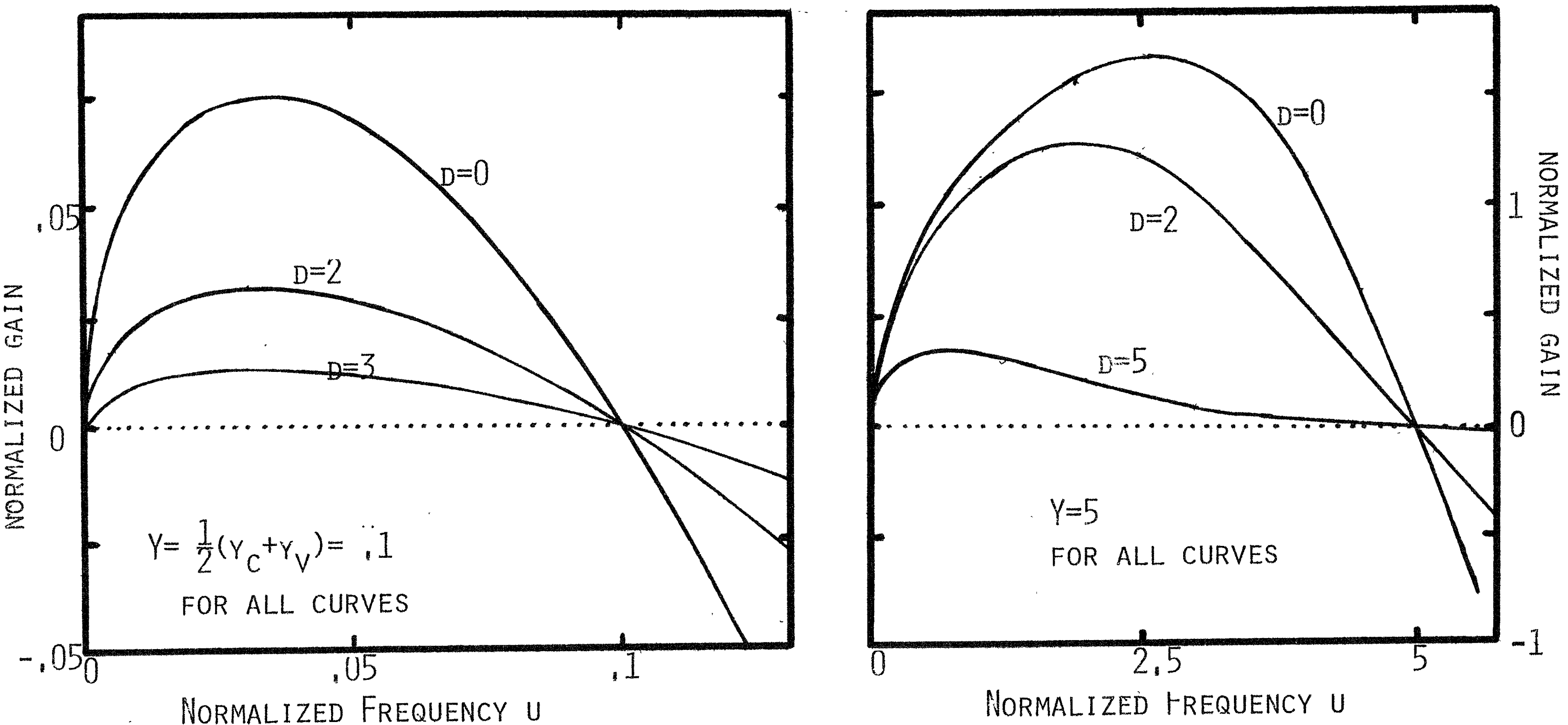

FIGURE 55: FREQUENCY DEPENDENCE OF NORMALIZED GAIN

IN EACH SET OF GRAPHS THE QUASIFERMI LEVEL SEPARATION IS KEPT CONSTANT, WHILE THEIR AVERAGE VALUE IS VARIED WIDELY; THE GAIN LINESHAPE IS FOUND NOT TO CHANGE VERY MUCH.

FIGURE 56: EFFECT OF BROADENING ON THE FREQUENCY DEPENDENCE OF THE GAIN

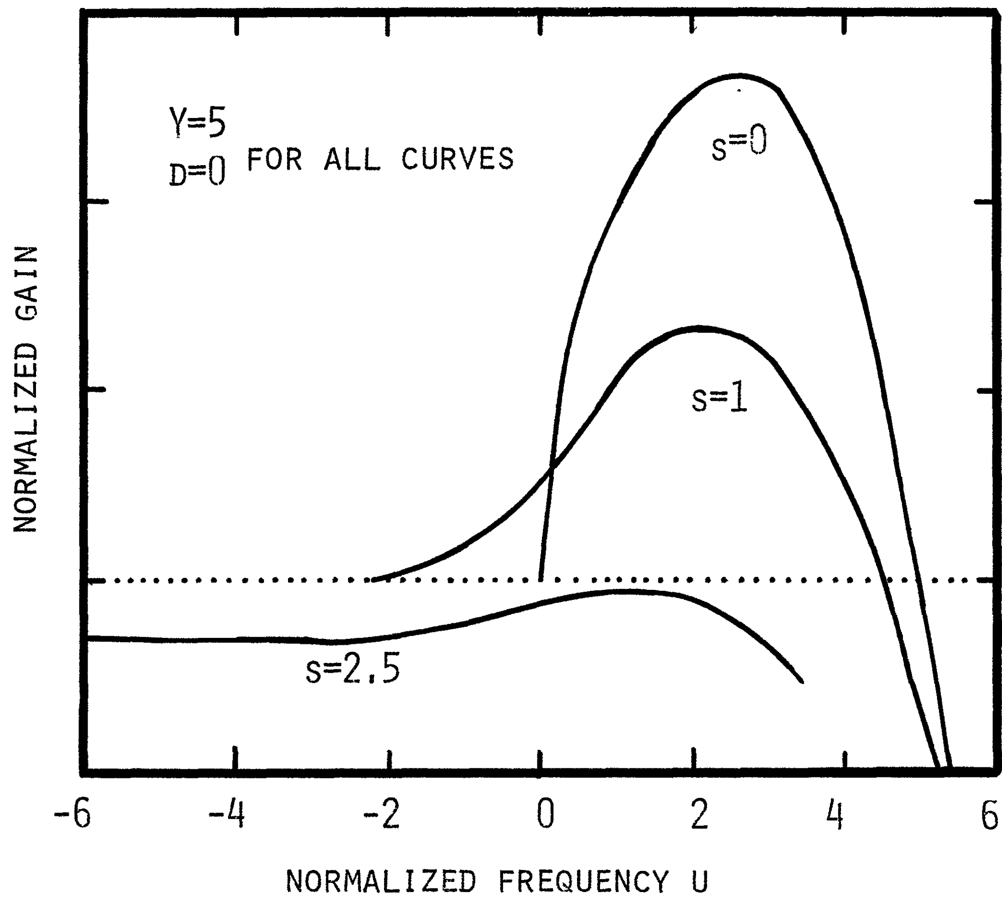

Figure 57: Effect of Broadening on the Maximum Value of the Gain

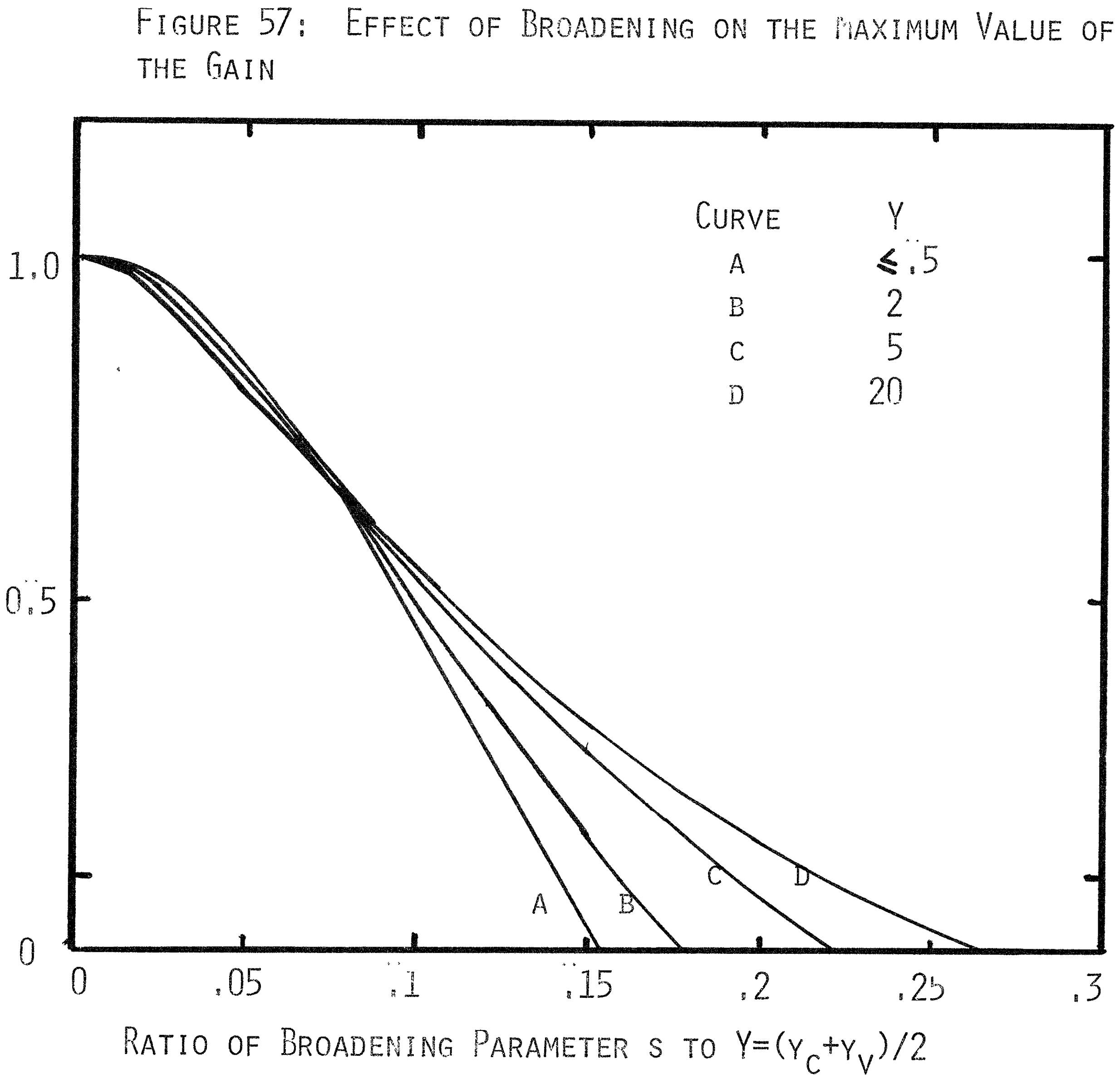

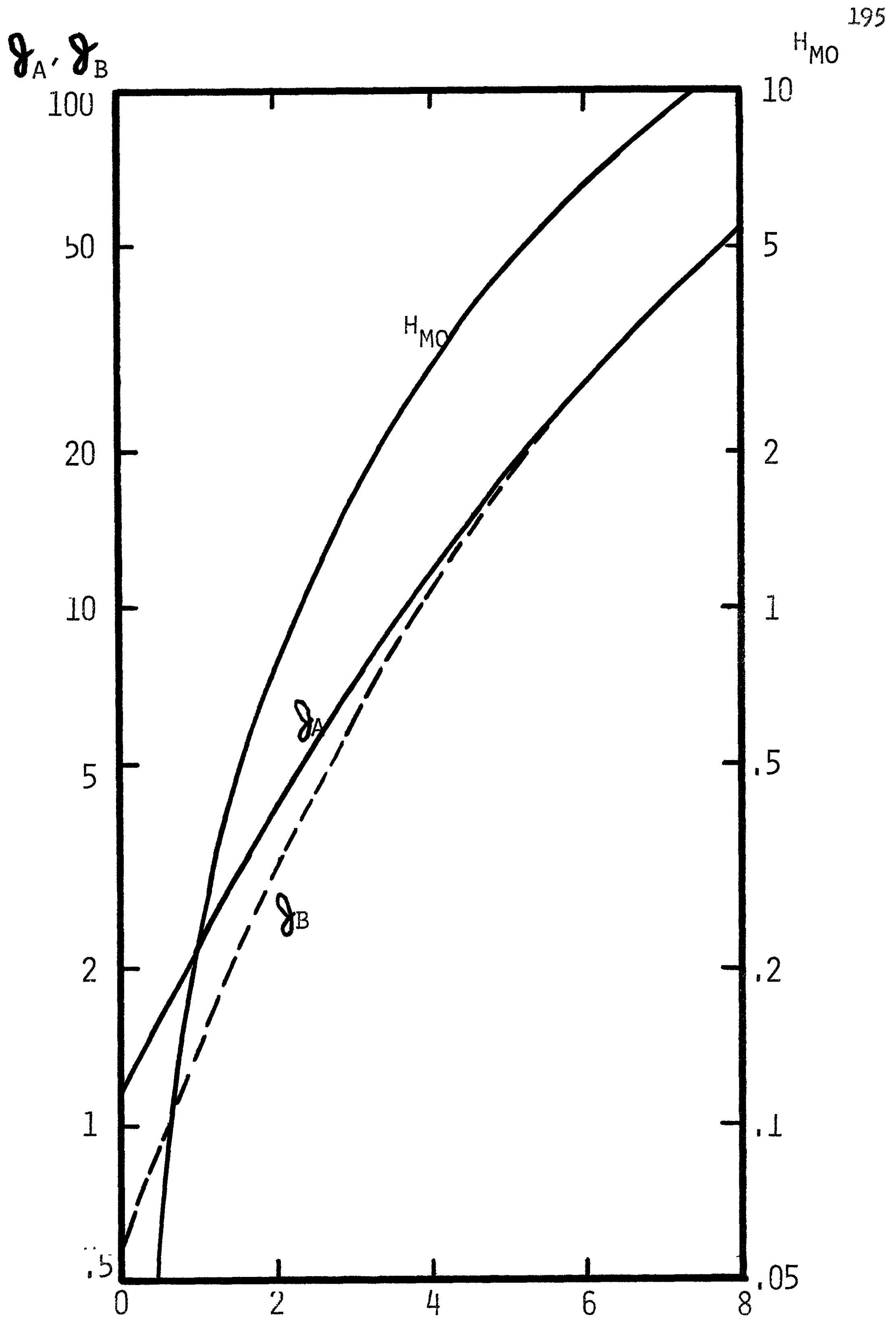

FIGURE 58: VARIATION WITH υ OF THE NORMALIZED INTEGRATED GAIN H_{MO} AND THE NORMALIZED CURRENT DENSITIES $\mathcal{J}_A$ AND $\mathcal{J}_B$

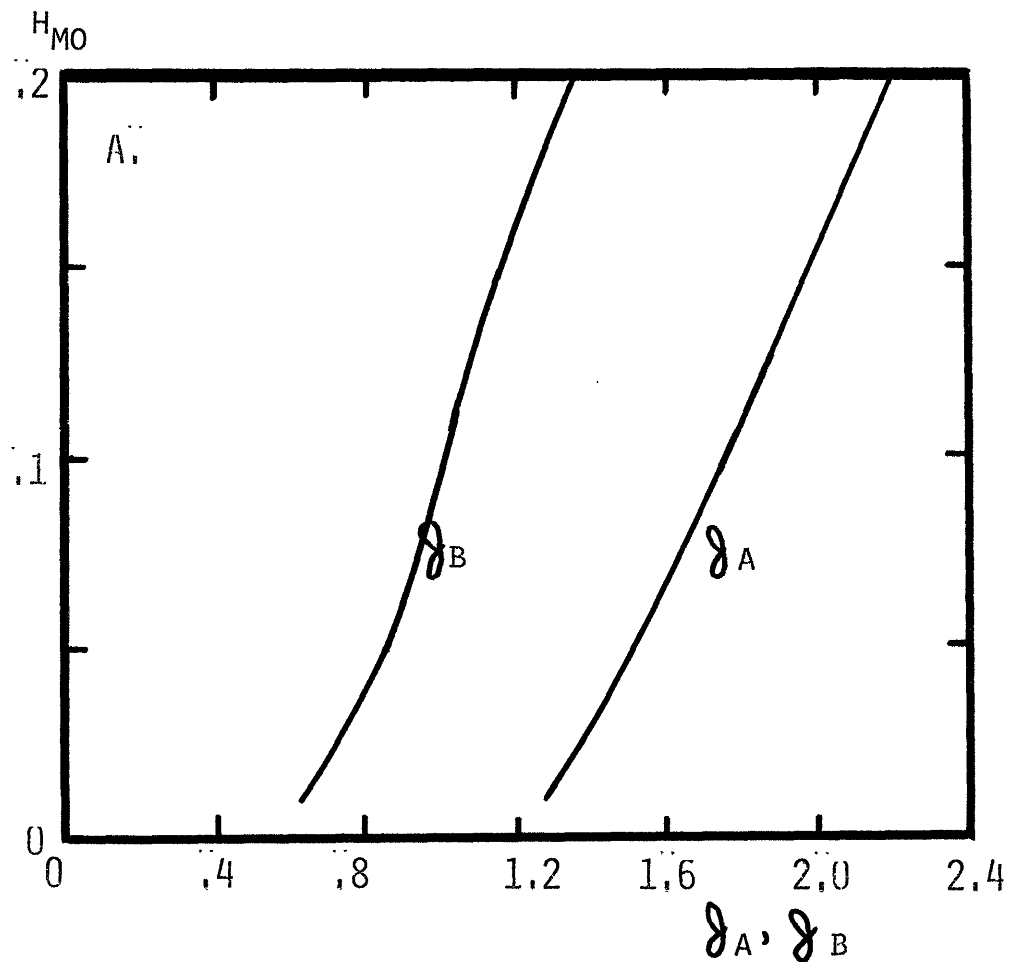

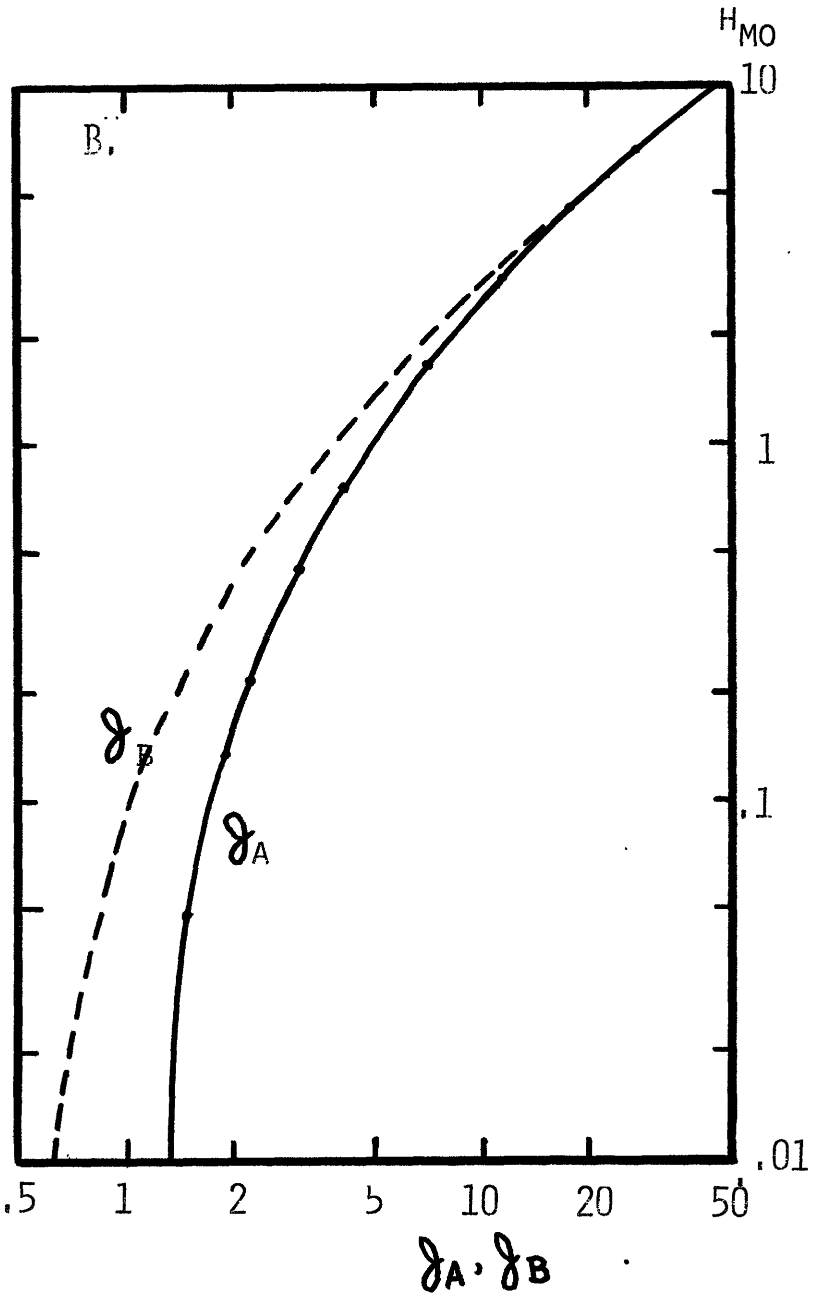

Figure 59: Relation between Normalized Integrated Gain H_{MO} and Currents γ_A and γ_B, obtained by varying ν and using $\lambda = 0$.
A. Linear scale ; B. log-log plot

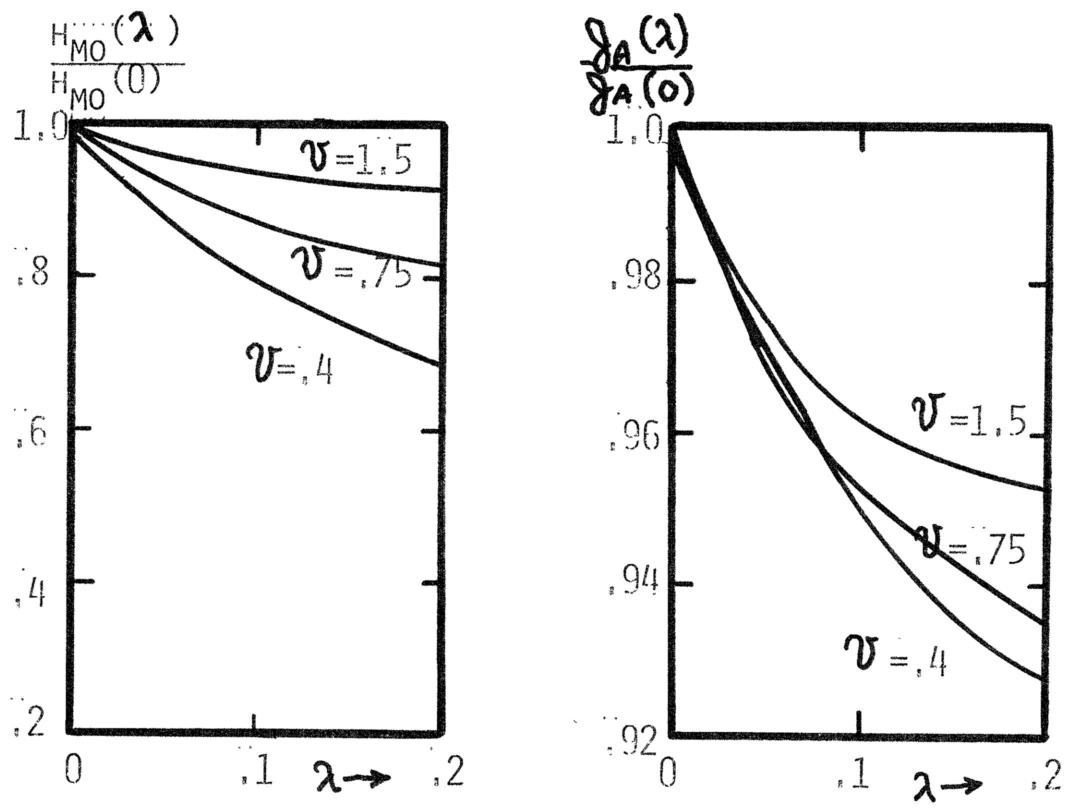

FIGURE 60: VARIATION OF H_{MO} AND $\mathcal{J}_A$ WHEN λ IS VARIED AT CONSTANT $\mathcal{V}$.

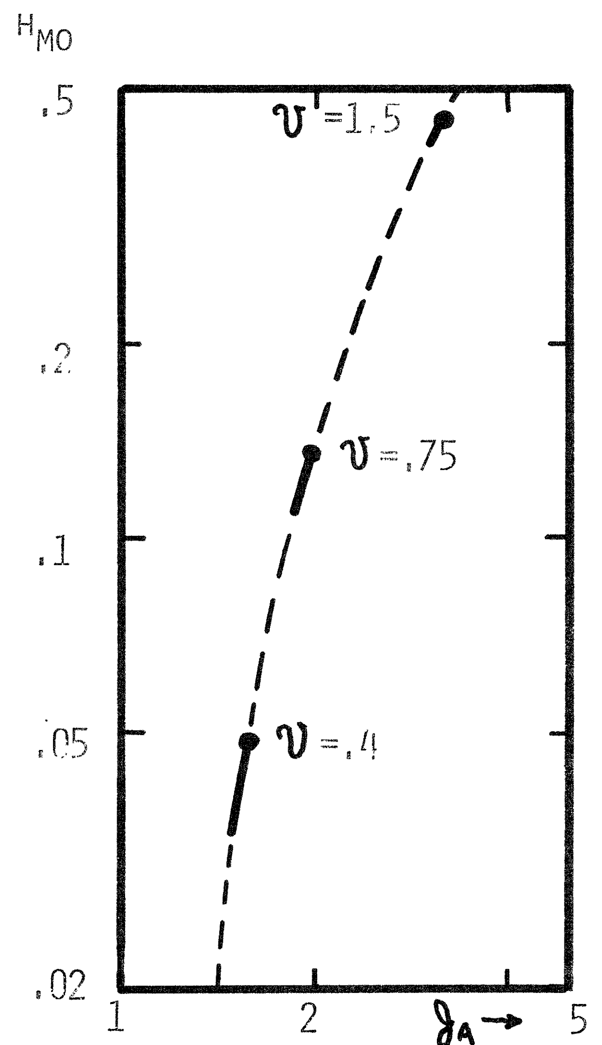

FIGURE 61: RELATION BETWEEN H_{MO} AND $\mathcal{J}_A$ PARAMETRIZED BY λ (DARK CURVES) ALSO, PARAMETRIZED BY $\mathcal{V}$ (DASHED LINE)

FIGURE 62: PREDICTED VARIATION OF THRESHOLD J WITH TEMPERATURE

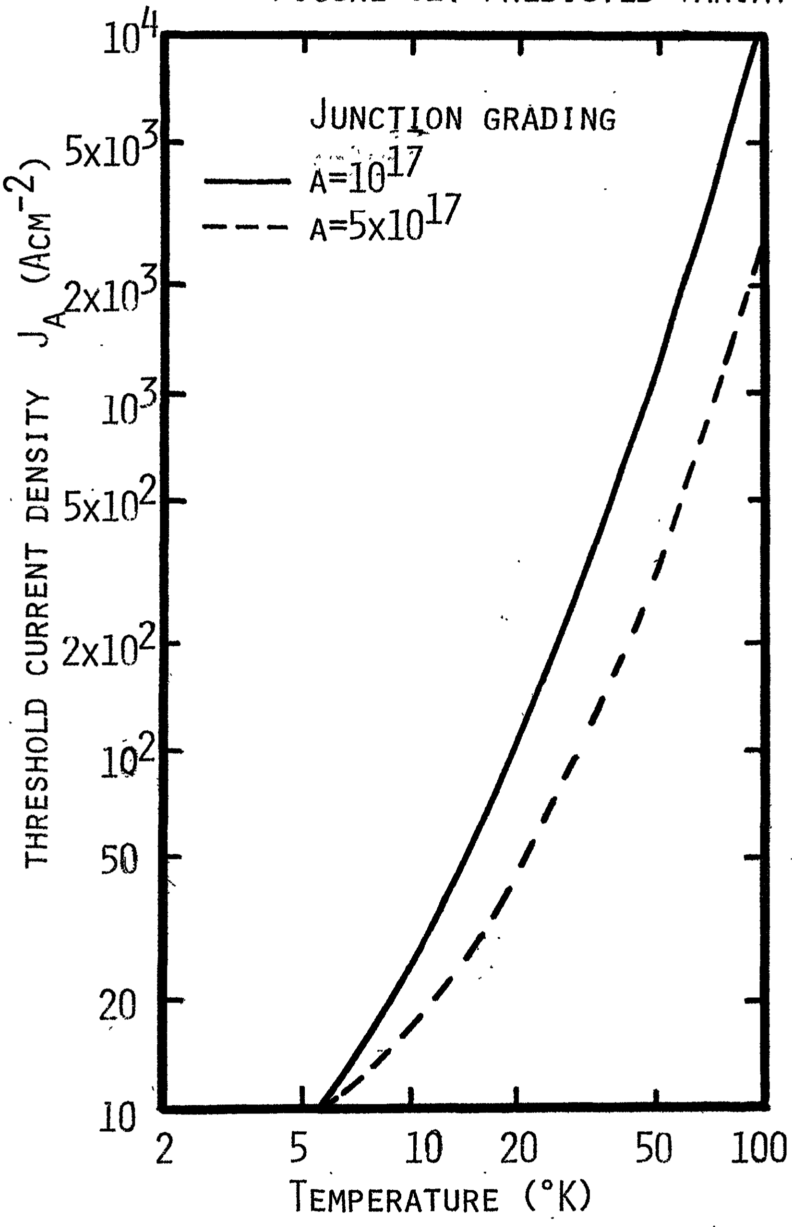

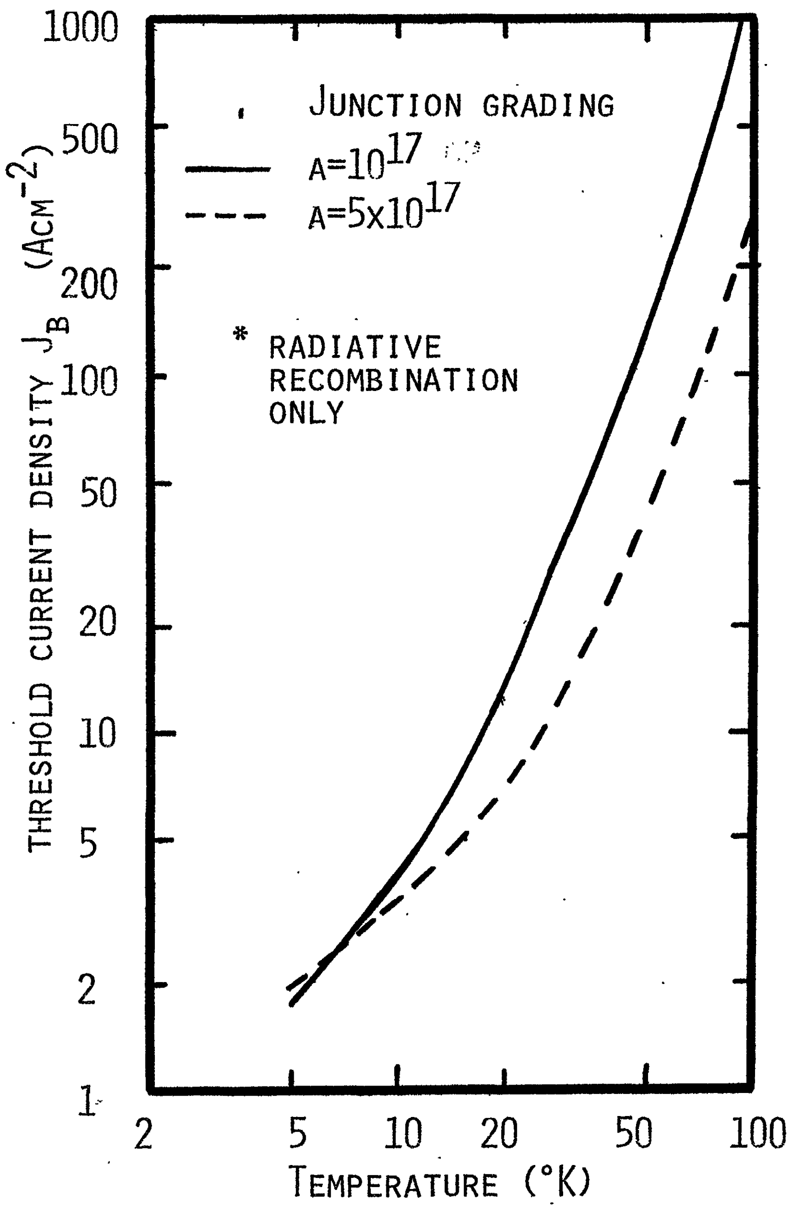

Figure 63: Calculated Variation of Threshold Current Density with Junction Grading Parameter

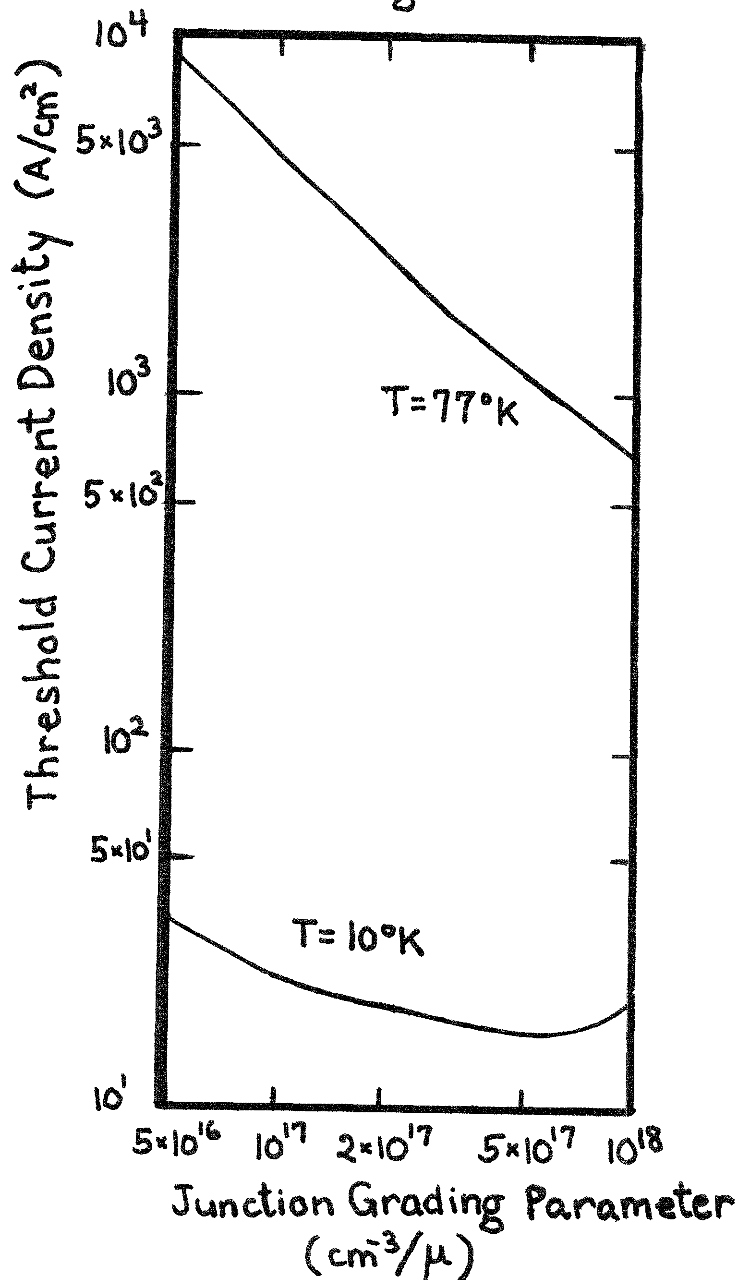

FIGURE 64: VARIATION WITH $\mathcal{V}$ OF INTEGRATED GAIN H_{MS}, INCLUDING THE EFFECTS OF HOMOGENEOUS BROADENING

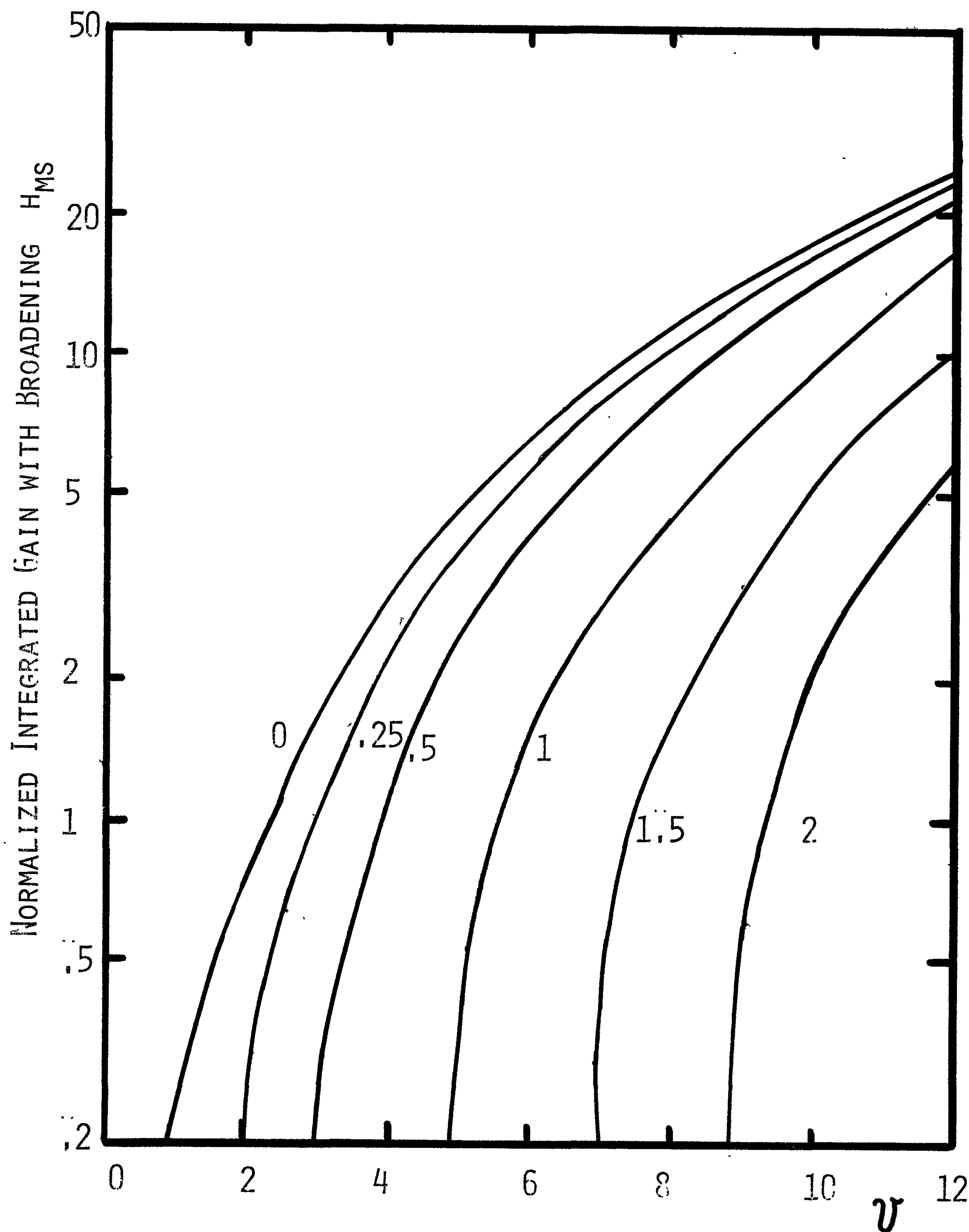

CURVES ARE LABELED WITH THE CORRESPONDING VALUE OF THE NORMALIZED LINEWIDTH PARAMETER S.

Figure 65: Calculated Variation of Threshold Current density with Temperature, including the effects of homogeneous broadening, and of high loss

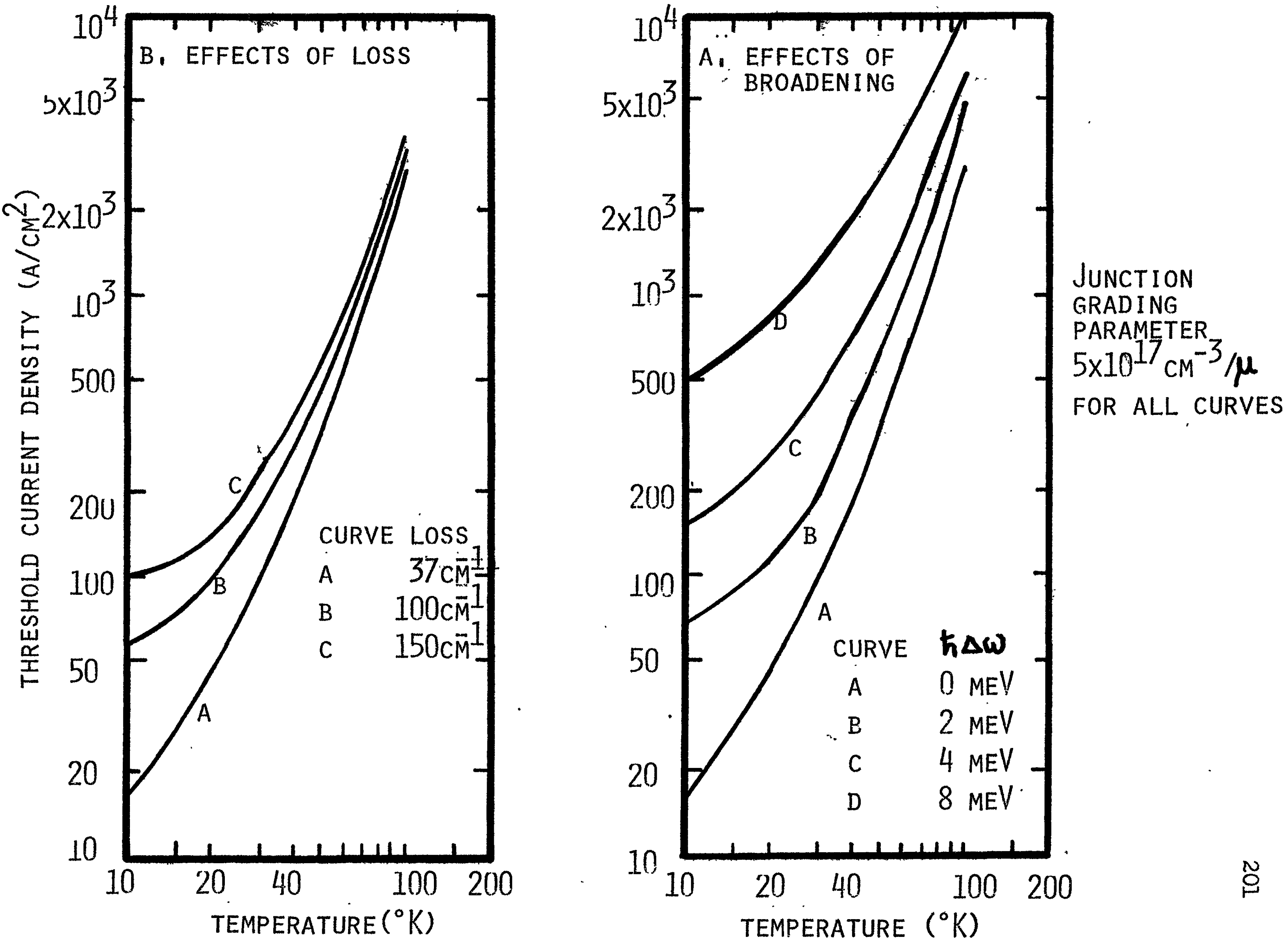

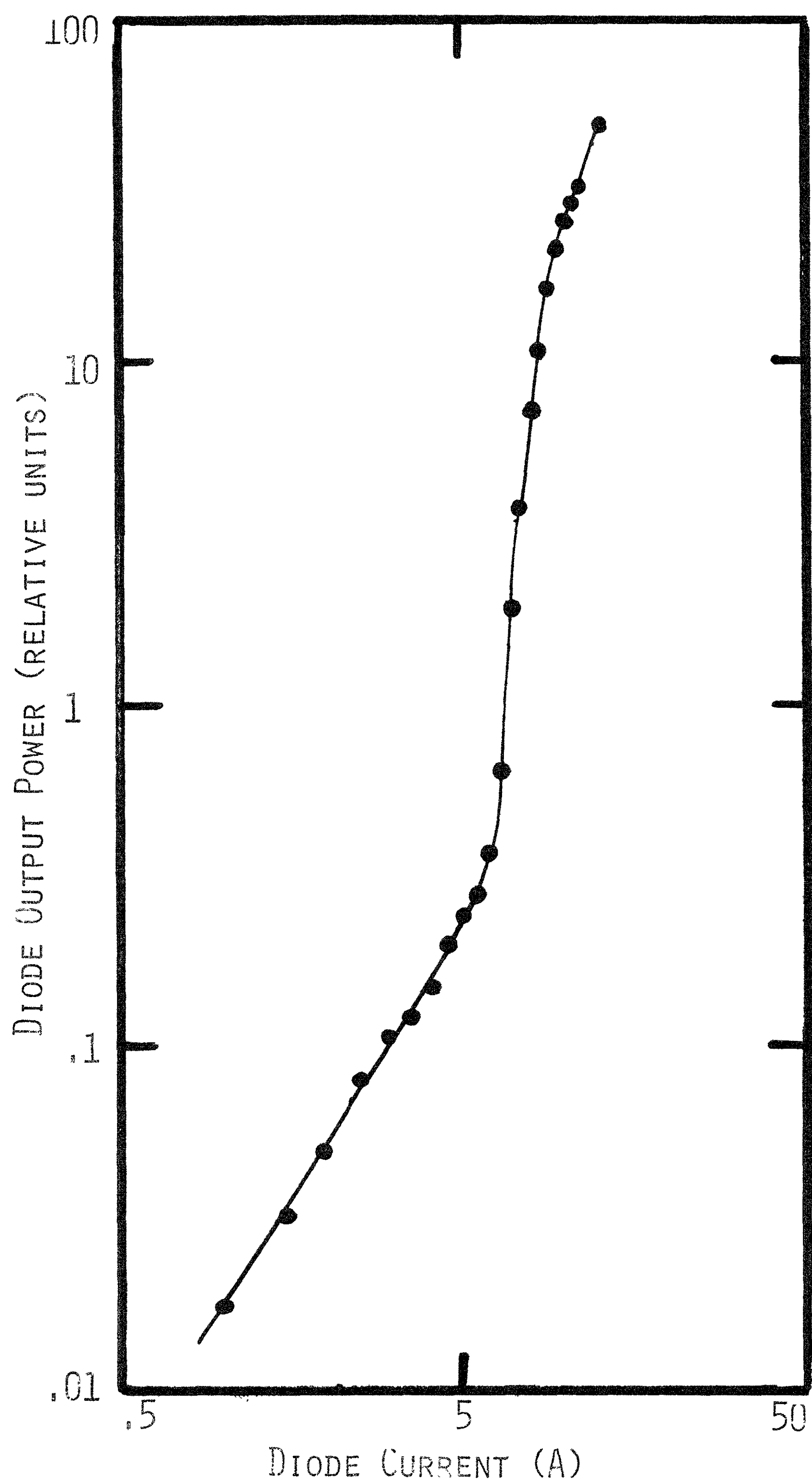

Figure 66: Typical Variation of Collected Diode Output Power with Current

FIGURE 67: MEASUREMENTS OF THRESHOLD CURRENT DENSITY VERSUS TEMPERATURE IN PBSE DIODES

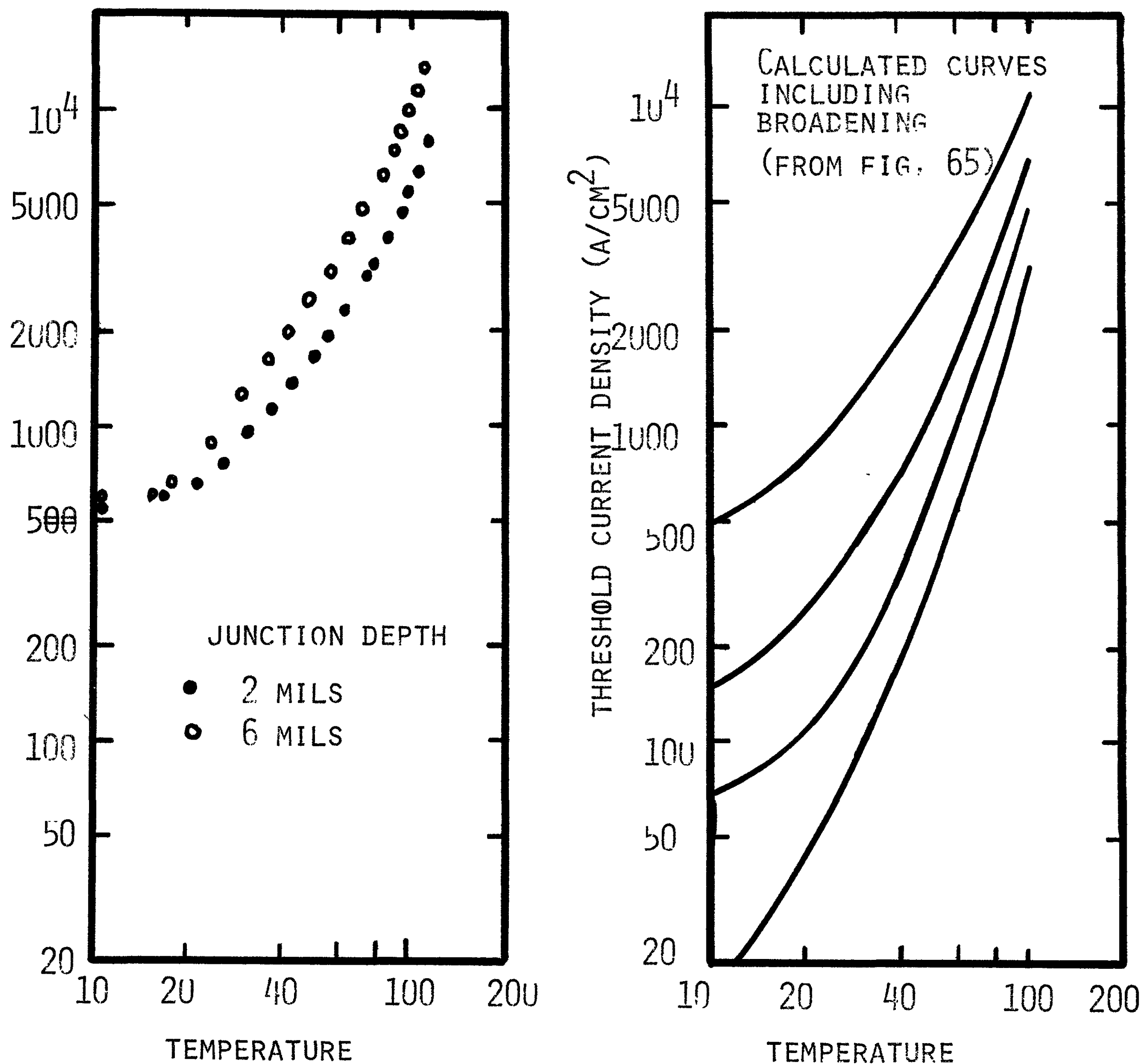

TABLE VII

DIODE PARAMETERS USED FOR THE CALCULATION OF J_{th}

	Diode 1	Diode 2
$a (cm^{-3}/\mu)$	10^{17}	5×10^{17}
$w_o (\mu)$	10	5.8
$L (\mu)$	500	500
$\alpha (cm^{-1})$	7.36	21.34
$\beta (cm^{-1}/Acm^{-2})$	1.43×10^{-3}	2.46×10^{-3}
$\delta (cm^{-1})$	15.3	15.3
τ_{rec} (nsec)	2	2

CHAPTER VI
SUMMARY AND CONCLUSIONS

In this thesis the spatial distribution of both the lasing mode intensity and the injected minority carrier density in the vicinity of the junctions of diffused PbSe homostructure lasers has been investigated. The theoretical results have shown that both distributions depend strongly on the grading of the net donor-acceptor density profile near the junction. As part of the experimental work this dependence was demonstrated explicitly for the optical mode distribution; for the case of minority carrier distribution the dependence was strongly suggested by the different variation of J_{th} with temperature for differently graded diodes.

Very detailed analysis of the confinement effects is complicated by the fact that the profile of stoichiometry obtained with p into n diffusions is imperfectly known. However, the theoretical treatement of Chapters III and IV based on reasonable models of the profile has shown that the relative amount of confinement of both variables that can be achieved in PbSe is considerably larger than in the case of GaAs or other wide bandgap semiconductor lasers. The optical confinement effect is enhanced in PbSe because of the low frequency of lasing, which in turn leads to strong variation of the dielectric constant with carrier density, and also by the low value of the density of states at the bandedge for PbSe, which leads to large Burstein, shifts. The minority carrier confinement effect is sizeable in PbSe also because of the low bandedge density of states.

The detailed model of the dielectric constant variation near the junction has led to reasonable agreement between theoretical and experimental mode widths. It may be expected, therefore, that other results

of the model presented in this thesis, including free carrier losses, end-losses and mode-spacings represent reasonable estimates of parameters not yet measured in PbSe lasers.

Qualitatively the confinement effects obtainable in other lead salt lasers should be similar to those observed in PbSe. In many cases the analysis contained in this work is directly applicable to any semiconductor system with nearly equal electron and hole masses. This extendability has been made possible by the use of dimensionless variables whenever feasible in the numerical calculations. Of particular importance should be the calculation of threshold current density, since in the high temperature regime the expression commonly used is inaccurate for the lead salts.

Specific conclusions emerge from the calculation of confinement effects that apply to the fabrication of devices with low values of threshold current. For the regime of junction depths (and hence junction grading parameters) considered here, it is found the most sharply graded junctions have the lowest value of threshold current density at high temperature. Thus, for example, devices fabricated on the basis of n into p diffusions with reasonably large junction depths in PbSe are not expected to perform well at high temperature. It may be noted, in addition, that according to Section V. 3 devices optimized for low temperature performance may not be optional at higher temperatures.

If the junction grading parameter is very high (such as might be obtained, for example, in a nearly abrupt junction fabricated by evaporation techniques) the conclusion stated in the last paragraph is no longer valid, however. For such a case the dielectric constant gradients exist only over a narrow region near the junction; the optical mode will "spill-over" into the homogeneously doped regions

adjacent to the junction where there is no confining dielectric constant gradient. The limitations on the mode width in the case of very rapidly graded junctions may be examined with the aid of Model B of Appendix D. A similar effect occurs for the minority carrier confinement. If the junction is not linearly graded over the entire region of interest next to the junction, then minority carriers may diffuse into the ungraded regions and recombine there; for very narrow regions of junction grading this unconfined current component may dominate the total junction current.

Appreciation of the large change in dielectric constant due to the effect of carriers is important for the design of heterostructure lasers, since the wider-bandgap semiconductors that clad the active region must be chosen so the dielectric constant discontinuities are not eliminated by the effects of injected carriers at the temperature of interest.

An additional aspect of the work of potential interest in the development of improved lead salt lasers is the method used for the measurement of the minority carrier recombination lifetime, which should be readily extendable to other systems. It was found in this work that the internal quantum efficiency of radiative recombination was law in the lasers fabricated. Similar studies on lasers produced with different techniques might lead to identification of the causes of this low efficiency.

APPENDIX A
LASER FABRICATION PROCEDURES

The procedures followed in this work with regard to PbSe handling and processing often closely paralled and made use of facilities established for other research efforts performed in this laboratory, including those of Guldi, McMullin, Tomasetta and St. Onge. Additional techniques, particularly with regard to contacting, and mounting diodes, were adopted following suggestions from J.N. Walpole and A.R. Calawa of Lincoln Laboratory, M.I.T.

The starting material used for diode fabrication was grown from the melt by the Bridgman method by M. Lichtensteiger of the Metallurgy Department, M.I.T. As-grown material was p type with hole density in the range 10^{18} - 10^{19} cm^{-3}. Portions of the boule, particularly the periphery and tail, had numerous voids and inclusions; the portions used in this work in general had less than one inclusion per cm^2 and no voids, however. Small angle grain boundaries revealted by prolonged etching in Coates' etch (10 parts KOH satuated solution in water, 10 parts ethylene glycol, 1 part $H_2 0_2$) were also present in the material. The size of the grains enclosed by these boundaries was typically several mm. in each dimension (such that the probability was high than an individual laser was free of these defects). The dislocation density was believed to be of the order of 10^7 cm^{-2}. Additional defects believed to be present in the material were microprecipitates of Se, formed within the crystal during cooling from the growth temperature due to the retrograde solubility of Se in PbSe. Spectroscopic analysis of a similarly grown boule yielded the following impurity concentrations: Mg and Si (1 -10ppm), Cu, Ca and Fe (.3 -3ppm), Ag (.1 -1ppm).

Slices approximately 40 mils thick were cut from the boule by means of a string saw using a slurry with silicon carbide size 600 grit. The same saw was used to cut the slice into slabs of dimensions near 1 cm x 1.5 cm. The orientation of the slices was not accurately determined; in some cases it was slightly misaligned from a (110) face while in others it was slightly off a (100) face.

Both faces of the slab were then lapped and polished. In order to eliminate damaged material, 10 mils was removed from each face. Lapping was done with alumina grit of sizes 9 μ, 5 μ and 2 μ at successive stages on a glass lapping block. Polishing was done with a combination of abrasion and chemical etching. Samples were first polished on Pellon paper on a glass block using an etch made by dissolving approximately 1 cm^{-3} of CrO_3, in 100 ml of water; subsequently they were polished on Beuhler AB Microcloth using the same etch and .3 μ alumina grit until the surfaces appeared damage free under microscope observation.

As described in Section II-3, the preparation of the laser junctions required 2 anneals: during the 1st, anneal N, substrates were uniformly saturated with Pb and became uniformly n type; in the 2nd, anneal P, the surfaces were saturated with Se, converting them to p type and creating junctions within the crystal.

Both anneals were done following the isothermal anneal techniques described by A. R. Calawa et. al.[28] Substrates were placed on the shelf of a quartz ampoule of the type used in Reference 28, while below the shelf was placed an amount of (Pb, PbSe) powder or (Se-, PbSe) powder whose volume was greater than that of the substrates. The ampoules were placed in a furnace inside which the temperature was uniformly 500°C. According to this technique the powder at the anneal temperature becomes a solid-liquid mixture and

establishes vapor pressure of all species inside the ampoule. The substrate surface is brought into equilibrium with the mixture via the vapor phase.

The (Pb, PbSe) and (Se-PbSe) powders were prepared by reacting the elements with an oxyhydrogen torch after placing them in an evaculated quartz ampoule. The mixture was then homogenized by placing it in a furnace set at 1200°C (which is above the PbSe melting temperature) for a period of one hour. The amount of each element to be reacted was weighed out to be 52 atomic percent Pb, 48% Se for the (Pb, PbSe) powder and 48% Pb, 52% Se for the (Se, PbSe) powder.

Prior to both anneal N and P, the quarz ampoules were cleaned with soap and water, etching in aqua regiaand heating to 800°C for over one hour under high vacuum. The substrates were cleaned by swabbing with a cotton-tipped Q-tip under hot acetone, boiling in acetone, trichloroethylene and methanol, etching for one minute in a 5% HNO_3 solution followed by a distilled water rinse, and finally boiling in methanol followed by flowing dry with N_2.

Anneal N lasted 90 days. This time is in excess of the period estimated to be necessary to convert the entire slabs to n type conductivity on the basis of the work of Calawa, et. al.[28]

After anneal N, one surface of the sample was lapped and polished again because of the occurence of slight thermal etching. During the lapping, care was taken to obtain flat substrates with parallel faces.

Anneal P lasted a carefully controlled short time, calculated on the basis of the data of (References 28 and 29) in order to achieve the desired junction depth. The anneal was terminated by rapid quenching of the ampoule in water in order to avoid internal precipitation of Se near the surface.

After anneal p substrates had p layers covering both top and bottom surfaces. The unpolished surface p layer was lapped off with 2μ alumina grit, leaving slabs of thickness 8 mils with a single p-n junction.

These slabs were then metallized to provide ohmic contacts. The n side was first covered with an evaporated layer of In of thickness approximately 3000 A$^{\circ}$. The p side was plated with a thin layer of gold. Subsequently each side was plated with a thickness (approximately 1 mil) layer of In to facilitate bonding. With this scheme, contact resistances of the order of .2Ω for a diode area of $10^{-3}cm^{2}$ were achieved. On the basis of work at Lincoln Laboratory it is believed that most of the resistance is obtained at the p contact.[44]

Bars of 1 mm width were cut from the slabs with a string saw. Sides of the bars along their long dimension were then polished to provide front and back morror facets of the lasers. In order to mount the thin bars for polishing, they were fitted between two slices of Si scrap material which had well-formed square edges; all these structures were waxed to each other and to the polishing block with Crystalbond 509 wax. The lapping and polishing procedures used were identical to those described earlier, except that the final step was abbrieviated in order to avoid rounding of the mirror facets. The flatness and perfection of the mirror facets obtainable in this way is visible in Fig. 68, where the front face of a completed diode is viewed with an interferometric microscope at a wavelength of 5892 Å. A major drawback of this fabrication scheme, however, is the difficulty of obtaining mirror facets accurately parallel to one another and normal to the plane of the junction. By viewing the reflection of a He-Ne laser beam off the front and back surfaces of the polished bars, it was found that the angles of misalignment in the x-z plane of front and back facets

of the lasers used in this study ranged between 10' and 45' of arc. It is likely that these values also are indicative of the misalignment between the mirror normals and the junction plane.

Mirror facets may also be produced by cleaving the PbSe slabs, which readily break along 100 planes. Accurate orientation of the junction plane is, of course, then required to produce good lasers. The lasers of this work were produced with polished facets because the small steps unavoidably present on cleaved surfaces were found to cause irregular far-field patterns in lasers fabricated by cleaving. This is consistent with and was motivated by the results found by J.N. Walpole concerning the improved output power of Pb salt lasers when their facets are polished.[13]

A string saw was used to cut individual lasers of width approximately 8 mils from the polished bars. The sawed sidewalls of the diodes were left unpolished and unetched.

Diodes were mounted on oxygen-free high conductivity copper blocks which served as heat sinks by In cold-compressing bonding. In order to carry this out, the Cu blocks were first plated with approximately 1 mil of In in the region where the diode was to be mounted. To produce the bond, a drop of HCl was placed on the In cladded heat-sink surface, the diode was put in its proper location and uniform pressure of approximately 10 atmospheres was applied to the diode for 30 minutes.

Diodes were mounted overhanging very slightly the edge of the Cu heatsink in order to avoid reflections of the laser light from the copper surface. Such reflections are known to cause interference patterns in the far field of the laser output.

Electrical connection to the remaining diode contact was made

with a 3 mil Au wire previously bonded to an insulated post attached to the heat sink. A 5 mil diameter In ball was attached to the tip of the Au wire and the structure was then soldered to the In coated diode surface with a soldering iron whose tip was extended by a 15 mil Au wire.

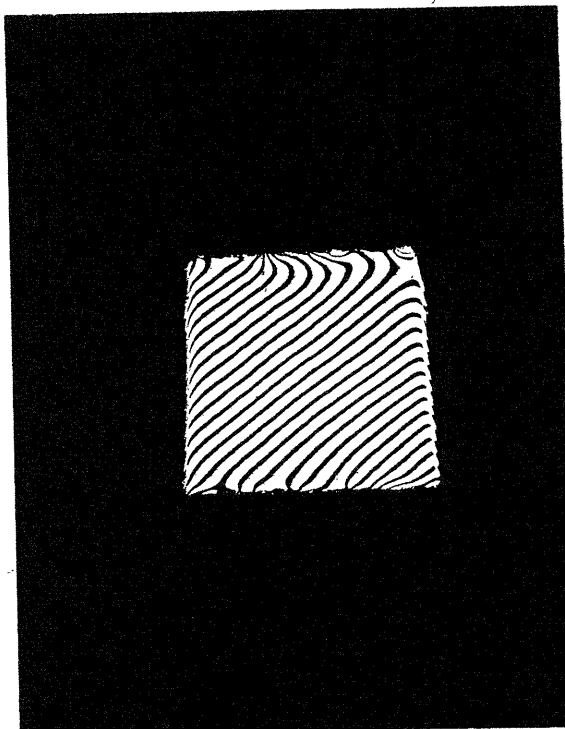

FIGURE 68: INTERFERENCE MICROPHOTOGRAPH OF A TYPICAL POLISHED MIRROR FACET
WAVELENGTH OF ILLUMINATING RADIATION: 5892 Å

APPENDIX B
BAND MODEL FOR PbSe

PbSe crystallizes in the rocksalt (f. c. c.) structure. Extrema of the conduction and valence bands are known to lie at the L points of the Brillouin zone, and thus exhibit 4-fold degeneracy. The conduction and valence bands of PbSe, as those of other narrow gap semiconductors, display substantial nonparabolicity. As a result, values of effective mass and interband momentum matrix element vary with k over the region of interest of the Brillouin zone; the density of states in energy function and the fermi-level variation with carrier concentration also have complex forms. In this chapter an approximate model of the conduction and valence band dispersion is described, and functions useful in the rest of this work are derived from it. Work reported in this chapter has been taken from the literature, with some simplifications introduced where appropriate.

First principles calculations of the band structure (obtained with the APW method) are available for all the lead chalcogenides.[117-119] These show that the k.p model most appropriate to the lead salts takes into account the interaction at the L points of 6 relatively closely spaced bands near the fermi level. The bands emerge from the s and p shells of Pb and Se; their energies are known to be strongly influenced by relativistic corrections and spin-orbit splitting. It is believed that the most accurate set of matrix elements and band separations available at present are those given by Bernick,[56] who using orderings given by the earlier work, adjusted pseudopotentials to fit a variety of data. Martinez has further demonstrated that a k.p model using the numerical values of Bernick is capable of giving good agreement with experimental results in PbSnSe alloys.[120] The matrix elements and band separations do not differ significantly from those obtained from

first principles by Rabii.[119]

When the k.p. matrix corresponding to the interactions of the six bands is solved (using perturbation theory to account for the far-band effects), the following general dispersion relation is derived, in the coordinate system of one L point:

$$\left[E-\frac{1}{2}E_g-\frac{\hbar^2}{2m_t^-}(k_x^2+k_y^2)-\frac{\hbar^2}{2m_l^-}k_z^2\right]\left[E+\frac{1}{2}E_g+\frac{\hbar^2}{2m_t^+}(k_x^2+k_y^2)+\frac{\hbar^2}{2m_l^+}k_z^2\right]$$

$$=\frac{\hbar^2}{m^2}\left[P_\perp^2(k_x^2+k_y^2)+P_\parallel^2k_z^2\right] \qquad \text{(B-1)}$$

Here $P_\parallel$ and $P_\perp$ are the longitudinal and transverse momentum matrix elements between the extremal valence and conduction bands, and $m_t^\pm$ and $m_l^\pm$ represent the contribution of the more distant bands.

Band parameters obtained by Bernick, as well as those of several other authors, are reported in terms of the notational scheme of Mitchell and Wallis.[76] Their relation to the parameters defined in (B-1) is given by

$$\frac{m}{m_t^+}=\frac{(\cos\theta^+\cos\theta^-P_{31}+\sin\theta^+\sin\theta^-P_{13})^2}{m(\epsilon_1^- - \epsilon_2^+)}+\frac{\cos^2\theta^-P_{31}^2+2\sin^2\theta^-P_{22}^2}{m(\epsilon_1^- - \epsilon_3^+)}$$

$$\frac{m}{m_l^+}=\frac{2(\cos\theta^+\sin\theta^-P_{21}-\sin\theta^+\cos\theta^-P_{11})^2}{m(\epsilon_1^- - \epsilon_2^+)}$$

$$\frac{m}{m_t^-}=\frac{(\cos\theta^+\cos\theta^-P_{13}+\sin\theta^+\sin\theta^-P_{31})^2}{m(\epsilon_1^+ - \epsilon_2^-)}+\frac{\cos^2\theta^+P_{13}^2+2\sin^2\theta^+P_{22}^2}{m(\epsilon_1^+ - \epsilon_3^-)} \qquad \text{(B-2)}$$

$$\frac{m}{m_l^-}=\frac{2(\cos\theta^+\sin\theta^-P_{11}-\sin\theta^+\cos\theta^-P_{21})^2}{m(\epsilon_1^+ - \epsilon_2^-)}$$

$$P_\parallel^2=(\cos\theta^+\cos\theta^-P_{11}+\sin\theta^+\sin\theta^-P_{21})^2$$

$$P_\perp^2=\frac{1}{2}(P_{13}\cos\theta^+\sin\theta^- - P_{31}\sin\theta^+\cos\theta^-)^2$$

The parameters used and the results obtained from (B-2) are shown in Table VIIIa. In Table VIIIb are given the values of band edge effective masses obtained from the model and for comparison experimental values obtained by Cuff, et. al. at 4.2°K.[121]

A major simplification of the band model is introduced in this work. Based on the closeness of measured and predicted mass values for conduction and valence bands, it is assumed that the bands are in fact completely symmetric. A similar approximation is made by Melngailis et. al.[122] In terms of the model it is assumed

$$\frac{1}{m_t^+} \approx \frac{1}{m_t^-} = \frac{1}{m_t^\pm} \qquad \frac{1}{m_\ell^+} \approx \frac{1}{m_\ell^-} = \frac{1}{m_\ell^\pm} \tag{B-3}$$

With this approximation resulting expressions for quantities of interest are rendered a great deal simpler, and approach the form of results of the Kane 2-band model. The dispersion relation for the conduction and valence bands is given by

$$E^2 - \frac{E_g^2}{4} = \left(\frac{\hbar^2 P_\perp^2}{m^2} + \frac{E_g \hbar^2}{2m_t^\pm}\right)(k_x^2 + k_y^2) + \left(\frac{\hbar^2 P_\parallel^2}{m^2} + \frac{E_g \hbar^2}{2m_\ell^\pm}\right)k_z^2 \tag{B-4}$$

where terms of the order of k^4, known to be negligible for attainable carrier concentrations, have been dropped from the r.h.s. Here E denotes the energy of electron states measured from midgap.

For this model, the band edge mass values are given by:

$$\frac{m}{m_{\ell o}} = \frac{2P_\parallel^2}{mE_g} + \frac{m}{m_\ell^\pm} \qquad \frac{m}{m_{to}} = \frac{2P_\perp^2}{mE_g} + \frac{m}{m_t^\pm} \tag{B-5}$$

and the conductivity effective mass is

$$\frac{m}{m_{\ell c}} = \frac{m}{m_{\ell o}} \cdot \frac{E_g}{2E} \qquad \frac{m}{m_{tc}} = \frac{m}{m_{to}} \cdot \frac{E_g}{2E} \tag{B-6}$$

The density of states per unit energy and volume in a band (spin degeneracy included) is given by

$$\rho(\epsilon) = \frac{\sqrt{2}\, M_v m_{to} m_{lo}^{1/2}}{\pi^2 \hbar^3} \left[\epsilon\left(1+\frac{\epsilon}{E_g}\right)\right]^{1/2} \left(1+\frac{2\epsilon}{E_g}\right) \tag{B-7}$$

where ϵ is measured with respect to the band edge, and M_v is a factor to take into account the number of equivalent extrema of the band. This is readily found by using

$$\rho(\epsilon) = \frac{d}{d\epsilon}\left[\frac{1}{6\pi^2} k_{t\,max}^2(\epsilon)\, k_{l\,max}(\epsilon)\right] \tag{B-8}$$

which makes use of the fact that constant energy surfaces are ellipsoidal. A similar technique allows ready evaluation of the reduced density of states employed in Chapter IV-2 for valence-conduction band transitions. Using $\xi = E_c(\bar{k}) - E_v(\bar{k}) = 2E(\bar{k})$ as defined in (B-4), the reduced density of states per unit energy and volume for a single valley and spin is

$$\rho_{red}(\xi) = \frac{\sqrt{2}\, m_{to} m_{lo}^{1/2}\, \xi}{4\pi^2 \hbar^3 E_g} \left(\frac{\xi^2}{E_g} - E_g\right)^{1/2} \tag{B-9}$$

The variation with k of the momentum matrix element connecting conduction and valence band states at a given k has been considered by Martinez.[120] It is shown that negligible error is incurred by assuming a constant matrix element over the occupied Brillouin zone up to carrier concentrations of 10^{19} cm^{-3}.

The values of band parameters at various temperatures have been obtained on the following basis: values of $P_\perp^2$, $P_\parallel^2$, $m_l^\pm$ and $m_t^\pm$ have been assumed temperature independent, and given by the values

of Bernick for 0°K. The temperature dependence of the energy gap (taken from Ref. 96) has been properly taken into account.

The directionally averaged conductivity effective mass, given by

$$\frac{m}{m_c^*} = \frac{1}{3}\left(\frac{m}{m_{\ell c}^*} + \frac{2m}{m_{tc}^*}\right) \tag{B-10}$$

as evaluated within the quasi-two-band model is shown vs. energy at 77°K in Fig. 25. The dependence of carrier concentration on fermi-level at 77°K (equal for holes and electrons within this model) is shown in Fig. 69. This curve has been obtained by numerical evaluation of

$$n = \int_0^\infty \rho(\epsilon) f(\epsilon, \epsilon_f)\, d\epsilon \tag{B-11}$$

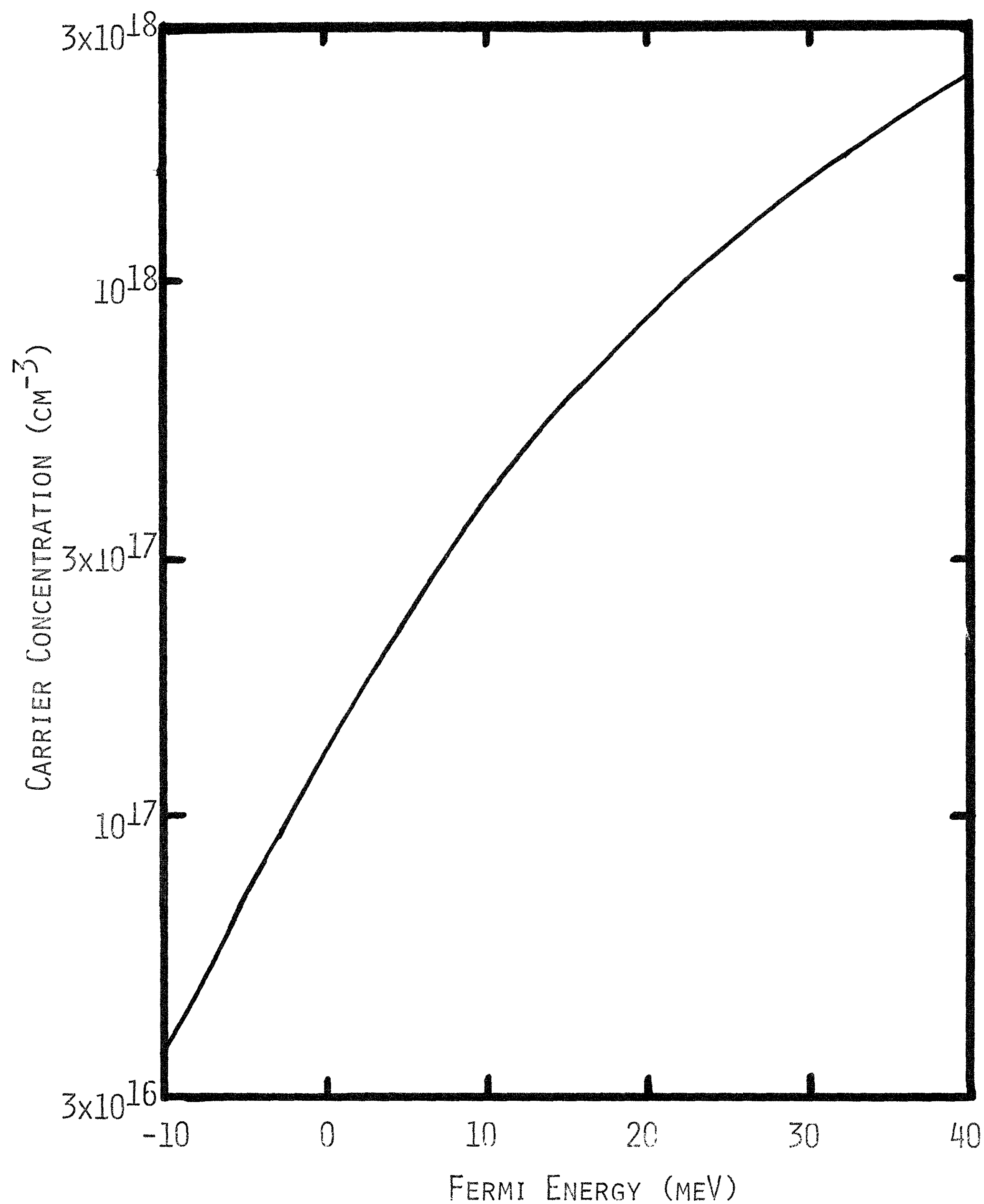

Figure 69: Calculated Variation of Carrier Concentration with Fermi Energy for PbSe at 77°K

TABLE VIII

a. PARAMETERS OF k.p MODEL FOR PbSe

(atomic units)

$\sin\theta^+ = -.138$	$P_{11} = .37$	$\epsilon_1^- = .012$
$\cos\theta^+ = .990$	$P_{13} = .708$	$\epsilon_2^- = .089$
$\sin\theta^- = .573$	$P_{31} = .677$	$\epsilon_3^- = .131$
$\cos\theta^- = .819$	$P_{21} = .263$	$\epsilon_2^+ = -.144$
	$P_{22} = .431$	$\epsilon_3^+ = -.139$

b. CALCULATED AND MEASURED VALUES OF THE BANDEDGE EFFECTIVE MASS (0°K)

(units of m_o)

	Calculated	Measured[r]
m_v^t	.0373	.034 ± .007
m_c^t	.0382	.04 ± .008
m_v	.0693	.068 ± .015
m_c	.0641	.07 ± .015

r = Reference 121

APPENDIX C
MANY-BODY EFFECTS ON THE ABSORPTION EDGE OF PbSe

(i) Introduction

The calculation of the interband dielectric constant contribution detailed in Section IV. 2 is based on the single-electron-state picture of the behaviour of a solid, and it assumes that the electron states remain unchanged when vacancies and free carriers are added to the material. Further, it ignores the effects of lattice vibrations on the interband dielectric constant. In this appendix corrections to the calculations are considered.

In a PbSe crystal in which a substantial number of vacancies and free carriers are present, perturbations to the single electron states of the following types should be considered:

(a) Coulomb and core potential interactions with the vacancy centers.

(b) Coulomb interactions with the electron sea (assuming n type material).

(c) Acoustic and optical deformation potential interactions with phonons, and coulomb interaction with the LO phonon branch.

(d) Coulomb interaction of the electron-hole pair participating in a transition.

Detailed calculation of the dielectric constant taking simultaneous account of these perturbations is a very difficult task, and will not be attempted. Semiquantitative discussion of most of the interactions is given in what follows.

(ii) Defect Center Effects

Only the contribution of the Coulomb portion of the defect potential will be treated in this section; no adequate model exists to date of the core potential interaction appropriate to vacancies in the lead salts. Effects of the Coulomb interaction have been widely studied in the literature. It is known that in GaAs they are responsible for the formation of impurity states, impurity bands and band tails (extending up to 80 meV into the gap) in different regimes of defect center density.[113]

The interaction of free electrons and defects does not allow energy transfer between the particles, and is shielded by the lattice as well as the fermi sea.[123] The matrix element for electron scattering with momentum transfer q from a single defect center is given (neglecting nonparabolicity) by

$$V(q) = \frac{4\pi e^2}{q^2 \Omega} \cdot \frac{1}{\epsilon_s + \frac{4\pi e^2}{q^2} P(q, \omega = 0)} \quad \text{(C-1)}$$

Here Ω is the volume of crystal considered, ϵ_s is the static dielectric constant and $P(q, w)$ is the electron-intraband hole pair propagator for the fermi sea. An adequate approximation to $P(q, w)$ in many cases is given by the Fermi-Thomas result

$$P(q = 0, \omega = 0) = N(\epsilon_f) \quad \text{(C-2)}$$

where $N(\epsilon_f)$ is the density of states per unit energy and volume evaluated at the fermi surface (a degenerate semiconductor is assumed).

Wolff has demonstrated that the effects of a random distribution of vacancies on electron states high above the bandedge are adequately treated by lowest order perturbation theory in highly degenerate semi-

conductors (although near the bottom of the band higher order corrections are necessary).[123] In the other extreme, the theory of Halperin and Lax is widely accepted as an adequate treatment of the states perturbed far into the gap by the defect potentials (bandtails).[124] These two limits will be examined here.

According to Wolff, within the regime of the validity of perturbation theory, the contribution to electron self-energies produced by the defect centers is given by

$$\Sigma(p,\omega) = \frac{4\pi m^* e^4 n}{Q_s \epsilon^2} \cdot \frac{1}{2m^*\omega - p^2 - Q_s^2 + 2iQ_s\sqrt{2m\omega}} \qquad \text{(C-3)}$$

Here ω is the electron energy variable, n is the density of electrons present and Q_s is the Fermi-Thomas screening wavevector. Typical (real) energy level shifts may be obtained by evaluating the real part of this expression at $\omega = p^2/2m^*$, which gives approximately

$$\Delta E = \beta \frac{p^2}{2m^*} \cdot \frac{2Q_s}{p} \cdot \frac{1}{1 + \frac{4p^2}{Q_s^2}} \qquad \text{(C-4)}$$

where β is a dimensionless parameter that describes the strength of the electron-defect center interactions, given by

$$\beta = \frac{8\pi m^{*2} e^4 n}{Q_s^5 \epsilon^2} \qquad \text{(C-5)}$$

Expression (C-4), evaluated with material parameters typical of PbSe at 0°K, gives $\Delta E = 0.17$ meV for $p = k_{fermi}$, and $\Delta E = 0.32$ meV for $p = 1/2\ k_{fermi}$ for 10^{18} cm^{-3} carriers and vacancies. These energies are negligible on the scale of interest in calculating $\Delta \mathrm{Re}\ \epsilon_{cv}$. The material parameters used for PbSe at 0°K containing 10^{18} cm^{-3}

carriers are shown in Table IX; other derived quantities, including β and Q are also shown.

Wolff's expression additionally provides the imaginary self-energy,[123] a quantity that may be related to the electron effective lifetime and to the effective spread in k space of a state (and thus is a measure of the extent of non-k conservation in transitions between bands). The spectral density function $A(p, \omega)$ may be found from the above expression through the relations

$$A(p,\omega) = \frac{1}{\pi}\left|\mathrm{Im}\, G(p,\omega)\right| = \frac{1}{\pi}\left|\mathrm{Im}\frac{1}{\omega - p^2/2m^* - \Sigma(p,\omega)}\right| \qquad \text{(C-6)}$$

It is given by

$$A(p,\omega) = \frac{2\beta}{E_Q}\cdot\frac{\gamma^{1/2}}{[(\gamma-\xi^2)^2-\gamma+\xi^2-\beta]^2+4\gamma(\gamma-\xi^2)^2} \qquad \text{(C-7)}$$

where γ is the dimensionless energy ω/E_{Qs}, ξ is the dimensionless momentum p/Q_s and $E_{Qs} = h^2Q_s^2/2m^*$.

Typical lineshapes of quasiparticle states obtained from expression (C-7) are shown in Fig. 70, where carrier and vacanty densities of $10^{18}\mathrm{cm}^{-3}$ have again been assumed. Typical values of the energy linewidty are found to be .3 to .5 E_Q or 0.8 to 1.3 meV. The smallness of these values indicates that quasiparticle states are very well defined, and that k conservation should be an excellent approximation in highly doped PbSe at low temperatures.

The theory of Halperin and Lax yields the expression

$$\rho(E) = \frac{Q_s^3}{\beta^2 E_Q}\, a(\gamma)\exp\left[-\frac{b(\gamma)}{2\beta}\right] \qquad \text{(C-8)}$$

for the density of states in the tail, where β and γ are the same dimensionless parameters as in the theory of Wolff, and a(z) and b(z) are functions supplied by Ref. 124. The density of states has been evaluated here for PbSe at 0° and 77^oK for $10^{18} cm^{-3}$ and $10^{17} cm^{-3}$ carriers and vacancies as typical examples; the results are shown in Fig. 71. For the latter case the criterion of linear screening of the HL theory is not strictly valid, however. The static value of the dielectric constant was used. Rigid shifts in energy of the bands have been ignored, since these apply to both conduction and valence bands; for the symmetric bands of PbSe, the effect of the shifts on the energy gap is identically zero. From the graphs, bandtails are found to extend less than 1 meV into the bandgap of PbSe, and they contain fewer than 10^{15} states per cm^3. Thus their effects may be safely neglected for this range of doping. Self-consistently, the value of Q used in the calculation (which neglects bandtailing) is shown to be appropriate.

In discussions of the GaAs heavily doped with acceptors it is conventional to assume that the localized wavefunctions of the tail have approximately the size and shape of the shallow acceptor states $\psi_{acc}(r)$ determined by the use of effective mass theory. Within this approximation the spectral density $A(p, \omega)$ is given by[124]

$$A(k,\omega) = \frac{1}{\Omega} \rho_{tail}(\omega) \left| \int e^{i\bar{k}\cdot\bar{r}} \psi_{acc}(\bar{r}) d^3r \right|^2$$

$$= \frac{a^3}{\Omega} \rho_{tail}(\omega) \left(1 + a^2k^2\right)^{-4} \qquad \text{(C-9)}$$

where a is the value of the Bohr radius in the semiconductor. Equivalently, in the evaluation of the interband dielectric constant the localization of the states may be taken into account by assuming that the matrix element connecting valence band tail states and the (unperturbed) conduction band state k_c is[55]

$$|\langle i|p|k_c\rangle|^2 = P_{cv}^2 \cdot \frac{a^3}{\Omega} \cdot (1+a^2k_c^2)^{-4} \qquad \text{(C-10)}$$

When (C-10) is used in the calculation of ϵ near the bandedge of heavily doped GaAs it is found that the change in the denominator over the energy range of interest is slight. For example, $k_c a=1$ is not satisfied till $E_c = 25$meV. With this fact in mind it is frequently assumed that k conservation is totally invalid, and each valence band state couples to each conduction band state with the same matrix element. An equivalent calculation for PbSe yields the result $k_c a = 1$ for $E_c = 0.09$ meV. Thus it is clear that the same justification of the violation of k conservation is not effective in PbSe.

(iii) Exchange Energy Shifts

Interactions between electrons and the fermi sea have been studied at length using the techniques of many-body theory.[125,126] In moderately doped PbSe (10^{18}cm^{-3}) at low temperature it may be shown that a "high-density" (r_s less than 1) electron gas is established. Wolff has shown that under such conditions one of the major effects of the electron-electron interaction is to produce a shift in the effective electron energy levels.[123] This shift is approximately equal for each state, and is primarily due to the exchange interaction between electrons (long known to be the source of binding for high density electron gases).

The evaluation of the exchange energy shift for PbSe is not direct because of the energy dependence of the dielectric constant(which must be included in the calculation to describe the shielding of the Coulomb interaction between electrons). Part of this energy dependence occurs because the resonance of the lattice polarization takes place

in the energy range of interest. An approximate calculation is given here in which proper account is taken of the lattice.

The new system under consideration is assumed to consist of conduction band electrons in 4 pockets in k space interacting via Coulomb forces, background positive charge to achieve neutrality and longitudinal optical phonons that interact with the electrons via the Frohlich interaction. Its Hamiltonian is written:

$$H = \sum_{\nu=1}^{4}\sum_{k} \epsilon_k c^{+}_{k\nu} c_{k\nu} + \sum_{q} \hbar\omega_{\ell o} a^{+}_{q} a_{q} + \frac{1}{2}\sum_{\nu}\sum_{\mu}\sum_{k,k_1,q\neq 0} \frac{4\pi e^2}{q^2 \epsilon_\infty} c^{+}_{k_1-q\nu} c^{+}_{k+q\mu} c_{k\mu} c_{k_1\nu}$$
$$+ \sum_{\substack{q\neq 0 \\ k,\nu}} \left[V_q a_q c^{+}_{k+q,\nu} c_{k\nu} + V^{+}_{q} a^{+}_{q} c^{+}_{k-q\nu} c_{k\nu} \right] \tag{C-10}$$

where V_q corresponds to the bare Frohlich interaction:

$$V_q = -\frac{i\hbar\omega_{\ell o}}{q}\left(\frac{4\pi\alpha}{\Omega}\right)^{1/2}\left(\frac{\hbar}{2m^{*}\omega_{\ell o}}\right)^{1/4} \tag{C-11}$$

and

$$\alpha = \frac{e^2}{\hbar}\left(\frac{1}{\epsilon_\infty}-\frac{1}{\epsilon_s}\right)\left(\frac{m^{*}}{2\hbar\omega_{\ell o}}\right)^{1/2} \tag{C-12}$$

We wish to analyze the effects of including the last two terms.

If the last terms are evaluated in lowest order perturbation theory for an electron state at k=0 in the noninteracting ground state, the resulting energy shifts are well-known to be the following:

(a) Electron-electron term:

$$\Delta E = -\frac{4}{\pi \beta r_s} \cdot \frac{m e^4}{2\hbar^2 \epsilon_\infty^2} \qquad \text{(C-13)}$$

where

$$\beta = \left(\frac{4}{9\pi}\right)^{1/3} \quad , \quad r_s = \frac{m^* e^2}{\hbar^2 \epsilon_\infty} \left(\frac{3}{\pi n}\right)^{1/3} \qquad \text{(C-14)}$$

This is just the exchange energy of an electron at k=0. We note that the conventional parameter r_s is evaluated in (C-14) for a medium of dielectric constant ϵ_∞ and with a carrier density corresponding to the population of just one valley.

(b) Electron-phonon term: Provided that the fermi energy is small with respect to the optical phonon energy, the result is the polaron binding energy given by

$$\Delta E = -\alpha \hbar \omega_{lo} \qquad \text{(C-15)}$$

These lowest-order results fail to take into account phenomena that seem important for the calculation, among them:

(a) modification of the dielectric constant at low frequencies from ϵ_∞ to ϵ_{static}, which would profoundly affect the electron-electron interaction result;

(b) decrease of the electron-phonon interaction strength due to shielding by free carriers;

(c) change of the optical phonon frequency due to shielding.

Formalism of time-dependent field theory may be invoked to obtain more exact results. Following standard many-body practice, the electron-phonon interaction in (C-10) may be properly taken into account by considering an equivalent (bare) interaction between electrons mediated by the phonons. The (time-dependent) equivalent electron-electron interaction potential is:[127, 128]

$$V^{ph}(q,\omega) = |V_q|^2 \, D(q,\omega) \tag{C-16}$$

where

$$D(q,\omega) = \frac{2\omega_{LO}}{\omega^2 - \omega_{LO}^2 + i\delta} \quad , \; \delta = 0^+ \tag{C-17}$$

$D(q,\omega)$ is the T=0 phonon propagator. The (bare) interaction between electrons is written (as in (C-10)):

$$V^c(q,\omega) = \frac{4\pi e^2}{q^2 \Omega \epsilon_\infty} \tag{C-18}$$

It has been shown that when both interactions (C-16) and (C-18) are present, it is sufficient to consider a single (dressed) interaction potential between electrons, given by[128-130]

$$V^{tot}(q,\omega) = \frac{V^c(q,\omega) + V^{ph}(q,\omega)}{1 - [V^c(q,\omega) + V^{ph}(q,\omega)] \, P(q,\omega)} \tag{C-19}$$

$P(q,\omega)$ denotes the net electronic polarization propagator. The 4 distinct valleys are taken into account by writing

$$P(q,\omega) = \sum_{u=1}^{4} P_u(q,\omega) = 4P_u(q,\omega) \tag{C-20}$$

The dressed interaction of (C-19) contains terms of direct perturbation theory to all orders.

With algebraic manipulation, (C-19) may be reexpressed in the following way:

$$V^{tot}(q,\omega) = \frac{4\pi e^2}{q^2\Omega\, \epsilon_{tot}(q,\omega)} \tag{C-21}$$

where

$$\epsilon_{tot}(q,\omega) = \epsilon_\infty + \frac{\epsilon_0 - \epsilon_\infty}{1 - \frac{\omega^2}{\omega_{TO}^2}} - \frac{4\pi e^2}{q^2\Omega} P(q,\omega) \tag{C-22}$$

The relation (C-21) suggests that the present formalism includes properly the elements we wished to take into account (i.e., lattice dispersion). Further albegraic manipulation allows (C-19) to be re-written

$$V^{tot}(q,\omega) = U^c(q,\omega) + U^{ph}(q,\omega) \tag{C-23}$$

here $U^C(q,\omega)$ is the screened Coulomb interaction between electrons given by

$$U^c(q,\omega) = \frac{4\pi e^2}{q^2\Omega\,\epsilon_\infty} \cdot \frac{1}{1 - \frac{4\pi e^2}{q^2\Omega\,\epsilon_\infty} P(q,\omega)} \tag{C-24}$$

and $U^{ph}(q, w)$ is the screened phonon-induced interaction defined by

$$U^{ph}(q,\omega) = \frac{|V_q|^2}{\left(1 - \frac{4\pi e^2}{q^2 \Omega \epsilon_\infty} P(q,\omega)\right)^2} \cdot \frac{\omega_{LO}}{\Omega_q} \cdot D^*(q,\omega) \qquad \text{(C-25)}$$

The propagator $D^*(q, w)$ is defined by

$$D^*(q,\omega) = \frac{2\Omega_q}{\omega^2 - \Omega_q^2 + i\delta} \qquad \text{(C-26)}$$

and Ω_q is the renormalized longitudinal optical phonon frequency which satisfies

$$\Omega_q^2 = \omega_{TO}^2 \frac{\epsilon_s - \frac{4\pi e^2}{q^2 \Omega} P(q,\Omega_q)}{\epsilon_\infty - \frac{4\pi e^2}{q^2 \Omega} P(q,\Omega_q)} \qquad \text{(C-27)}$$

(C-27) is very reminiscent of the Lyddane-Sachs-Teller relation which applies in materials in the absence of carriers. The screening of the LO phonon near k=0 indicated by (C-27) is well-known theoretically and experimentally.

Within the Green's function formalism, the self energy $\Sigma(p,\omega)$ of an electron may be evaluated by[127]

$$\Sigma(p,\omega) = i \sum_k \int_{-\infty}^{\infty} \frac{d\omega'}{2\pi} V_{eff}(p-k, \omega-\omega') G(k,\omega') \qquad \text{(C-28)}$$

The first term in an expansion in powers of V is given by

$$\Sigma_0(p,\omega) = i \sum_k \int_{-\infty}^{\infty} \frac{d\omega'}{2\pi} V_{eff}(p-k, \omega-\omega') G_0(k,\omega') \qquad \text{(C-29)}$$

Here $G(p, \omega)$ is the electron Green's function in the interacting system, given by

$$G(p,\omega) = \frac{1}{\omega - \frac{p^2}{2m^*} - \Sigma(p,\omega) + i\eta_p} \qquad \text{(C-30)}$$

and G_o is the corresponding function in the absence of interactions

$$G_o(p,\omega) = \frac{1}{\omega - \frac{p^2}{2m^*} + i\eta_p}, \quad \begin{matrix} \eta_p = 0^+ \text{ for } p > p_f \\ \eta_p = 0^- \text{ for } p < p_f \end{matrix} \qquad \text{(C-31)}$$

In this appendix the approximation (C-29) is used to find the self-energy, For simplicity, Σ is evaluated for p=0 only. The form of $V^{tot}(q, w)$ indicated in (C-23) is convenient to use in the integration. From this expression it may be seen that two contributions to the self-energy must be considered: one arising from the screened electron-electron interaction, and one from a Frohlich-type interaction involving screened phonons.

Wolff has demonstrated that to order r_s the contribution to of the screened Coulomb interaction is just[123]

$$\Sigma^c(p=0,\omega) = -\frac{4}{\pi\beta r_s} \cdot \frac{m^* e^4}{2\hbar^2 \epsilon_\infty} \qquad \text{(C-32)}$$

This is the same result found in the absence of phonons and screening. It may be noted that r_s less than unity is obtained for carrier densities greater than $5\text{x}10^{16}\text{cm}^{-3}$ for PbSe.

To find the self-energy term contributed by the phonons, the integration indicated in (C-29) has been carried out, with the use of

additional approximations:

(a) The screening-induced phonon dispersion is ignored, and Ω_q is taken to be equal to ω_{lo} for all q. Although this appears very drastic, numerical estimates of the integral with the full expression for Ω_q indicate that little error is made with the approximation.

(b) The electronic polarization propagator is approximated by the Fermi-Thomas result. It has been argued that this is valid if $\omega_p \gg \omega_{lo}$.[128]

(c) The energy of a quasiparticle with p=0 is taken to be Σ (p=0, ω=0) instead of the proper result given by the solution to $\omega = \Sigma(o,\omega)$. This approximation is valid if $\Sigma(o,\omega)$ varies slowly with ω.

With these approximations, the integral becomes

$$\Sigma^{ph} = \frac{i\,4\pi e^2}{\Omega}\left(\frac{1}{\epsilon_\infty}-\frac{1}{\epsilon_s}\right)\frac{\hbar\omega_{lo}}{2}\sum_k \int_{-\infty}^{\infty}\frac{d\omega'}{2\pi}\cdot\frac{k^2}{[k^2+Q^2]^2}\times \tag{C-33}$$
$$\times\frac{2\omega_{lo}}{\omega'^2-\omega_{lo}^2+i\delta}\cdot\frac{1}{\omega'-\frac{k^2}{2m^*}+i\eta_k}$$

which yields

$$\mathrm{Re}\,\Sigma^{ph} = \frac{e^2}{\pi}\left(\frac{1}{\epsilon_\infty}-\frac{1}{\epsilon_s}\right)k_{lo}\times\left[\frac{x^3}{2(x^2+1)^2}\ln\left|\frac{y-x}{y+x}\right| + \frac{3x^2+1}{2(x^2+1)^2}\tan^{-1}y + \right.$$
$$\left. + \frac{3x^2-1}{2(x^2-1)^2}\tan^{-1}y + \frac{2x^3-3x^2+1}{(x^2-1)^2}\cdot\frac{\pi}{4} - \frac{yx^2}{(x^4-1)(y^2+1)}\right] \tag{C-34}$$

where $x^2 = h\,\omega_{lo}/E_Q$ and $y^2 = E_f/E_Q$. The expression (C-34) contains a logarythmic singularity for the carrier concentration that makes the fermi energy coincide with the optical phonon singularity. It is known from similar calculations that the quasi particle energy corresponding

to such carrier concentrations does not grow without bound; the expression $\omega = \Sigma(o,o)$ is no longer valid, however, and solutions of $\omega = \Sigma(o,\omega)$ must be obtained explicitly.[131] This refinement was omitted in this work.

The results obtained for Σ^c, Σ^{ph} and $\Sigma^c + \Sigma^{ph}$ for PbSe at 0^oK are shown vs. carrier concentration in Fig. 72. The dashed line is a smoother interpolated curve covering the region where Σ^{ph} is unknown due to the logarithmic singularity mentioned earlier. It should be noted that for carrier concentrations below $10^{17} cm^{-3}$ the approximation is $\omega_p \gg \omega_{lo}$ is not valid. The calculated curve, however, seems physically reasonable since it extrapolates to the polaron binding energy $\alpha \hbar\omega_{lo}$ properly at very low carrier concentrations.

The curve of Fig. 72 indicates that at high carrier densities the exchange energy shift approaches the value indicated by the well-known expression (C-13), in which the dielectric constant is given by ϵ_∞. In the region of 10^{17} - 10^{18} cm^{-3} carriers of interest for PbSe lasers, however, the change in the exchange energy shift is slight.

The numerous approximations made in this analysis have eliminated many physical effects from the problem. For example, in a certain range of carrier concentration it is known that the ground state of the system described by (C-10) is superconducting. It is nonetheless believed that the results are representative of the effects of interest for PbSe injection lasers.

(iv) Indirect Absorption Effect

In the preceding discussion only the contribution of optical phonons to the real part of the self-energy were considered, and only at $T=0^{o}K$. The consideration of Im Σ (p, ω) and thermal phonon effects is known to lead to additional changes in the behavior of ϵ_{cv} near the band edge. One major contribution of this type is the process of indirect absorption, whereby a photon and one or more phonons are simultaneously absorbed in the valence-conduction band transition. This process allows photons of energy less than the bandgap to be absorbed, and may contribute importantly to the shape of the absorption edge in PbSe. It has been postulated that the Urbach-type edge observed in lead salts is due to optical phonon-assisted indirect absorption.[81] Since the absorption tails extend far below the frequency of the bandgap, an adequate treatment of the effect must include multiphonon processes. Dunn[132] and Mahan[133] have shown that when phonon-assisted processes of all orders are considered, absorption coefficients with approximately exponential variation with frequency result; their analysis is not directly applicable to PbSe, however, since they consider only crude models of the conduction and valence bands, and omit the effect of carriers on the strength and k dependence of the electron-phonon coupling. No more refined calculation is attempted here. The experimental evidence concerning the absorption edge of lead salts reviewed in Section IV. 2(ii) suggests that the characteristic energy E_s of the tail in PbSe is near 3 meV at $77^{o}K$, which is adequately taken into account by the homogeneous brodening. The similarity of shape of the predicted tails is evident in Fig. 73, where an appropriate broadened parabolic absorption edge (with no carriers present) is compared with the exponential edge shape, using parameters approximately applicable to PbSe at $77^{o}K$.

Potentially important for lead salt lasers are mode losses due to indirect absorption at the lasing frequency. The burstein shift has the effect of eliminating interband absorption near the bandgap in material that is degeneratley doped; at fininte temperature, however, the phonon-assisted processes counteract the effect of this shift, and might lead to appreciable absorption coefficients at the bandgap in unpumped material. No proper calculation of this absorption is available in the literature. It is taken into account in this work again by the ad hoc assumption of homogeneous broadening, which, as demonstrated in Chapter V, considerably reduces the gain at a given frequency for large enough values of $\Delta\omega$. The most appropriate value of $\Delta\omega$ as a function of temperature and carrier concentration is not known, however.

(v) Lifetime Effects

In many cases the imaginary part of the self-energy $\Sigma(p,\omega)$ varies slowly with ω for constant p, and for such cases it is adequately taken into account by a quasiparticle lifetime τ_p (which varies, in general, with p and thus with $E = p^2/2m^*$). It is of interest to detmine the most appropriate value of τ_p for use in the calculations of $\epsilon_{interband}$.

Several different regimes of quasiparticle energy and carrier concentration must be considered. For the calculation of Im ϵ at the lasing frequency (i.e., the mode gain), states very near the bandedge are important. Furthermore, the largest contributions to the net gain come from regions where the carrier quasifermi levels are near the bandedge. Thus typical states to be considered are those shown in the diagram of Fig. 74a. Scattering events with the emission of optical phonons and plasmons are not allowed in this case; important scattering mechanisms are expected to be acoustic phonon scattering,

defect scattering and scattering with the absorption of optical phonons. An approximate figure for the quasiparticle lifetime may be obtained from the momentum relaxation time τ_{rel} that is inferred from DC mobility measurements; using a value of mobility at 77°K of 20,000 $cm^2/Vsec$, the lifetime is found to be

$$\tau = \frac{m^* \mu}{e} = 5.7 \times 10^{-13} sec \tag{C-35}$$

or $\hbar/\tau$ = 1.15 meV. Calculations by Ravich et. al.[134] have led to the conclustion that at 77°K the lifetime is dominated by polar optical phonon scattering at concentrations below 9 x $10^{18} cm^{-3}$ carriers, although there are substantial components due to the remaining mechanisms. Straightforward application of the Golden Rule leads to an estimate for the lifetime of an electron at k=0 due to polar optical phonon absorption given by

$$\frac{\hbar}{\tau} = 2\alpha E_{lo} \cdot \frac{E_{lo}}{E_{lo} + E_{Q\infty}} \cdot \frac{1}{\exp(E_{lo}/kT) - 1} \cdot \left[1 - f(E_{lo})\right] \tag{C-36}$$

Here E_{lo} is the energy of the LO phonon that is capable of satisfying the energy conservation requirement when interacting with the k=0 electron (keeping in mind the dispersion of that branch in the presence of carriers), and

$$E_{Q\infty} = \frac{\hbar^2}{2m^*} \cdot \frac{4\pi e^2}{\epsilon_\infty} \cdot P(q=0, \omega=0) \tag{C-37}$$

For PbSe with $10^{17} cm^{-3}$ carriers at 77°K, a reasonable estimate for E_{lo} might be 15 meV; with this value, (C-36) yields $\hbar/\tau$ = 0.35 meV, which appears to be in rough agreement with the conclusion of Ravich.

The effects of electron-electron interactions are not included in the number derived from measured mobilities, since these interactions conserve the momentum of the charge carriers; however, they are expected to be small. It should be noted that since electrons and holes are affected equally, the rate at which the phase of the optical interaction is disturbed is twice the relaxation rate of either carriers.

In material that contains greater carrier densities, other scattering mechanisms may occur. As indicated in Fig. 74b, interactions with the emission of optical phonons and plasmons are possible in the final state of an electron-hole recombination. For this case, the optical phonon limited lifetime is given by an expression analogous to (C-36) which contains a factor of $(1 + n_{ph})$ rather than n_{ph} (where n_{ph} is the phonon mode occupation number). With $10^{18}cm^{-3}$ carriers in PbSe at $77^{O}K$, this limit is obtained; using an estimated value of ϵ_{lo} of 11 meV, application of (C-36) gives near 1.1 meV. The value of $\epsilon_{lo} / (\epsilon_{lo} + \epsilon_{Q})$ is near 0.25, indicating that the electron-phonon strength is substantially reduced by the carriers.

In the calculation of Re ϵ_{cv}, the states of interest are distributed over a wide range of energies. Relaxation processes involving the final states of the created electron-hole pair are illustrated in Fig. 74c. In addition to the processes mentioned above, electron-electron interactions are expected to have a substantial effect in this case. According to Wolff, the relaxation rate of the created hole due to the formation of single particle excitations in the sea of electrons (at $T=0^{0}K$) is given by

$$\frac{\hbar}{\tau} = \frac{8k_f}{\pi Q_\infty} \cdot \frac{e^4 m^*}{\hbar^3 \epsilon_\infty} \cdot \left[\frac{2}{3} \frac{p}{Q_\infty} + \tan^{-1}\left(\frac{2p}{Q}\right) - \frac{16}{9} \ln\left(1 + \frac{3p}{2Q}\right)\right] \qquad \text{(C-38)}$$

where p is the hole momentum, k_f is the fermi momentum of the electrons, and

$$Q_\infty^2 = \frac{4\pi e^2}{\epsilon_\infty} P(q=0, \omega=0) \tag{C-39}$$

When (C-38) is evaluated for PbSe at 77°K with parameters corresponding to 10^{18}cm^{-3} carriers, the result is $\hbar/\tau = 0.6$ meV for $p = k_f$. If the energy of the hole is large enough to allow plasmon emission, then the relaxation rate will be substantially greater. Also, optical phonon emission rates are likely to be faster than indicated by (C-36) due to a higher density of final states than considered in the earlier case. An experimental indication of the relaxation rate for states high in a band (except for the electron-electron processes) is given by the observed results of broadening of the plasma reflectivity lineshape given by Mijcielski, et. al., who report $\hbar/\tau = 4.2$ meV for PbSe at 30°K.[72]

It should be remarked that the proper value of the broadening parameter $\Delta\omega$ of a homogeneous lineshape, as defined, for example, in (V-6), is $\Delta\omega = 1/\tau$. The resulting full width (between half-amplitude points) of the Lorentzian line is $2/\tau$.

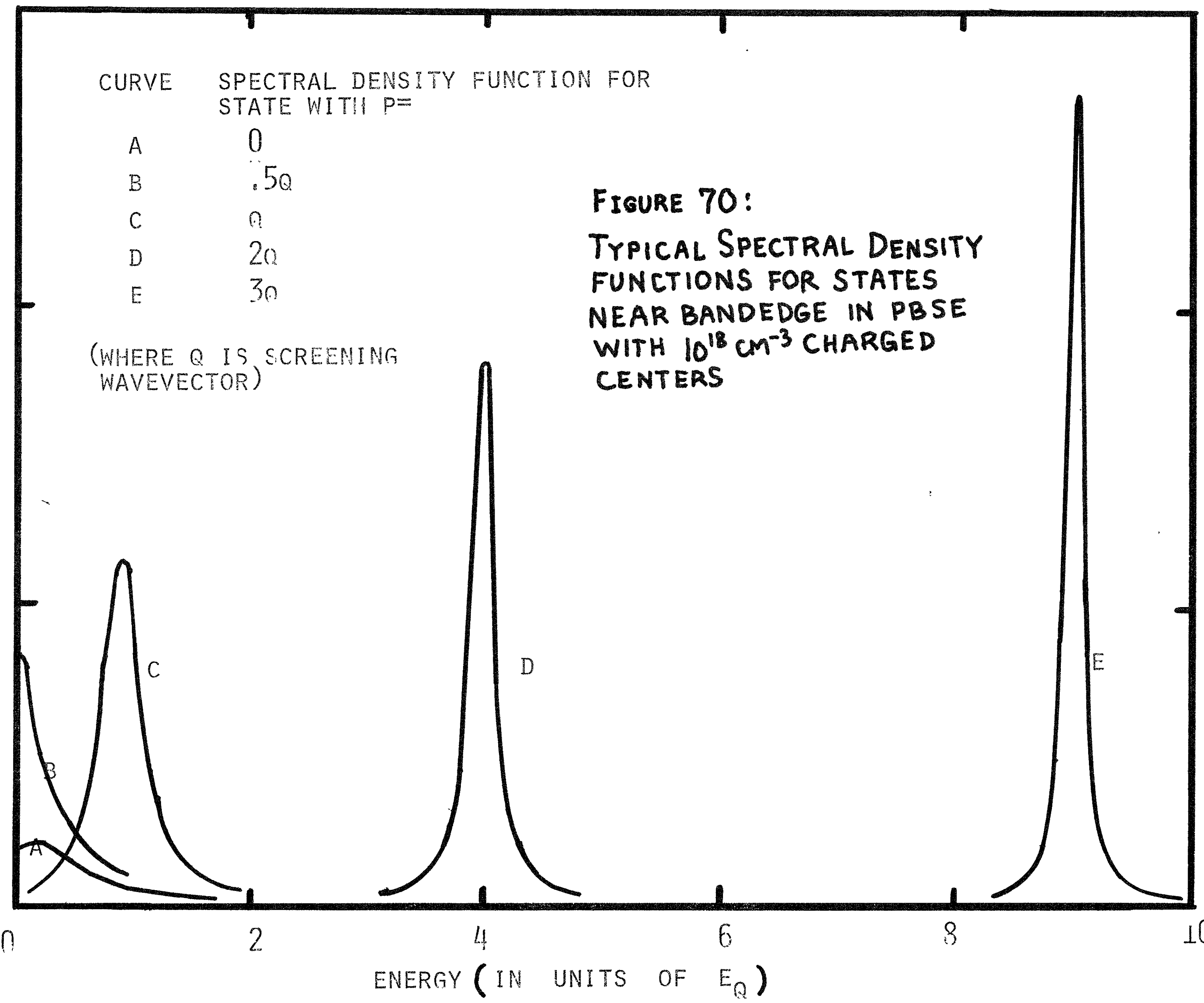

FIGURE 70: TYPICAL SPECTRAL DENSITY FUNCTIONS FOR STATES NEAR BANDEDGE IN PBSE WITH 10^{18} CM^{-3} CHARGED CENTERS

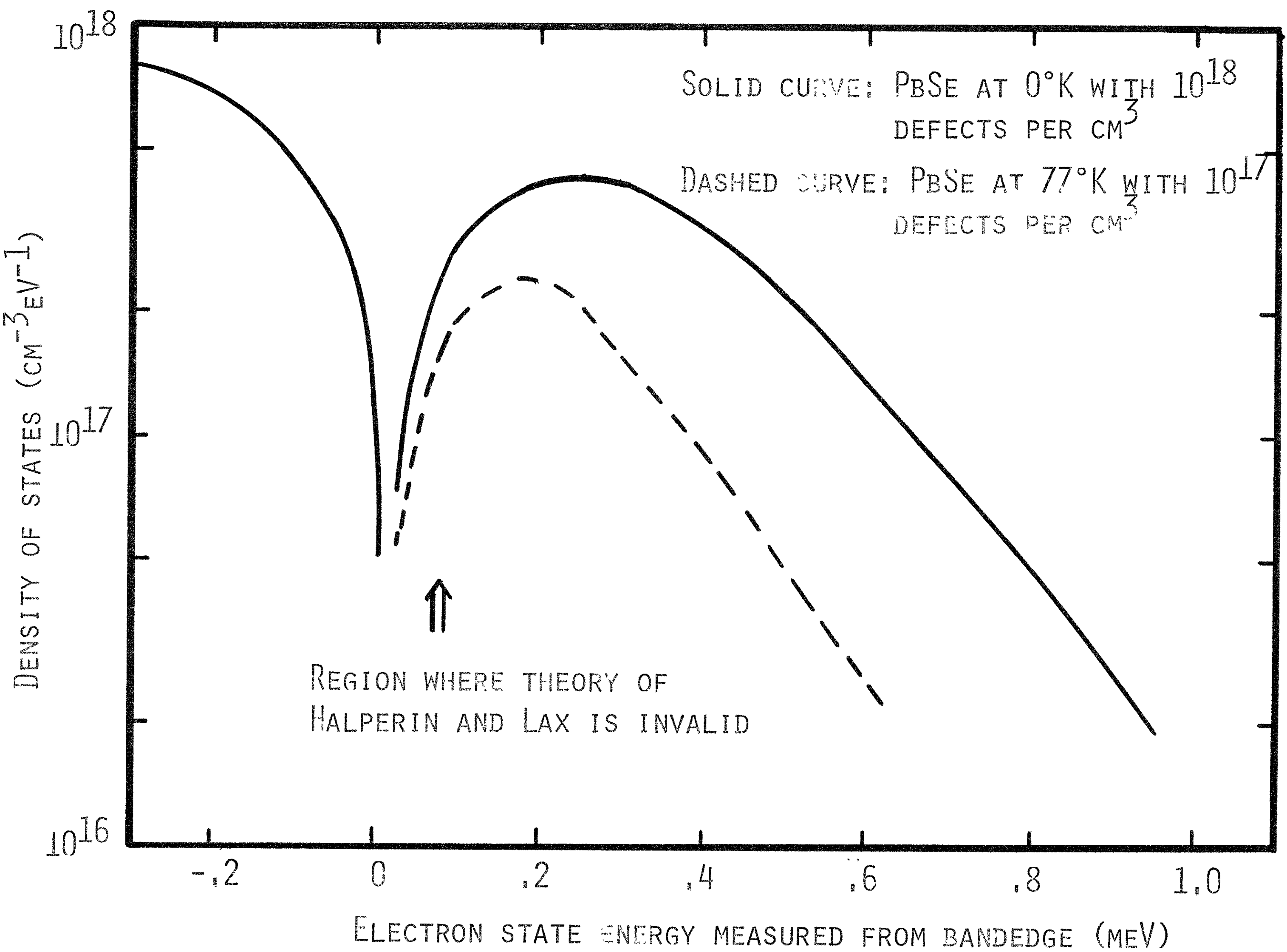

FIGURE 71: DENSITY OF STATES IN BANDTAILS, CALCULATED WITH THE THEORY OF HALPERIN AND LAX, APPLIED TO PBSE

Figure 72: Calculated Variation of Exchange Energy Shifts with Carrier Concentration in PbSe at T=0°K

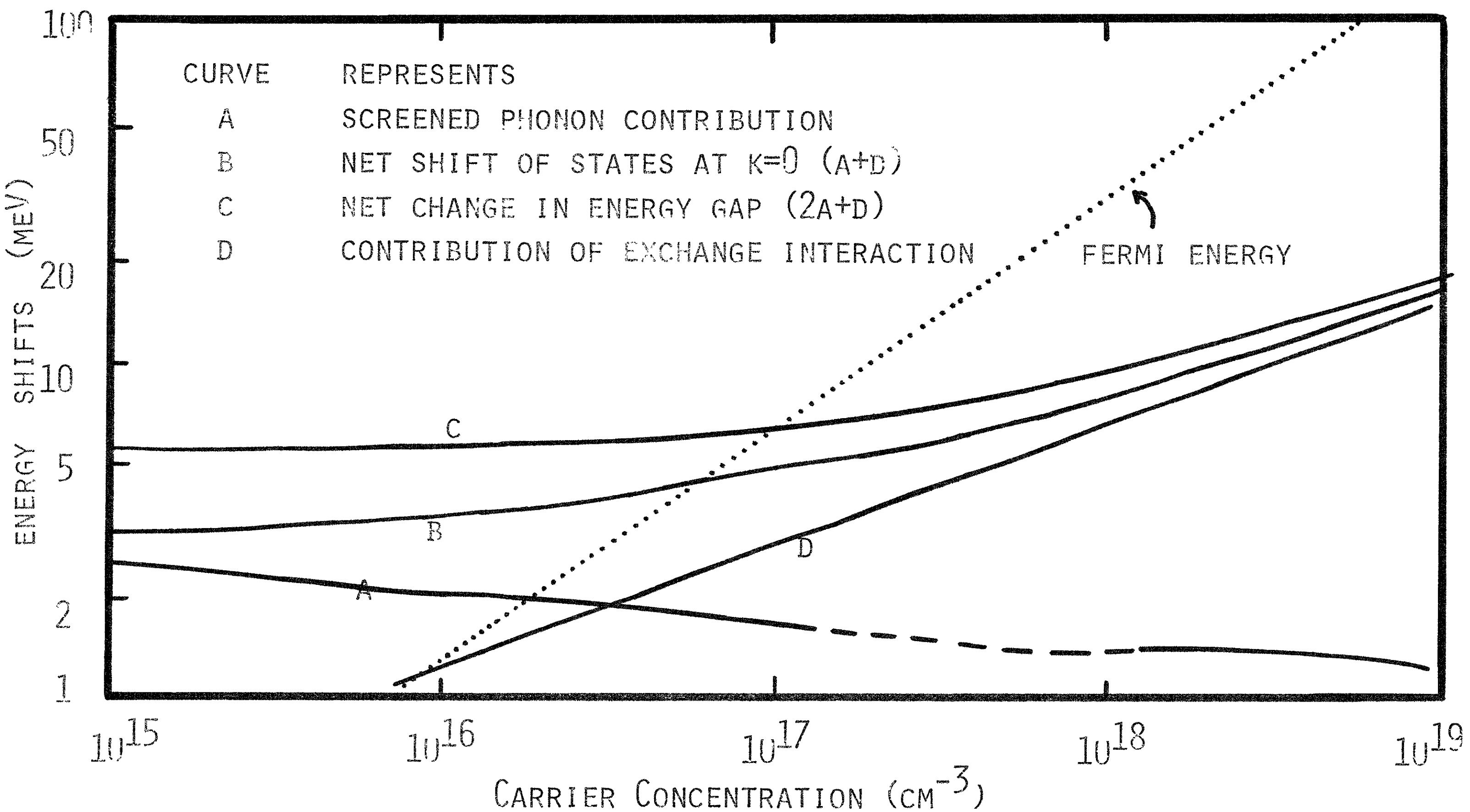

FIGURE 73: COMPARISON OF FREQUENCY DEPENDENCE OF HOMOGENEOUSLY BROADENED ABSORPTION EDGE AND EDGE SATISFYING URBACH'S RULE

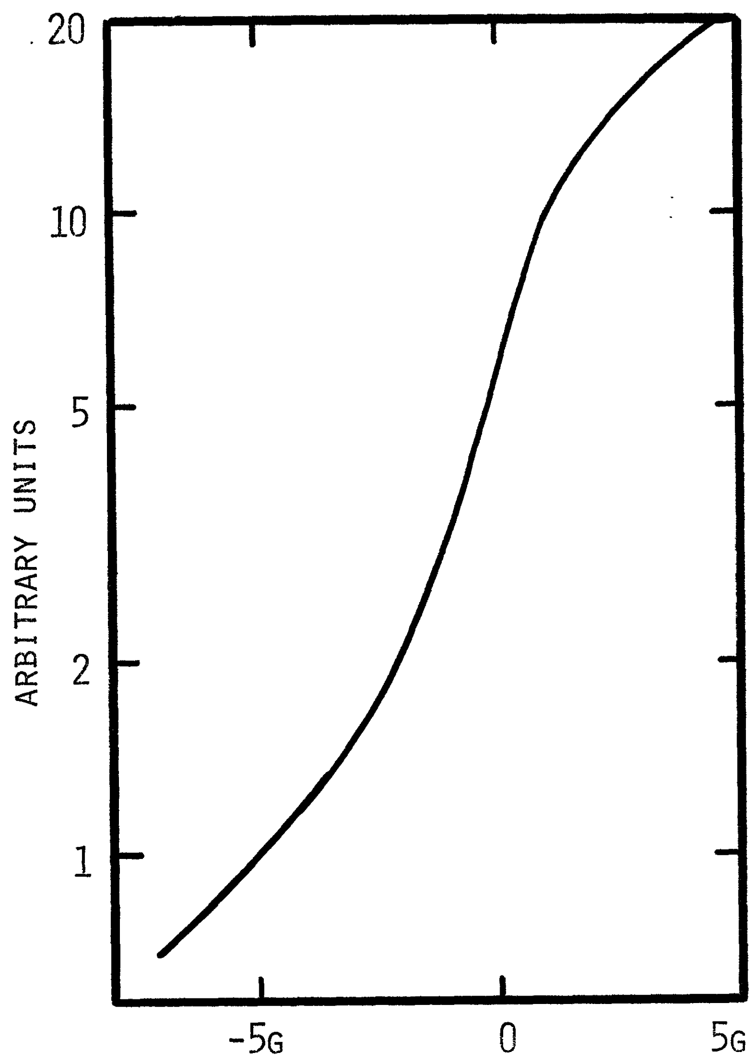

PARABOLIC ABSORPTION EDGE HOMOGENEOUSLY BROADENED, WITH A LINEWIDTH G.

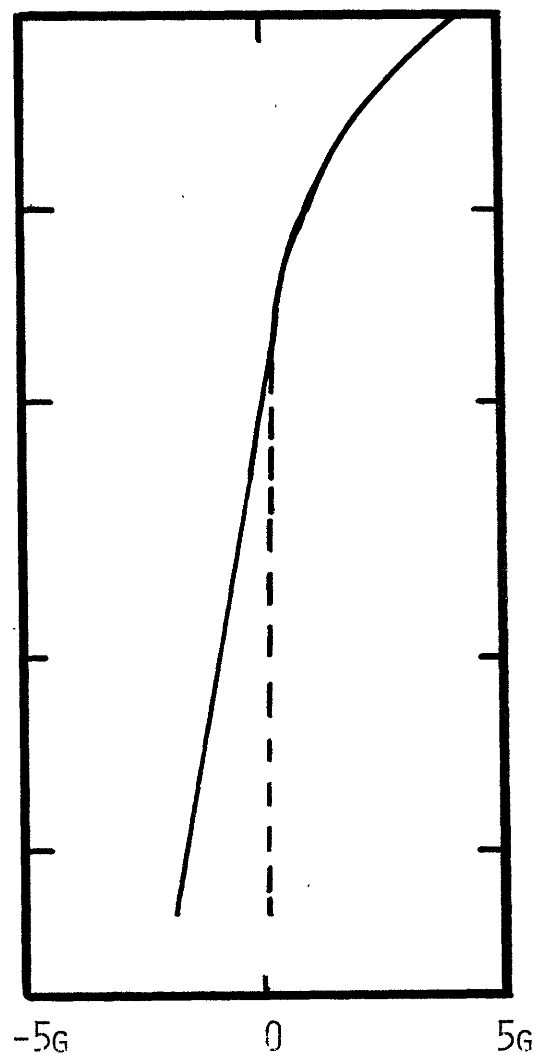

PARABOLIC ABSORPTION EDGE EXTENDED WITH AN EXPONENTIAL TAIL HAVING A CHARACTERISTIC ENERGY G.

FIGURE 74: SCHEMATIC OF DIFFERENT REGIMES OF INTEREST IN THE CALCULATION OF τ

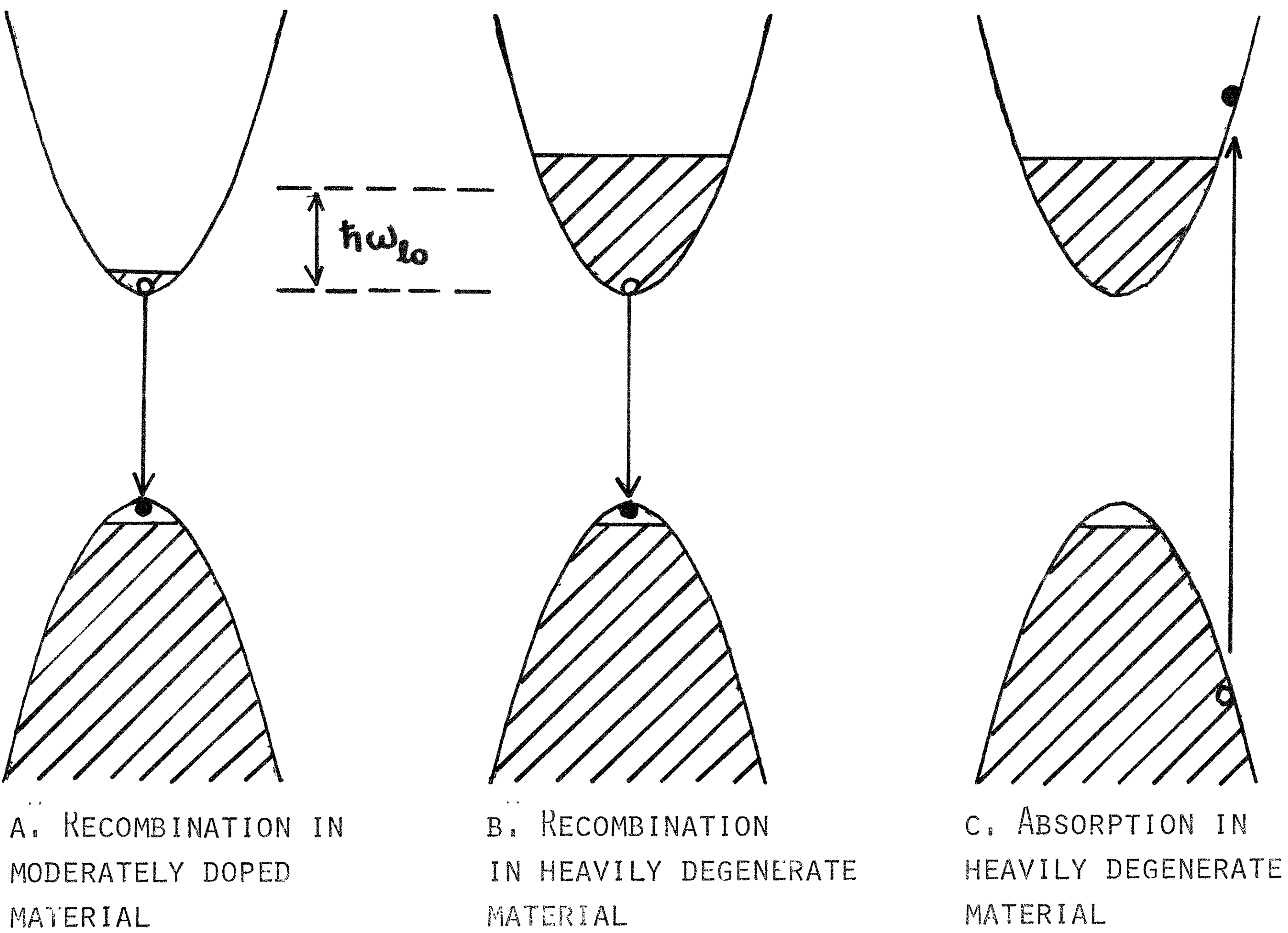

TABLE IX

PARAMETERS USED IN ESTIMATION OF MANY- BODY EFFECTS IN PbSe

Fundamental Parameters

$m^* = .05m_o$ $\hbar\omega_{lo} = 19$ meV

$\epsilon_\infty = 26$ $\hbar\omega_{to} = 5.8$ meV

$\epsilon_s = 280$ $\alpha = 0.21$

Derived Parameters[a] for $n = 10^{18}$ cm^{-3} and $T = 0^oK$

$E_f = 30$ meV

$\beta = 0.446$

$\frac{Q_s}{k_{fermi}} = 0.296$ $\frac{Q}{k_{fermi}} = 0.875$

$E_{Q_s} = 2.55$ meV $E_Q = 22.3$ meV

r_s (obtained using ϵ_s) = .033

r_s (obtained using ϵ_∞) = .3

[a] Parabolic bands were assumed for these calculations.

APPENDIX D
ADDITIONAL WAVEGUIDE MODELS

In this appendix, solutions are presented for the propagating modes of dielectric waveguides with several additional model profiles. The results obtained here have the primary purpose of examining the regime of applicability of, and obtaining corrections to, the waveguide model discussed in Chapter IV. The dielectric profiles to be discussed are shown in Fig. 75. Model A is useful for determining corrections to the mode width of the symmetric profile model discussed earlier, particularly with respect to effects of injected minority carriers. Model B is useful for determining the amount of "mode-spillover" that occurs, that is, the extent to which the optical field penetrates the homogeneous n type bulk; this is of particular concern in the discussion of very shallow junctions.

(i) Model A

According to this model, the dielectric constant is assumed to have the form

$$\begin{aligned} \epsilon(x) &= \epsilon_p - \epsilon_0 \beta |x| \quad \text{for } |x| > L_A \text{ (region i)} \\ \epsilon(x) &= \epsilon_p - \epsilon_0 \beta L_A \quad \text{for } |x| \leq L_A \text{ (region ii)} \end{aligned} \qquad \text{(D-1)}$$

Only the fundamental mode, which is even about the origin, will be discussed. The solution to the wave equation in region i may be readily shown to be

$$\psi_i(x) = A \cos kx \qquad \text{(D-2)}$$

where

$$k = (\omega^2\mu_0\epsilon_p - \omega^2\mu_0\epsilon_0\beta L_A - \gamma^2)^{1/2} = \frac{1}{x_0}(\lambda_m - \frac{L_A}{x_0})^{1/2} \quad \text{(D-3)}$$

and $e^{i\gamma z}$ propagation has been assumed. In region ii the wave equation is identical to that discussed in Chapter IV. 3, and solutions may again be expressed as

$$\psi_{ii}(x) = Ai\left(-\lambda_m + \frac{|x|}{x_0}\right) \quad \text{(D-4)}$$

where

$$\lambda_m = \frac{\omega^2\mu_0\epsilon_p - \gamma^2}{(\omega^2\mu_0\epsilon_0\beta)^{2/3}} \quad , \quad x_0 = (\omega^2\mu_0\epsilon_0\beta)^{-1/3} \quad \text{(D-5)}$$

The boundary conditions along the surface $x = L_A$ are given by

$$\begin{aligned} \psi_i(L_A) &= \psi_{ii}(L_A) \\ \psi_i'(L_A) &= \psi_{ii}'(L_A) \end{aligned} \quad \text{(D-6)}$$

while equivalent expressions hold at $x = -L_A$. Since the solution is even about $x = 0$, only $x = L_A$ need be considered. Algebraic manipulation allows (D-6) to be expressed as

$$\frac{Ai'(-u)}{Ai(-u)} = -\sqrt{u}\tan\left(\frac{L_A}{x_0}\sqrt{u}\right) \quad \text{(D-7)}$$

where $u = \lambda_m - \frac{L_A}{x_0}$

(D-8)

Equations (D-7) and (D-8) have been solved numerically in order to obtain the variation of the eigenvalue λ_m with the parameter L_A/x_o; solutions are shown in Fig. 76a. For a given value of λ_m, the solution $\psi_i(x)$ may be conveniently written

$$\psi_i(x) = \frac{Ai\left(-\lambda_m + \frac{L_A}{x_o}\right)}{\cos\left(\frac{L_A}{x_o}\sqrt{\lambda_m - \frac{L_A}{x_o}}\right)} \cos\left(\frac{x}{x_o}\sqrt{\lambda_m - \frac{L_A}{x_o}}\right) \qquad \text{(D-9)}$$

The mode shape obtained for several values of L_A/x_o is shown in Fig. 77. The variation of mode width w_o (full width between e^{-1} amplitude points) with L_A/x_o is given in Fig. 78 in terms of x_o.

(ii) Model B

The dielectric constant variation is assumed to follow

$$\begin{aligned} \epsilon(x) &= \epsilon_p - \epsilon_o \beta L_B \quad \text{for } x < 0 \qquad \text{(region i)} \\ \epsilon(x) &= \epsilon_p - \epsilon_o \beta x \quad \text{for } x > 0 \qquad \text{(region ii)} \end{aligned} \qquad \text{(D-10)}$$

The wave equation solutions in regions i and ii are given in this case by the forms

$$\begin{aligned} \psi_i(x) &= A \exp \frac{x}{W} \\ \psi_{ii}(x) &= Ai\left(-\lambda_m + \frac{x}{x_o}\right) \end{aligned} \qquad \text{(D-11)}$$

Here

$$W = (\gamma^2 - \omega^2\mu_o\epsilon_p + \omega^2\mu_o\epsilon_o\beta L_B)^{-1/2} = x_o\left(\lambda_m - \frac{L_B}{x_o}\right)^{-1/2} \qquad \text{(D-12)}$$

To match boundary conditions at x = 0, the following equation must be satisfied:

$$\frac{Ai'(-\lambda_m)}{Ai(-\lambda_m)} = \sqrt{\frac{L_B}{x_o} - \lambda_m} \qquad \text{(D-13)}$$

The variation of λ_m with L_B/x_o obtained from (D-13) is shown in Fig. 76b. It may be noted that for $L_B/x_o < 1.03$ no confined modes are possible. Several examples of the modes obtained are shown in Fig. 79. For a given value of λ_m, the solution $\psi_i(x)$ is conveniently given by

$$\psi_i(x) = Ai(-\lambda_m)\exp\left(\frac{x}{x_o}\sqrt{\frac{L_B}{x_o} - \lambda_m}\right) \qquad \text{(D-14)}$$

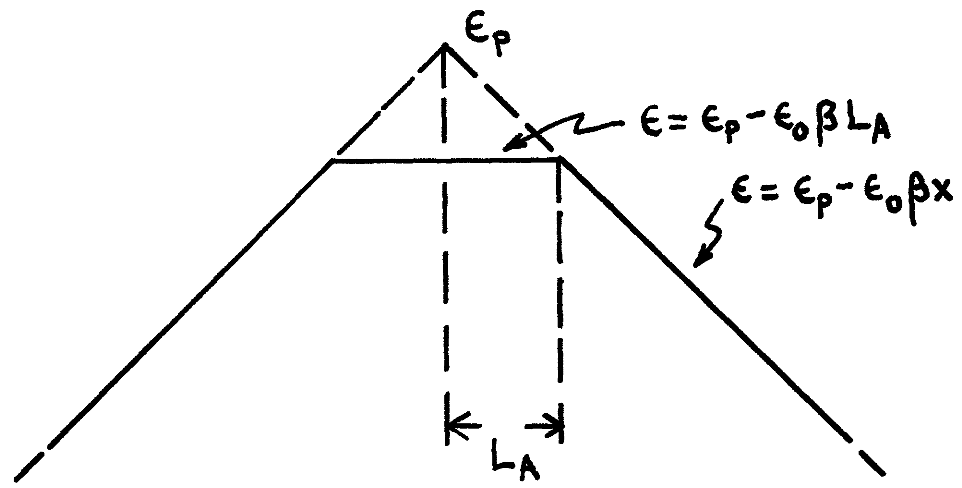

PROFILE MODEL A

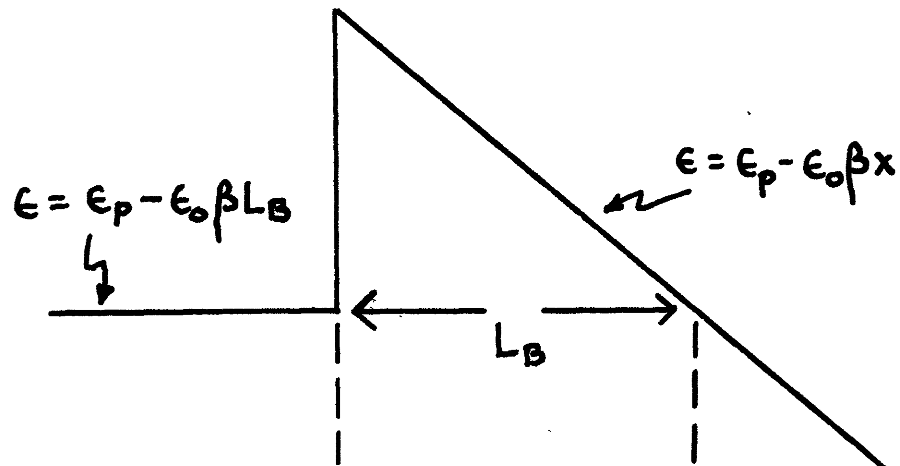

PROFILE MODEL B

FIGURE 75: DIELECTRIC WAVEGUIDE MODELS A AND B

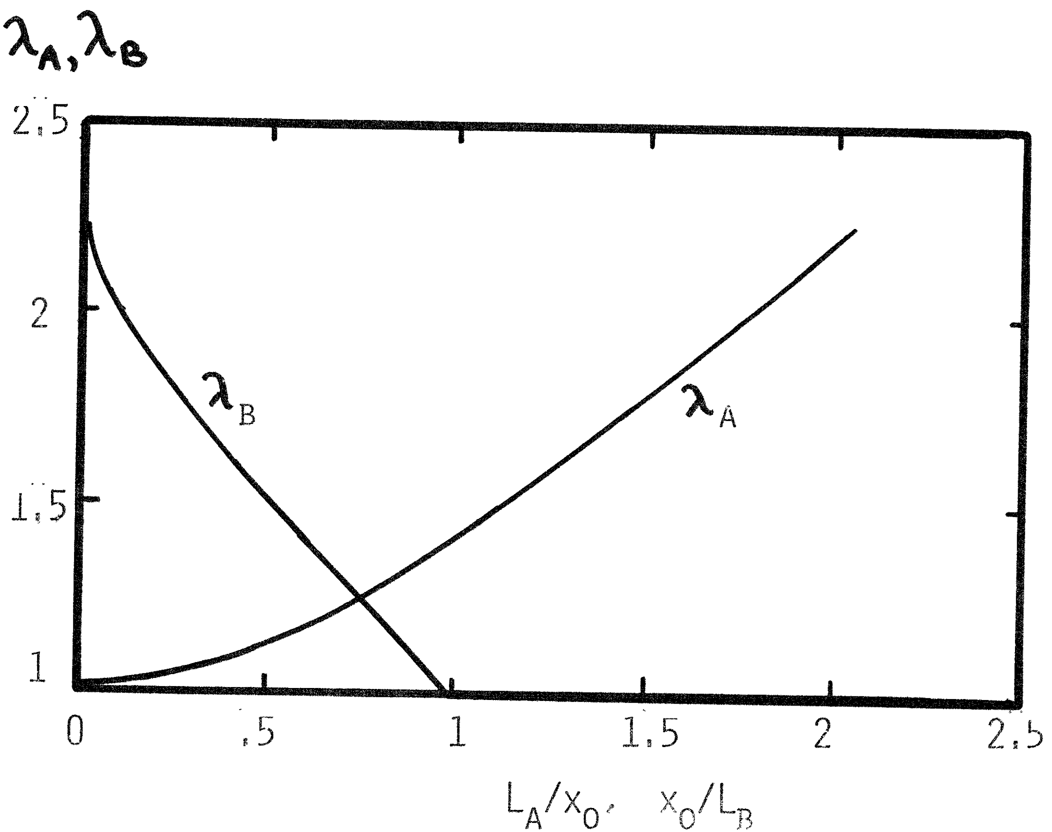

FIGURE 76: VARIATION OF EIGENVALUES λ_A AND λ_B WITH PARAMETERS L_A/x_0 AND x_0/L_B

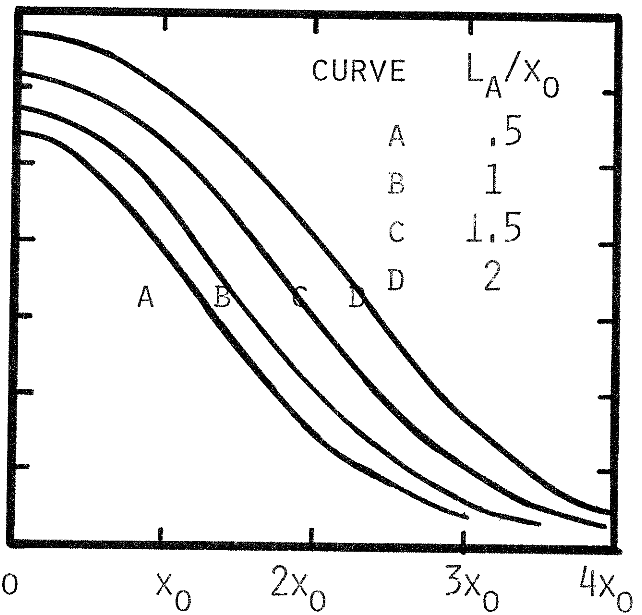

FIGURE 77: TYPICAL MODESHAPES FOR FUNDAMENTAL MODE OF DIELECTRIC PROFILE MODEL A

(CURVES ARE SYMMETRIC ABOUT x=0)

Figure 78: Variation of Mode Width w_0 with L_A/x_0

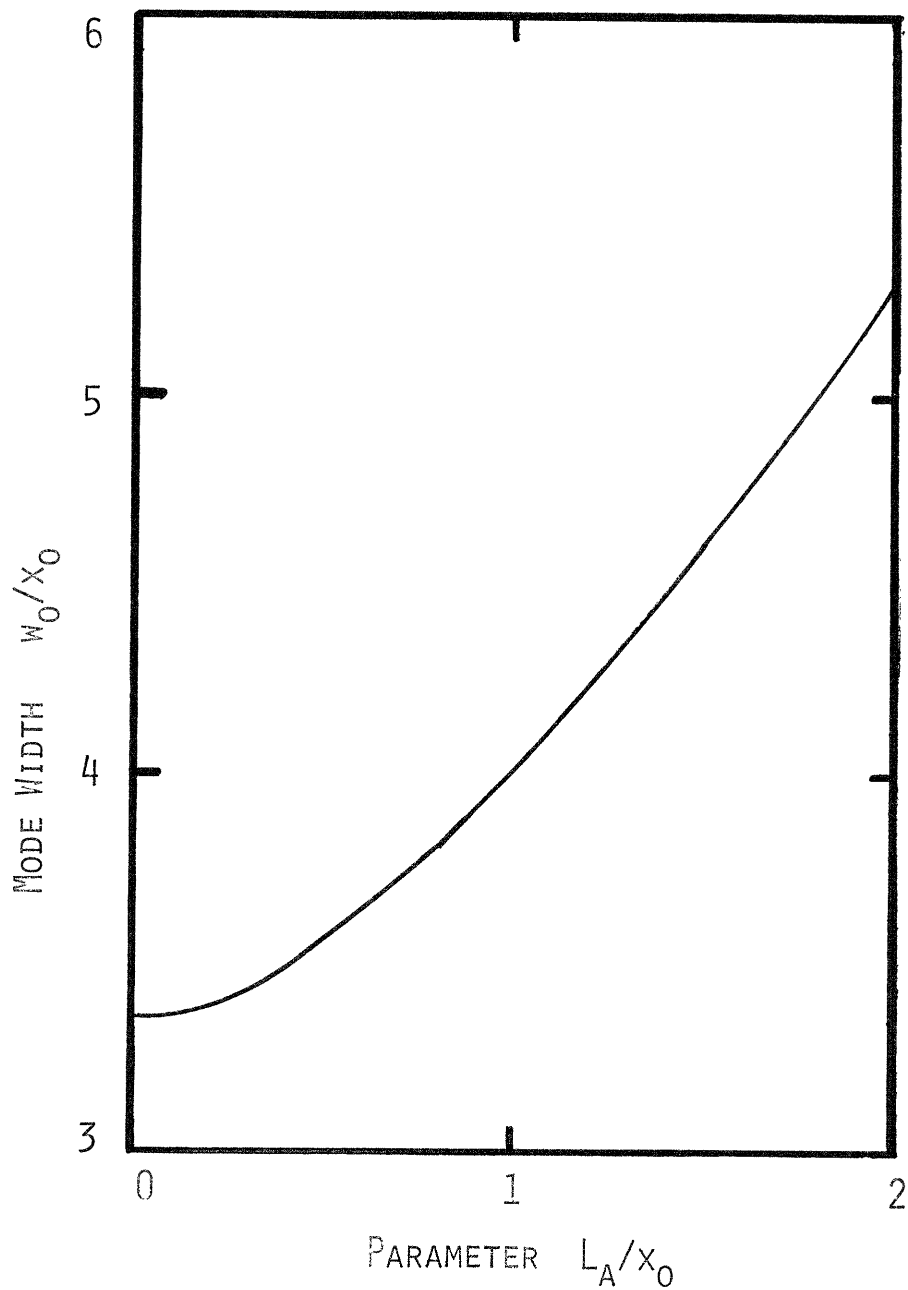

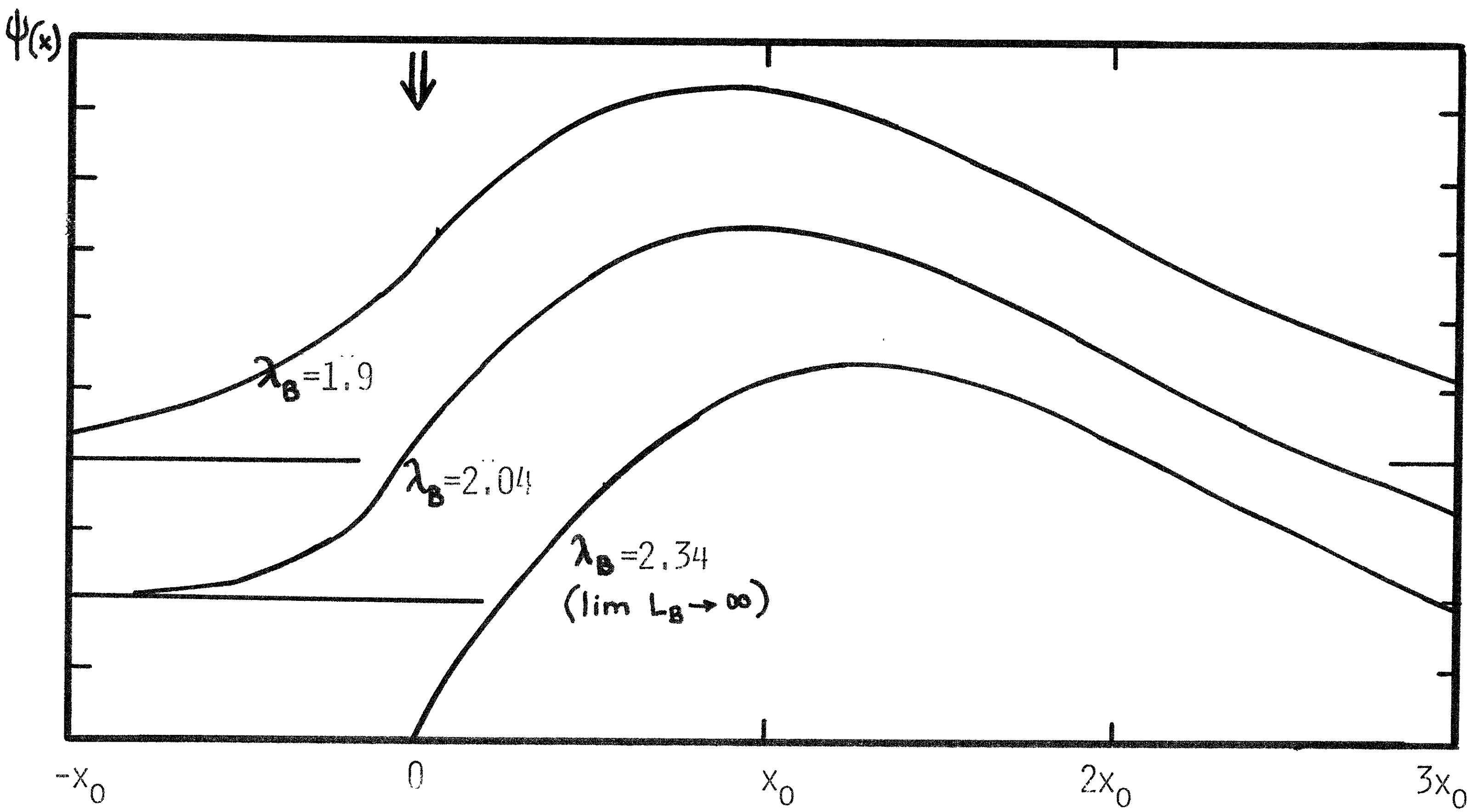

FIGURE 79: TYPICAL MODESHAPES OF FUNDAMENTAL MODE FOR DIELECTRIC PROFILE MODEL B

REFERENCES

1 J.F. Butler, A.R. Calawa, R.J. Phelan, Jr., T.C. Harman, A.J. Strauss and R.H. Rediker, Appl. Phys. Letters 5, 75 (1964).

2 T.C. Harman in The Physics of Semimetals and Narrow-Gap Semiconductors, eds. D.L. Carter and R.T. Bate, Pergamon Press, 1971, p. 363.

3 I. Melnagailis in Proceedings of the 6th Dept. of Def. Conference on Laser Technology (Colorado Springs, March 26-28, 1974).

4 E.D. Hinkley, T.C. Harman and C. Freed, Appl. Phys. Letters 13, 49 (1968).

5 E.D. Hinkley, and C. Freed, Phys. Rev. Letters 23, 277 (1969).

6 K.W. Nill, F.A. Blum, A.R. Calawa and T.C. Harman, J. Nonmetals 1 , 211 (1973).

7 E.D. Hinkley, A.R. Calawa, P.L. Kelley and S.A. Clough, J. Appl. Phys. 43, 3222 (1972).

8 E.D. Hinkley, Appl. Phys. Letters 16, 351 (1970).

9 K.W. Nill, F.A. Blum, A.R. Calawa and T.C. Harman, Chem. Phys. Letters 14, 234 (1972).

10 F.A. Blum, K.W. Nill, P.L. Kelley, A.R. Calawa and T.C. Harman, Science 177, 694 (1972).

11 I. Melngailis, IEEE Trans. Geoscience Electronics GE-10, 7 (1972).

12 R.W. Ralston, I. Melngailis, A.R. Calawa and W. T. Lindley, IEEE JQE QE-9, 350 (1973).

13 J.N. Walpole, A.R. Calawa, R.W. Ralston and T.C. Harman, J. Appl. Phys. 44, 2905 (1973).

14 J.N. Walpole, A.R. Calawa, R.W. Ralston, T.C. Harman and J.P. McVittie, Appl. Phys. Letters 23, 620, (1973).

15 L.R. Tomasetta and C.G. Fonstad, Appl. Phys. Letters 24, 567 (1974); S. H. Groves, K.W. Nill and A.J. Strauss, Appl. Phys. Letters 25, 331 (1974).

16 A.L. McWhorter, Sol. St. Electronics 6, 417 (1963).

17 A. Yariv and R.C.C. Leite, Appl. Phys. Letters 2, 55, (1963).

18 M.B. Panish, I. Hayaski and S. Sumski, Appl. Phys. Letters 16, 326 (1970).

19 Zh.J. Alferor, V.M. Andreer, V.I. Korol'kov, E.L. Portnoi and D.N. Tret'yakov, Sov. Phys. Semicond. 2, 843 (1969).

20 R.J. Hall and D. Olechna, J. Appl. Phys. 34, 2565 (1963).

21 F. Stern, Phys. Rev. 133, A1653 (1964).

22 F. Stern, in Proc. Intel. Conf. on Phys. of Semicond., Paris, 1964, p. 165.

23 A.L. McWhorter, J.H. Zeiger and B. Lax, J. Appl. Phys. 34, 235 (1963).

24 I. Hayashi, M.B. Panish and F.K. Reinhart, J. Appl. Phys. 42, 1929 (1971).

25 I. Hayashi, M.B. Panish, P.W. Foy and S. Sumski, Appl. Phys. Letters 17, 109 (1970).

26 R.W. Ralston, J.N. Walpole, A.R. Calawa, T.C. Harman and J.P. McVittie, J. Appl. Phys. 45, 1323 (1974).

27 T.C. Harman (to be published in J. Non-Metals).

28 A.R. Calawa, T.C. Harman, M. Finn and P Youtz, Trans. Met. Soc. AIME 242, 374 (1968).

29 R.L. Guldi, PhD. Thesis, M.I.T. E.E. Dept. (1971).

30 N. Parada and G.W. Pratt, Jr., Phys. Rev. Letters 22, 180 (1969); G.W. Pratt, Jr., J. Nonmetals 1, 103 (1973).

31 A.J. Strauss and R.F. Brebick, J. de Physique, 29, Supplement to No. 11, p.4 (1968).

32 W.W. Scanlon, Phys. Rev. 126, 509 (1962).

33 R.W. Brodersen, J.N. Walpole and A.R. Calawa, J. Appl. Phys. 41, 1484 (1970).

34 R.L. Guldi, J.N. Walpole and R.H. Rediker, J. Appl. Phys. 44, 4896 (1973).

35 J.N. Walpole and R.L. Guldi, J. Nonmetals 1, 227 (1973).

36 B.I. Boltaks, Diffusion in Semiconductors, Academic Press, New York, 1963.

37 W.A. Keenan and P.A. Schumann, Jr., J. Electrochem. Soc. 118, 2010 (1971).

38 C.O. Thomas, D. Khang and R.C. Mang, J. Electrochem. Soc. 109, 1055 (1962).

39 B.L. Morris, J. Electrochem. Soc. 121, 422 (1974).

40 M.R.E. Bichara and J.P.R. Poiterin, IEEE Trans. Instr. Meas. IM-13, 323 (1968).

41 S. Ramo, J.R. Whinnery and T. Van Duzer, Fields and Waves in Communication Electronics, John Wiley and Sons, 1965.

42 J.M. Ziman, Principles of the Theory of Solids, Cambridge Univ. Press, London, 1964

43 J.R. Wait, Electromagnetic Waves in Starified Media, Pergamon Press, New York, 1962.

44 A.R. Calawa (private communication).

45 S.M. Sze, Physics of Semiconductor Devices, John Wiley and Sons, 1969.

46 K.W. Nill, J.N. Walpole, A.R. Calawa and T.C. Harman, in The Physics of Semimetals and Narrow-Gap Semiconductors, eds. D.L. Carter and R.T. Bate, Pergamon Press, 1971, p. 383.

47 A.J. Strauss, J. Electron. Mat. 2, 553 (1973).

48 P.J.A. Zountendyk, PhD. Thesis, California Institute of Technology, E.E. Dept, 1968.

49 K.J. Sleger, G.F. McLane and D.L. Mitchell, J. Nonmetals 1 , 297 (1973).

50 K. Konnerth and C. Lanza, Appl. Phys. Letters 12, 365 (1964).

51 J.E. Ripper, J. Appl. Phys. 43, 1762 (1972).

52 J.C. Dyment, J.E. Ripper and T.P. Lee, J. Appl. Phys. 43, 452 (1972).

53 V.A. Gorbylev, G.T. Pak, A.I. Petrov, N.P. Chernousov, V.I. Shevikin and I.V. Yashumov, Sov. J. Quant. Electron. 1, 505 (1972)

54 R. Dalven, Infrared Phys. 9, 141 (1969).

55 G. Lasher and F. Stern, Phys. Rev. 133 , A553 (1964).

56 R.L. Bernick and L. Kleinman, Sol. St. Comm. 8, 568 (1970).

57 N.S. Baryshev and K. Ya Shtivel'man, Sov. Phys. Semicon. 1, 136 (1967).

58 D.A. Cammack, PhD. Thesis, M.I.T., EE Dept. (1974).

59 H.K. Gummel, IEEE Trans. Electron Devices ED-11, 455 (1964).

60 A. DeMari, Solit-St. Electron. 11, 33 (1968).

61 S. C. Choo, Solid-St. Electron. 14, 1201 (1971).

62 G. Hachtel, R.C. Joy and J.W. Cooley, Proc. IEEE 60, 86 (1972).

63 C. T. Sah, Proc. Instrn. Radio Engrs. 49, 603 (1961).

64 D. P. Kennedy and R. R. O'Brien, IBM J. Res. Dev. 11, 252 (1967).

65 S. P. Morgan and F. M. Smits, Bell Syst. Tech. Jour. 39, 1573 (1960).

66 J. L. Moll (unpublished work), as quoted in Reference 65.

67 J. S. Blakemore, Semiconductor Statistics, Pergamon Press, 1962.

68 W. Shockley, Bell Syst. Tech. Jour. 28, 435 (1949).

69 H. K. Gummel and D. L. Scharfetter, J. Appl. Phys. 38, 2148 (1967).

70 J. N. Zemel, J. D. Jensen and R. B. Schoolar, Phys. Rev. 140, A330 (1965).

71 M. S. Dresselhaus, Notes for Course 6.648, 1972 (unpublished).

72 A. Mycielski, A. Aziza, M. Balkanski, M. Y. Moulin and J. Mycielski, Phys. State. Sol (b) 52, 187 (1972).

73 A. Mycielski, J. Mycielski, A. Aziza and M. Balkanski, in Proc. 10th Int. Conf. on Phys. of Semicond., Warsaw, 1972, p. 1214.

74 E. Burstein, Phys. Rev. 93, 632 (1954).

75 M. Cardona, Modulation Spectroscopy, Sol. St. Phys. Supplement 11, Academic Press, New York (1969).

76 D. L. Mitchell and R. F. Wallis, Phys. Rev. 151, 581 (1966).

77 A. Yariv, Quantum Electronics, John Wiley and Sons, N. Y. 1967.

78 W. W. Scanlon, Phys. Rev. 109, 47 (1958)

79 R. B. Schoolar and J. R. Dixon, Phys. Rev. 137, A667 (1965).

80 V. Prakash, Technical Report HP-13, Div. Eng. Appl. Phys, Harvard Univ. June (1967).

81 M.B. Kurik, Phys. Stat. Solidi 8, 51 (1971).

82 N. Piccioli, J.M. Besson and M. Balkanski, J. Phys. Chem. Solids 35, 971 (1974).

83 F. Wooten, Optical Properties of Solids, Academic Press, New York, 1972.

84 R.F. Wallis, ed., Localized Excitations in Solids, Plenum Press, New York, 1968.

85 B.B. Varga, Phys. Rev. 137, A1896 (1965).

86 C. Kittel, Introduction to Solid State Physics, John Wiley and Sons, New York, 1971.

87 G.W. Pratt, Jr. and J.E. Ripper, J. Appl. Phys. 36, 1525 (1965).

88 L.G. Ferreira, Phys. Rev. 137, A1601 (1965).

89 J.M. Besson, J.F. Butler, A.R. Calawa, W. Paul and R.H. Rediker, App. Phys. Letters 7, 206 (1965).

90 J.M. Besson, W. Paul and A.R. Calawa, Phys, Rev. 173, 699 (1968).

91 P.G. McMullin, PhD. Thesis, M.I.T. , E.E. Dept. (1971).

92 N. Ohashi and K Igaki, Trans. Jap. Inst. Metals 5, 94 (1964).

93 R.F. Bis and J.R. Dison, J. Appl. Phys. 40, 1918 (1969).

94 Y.V. Ilisavskii, Sov. Phys. Solid. St. 4, 674 (1962).

95 I. Chambouleyron, J.M. Besson, M. Balkanski, H. Rodot and H. Abrales, In Proceedings of the 9th Int. Conf. on Phys. of Semicond. (Nauka, Leningrad, 1968), p. 546.

96 T.C. Harman, A.R. Calawa, I. Melngailis and J.D. Dimmock, Appl. Phys. Letters 14, 333 (1969).

97 E.A.J. Mercatili, Bell Syst. Tech. Jour. 43, 2887 (1964).

98 T.H. Zachos and J.E. Ripper, IEEE J. Quant. Electron QE-3, 656 (1967).

99 J. Hatz and E. Mohn, IEEE J. Quant. Electron QE-3, 656 (1967).

100 W.W. Anderson, IEEE J. Quant. Electron, QE-1, 228 (1965).

101 D.F. Nelson and J. McKenna, J. Appl. Phys. 38, 4057 (1967).

102 R.G. Allakhverdyan, A.N. Oraevskii and A. F. Suchkov, Sov. Phys. Semicond. 4, 277 (1970).

103 M. Abramowitz and I.A. Stegun eds., Handbook of Mathematical Functions, U.S. Govt. Printing Office, Washington, D.C. 1964.

104 J.N. Walpole (private communication).

105 T. Ikegami, IEEE J. Quant. Electron. QE-8, 470 (1972).

106 P. McMullin (private communication).

107 E.I. Gordon, IEEE J. Quant. Electron QE-9, 772 (1973).

108 J.K. Butler and J. Zoroofchi, IEEE J. Quant. Electron. QE-10, 809 (1974).

109 J.W. Goodman, Introduction to Fourier Optics, McGraw-Hill, 1968.

110 M. Born and E. Wolf, Principles of Optics, Pergamon Press, 1970.

111 A.R. Goodwin and P.R. Selway, IEEE J. Quant. Electron. QE-6, 285 (1970).

112 R.A. Smith, Wave Mechanics of Crystalline Solids, Chapman and Hall Ltd., London, 1961.

113 C.J. Hwang, Phys. Rev. B 2, 4117 (1970).

114 N.N. Winogradoff and H.K. Kessler, Sol. St. Electronics

9, 217 (1967).

115 G. E. Pikus, Sov. Phys. Sol. St. 7, 2854 (1966).

116 J. N. Walpole (private communication)

117 J. B. Conklin, jr., L. E. Johnson and G. W. Pratt, Jr., Phys. Rev. 137, A1282 (1965).

118 G. W. Pratt, Jr., and L. G. Ferreira, in Proc. Int. Conf. on Phys. Semicon., Dunod, Praid, 1964.

119 S. Rabii, Phys. Rev. 167, 801 (1968).

120 G. Martinez, PhD. Thesis, University of Paris, 1972.

121 K. F. Cuff, M. R. Ellett, C. D. Kuglin and L. R. Williams, Proc 6th Int. Conf. Phys. Semicond., Dunod, Paris, 1964, p. 677.

122 J. Melngailis, T. C. Harman and W. C. Kernan, Phys. Rev. B 5, 2250 (1972).

123 P. A. Wolff, Phys. Rev. 126, 405 (1962).

124 B. I. Halperin and M. Lax, Phys. Rev. 148, 722 (1966).

125 M. Gell-Mann and K. A. Brueckner, Phys. Rev. 106, 364 (1957).

126 J. Hubbard, Proc. Roy. Soc. (London) A240, 539 (1957).

127 J. Schrieffer, Theory of Superconductivity, Benjamin, New York, 1964.

128 G. Mahan, in Polarons in Ionic Crystals and Polar Semiconductors, ed. J. Devreese, North-Holland, 1972.

129 A. Ron, Phys. Rev. 132, 978 (1963).

130 D. Pines, Elementary Excitations in Solids, Benjamin, New York, 1963.

131 P. Wolff (private communication).

132 D. Dunn, Phys. Rev. 174, 855 (1968).

133 G.D. Mahan, Phys. Rev. 145, 602 (1966).

134 Yu.I. Ravich, B.A. Efimora and V.I. Tamarchenko, Phys. Sol. (b) 43, 11 (1971).

135 P. Wolff (unpublished work); see J.J. Quinn, Phys. Rev. 126, 1453 (1962).

BIOGRAPHICAL NOTE

Peter M. Asbeck was born in September, 1947 in Cleveland, Ohio. He studied as an undergraduate at the Massachusetts Institute of Technology. As part of the Co-operative Program of the Department of Electrical Engineering, he worked during several undergraduate terms at RCA Laboratories, Princeton, New Jersey. His graduate studies also have been pursued at the Massachusetts Institute of Technology. He was awarded the S. B., S. M. and E. E. degrees simultaneously in June, 1969. During his graduate program he has been supported by the National Science Foundation, by the Sloan Foundation, and as a Teaching and Research Assistant in the Department of Electrical Engineering.

In October, 1974 he was married to the former Marcia Lynn Burch.